Source and reservoir rocks characterization of the Ling Depression, Central North Sea

Ole Kristian Bergsland Hansen

Master Thesis in Sedimentology
60 Credits

Department of Geosciences
Faculty of Mathematics and Natural Science

UNIVERSITY OF OSLO

01.12.2018

Supervisors: Nazmul Haque Mondol and Jens Jahren

Source and reservoir rocks characterization of the Ling Depression, Central North Sea

The work is published digitally through DUO – “Digitale Utgivelser ved UiO”

http://www.duo.uio.no/

Printing: Reprosentralen, University of Oslo

Preface

The research was carried out through 2018 (1st January to 30th November) at the Department of Geosciences, University of Oslo (UiO), under supervision by Associate Professor Nazmul Haque Mondol and Professor Jens Jahren.

The thesis is completed as part of the "*ReSource - Quantitative Analysis of Reservoir, Cap and Source Rocks of the Central North Sea*" project in candidacy of the degree of Master of Science in Sedimentology.

Acknowledgments

I would like to express my gratitude to my supervisors Associate Professor Nazmul Haque Mondol and Professor Jens Jahren for providing this project along with guidance and motivation throughout this year. Their vast knowledge has been of great value and inspiration during the Master program and while writing this thesis.

Eni Norge is thanked for funding of the ReSource project. Contributions and assistance from the other project members are also acknowledged, especially PhD candidate Jørgen André Hansen. Also, thanks to the BMGB team in Equinor for providing relevant work during my summer internship and sharing their enthusiasm for petroleum systems and source rocks.

I am forever grateful for the continuous support from my friends and family. Special thanks to my fellow students and “roommates” Even and Muna, and to my friends in *Kunstes*. Shout out to Jarle for proofreading.

Abstract

This study presents source and reservoir characterization of Jurassic rocks by conducting compaction study, petrophysical analysis and rock physics diagnostics on data from 18 exploration wells in the Central North Sea, focusing on the Ling Depression and adjacent areas. Reservoir potential has been analyzed for the Jurassic Hugin, Sandnes and Bryne Formations, while source rock potential has been assessed for the Jurassic Draupne, Tau, Bryne and Fjerritslev Formations.

The compaction study utilizes published V_P- and density-depth trends, uplift estimates, rock physics cement models and shear modulus-density plots and reveals an average transition zone between mechanical and chemical compaction regime at 1706 m BSF present depth and 1942 m BSF corrected for uplift. A more general transition zone is proposed, represented by a shear wave velocity of 1.45 km/s and shear modulus of 5-6 GPa, as both parameters show a distinct change compared to density at these values. This indication of increasing stiffness correlate with predicted onset of cementation and thus, chemical compaction. All Jurassic reservoirs are calculated to be situated below the transition zone at maximum burial, which is in line with calculated cement volumes from ~4-22%. Deeper burial compared to estimated transition zone correlates well with increasing calculated cement volume. Jurassic source rock intervals are observed to deviate from normal compaction trends of shale/clay. Comparison of source rock formation with different levels of maximum burial depths show that increasing compaction and diagenesis are the primary cause of changing elastic parameters in organic-rich shales. However, increasing TOC and deep resistivity (maturation indicator) are individually observed to shift the data towards lower V_P/V_S and AI compared to organic-lean shales, which is noticeably different than expected from only increasing burial and compaction.

Petrophysical analysis identified reservoir potential in Hugin, Sandnes and Bryne Formation in all wells they were present. Full formation interval analysis reveals superior reservoir potential in Hugin Formation, with lowest shale volume, highest porosity and highest net-to-gross. Sandnes and Bryne Formation show excellent reservoir potential in some wells (e.g. 17/3-1 and 17/12-3) but generally have a higher shale volume and lower porosities than Hugin Formation.

Available geochemical data indicate mainly oil-prone immature-early mature kerogen type II in the Tau and Draupne Formations, while slightly more mature but lower quality kerogen type III is indicated for Bryne and Fjerritslev Formations. Estimated values of TOC, using the ΔlogR method, correlate well with measured values and generally reveal an upwards increasing TOC profile for Tau, Draupne and Bryne Formations. This is observed to yield an upwards-decreasing AI trend and, consequently, expected to produce the highest seismic amplitude at the top of the formation. High TOC correlates with high intrinsic anisotropy and, thus, a AVO Class 4 signature is generally expected from the top Tau and Draupne Formations seismic reflections.

Table of Contents

Preface ... III
Acknowledgments ... IV
Abstract ... V
Table of Contents ... VII
List of Figures ... X
List of Tables ... XVI
1. Introduction ... 1
  1.1. Background and motivation ... 1
  1.2. Research objectives ... 2
  1.3. Study area ... 2
  1.4. Database and software ... 3
  1.5. Chapter descriptions ... 6
  1.6. Limitations and further work ... 7
2. Geological setting ... 8
  2.1. Regional tectonic and structural evolution ... 8
  2.2. Structural elements ... 10
    2.2.1. Ling Depression ... 11
    2.2.2. Åsta Graben ... 11
    2.2.3. Egersund Basin ... 11
    2.2.4. Southern Viking Graben ... 12
  2.3. Stratigraphy ... 12
    2.3.1. Rotliegend Group ... 13
    2.3.2. Hegre Group ... 13
    2.3.3. Vestland Group ... 13
    2.3.4. Boknfjord Group ... 17
    2.3.5. Viking Group ... 17
  2.4. Petroleum system ... 21
    2.4.1. Source rocks ... 22
    2.4.2. Reservoir rocks ... 25
    2.4.3. Cap rocks and traps ... 26
    2.4.4. Uplift and seal failure ... 27

3. Research methodologies and theoretical background 29
3.1. Workflow 29
3.2. Compaction study and uplift estimation 29
3.2.1. Compaction 29
3.2.2. Uplift estimation 33
3.3. Petrophysical analysis 35
3.3.1. Lithology discrimination and net-to-gross estimation 36
3.3.2. Shale volume calculation 37
3.3.3. Porosity estimation 38
3.3.4. Water saturation and pay zone identification 42
3.3.5. Permeability estimation 44
3.3.6. Source rock identification and TOC prediction 44
3.4. Rock physics 46
3.4.1. Cement models 46
3.4.2. Rock physics templates 49
4. Compaction Study 52
4.1. Results 52
4.1.1. Geothermal gradient 52
4.1.2. Compaction trends 52
4.1.3. Shale compaction 55
4.1.4. Sandstone compaction 59
4.1.5. Transition zone identification 60
4.1.6. Uplift estimation 66
4.1.7. Reservoir rock analysis 68
4.1.8. Source rock analysis 74
4.2. Discussion 77
4.2.1. Temperature 77
4.2.2. Compaction 78
4.2.3. Transition zone 79
4.2.4. Uplift estimates 81
4.2.5. Effects on elastic properties of source rocks 82
4.2.6. Implications 83
4.3. Uncertainties 85

5. Petrophysical Analysis 86
  5.1. Results 86
    5.1.1. Evaluation of reservoir potential 88
    5.1.2. Sandnes Formation 89
    5.1.3. Bryne Formation 92
    5.1.4. Hugin Formation 94
    5.1.5. Permeability 97
    5.1.6. TOC estimation 99
  5.2. Discussion 104
    5.2.1. Jurassic reservoirs 104
    5.2.2. CO_2 storage potential 110
    5.2.3. Jurassic source rocks 113
  5.3. Uncertainties 118
6. Summary and conclusions 121
References 126
Appendix A – Uplift corrections 135
Appendix B – Well sections 151

List of Figures

Figure 1.1: Map from NPD displaying their availability of data in the North Sea. The Ling Depression study area is marked by the white box, Yme field is shown in green circle (modified from Halland et al., 2014)………………………………………………...1
Figure 1.2: Map shows the study area, including Ling Depression (black line) and all well included in the study (red circles). Small map showing regional position of the study area (modified after NPD, 2018)…………………………….................………3
Figure 2.1: Regional map of the North Sea region, including main faults trends and shear zones. Note how the Ling Depression is a continuation of the Hardangerfjord Shear Zone. HZF, Hardangerfjord Shear Zone; BASZ, Bergen Arcs Shear Zone; NSD, Nordfjord-Sogn Detachment; KSZ, Karmøy Shear Zone; RSZ, Røldal Shear Zone. From (Fossen & Hurich, 2005)…………………………………………………...9
Figure 2.2: Structural map of the Norwegian North Sea (modified from Halland et al., 2014)………………………………………………………………………….10
Figure 2.3: Cross-section of Egersund Basin (modified from Halland et al., 2014)..…….....12
Figure 2.4: Core photographs of the Sandnes Formation (3155-3160 m MD) from well 9/2-2 (left) and Bryne Fm (2410-2415 m MD) from well 17/3-1 (right) (Source: NPD, 2018)..14
Figure 2.5: Core photograph of Hugin Formation (3248-3254m MD) from well 15/9-18 (not included in this study). No core photographs of Hugin Formation from studied wells were available (Source: NPD, 2018)..15
Figure: 2.6: Lithostratigraphy of the North Sea. The columns of Norwegian-Danish Basin and Southern Viking Graben are most representative for the study area (from Halland et al., 2014)..16
Figure 2.7: Core photograph of the Draupne Fm (2750-2755m MD) from well 30/9-10 (not included in this study. No core photographs of Hugin Formation from studied wells were available (Source: NPD, 2018)..18
Figure 2.8: Main reasons reported for dry targets in the North Sea, Norwegian Sea and Barents Sea in percentages (Source: NPD, 2018)..22
Figure 2.9: Well correlation of the nine wells in the western part of the study area where Draupne Formation is the dominating Upper Jurassic source rock unit. It is easily recognizable in this figure by mainly red and orange colors in the gamma ray log. The wells are flattened on Top Draupne Formation...24
Figure 2.10: Upper Triassic, Lower to Middle Jurassic and Sub-Triassic plays in the Central North Sea (modified from NPD, 2017)..25
Figure 2.11: Correlation between hydrocarbon phase and caprock quality. Upper figure is typical type 1 trap which will spill oil and only leak gas due to potential fracturing. Type 2/3 trap is shown in lower figure, where gas will leak due to membrane fail, while oil will be retained (Ohm et al., 2008)...28
Figure 3.1: Chart of preferred workflow in this study...29
Figure 3.2: Overview of sandstone diagenesis (Bjørlykke and Jahren, 2015).........................30
Figure 3.3: Illustration of how uplift estimation workflow. A maximum burial example is showed to the left with an associated porosity/velocity versus depth curve. This curve is typically projected using a suitable normal compaction trend. Uplift, erosion and the resulting curve is depicted in the middle. The difference between the normal compaction curve and the uplifted one equals the gross exhumation. An example of post exhumation re-burial is portrayed to the right. Re-burial will shift the uplifted curve towards the normally compacted one, depending on the amount of re-burial.

B_{max} is the maximum burial, E_G is the gross exhumation, B_E is the thickness of post exhumation reburial and E_N is net exhumation (modified from Corcoran and Doré, 2005)........34
Figure 3.4: Overview of main logs used in petrophysical analysis. Several of these logs are referred to with different names in other wells, e.g. DEN=RHOB and NEU=CN. Example from well 17/12-4........35
Figure 3.6: Neutron versus density crossplots of the Sandnes Fm in well 9/2-1. A) Color coded by shale volume showing decreasing shale volume towards the sandstone line. B) Color coded by deep resistivity to identify hydrocarbons with direct measurements. Also note how increasing density and neutron readings is indicative of increasing porosities. C) Color coded by calculated water saturation. As expected in a sandstone reservoir, hydrocarbon accumulations plot from the sandstone line towards lower densities. SS: sandstone, LS: limestone, DOL: dolomite........40
Figure 3.7: Different definitions of formation volumes. The subscripts ma: matrix, dcl: dry clay, cl: wet clay, cbw: clay bound water, cap: capillary bound water, fw: free water, hyd: hydrocarbon, b: bulk, p: porosity, e: effective and t: total (Ellis & Singer, 2007)........42
Figure 3.8: Deep Resistivity (RD) and sonic (DT) log separation example from well 15/12-2. The curves follow each other close in the organic-lean Åsgard Fm, while showing significant negative separation in the organic-rich Draupne Fm. The lack of response of the resistivity log suggests immature source rock........45
Figure 3.9: Three effective medium models for high-porosity sands in the elastic-modulus-porosity plane (Avseth, et al., 2000)........48
Figure 3.10: Interpretation of a rock physics template in terms of shale/clay volume, fluid content, compaction/cementation. Increasing TOC and maturation of source rock are expected to have similar effects on the shale trend as the increasing gas saturation has on a brine sand (Ødegaard and Avseth, 2003)........50
Figure 3.11: Lambda-Mu-Rho crossplot with lithology separation. SH: Shale, SS: sandstone, SS_G: gas sand, SS_T: cemented sandstone, CO_3: carbonate (Gray & Andersen, 2000)..51
Figure 4.1: Present day geothermal gradient in the study area based on bottom hole temperatures reported by NPD (2018)........52
Figure 4.2: Density versus depth (left) and V_p versus depth (right) plots. All wells (except 15/3-8 and 15/8-2) included in the plots. All depths in meters below sea floor (m BSF). The color code is temperature. MC=mechanical compaction, CC=chemical compaction........53
Figure 4.3: Density versus V_p crossplots including all data (left) and shale only (V_{sh}>0.67) (right). Color coded by temperature. CC=chemical compaction, MC=mechanical compaction, TZ=transition zone........54
Figure 4.4: V_p versus depth plot including all wells (except 15/3-8 and 15/8-2). Color coded by temperature. Published compaction trends (see legend) are plotted on top of the data for comparison........55
Figure 4.5: V_p versus depth plot with shale only (V_{sh}>0.67 cutoff). Color coded by temperature. Published clay compaction trend added for comparison (see legend for detail)........56
Figure 4.6: Well 15/12-2 V_p versus depth crossplots color coded with formation names (a), temperature (b) and lithology (c). Well 16/10-3 V_p versus depth crossplots color coded with formation names (d), temperature (e) and lithology (f). c) and f) includes shale points only with V_{sh}>0.5 cutoff. MC=mechanical compaction, CC=chemical compaction, TZ=transition zone........57

Figure 4.7: V_p versus depth plot of only shale points from Tau Formation in the studied wells. The color bar is temperature. Published clay compaction trends (see legend) are added for comparison....58
Figure 4.8: V_p versus depth plot of sandstone data ($V_{sh}<0.33$ cutoff) for all wells (excluding 15/3-8 and 15/8-2), color coded by temperature. Sandstone-relevant compaction trends (see legend) plotted for comparison....59
Figure 4.9: V_p versus depth plots of well 17/3-1 (left) and 17/12-1 (right) only showing sandstone points ($V_{sh}<0.33$) color coded by temperature. Published sand compaction trends (see legend) plotted for comparison....60
Figure 4.12: V_p versus depth plot of a) well 15/12-3 and b) well 17/4-1 color coded by shale volume. MC=mechanical compaction, CC=chemical compaction, TZ=transition zone....61
Figure 4.13: Density versus V_s plot including all wells with V_s data available. Color coded by shale volume....62
Figure 4.14: Density versus shear modulus plot of all wells with V_s data available. Color coded by temperature. Shaly lithologies only ($V_{sh}>0.5$ cutoff). Stippled line indicates estimated transition zone....63
Figure 4.15: Density versus V_s crossplot, color coded with shear modulus. Stippled line indicate estimated transition zone....65
Figure 4.17: V_p versus depth plot of well 17/3-1 showing uplift estimation. Depth is adjusted to provide best fit with trend (see legend) and hence simulate maximum burial....67
Figure 4.18: Uplift estimation gradient map of the study area. Western border of dark blue indicates zero uplift....67
Figure 4.19: V_p versus depth plots of the Hugin and Sandnes Formations, the main reservoir intervals. a) Present day depth BSF, b) depth BSF corrected for uplift. Color coded by temperature. Published sand compaction trends (see legend) plotted for comparison.70
Figure 4.20: V_p versus depth plots (corrected for uplift) of the a) Hugin Formation in well 15/12-22 and b) the Sandnes and Bryne Formations in well 17/3-1....71
Figure 4.21: Sandnes Formation (9/2-11, 17/6-1, 17/12-4) and Hugin Formation (15/12-22) in V_s versus total porosity crossplot (left). The same data color-coded with calculated cement volume (right)....72
Figure 4.22: V_s versus total porosity crossplot Bryne Formation (from well 9/2-11, 17/6-1 and 17/12-4) (left). The same data color-coded with calculated cement volume (right).....72
Figure 4.23: Sandnes Formation from well 9/2-11 and Hugin Formation from well 15/12-22 in the LMR crossplot (left) color coded by cement volume (right)....74
Figure 4.24: Comparison of source rock formations at four different levels of maximum burial in a V_p/V_s versus AI crossplot. Color coded by well (left) and uplift-corrected depth BSF (right)....75
Figure 4.25: Comparison of source rock formations at four different levels of maximum burial in a V_p/V_s versus AI crossplot (color coded by estimated TOC (left) and deep resistivity (right)....76
Figure 4.26: Comparison of source rock formations at four different levels of maximum burial in a LMR crossplot (color coded by wells (left) and deep resistivity data (right)........77
Figure 4.27: V_p versus depth plot for shales in well 15/12-1 overlain by the Kaolinite-Silt compaction curve from Mondol (2009), and corresponding compositions of quartz and K-feldspar and quartz from Berstad and Dypvik (1982) (Koochak Zadeh, et al., 2014)....78
Figure 4.28: Stratigraphy, gamma ray, TOC, density and V_p plots with compaction trend from Mondol (2009) and quantitative mineralogy from well 9/2-1. Labels represent (a)

transition zone suggested in this study, (b) onset of and (c) intense chemical compaction suggested by Kalani et al. (2015)..........79
Figure 4.29: Thin section of core sample from 2831.8 mBSF in Hugin Formation from well 15/12-2. Label a) indicate illitizated kaolinite. From petrographic study of well 15/12-2 available from NPD (2018)..........80
Figure 4.30: The role of uplift and erosion on processes affecting hydrocarbon prospectivity (modified from Henriksen et al., 2011)..........83
Figure 4.31: Illustration of how remigration may occur due to differential uplift as a result of isostatic rebound (Wesenlund, 2016)..........84
Figure 5.1: Left: Top Sandnes Formation depth map. Depth in m MDKB. Right: Thickness map of the Sandnes Formation based on interpolation between wells. Yellow lines represent structural elements. Mainland Norway is situated in the upper right corner.89
Figure 5.2: Sandnes Formation in well 17/6-1 (Svaneøgle). The whole formation is considered a reservoir in this well. The depth interval is 2630-2647 m MDKB..........90
Figure 5.3: The Sandnes Formation in well 9/2-1 (Yme). Reservoir interval in blue shading.91
Figure 5.4: Top Bryne Formation depth map. Depths in MDKB..........92
Figure 5.5: The Bryne Formation in well 17/12-4 (Vette)..........94
Figure 5.6: Top Hugin Formation depth map. Depth in MDRKB..........95
Figure 5.7: Hugin Formation in well 16/10-3. Draupne Formation is above, and Skagerrak Formation is below..........96
Figure 5.8: Comparison of measured and estimated porosity- and permeability data from well 17/3-1. PERMT: Timur equation, PERMWRT: Wylie-Rose equation with Timur parameters, PERMWRMB: Wylie-Rose equation with Morris-Biggs parameters.......97
Figure 5.9: Example of permeability prediction from well 9/2-1 (Yme). PERMT: Timur equation, PERMWRT: Wylie-Rose equation with Timur parameters, PERMWRMB: Wylie-Rose equation with Morris-Biggs parameters..........98
Figure 5.10: T_{max} versus HI plot with samples from Draupne and Tau Formations. The four lines indicate where the different types of kerogen should plot. The areas at the bottom indicate where samples should plot with respect to maturity..........99
Figure 5.11: T_{max} versus HI plot with samples from Bryne Fm. The four lines indicate where the different types of kerogen should plot. The areas at the bottom indicate where samples should plot with respect to maturity..........100
Figure 5.12: Well panel from Tau Formation of well 9/2-1 showing separation between the deep resistivity and velocity curves in the organic-rich part. The estimated TOC using the Passey et al. (Passey, et al., 1990) and Vernik and Landis (Vernik & Landis, 1996) methods are also shown in a panel with measured TOC..........101
Figure 5.13: Diagram with measured TOC and TOC estimates for each of the four relevant formations. Template with shades of green indicates TOC richness classification. All value in wt.%. No measurement available is indicated by the value 0..........103
Figure 5.14: Average reservoir properties for the three formations with reservoir potential in this study..........104
Figure 5.15: Depositional environments of selected formations found in the North Sea. From Halland et al. (2014)..........105
Figure 5.16: A) Lithology log of Sandnes Formation, well 17/3-1 (modified from Javed, 2013). B) Core and well logs with facies associations of Sandnes Formation, well 9/2-1 (modified from Mannie et al., 2014). FS: possible flooding surface..........106
Figure 5.17: Thorium/Uranium-ratio from spectral gamma log in well a) 9/2-1, b) 15/12-23, c) 17/6-1 and d) 17/12-4. Note that different formations are included in each plot. Note also different colors for similar formations..........108

Figure 5.18: Typical approach for assessing the suitability of geological formations for CO_2 storage (Halland, et al., 2014)........111
Figure 5.19: Formation of marine source rocks. Note how only a small fraction of the organic matter is preserved (Bjørlykke, 2015d)........114
Figure 5.20: a) 17/6-1 well log data b) TOC versus AI crossplot of Tau Formation from 17/6-1........115
Figure 5.21: Example of density log (g/cm^3), TOC profile and associated near trace seismic section of an Upper Jurassic organic-rich shale (Spekk Formation) (modified from Løseth et al., 2011)........115
Figure 5.22: a) 17/6-1 well log data b) TOC versus AI crossplot of Bryne and Fjerritslev Formations of well 17/6-1........118
Figure A.1: V_P-depth plot showing shale data from well 9/2-1 corrected for uplift. Depth is adjusted to provide best fit with Kaolinite-Silt 50:50 trend (see legend) above assumed transition zone and hence simulate maximum burial........134
Figure A.2: V_P-depth plot showing shale data from well 9/2-2 corrected for uplift. Depth is adjusted to provide best fit with Kaolinite-Silt 50:50 trend (see legend) above assumed transition zone and hence simulate maximum burial........135
Figure A.3: V_P-depth plot showing shale data from well 9/2-11 corrected for uplift. Depth is adjusted to provide best fit with Kaolinite-Silt 50:50 trend (see legend) above assumed transition zone and hence simulate maximum burial........136
Figure A.4: V_P-depth plot showing shale data from well 15/12-2 corrected for uplift. Depth is adjusted to provide best fit with Kaolinite-Silt 50:50 trend (see legend) above assumed transition zone and hence simulate maximum burial........137
Figure A.5: V_P-depth plot showing shale data from well 15/12-3 corrected for uplift. Depth is adjusted to provide best fit with Kaolinite-Silt 50:50 trend (see legend) above assumed transition zone and hence simulate maximum burial........138
Figure A.6: V_P-depth plot showing shale data from well 15/12-22 corrected for uplift. Depth is adjusted to provide best fit with Kaolinite-Silt 50:50 trend (see legend) above assumed transition zone and hence simulate maximum burial........139
Figure A.7: V_P-depth plot showing shale data from well 15/12-23 corrected for uplift. Depth is adjusted to provide best fit with Kaolinite-Silt 50:50 trend (see legend) above assumed transition zone and hence simulate maximum burial........140
Figure A.8: V_P-depth plot showing shale data from well 16/8-3S corrected for uplift. Depth is adjusted to provide best fit with Kaolinite-Silt 50:50 trend (see legend) above assumed transition zone and hence simulate maximum burial........141
Figure A.9: V_P-depth plot showing shale data from well 16/10-3 corrected for uplift. Depth is adjusted to provide best fit with Kaolinite-Silt 50:50 trend (see legend) above assumed transition zone and hence simulate maximum burial........142
Figure A.10: V_P-depth plot showing shale data from well 17/3-1 corrected for uplift. Depth is adjusted to provide best fit with Kaolinite-Silt 50:50 trend (see legend) above assumed transition zone and hence simulate maximum burial........143
Figure A.11: V_P-depth plot showing shale data from well 17/4-1 corrected for uplift. Depth is adjusted to provide best fit with Kaolinite-Silt 50:50 trend (see legend) above assumed transition zone and hence simulate maximum burial........144
Figure A.12: V_P-depth plot showing shale data from well 17/6-1 corrected for uplift. Depth is adjusted to provide best fit with Kaolinite-Silt 50:50 trend (see legend) above assumed transition zone and hence simulate maximum burial........145
Figure A.13: V_P-depth plot showing shale data from well 17/9-1 corrected for uplift. Depth is adjusted to provide best fit with Kaolinite-Silt 50:50 trend (see legend) above assumed transition zone and hence simulate maximum burial........146

Figure A.14: V_P-depth plot showing shale data from well 17/12-1 corrected for uplift. Depth is adjusted to provide best fit with Kaolinite-Silt 50:50 trend (see legend) above assumed transition zone and hence simulate maximum burial..................................147
Figure A.15: V_P-depth plot showing shale data from well 17/12-3 corrected for uplift. Depth is adjusted to provide best fit with Kaolinite-Silt 50:50 trend (see legend) above assumed transition zone and hence simulate maximum burial..................................148
Figure A.16: V_P-depth plot showing shale data from well 17/12-4 corrected for uplift. Depth is adjusted to provide best fit with Kaolinite-Silt 50:50 trend (see legend) above assumed transition zone and hence simulate maximum burial..................................149
Figure B.1: Complete well 9/2-1 for reservoir target formations..150
Figure B.2: Complete well 9/2-2 for reservoir target formations..151
Figure B.3: Complete well 9/2-11 for reservoir target formations..152
Figure B.4: Complete well 17/3-1 for reservoir target formations..153
Figure B.5: Complete well 17/6-1 for reservoir target formations..154
Figure B.6: Complete well 17/9-1 for reservoir target formations..155
Figure B.7: Complete well 17/12-1 for reservoir target formations......................................156
Figure B.8: Complete well 17/12-3 for reservoir target formations......................................157
Figure B.9: Complete well 17/12-4 for reservoir target formations......................................158
Figure B.10: Complete well 15/8-2 for reservoir target formations......................................159
Figure B.11: Complete well 15/12-2 for reservoir target formations....................................160
Figure B.12: Complete well 15/12-22 for reservoir target formations..................................161
Figure B.13: Complete well 16/10-3 for reservoir target formations....................................162
Figure B.14: Complete well 17/4-1 for reservoir target formations......................................163

List of Tables

Table 1.1: General information about the wells included in this study (NPD, 2018)................4
Table 1.2: Available well log data from each well...5
Table 2.1: Depth of penetrated stratigraphic units in the eastern part of the study area. Based on data from NPD (2018)...19
Table 4.2: Depth of penetrated stratigraphic units in the western part of the study area. Based on data from NPD (2018)...20
Table 3.1: Utilized cutoff values for calculation of net thicknesses. Values are chosen with inspiration from Worthington and Cosentino (2005)..37
Table 3.2: Mineral parameters utilized for rock physics diagnostics. Based on Mavko et al. (2009)...49
Table 4.1: Results from uplift and transition zone estimation using P-wave velocities and temperature...66
Table 4.2: Top reservoir depths compared with two different transition zone estimates.........68
Table 4.3: Average cement volume of reservoir formations calculated using the relation from Marcussen et al. (2010). Red indicating formation not present in well.......................69
Table 4.4: Comparison of uplift estimation from this study and other published studies, for a selection of wells in the study area...82
Table 5.1: Results from evaluation of the overall reservoir potential of the Sandnes, Bryne and Hugin Formations. Only wells penetrating the formations are included. Evaluations from well 17/12-1 is missing due to insufficient well data. Well 9/2-11 was drilled to TD at 2861 m MDKB within the Bryne Formation and thickness of the formation is therefore not known in this well..88
Table 5.2: Petrophysical analysis of reservoir intervals of the Sandnes Formation................90
Table 5.3: Petrophysical analysis of reservoir intervals in the Bryne Formation....................93
Table 5.4: Petrophysical analysis of reservoir cutoff intervals in the Hugin Formation..........96
Table 5.5: Results from TOC estimation using methods from Passey et al. (1990) and Vernik and Landis (1996) and comparison with measured data from samples made available by NPD (2018). All TOC values in weight percent. Depths in m MDKB.................102

1.Introduction

1.1. Background and motivation

This thesis is a part of the research project titled "ReSource - Quantitative Analysis of Reservoir, Cap and Source Rocks of the Central North Sea". The project investigates reservoir, cap and source rocks for better understanding of the hydrocarbon potential of the central North Sea. The source and reservoir rock units found in the structural element known as the Ling Depression and adjacent areas are focused in this study.

The Central North Sea has been explored for commercial hydrocarbon accumulations since the 1960s, but several parts, such as the NE Ling Depression and the Åsta Graben remains immature in regard to the low density of exploration wells. While many of the drilled wells have proved to be dry, most of them have proven a petroleum system with potential cap, reservoir and source rock units. One critical issue is the maturity of source rocks due to relatively shallow burial in the Central North Sea. Based on dry wells and source rock maturity, Halland et al. (2014) proposed a line of approximate limit for significant hydrocarbon migration across the North Sea (Figure 1.1).

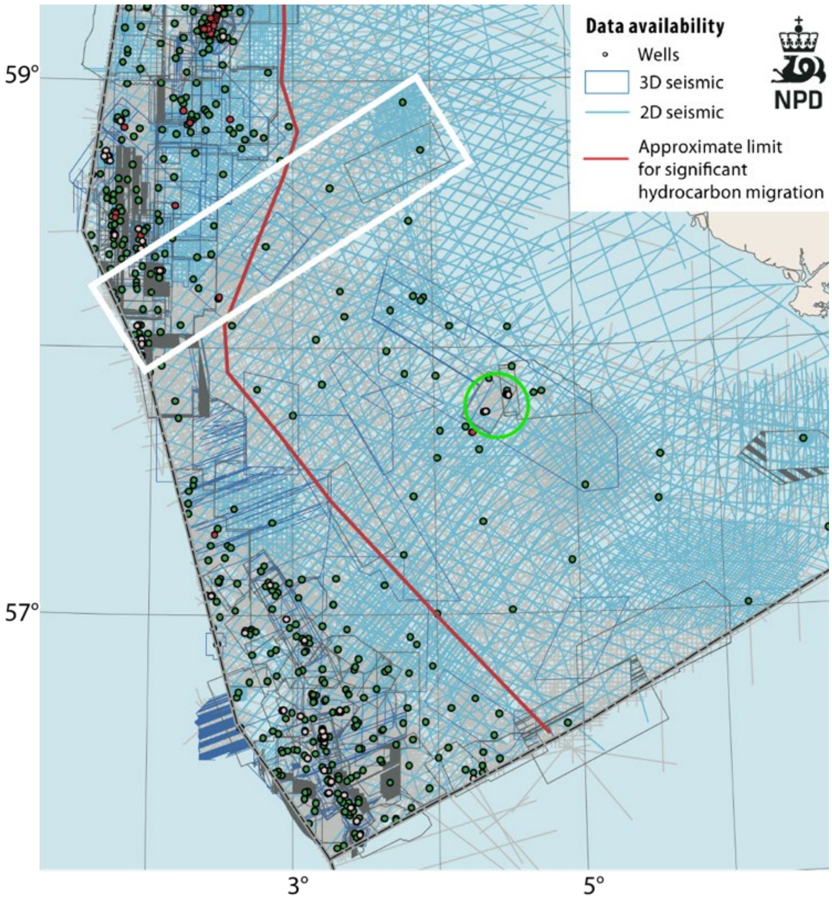

Figure 1.1: Map from NPD displaying their availability of data in the North Sea. The Ling Depression study area is marked by the white box, Yme field is shown in green circle (modified from Halland et al., 2014).

Most of the areas focused in this study are situated outside of the limit of hydrocarbon migration. However, despite unfavorable burial depths, some fields and discoveries have been made (e.g. Yme field) outside the proposed limit of significant petroleum migration.

Such outliers prove the potential of the area and are the reason for prolonged exploration interest. Understanding the factors controlling the maturity of the potential source rock units is the key to understand the true hydrocarbon potential in the area.

1.2. **Research objectives**

The main objective of this research is to characterize the source and reservoir rock intervals found in the Ling Depression and adjacent areas. This includes mainly the Sandnes Fm of the Middle Jurassic Vestland Gp and the Tau Fm of the Upper Jurassic Boknfjord Gp in the eastern part of the study area. The Hugin Fm of the Middle Jurassic Vestland Gp and the Draupne Fm of the Upper Jurassic Viking Gp are the most relevant units in the western part of the study area.

A selection of wells from the Ling Depression is utilized, as well as examples from nearby discoveries such as Yme and Gudrun are considered for comparison to investigate working petroleum systems in the study area. The research tasks focused in the study are as follows:

- Establish well-to-well correlation and QC of available well log data. Petrophysical analysis is performed to evaluate reservoir quality and source rock potential. This includes estimation of shale volume, net-to-gross ratio, porosity, permeability and hydrocarbon saturation of the reservoir and TOC estimation of source rock units.
- Compaction study is performed to identify zones of mechanical and chemical compaction. By utilizing depth trends, the transition zones are constrained, and uplift is estimated.
- Rock physics diagnostics is utilized to link elastic parameters to geological processes. This allows for interpretation of sorting and cement trends and effects of hydrocarbon presence, organic content and thermal maturity.

1.3. **Study area**

The major focus of the study is the Ling Depression (Figure 1.2). The Ling Depression is a structural depression located in the Central North Sea. Bordering the Ling Depression are the Sleipner Terrace, the Utsira High, Øygarden Fault Complex and the Stavanger Platform in the north, the Åsta Graben, the Sele High, the Danish-Norwegian Basin and Jæren High in the south, and the Maureen Terrace, the Andrew Ridge and the Ve Sub-basin in the west. Most of the analyzed wells are from the Ling Depression. Wells from Åsta Graben (17/9-1) and the Egersund Basin (17/12-1, 17/12-3, 17/12-4, 9/2-1, 9/2-2 and 9/2-11) are included for better understanding of the petroleum potential and geology in the adjacent areas. Well 15/3-8 (Gudrun) and 15/8-2 is situated in the southern Viking Graben and include mature source rock units used for comparison with the more immature source rock units found in the Ling Depression. All study areas are marked in Figure 1.2.

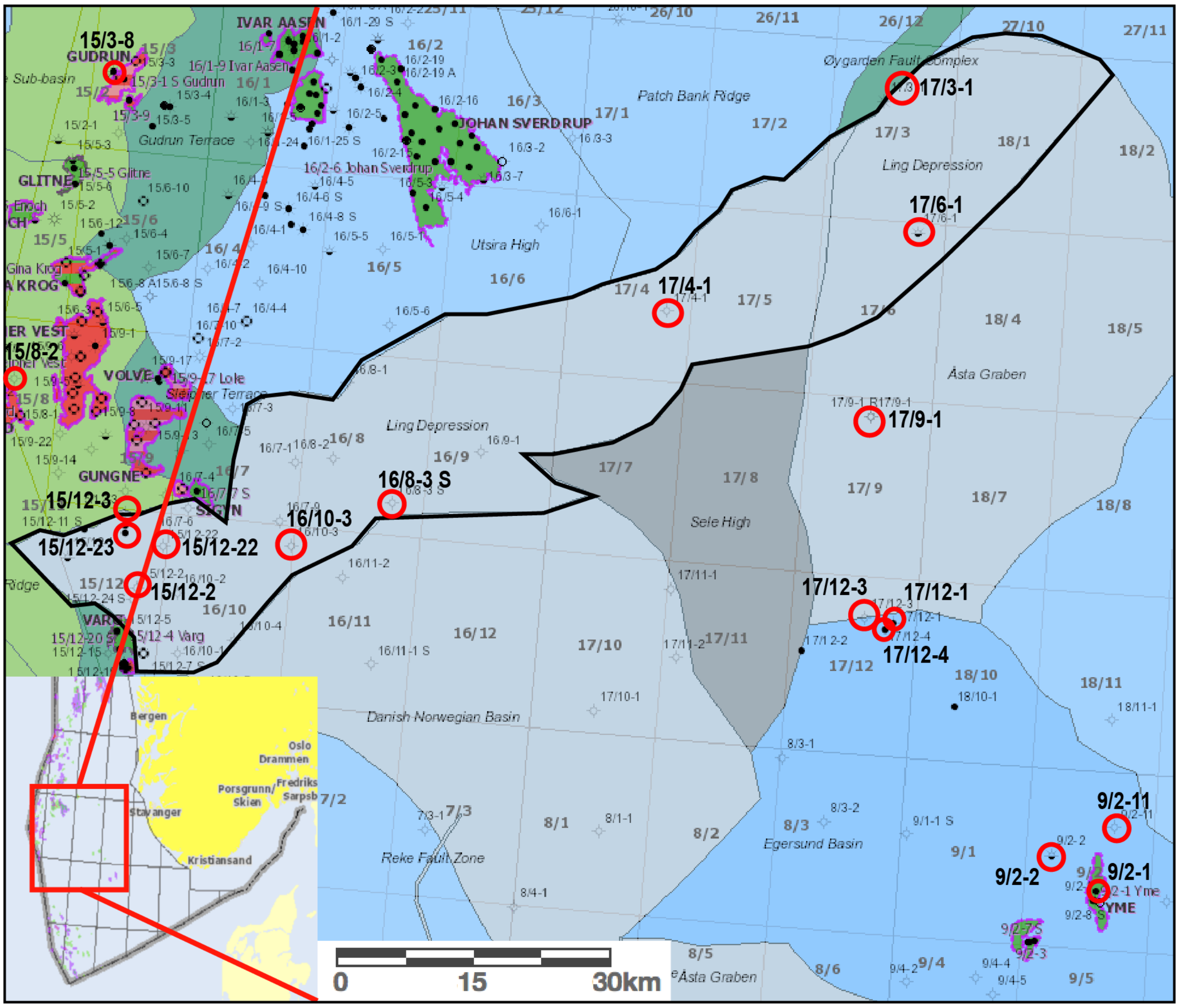

Figure 1.2: Map shows the study area, including Ling Depression (black line) and all well included in the study (red circles). Small map shows regional position of the study area (modified after NPD, 2018).

1.4. Database and software

This study is based on the available data from 18 wells drilled between 1968 and 2013 in the Central North Sea. All the analyzed wells are situated within the marked areas of Figure 1.2. Published literature and information available on the NPD website are utilized throughout the thesis.

General information about the evaluated wells is provided in Table 1.1. Available well logs from each well are presented in Table 1.2.

Table 1.1: General information about the wells included in this study (NPD, 2018).

Well	9/2-1	9/2-2	9/2-11	15/3-8	15/8-2	15/12-2	15/12-3	15/12-22	15/12-23	16/8-3 S	16/10-3	17/3-1	17/4-1	17/6-1	17/9-1	17/12-1	17/12-3	17/12-4
NS Degrees	57° 49' 58.1" N	57° 52' 44.35" N	57° 55' 21.46" N	58° 51' 21.7" N	58° 24' 55.1" N	58° 8' 31.05" N	58° 14' 36.59" N	58° 12' 12.3" N	58° 13' 0.78" N	58° 17' 43.4" N	58° 13' 18.54" N	58° 55' 2.5" N	58° 35' 54" N	58° 44' 15.46" N	58° 28' 27.26" N	58° 11' 17.3" N	58° 11' 32.84" N	58° 10' 37.58" N
EW Degrees	4° 31' 27.92" E	4° 24' 0.69" E	4° 33' 35.71" E	1° 43' 17" E	1° 32' 49.9" E	1° 55' 47.27" E	1° 52' 45.67" E	1° 59' 14.4" E	1° 53' 3.87" E	2° 34' 54.5" E	2° 19' 34.3" E	3° 48' 21.33" E	3° 16' 5" E	3° 55' 34.93" E	3° 50' 16.18" E	3° 56' 22.2" E	3° 51' 44.06" E	3° 55' 11.05" E
Year completed	1987	1987	2010	2006	2011	1976	1980	2010	2010	2013	1996	1995	1968	2011	1973	1972	1980	2009
Content	OIL	OIL SHOWS	DRY	OIL/GAS	DRY	DRY	DRY	DRY	OIL	DRY	DRY	GAS	DRY	OIL SHOWS	DRY	OIL	DRY	OIL
Prospect name	Yme	Alpha	Aubrey	Gudrun	Dr. No	N/A	N/A	Storkollen	Grevling	Lupin	Tyr Central	Bark	N/A	Svaneøgle	N/A	Bream	N/A	Vette
KB [m]	29.0	22.0	26.0	23.5	25	25.0	25.0	25.0	26.0	25.0	40.0	25.0	27.0	18.0	9.0	27.0	25.0	18.0
Water depth [m]	99.0	99.0	101.0	109.0	119	86.0	86.0	82.5	86.5	72.0	75.0	273.0	105.0	272.0	159.0	115.0	111.0	110.0
Total depth [m RKB]	3756.0	3550.0	2861.0	4592.0	4386.0	2924.0	4450.0	3035.0	3485.0	3262.0	2850.0	2852.0	3997.0	3065.0	2816.0	4298.0	2730.0	2470.0
TVD [m RKB]	3755.0	3548.0	2836.0	4591.0	4382.5	2922.0	4449.0	3035.0	3478.0	3243.0	2849.0	2852.0	N/A	3064.0	N/A	4298.0	N/A	2470.0
Max. Inclination [˚]	3.3	11.1	16.6	2.2	8.7	5	3	0	9.9	13.3	3.2	3.19	N/A	2.4	2	1.75	1.2	0.75
Bottom hole temp. [˚ C]	116	104	N/A	145	143	81	136	N/A	128	109	103	98	98	N/A	121	101	76	84
Oldest penetrate age	Late Triassic	Late Triassic	Middle Jurassic	Late Jurassic	Middle Jurassic	Late Permian	Early Permian	Late Triassic	Late Triassic	Permian	Triassic	Pre-Devonian	Early Permian	Late Triassic	Middle Jurassic	Late Permian	Late Triassic	Late Triassic
Oldest penetrated formation	Skagerrak Fm	Skagerrak Fm	Bryne Fm	Draupne Fm	Sleipner Fm	Zechstein Gp	Rotliegend Gp	Skagerrak Fm	Skagerrak Fm	Rotliegend Gp	Smith Bank Fm	Basement	Rotliegend Gp	Skagerrak Fm	Vestland Gp	Zechstein Gp	Skagerrak Fm	Skagerrak Fm
1st level with HC, age	Late Jurassic			Late Jurassic					Middle Jurassic			Middle Jurassic				Middle Jurassic		Middle Jurassic
1st level with HC, formation	Sandnes Fm			Intra Draupne Fm SS					Sleipner Fm			Sandnes Fm				Sandnes Fm		Bryne Fm

Table 1.2: Available well log data from each well.

Well log	9/2-1	9/2-2	9/2-11	15/3-8	15/8-2	15/12-2	15/12-3	15/12-22	15/12-23	16/8-3 S	16/10-3	17/3-1	17/4-1	17/6-1	17/9-1	17/12-1	17/12-3	17/12-4
Caliper	✓	✓	✓	✓	✓		✓	✓	✓	✓		✓	✓	✓	✓	✓	✓	✓
Bit size			✓	✓	✓			✓	✓	✓		✓		✓				✓
Gamma ray	✓	✓	✓	✓	✓	✓	✓	✓	✓	✓	✓	✓	✓	✓	✓	✓	✓	✓
Spectral Gamma	✓			✓					✓	✓				✓				✓
SP	✓						✓								✓			
Density	✓	✓	✓	✓	✓	✓	✓	✓	✓	✓	✓	✓	✓	✓	✓	✓	✓	✓
Neutron	✓	✓	✓	✓	✓	✓	✓	✓	✓	✓	✓	✓	✓	✓	✓		✓	✓
Sonic P-wave	✓	✓	✓	✓	✓	✓	✓	✓	✓	✓	✓	✓	✓	✓	✓	✓	✓	✓
Sonic S-wave			✓	✓	✓			✓	✓	✓				✓				✓
Resistivity S	✓	✓	✓	✓					✓			✓	✓	✓	✓		✓	
Resistivity M	✓	✓	✓	✓	✓	✓	✓	✓	✓	✓	✓	✓	✓	✓	✓	✓	✓	✓
Resistivity D	✓	✓	✓	✓	✓	✓	✓	✓	✓	✓	✓	✓	✓	✓	✓	✓	✓	✓
Photoelectric			✓	✓	✓			✓	✓	✓								✓
Rate of penetration			✓		✓			✓	✓	✓								✓

Interactive Petrophysics (IP) software has been used for petrophysical analysis and cross plots and Petrel is used to correlate wells and generate thickness maps. In addition, Microsoft Excel is used for supplementary well log calculations and cross plotting.

1.5. Chapter descriptions

Chapter 1 describes the background of petroleum exploration in the study area and the motivation for conducting this research. The different areas are shown in a regional setting and available data are described in this section.

The second chapter aims to describe the regional geologic setting, including tectonic evolution, stratigraphy and existing petroleum system. Extent and characteristics of the different time-equivalent key formations is introduced, as well as events of uplift and erosion are described.

Research methodologies used in this study and the relevant theory behind this research are presented in chapter 3. The theories behind compaction study, petrophysical analysis and rock physics diagnostics are described together with the relevant equations.

Chapter 4 presents compaction study. The compaction study utilizes published compaction trends and rock physics diagnostics to constrain different compaction regimes and transition zone. Estimation of uplift is performed, and its implication discussed.

Chapter 5 includes the results of the petrophysical analysis and a subsequent discussion. Source and reservoir quality are assessed for different key formations utilizing the well logs. The quantification of properties is achieved through lithology discrimination, shale volume calculations, TOC prediction, porosity estimation, net-to-gross, permeability prediction and calculation of water saturation.

A summary and concluding remarks are presented in chapter 6.

1.6. Limitations and further work

- Due to time restriction and other priorities, a thorough sedimentological analysis with thin sections and mineralogical studies (SEM, XRD, XRF) was not considered. Such an analysis would provide a higher data resolution and calibration points for other analysis.
- The reservoir studies were focused on the Middle Jurassic Sandnes, Bryne and Hugin Formations, due to good data coverage and being typical well targets. Further work could include the Gassum, Skagerrak and Sleipner Formations and Rotliegend Group as these are potential exploration targets. Source rock studies were restricted to Tau, Draupne, Bryne and Fjerritslev Formations due to proven and suggested quality in the literature. Further studies could include Sauda and Egersund Formations.
- S-wave velocity data was not available in 10 wells (more than half of the studied wells).
- Seismic data should be included in future work for interpretation and inversion. Utilizing seismic data would provide better spatial understanding and interpolating between wells.

2.Geological setting

2.1. Regional tectonic and structural evolution

The North Sea is an example of an intracratonic, failed extensional basin. If a sedimentary succession is to develop within an intracratonic basin, crustal thinning by extension and a subsequent subsidence is necessary (Faleide, et al., 2015). The geological history of the North Sea is complex with several tectonic events, both compressional and extensional, affecting and shaping the basin. Post-Cambrian events are relevant to the creation and evolution of the structural elements in the North Sea, while the Late Jurassic extension proves to be a vital contributor to the active petroleum systems. Ziegler (1990) presents the five most important tectonic events shaping the North Sea area:

1. Caledonian Orogeny (Late Ordovician-Middle Silurian).
2. Collapse of the Caledonian Orogeny with resulting basins and large extensional shear zones (Early Devonian).
3. Formation of basins and half-graben structures in the North Sea due to tectonic rifting (Late Carboniferous-Early Permian).
4. Extensive rifting resulting in rotated fault blocks and a general NNE-SSW structural orientation (Late Jurassic).
5. Post-rift basin inversion, including reactivation of faults and structures (Late Cretaceous-Early Cenozoic)

Only a few of the wells drilled in the North Sea penetrate the complete sedimentary succession and into the underlying basement rocks. Wells penetrating the basement rock show intrusive igneous and low- to high-grade metamorphic rocks (Gautier, 2005). These basement rocks were formed during the Caledonian Orogeny, the large mountain chain formed when the Iapetus Ocean closed and Laurentia and Baltica collided. The post-Caledonian extensional events of Devonian are described by Fossen (1992). This phase of NW-SE extension caused the collapse of the Caledonian Orogeny and the development of NE-SW extensional shear zones. One such shear zone is the Hardangerfjord Shear Zone that affected both onshore south Norway and the framework of offshore North Sea (Fossen & Hurich, 2005). A regional lineament lines up from the Hardangerfjord Shear Zone onshore Norway and across the North Sea, as seen in Figure 2.1. The Ling Depression is the main structural element along this lineament (Færseth, et al., 1995).

Late Carboniferous-Early Permian magmatism and lithospheric stretching developed extensional basins, including two major sedimentary basins; Northern Permian Basin and Southern Permian Basin (Ziegler, 1990). The collapsing Variscan orogeny filled these basins with Early Permian, Rotliegend clastic deposits. Increased subsidence and global sea-level rise led to the Zechstein seas transgressing into the Permian basins (Glennie, 1972).

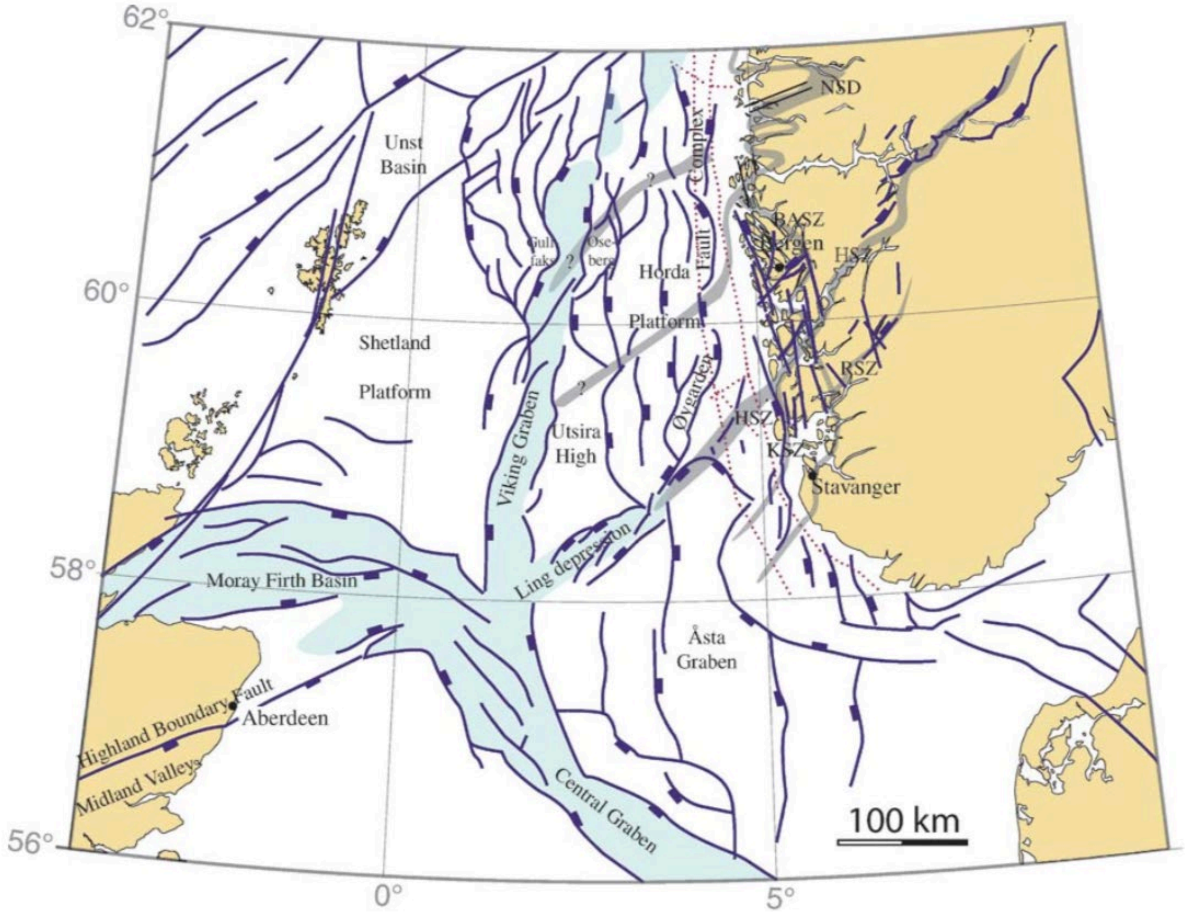

Figure 2.1: Regional map of the North Sea region, including main faults, trends and shear zones. Note how the Ling Depression is a continuation of the Hardangerfjord Shear Zone. HZF, Hardangerfjord Shear Zone; BASZ, Bergen Arcs Shear Zone; NSD, Nordfjord-Sogn Detachment; KSZ, Karmøy Shear Zone; RSZ, Røldal Shear Zone (Fossen & Hurich, 2005).

The present-day North Sea area was moving north at the time, resulting in an arid climate (Faleide, et al., 2015). This lead to evaporite formation and deposition of Zechstein salt units in the Permian basins (Glennie, 1972).

Triassic crustal thinning related to Pangea breakup caused reactivation of Paleozoic faults. Combined with the thermal subsidence after the Late Carboniferous-Permian rifting, the basin was able to accumulate thick successions of continental deposits due to high sediment input (Jarsve, et al., 2014). Salt mobilization was triggered as the Triassic succession increased (Hospers, et al., 1988).

The Central North Sea experienced uplift due to thermal doming in the Early Jurassic (Ziegler, 1982). A period of volcanism ended by Late Jurassic and areas connected to the rift system subsided. Normal faulting along the Viking Graben resulted in rotation of basement fault blocks and crest erosion. Late Jurassic subsidence and subsequent transgression resulted in deep water conditions in the Viking- and Central Grabens. The characteristic rift topography created deep basins with suboxic conditions, perfect for accumulation and preservation of organic-rich shales (Faleide, et al., 2015).

Early Cretaceous experienced a significant drop in relative sea-level, exposing vast areas for erosion, allowing the development of the Base Cretaceous Unconformity (BCU) (Rawson & Riley, 1982). Late Cretaceous and Cenozoic inversion phases due to the Alpine Orogeny (Lyngsie, et al., 2006) and the opening of the Atlantic Ocean is responsible for many of the anticline and monoclines present throughout the North Sea.

2.2. Structural elements

The structural elements in the North Sea include basins, platforms, terraces and intra-basinal elevations, as well as smaller highs and basins on platforms. The main structural elements relevant to this study are the Ling Depression, bounded by the southern Viking Graben in the west and the Egersund Basin in the southeast. A structural map (Figure 2.2) and a brief description of relevant structural elements is given below.

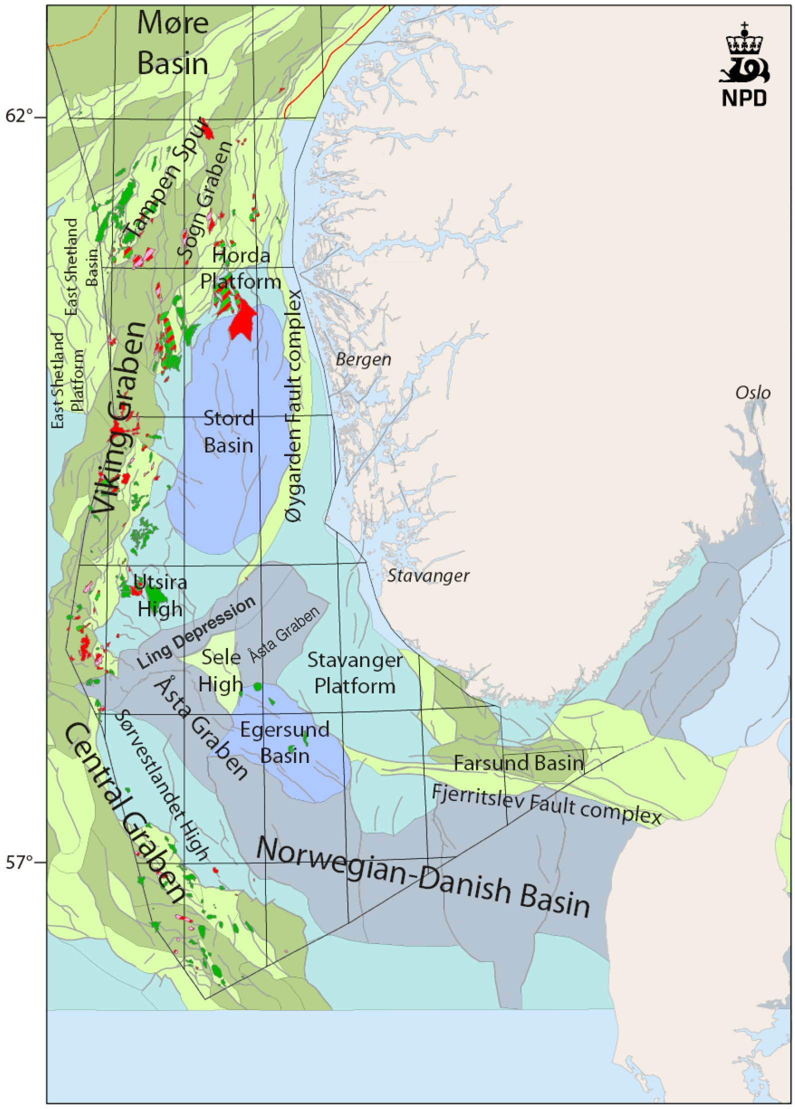

Figure 2.2: Structural map of the Norwegian North Sea (modified from Halland et al., 2014).

2.2.1. Ling Depression

The Ling Depression is a uniquely oriented structural element in the North Sea. With a striking NE-SW trend it acts as a continuation of the Hardangerfjord Shear Zone (Figure 2.1) (Færseth, et al., 1995). This continuous lineament indicates a weak zone underneath which has affected the trend and orientation of the Ling Depression and adjacent faults (Fossen & Hurich, 2005). The general N-S trend of structural elements and faults in the area are related to the Permo-Triassic and the Jurassic rifting stages. Utsira High in the North and Sele High in the south are separated by the Ling Depression. Heeremans & Faleide (2004) concludes that the Ling Depression, together with the Åsta Graben, mark the northern limit for the Zechstein Basin and its prominent deposits.

2.2.2. Åsta Graben

The Åsta Graben is located south of the northern part of the Ling Depression and is a west-tilted half graben with a NE-SW depositional axis trend (Figure 2.2). It is separated by the adjacent Egersund Basin by a E-W trending fault zone (Sørensen & Tangen, 1995). Compared to the Egersund Basin it lacks the presence and effects of halokinesis (Heeremans & Faleide, 2004).

2.2.3. Egersund Basin

South of the Åsta Graben and about 100km west of south Norway, a small extensional basin known as the Egersund Basin is located (Hermanrud, et al., 1990). It is a symmetrical basin bordering the Stavanger Platform in the North-East and the Norwegian-Danish Basin in the south (Figure 2.3). In terms of structural evolution, the Egersund Basin is more related to the Norwegian-Danish Basin in the south than the extensive grabens to the west. The main extensional zone of the Central and Viking Graben does not include the Egersund Basin and the Late Jurassic was therefore rather tectonically quiet in the Egersund Basin (Sørensen & Tangen, 1995). The Egersund Basin experienced only minor subsidence and local inversion caused by the extensive Late Jurassic rifting (Hermanrud, et al., 1990).

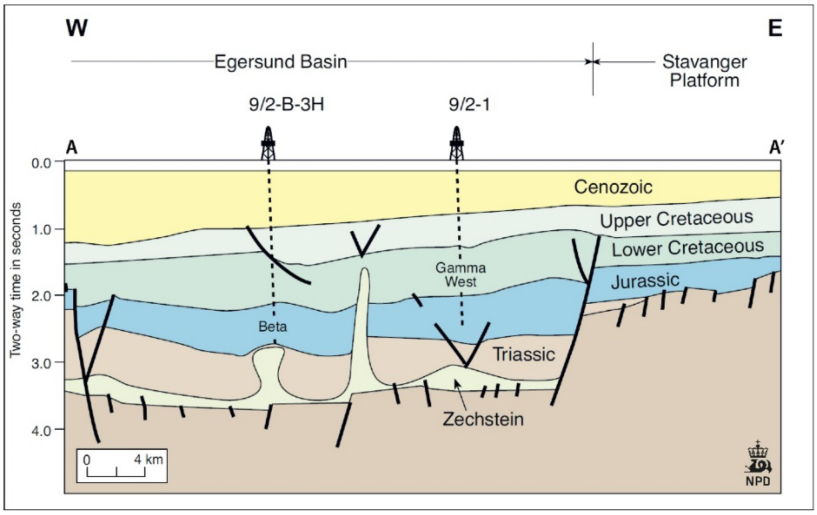

Figure 2.3: Cross-section of Egersund Basin (modified from Halland et al., 2014)

2.2.4. Southern Viking Graben

The Viking Graben is an elongated graben trending with an approximately N-S direction. It extends parallel to the entire South Norwegian mainland. More specifically, the Southern Viking Graben lacks definition but is used to describe the part of Viking Graben west of the Utsira High. As one of several sedimentary basins within the North Sea rift zone, it consists of asymmetric half-grabens associated with more or less orthogonal E-W extension and thinning of the crust (Fjeldskaar, et al., 2004).

2.3. Stratigraphy

This study includes wells and data from different areas in the central North Sea and consequently a variety of stratigraphic units. The entire Central North Sea contains parts of the Nordland, Hordaland, Rogaland, Shetland and Cromer Knoll Group in the upper sedimentary succession. Local highs are the only exceptions. Base Cromer Knoll Group is generally recognized as the Base Cretaceous Unconformity (BCU). As the succession reaches Jurassic level, the stratigraphy and nomenclature become more diversified. The Upper Jurassic succession is known as the Viking Group in the Southern Viking Graben and the western part of the Ling Depression. In the eastern part of the Ling Depression, Åsta Graben and Egersund Basin the Upper Jurassic succession is called Boknfjord Group. The Middle Jurassic Vestland Group is encountered throughout the study area but represented by different formations. The Sandnes and Bryne Formation represent the Vestland Group in the western study area while the Sleipner and Hugin Formation represent the Vestland Group in the more eastern parts. This distribution is presented in the lithostratigraphic chart in Figure 2.4 and Table 2.1 and Table 2.2. Within the study area, the Dunlin Group is only present in the Egersund Basin. The Triassic Hegre Group and Permian Zechstein Group and Rotliegend Group are localized across the entire study area but with local variations and thicknesses.

Groups and formations relevant for this study is presented below. The information is derived from NPD (2018) and is originally from Deegan and Schull (1977) and Vollset and Doré (1984).

2.3.1. Rotliegend Group

The continental red-beds of the Rotliegend Group consists of a sequence of claystones, shales and sandstones. Minor conglomerates and volcanic rocks are also present. Both the internal chronostratigraphy and spatial distribution is poorly understood. The limited available well data indicate extensive distribution in the southern part of the Norwegian North Sea.

2.3.2. Hegre Group

The Hegre Group is represented by the Skagerrak Formation and the Smith Bank Formation in the Central North Sea. However, incomplete Triassic successions are hard to subdivide based on lithostratigraphic pattern and absence of age diagnostic material.

2.3.2.1. Skagerrak Formation

The Skagerrak Formation is observed in the eastern part of the Central North Sea as well as western Skagerrak. Halokinesis and erosion may explain local absence. A lithology consisting of interbedded conglomerates, sandstones, siltstones and shales points to continental deposition from coalescing and prograding alluvial fans within a structurally controlled basin.

2.3.3. Vestland Group

The Vestland Group is distributed throughout most of the southern part of the Norwegian North Sea and is present throughout the study area. Sandy deltaic sequences with shale, siltstone and coal characterize the lower part, while more homogenous sandstone from marine conditions characterize the upper part. Overlying shale units make the upper boundary stand out in well logs as breaks on both sonic and gamma ray logs.

2.3.3.1. Fjerritslev Formation

The Norwegian-Danish Basin as well as NE Ling Depression, Åsta Graben and Egersund Basin host the grey to brown grey claystone of the Lower Jurassic Fjerritslev Formation. Deposition is suggested to be shallow marine during transgression. Only local remnants of a more widespread distribution are observed in the North Sea today, mostly due to mid-Jurassic erosion.

2.3.3.2. Bryne Formation

The Bryne Formation typically is a mix of sandstones, siltstones, shales and coals. The sandstones are white to grey and poorly sorted, while the shale is grey to brown and micaceous. Local variations and interbedded sandstones and shales are common (Figure 2.4). It is interpreted to represent fluvial/deltaic deposition which also support the generation of coal. Distribution is primarily limited to the Central Graben and the extended Norwegian-Danish Basin area.

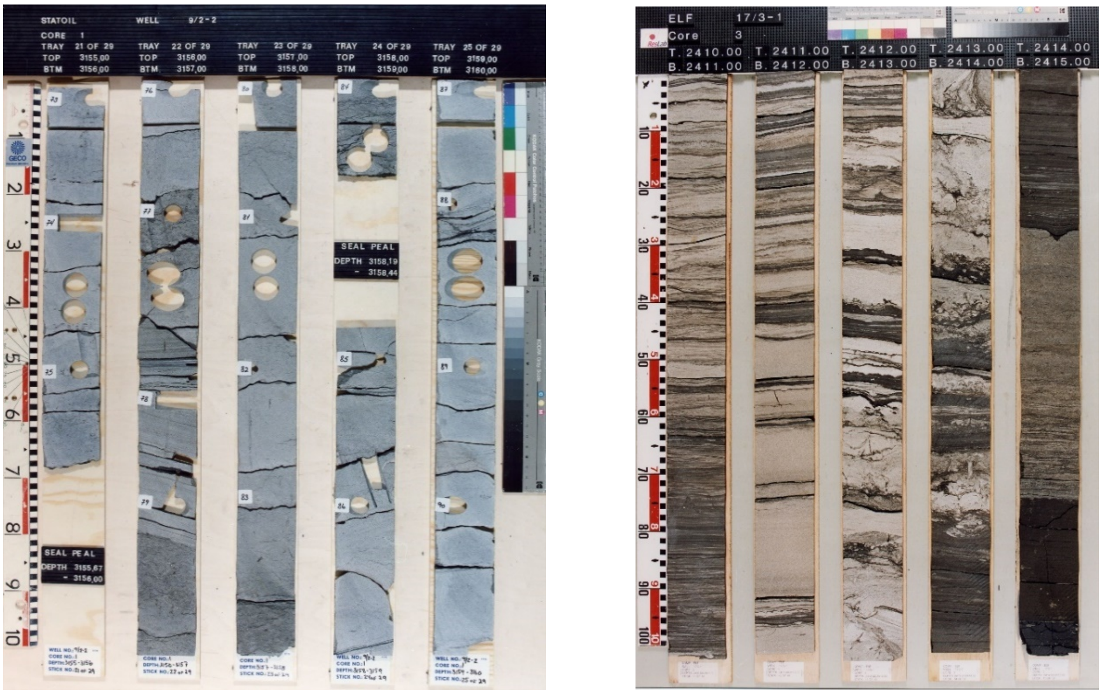

Figure 2.4: Core photographs of the Sandnes Formation (3155-3160 m MD) from well 9/2-2 (left) and Bryne Fm (2410-2415 m MD) from well 17/3-1 (right) (Source: NPD, 2018).

2.3.3.3. Sleipner Formation

The Sleipner Formation is time equivalent to the Bryne Formation and they show similar lithology. A fluvio-deltaic environment with local accumulations of coal is the depositional signature, similar to the Bryne Formation. However, a connection between the two deposits is yet to be made. The main distribution of the Sleipner Formation is in the southern Viking Graben.

2.3.3.4. Sandnes Formation

The lithology of the Sandnes Formation is described as massive white, very fine grained to coarser grained glauconitic sandstone (Figure 2.4). Depositional environment is interpreted to be shallow marine. Locally, interbedded sandstone and shales is observed. It is distributed in the eastern parts of the study area. An unconformable contact with Bryne Formation or other non-marine units of Jurassic/Triassic age represent the base of Sandnes Formation.

2.3.3.5. Hugin Formation

The Hugin Formation is deposited chronostratigraphically similar to the Sandnes Formation and shows a similar lithology. In addition to the very fine to medium grained sandstone, there is also some carbonaceous material and coal fragments. Bioturbation and occasional cross bedding can be observed (Figure 2.5). Together with Sleipner Formation its main distribution is in the southern Viking Graben.

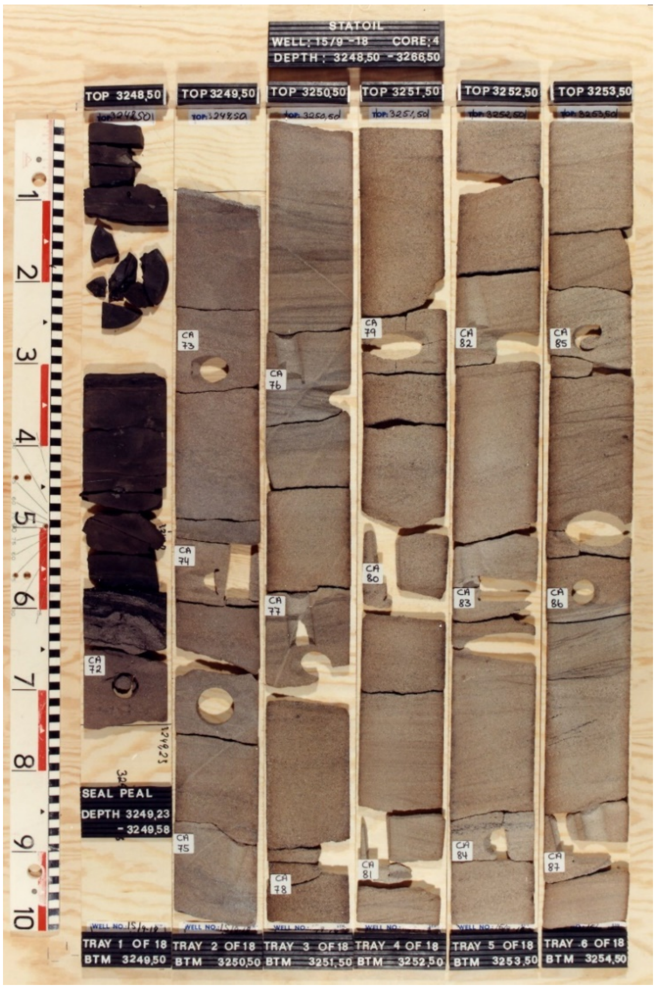

Figure 2.5: Core photograph of Hugin Formation (3248-3254m MD) from well 15/9-18 (not included in this study). No core photographs of Hugin Formation from studied wells were available (Source: NPD, 2018).

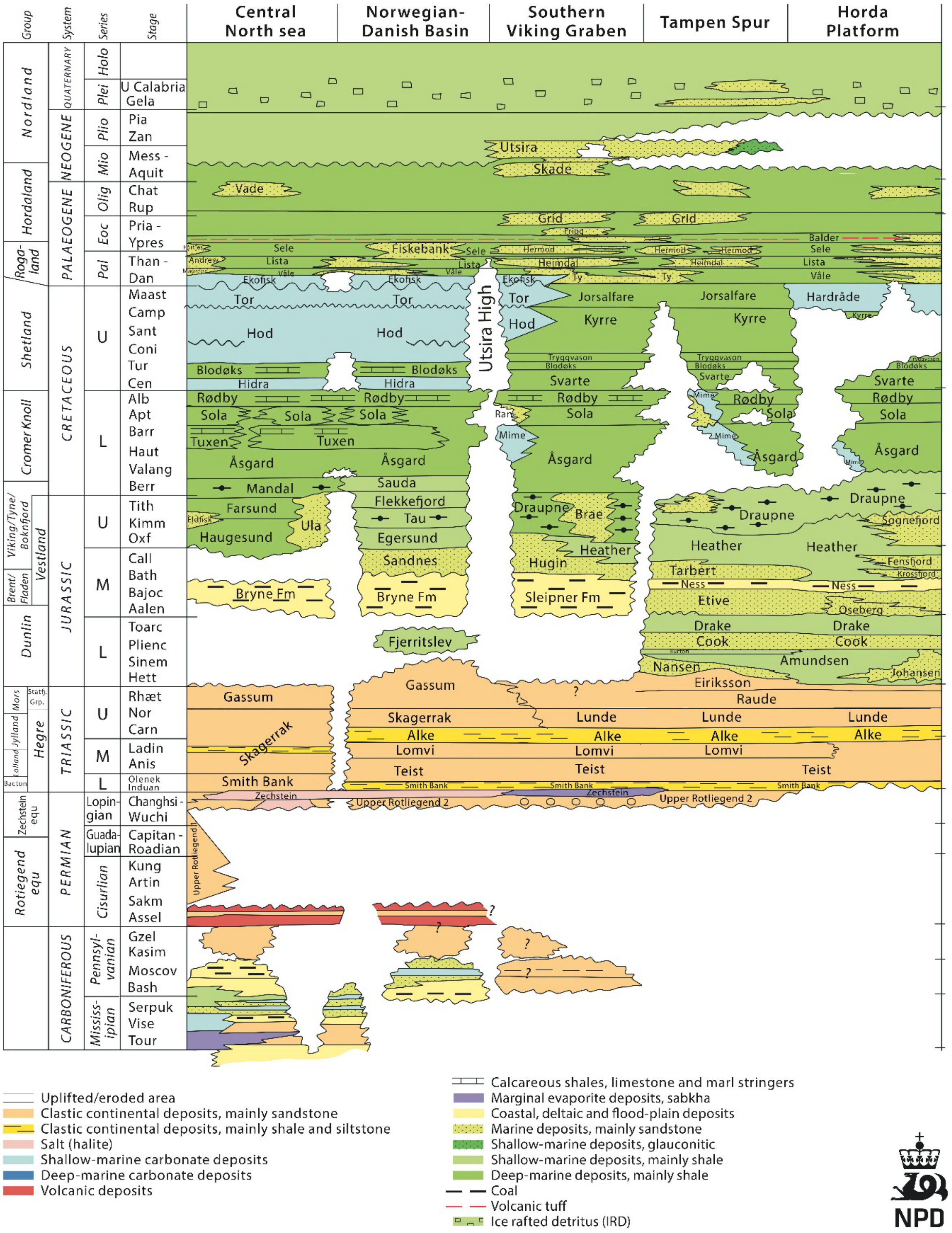

Figure: 2.6: Lithostratigraphy of the North Sea. The columns of Norwegian-Danish Basin and Southern Viking Graben are most representative for the study area (from Halland et al., 2014).

2.3.4. Boknfjord Group

The Boknfjord Group can be subdivided into four formations, the Egersund Formation (oldest), Tau Formation, Sauda Formation and Flekkefjord Formation (youngest). Entire group successions are mostly confined to the Egersund Basin and adjacent areas to the north, while the upper two formations also have an extended western distribution. The group is dominated by shales, but varying amounts of siltstone, sandstone, limestone and organic content make it possible to subdivide the group. Only the Tau Formation is of further interest in this study.

2.3.4.1. Tau Formation

The Tau Formation is typically recognized as a dark grey to black, pyritic, organic-rich shale. Deposition occurred in an anaerobic marine environment with high organic productivity and restricted bottom water circulation. Prominent boundaries can be observed in well logs due to high radioactivity. Well 17/3-1 in the eastern Ling Depression show a thickness of 28 meter and well 9/2-2 in the Egersund Basin show a thickness of 105 meter.

2.3.5. Viking Group

The widely distributed Heather and Draupne Formations are the most relevant subdivisions of the Viking Group in the study area. Shales, claystones and marine mudstones dominate throughout the group. Local sandstone successions are occasionally found within (Intra Draupne Formation Sandstone and Intra Heather Formation Sandstone). Areas adjacent to the Viking Graben in the North Sea and into the Norwegian Sea show presence of the Viking Group.

2.3.5.1. Heather Formation

Silty claystone makes the majority of the Heather Formation, with local presence of thin limestone streaks. Interpretation of depositional environment point to open marine environments as part of the Middle – Late Jurassic transgression. The Heather Formation also contains local interbedded sandstone units, known as Intra Heather Formation SS.

2.3.5.2. Draupne Formation

The Kimmeridge Clay equivalent Draupne Formation is typically dark grey-brown to black claystone (Figure 2.7). Deposition in marine environment with anaerobic conditions has preserved the high organic content. This is the reason for its characteristic high radioactivity. Upper and lower boundaries are easily recognized on well logs because of the very high gamma ray response and low velocity. Interbedded sandstone units, as Intra Draupne Formation Sandstones, are interpreted as gravity flow deposits.

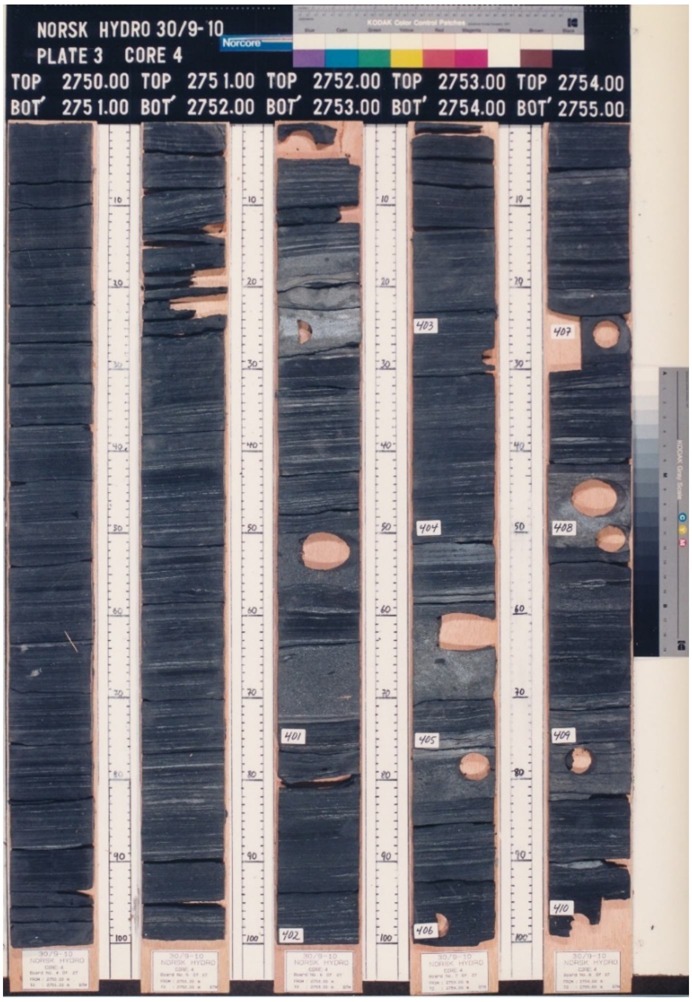

Figure 2.7: Core photograph of the Draupne Fm (2750-2755m MD) from well 30/9-10 (not included in this study. No core photographs of Hugin Formation from studied wells were available (Source: NPD, 2018).

Table 2.1: Depth of penetrated stratigraphic units in the eastern part of the study area. Based on data from NPD (2018).

Eastern Study Area										
Age	**Group**, Formation	NE Ling Depression		Åsta Graben	Egersund Basin					
		17/3-1	17/6-1	17/9-1	17/12-1	17/12-3	17/12-4	9/2-1	9/2-2	9/2-11
Neogene	**Nordland Gp**	298	290	168	142	137	128	128	121	127
Paleogene	**Hordaland Gp**	396	340	439	450	528	486	515	406	453
	Rogaland Gp	873	716	695	752	768	744	710	747	620
	Balder Fm	873	716	695	752	768	744	710	747	620
	Sele Fm	942	745	719	777	790		731	770	643
	Lista Fm	966	789	731	778	794		740	778	652
	Våle Fm	1001	865	738	781	798	773	756	795	665
Cretaceous	**Shetland Gp**	1030	878	746	785	801	780	765	803	671
	Ekofisk Fm				785	801	780	765	803	671
	Tor Fm	1030		746	807	817	799	829	873	745
	Hod Fm	1271		1085	1130	1157	984	1114	1161	880
	Blodøks Fm		1219	1195	1206		1209	1445	1425	
	Cromer Knoll Gp	1380		1220	1210	1266	1216	1482	1445	1159
	Rødby Fm	1380		1220	1210	1266	1216			
	Sola Fm	1425		1354	1339	1388		1482	1445	1159
	Åsgard Fm	1505		1464	1482	1555	1335	1601	1511	1233
Jurassic	**Boknafjord Gp**	1875	2020	1933	1902	1957	1992	2483	2381	2101
	Flekkefjord Fm	1875	2020	1933	1902	1957	1992	2483	2381	2101
	Sauda Fm	1980	2116	1954	1946	2010	2017	2550	2447	2180
	Tau Fm	2311	2489	2165	2167	2236	2149	2993	2957	2492
	Egersund Fm	2339	2542	2205	2215	2288	2198	3097	3062	2574
	Vestland Gp	2388	2630	2220	2290	2370	2277	3162	3123	2629
	Sandnes Fm	2388	2630	2220	2290	2370	2277	3162	3123	2629
	Bryne Fm	2410	2647	2237	2306	2396	2298	3309	3230	2761
	Fjerritslev Fm		2726	2835			2398	3601	3475	
Triassic	Gassum Fm		2800		2410	2617				
	Skagerrak Fm		2988	2992	2446	2638	2439	3685		
	Smith Bank Fm	2440			3965					
Permian	Zechstein Gp				4133					
	Rotliegend Gp									
(Pre-) Devonian	Basement	2811								

Table 2.2: Depth of penetrated stratigraphic units in the western part of the study area. Based on data from NPD (2018).

Western Study Area										
Age	**Group,** Formation	SW Ling Depression							Southern Viking Graben	
		15/12-2	15/12-3	15/12-22	15/12-23	16/8-3 S	16/10-3	17/4-1	15/3-8	15/8-2
Neogene	**Nordland Gp**	111	111	109	113	97	115	132	133	144
Paleogene	**Hordaland Gp**	1038	1317	1094	1116	830	1018	544	858	1027
	Rogaland Gp	1963	2285	2125	2344	1558	1829	1041	2164	2312
	Balder Fm	1963	2285	2125	2344	1558	1829	1041	2164	2312
	Sele Fm	2045	2348	2151	2365	1601	1889	1080	2223	2354
	Lista Fm	2075	2401	2233	2436	1612	1895	1108	2277	2399
	Våle Fm	2224		2317	2526	1712	2012	1150		
Cretaceous	**Shetland Gp**	2234	2472	2320	2532	1743	2029	1163	2740	2848
	Ekofisk Fm	2234	2472	2320	2532	1743	2029		2740	2848
	Tor Fm	2268	2479	2324	2543	1762	2076	1163		2904
	Hod Fm	2425	2675	2541	2731	1941	2250	1370		3114
	Blodøks Fm	2525	2752	2610	2813			1408	3673	3381
	Svarte Fm	2542					2350		3686	
	Hidra Fm			2643	2846			1438		3432
	Cromer Knoll Gp	2650	2791	2676	2907	2051	2361	1444	3794	3558
	Rødby Fm		2791	2676	2907	2051	2361	1444		3558
	Sola Fm	2650	2830	2683	2921	2123	2378		3859	3580
	Tuxen Fm				2924					
	Åsgard Fm	2667	2865	2730	2952	2167	2411	1706	3875	3643
	Mime Fm		2977					2080		
Jurassic	**Viking Gp**	2703	2998	2764	2966	2570	2501	2122	3933	3763
	Draupne Fm	2703	2998	2764	2966	2570	2501	2122	3933	3763
	Intra Draupne Fm SS								4073	
	Heather Fm	2765	3142	2799	3013			2217		3839
	Intra Heather Fm SS				3117					
	Vestland Gp	2818		2831	3164		2521	2265		3882
	Hugin Fm	2818		2831			2521	2265		3882
	Sleipner Fm				3164					4238
Triassic	Gassum Fm									
	Hegre Gp					2656				
	Skagerrak			2985	3192		2532	2352		
	Smith Bank Fm	2868					2626	2532		
Permian	Zechstein Gp	2888	3238			2734		2665		
	Kupferschiefer Fm							3829		
	Rotliegend Gp		4392			3015		3834		
(Pre-) Devonian	Basement									

2.4. **Petroleum system**

Magoon and Dow (1994) describes a petroleum system as a pod of active source rock and all its related oil and gas, in addition to every element and process vital for the existence of hydrocarbon accumulations. The vital elements include source rock, reservoir rock, seal/cap rock and overburden rock. Formation of traps and the generation-migration-accumulation of petroleum are the processes necessary. The timing of each element and process must be right for a petroleum accumulation to occur.

The different levels of petroleum investigations are also presented by Magoon and Dow (1994), with the petroleum system as one of them. A full-cycle hydrocarbon investigation includes sedimentary basin, petroleum system, play and prospect as separate investigations. Studies of sedimentary basins should be focused on the stratigraphic succession and structural style of sedimentary rocks. A description of how one particular pod of source rock is genetically related to any discovered petroleum should be included in the investigation of the petroleum system. These first two levels are basically unaffected by economic considerations. Investigations of plays aim to describe a series of related or similar present-day traps, while a prospect investigation only focuses on one particular trap and its economic viability. Acquisition of 3D seismic data and drilling of wells makes the last two levels of hydrocarbon exploration very expensive.

When conducting exploration work on a prospect each part of the petroleum system must be de-risked before a drilling decision is made. A chance of success is calculated based on direct and extrapolated data and regional knowledge of the target area/prospect. In an example with all petroleum system constituents present one may rate the quality of the trap to 50% due to the possibility of leakage from faults and the quality of the reservoir to 80% due to known regional homogeneity from adjacent well interpolation. Lastly, one wants to put a number on the possibility that the existing source rock has expelled hydrocarbons. Thin source rock succession and uncertainties about maturation may result in a suggestion of 40% source rock quality. This simplified example would give a chance of success of 16%, which is considered too low for most oil companies. The importance of thorough characterization of all petroleum system constituents is therefore acknowledged (Rose, 1992).

In addition to calculating chance of success before drilling, the reasons for failure or underperformance are identified post drilling. The Norwegian Petroleum Directorate keeps track on these reasons for failure across the whole NCS (Figure 2.8). Lack of source rock and/or expulsion and/or migration is reported to be the main reason for 46% of the dry wells in the North Sea. Reservoir related failures, as lack of presence or poor quality, is accountable for 26% of the dry wells. Finally, traps are cited as the principle cause of failure in 28% of the wells in the North Sea (NPD, 2018). The ratios vary for the different part of the NCS, with traps being an increasing problem further north. This is most likely due to higher rates of regional uplift and erosion.

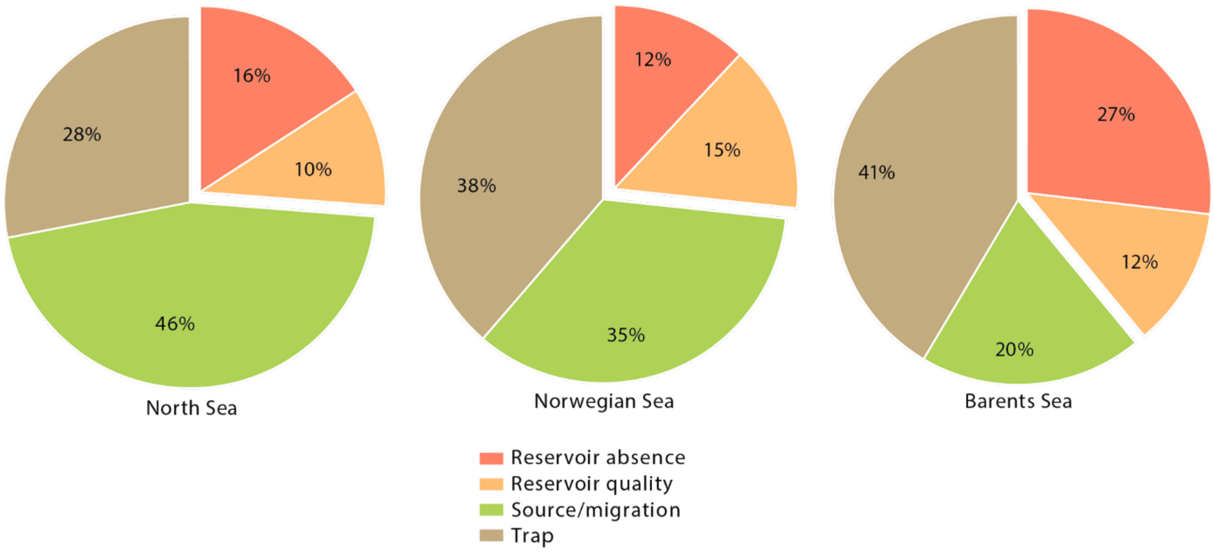

Figure 2.8: Main reasons reported for dry targets in the North Sea, Norwegian Sea and Barents Sea in percentages (Source: NPD, 2018).

The Jurassic succession in the North Sea contains multiple proved and possible candidates for source and reservoir rocks. Contributions from older source rocks and accumulations in younger reservoir rocks are also proved (Faleide, et al., 2015). It is important to note that some formations show significant lateral variations of lithology. A designated source rock formation may contain considerably more sand in a distant area and therefore also act as a reservoir.

2.4.1. Source rocks

The definition of a source rock is a sedimentary rock able to generate a significant volume of oil and/or gas (Cornford, 1998). A working source rock is typically an organic-rich, dark and laminated mudstone or shale. Demaison and Moore (1980) describe the typical depositional environment for such rocks. The required anoxic environments are the result of higher oxygen demand than oxygen supply in the water column.

After 50 years of exploration in the North Sea, several intervals and formations with source rock potential in the North Sea have been identified. Justwan et al. (2005) suggested four formations in the Southern Viking Graben with source rock potential:

- Middle Jurassic *Sleipner Formation* and *Hugin Formation*: Local coalbeds within these formations contain very high values of TOC and they are consequently prone to gas and volatile oil (NPD, 2018).
- Middle to Upper Jurassic *Heather Formation*: Variable organic facies has resulted in kerogen types II, III and IV, as well as degraded marine material. Sub-optimal preservation conditions and average TOC of 2-4% has put substantial limits for oil generation. (Thomas, et al., 1985)

- Upper Jurassic to Lower Cretaceous *upper and lower Draupne Formation*: The Upper Jurassic Kimmeridge Clay is considered the best source rock in the North Sea and its Southern Viking Graben equivalent is the Draupne Formation. TOC in the range of 5-12% and the highest maximum thickness of any North Sea source rock prove its quality (Thomas, et al., 1985). The syn-rift deposited lower part feature a mix of type II and III kerogen in addition to more gas prone and inert organic matter (Justwan, et al., 2006). Post-rift thermal subsidence caused less mass flow influence during deposition of the upper part, resulting in an oil-prone kerogen type II (Justwan, et al., 2006).

A well correlation of all studied well with the Draupne Formation present is shown in Figure 2.9.

The organic facies of the Kimmeridge Clay equivalents vary both stratigraphically and geographically, which is the reason for the different nomenclature. Even though the formations are considered “equivalents”, they are not part of a homogenous, consistent lithology. Maturity and facies vary regionally (Pedersen, et al., 2006). The NE Ling Depression, Åsta Graben and Egersund Basin have the Kimmeridge Clay equivalent Tau Formation of the Boknfjord Group as their main organic-rich formation. Despite excellent source rock properties in the Tau Formation, older source rocks (Lower to Mid Jurassic) are believed to be significant hydrocarbon contributors locally in the Egersund Basin (Ritter et al. 1987; Cornford 1998). This is most likely due to differences in maturity, and not source rock quality parameters (Cornford, 1998). Especially the Bryne Formation and Fjerritslev Formation have good (to excellent) source rock properties locally (NPD, 2018). Regional differences give no significant oil generating potential in other areas, due to insufficient organic carbon or unsuitable kerogen composition Although organic-rich hydrocarbon-prone source rocks are present throughout most of the study area, shallow burial and consequently low maturity (immature to early mature) are the major reasons for low expulsion volumes.

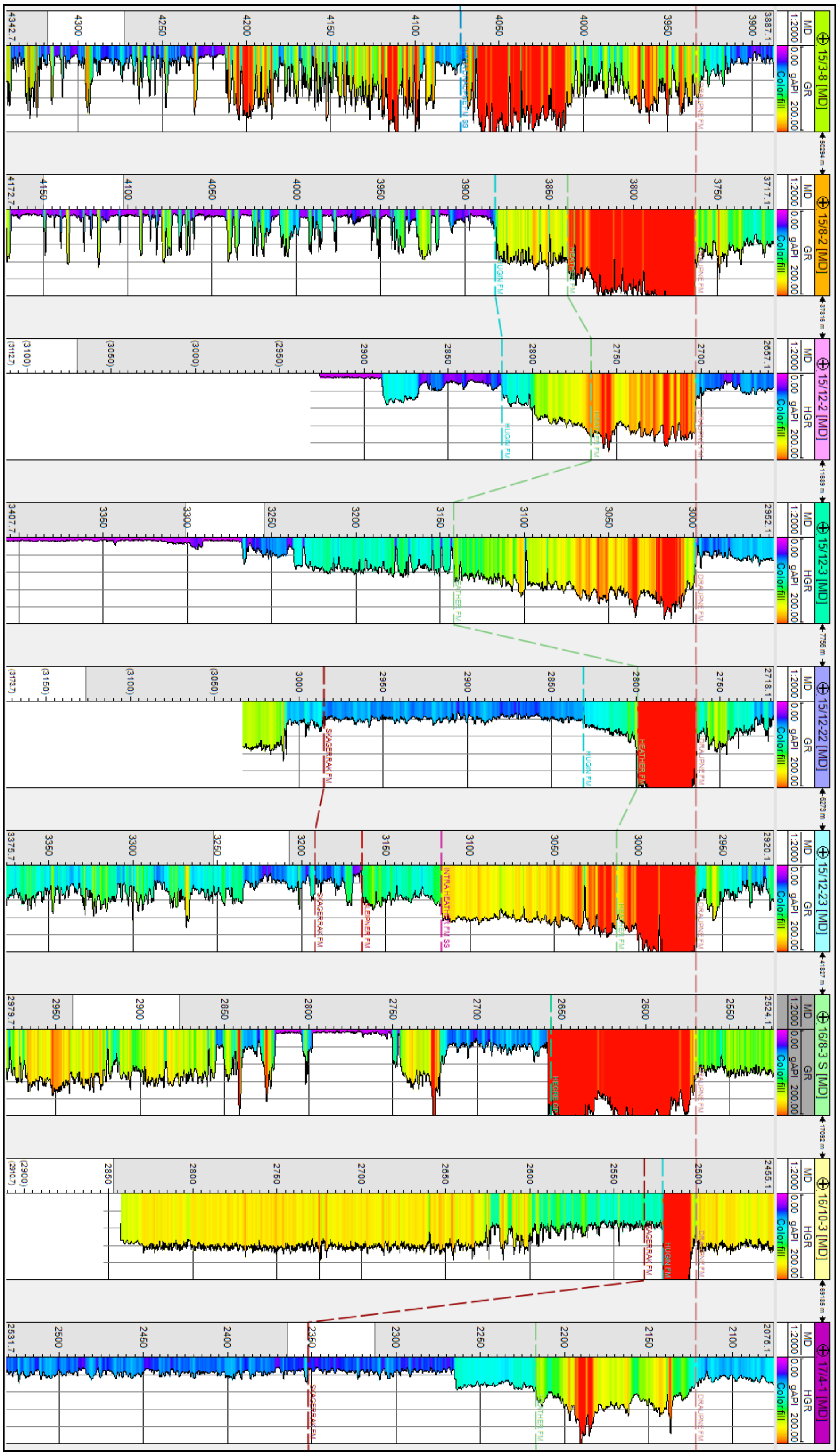

Figure 2.9: Well correlation of the nine wells in the western part of the study area where Draupne Formation is the dominating Upper Jurassic source rock unit. It is easily recognizable in this figure by mainly red and orange colors in the gamma ray log. The wells are flattened on Top Draupne Formation.

2.4.2. Reservoir rocks

A number of possible and proven plays in the North Sea have been summarized by NPD (2017). The Sandnes and Bryne Formations have been main exploration targets in the eastern part of the study area while Hugin and Sleipner Formations have been targeted in the western part. These are of Middle Jurassic age and part of the play known as njm-1 (Figure 2.10). Fluvial, deltaic and shallow marine deposits with good reservoir properties characterize this play (NPD, 2017). Sandnes and Sleipner Formations have mean values of porosity 23% and 16-20% porosity and permeability 400-500 mD and 0.1-4000 mD, respectively (Halland, et al., 2014). Considering the study area, a progressive thickening of the Vestland Group is observed in south-eastern direction. From tens of meters in the Ling Depression and Åsta Graben to several hundred meters in the Egersund Basin. A similar trend is observed in the burial depth of the Vestland Group. Lower maximum burial depth will generally result in better reservoir properties, due to less diagenesis and temperature effects (Bjørlykke & Jahren, 2015).

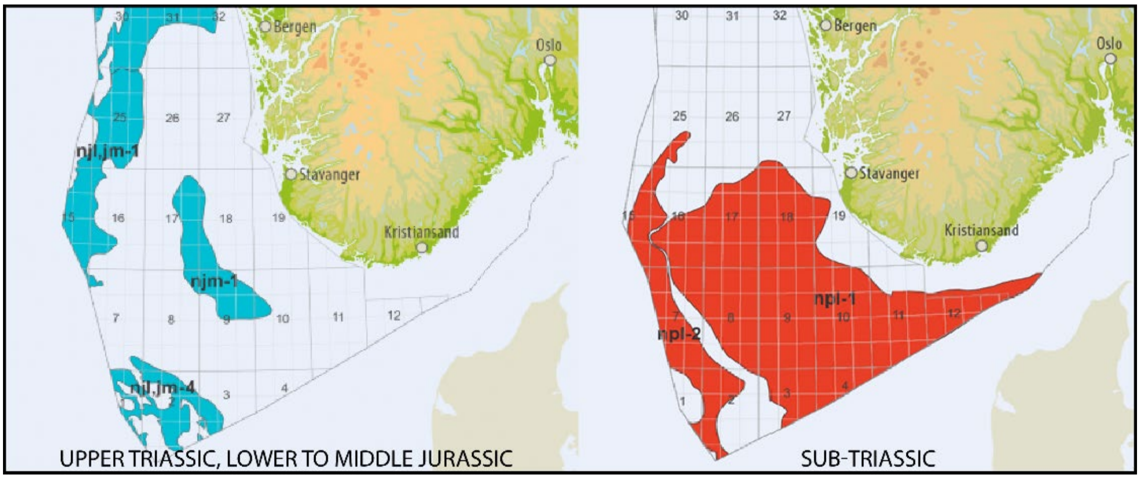

Figure 2.10: Upper Triassic, Lower to Middle Jurassic and Sub-Triassic plays in the Central North Sea (modified from NPD, 2017).

Upper Jurassic sands such as Intra Draupne SS Formation have been targeted with success in Southern Viking Graben and Utsira High. Such shallow marine deposits transported as gravity flows result in only local distribution. Regional differences in burial depth gives large differences in reservoir quality.

Sub-Jurassic plays include the Triassic Skagerrak Formation and the Permian Rotliegend Group. The internal lithology variations in the Skagerrak Formation give large reservoir quality variations, with mean values of 12.8% porostity and <10 mD permeability (Halland, et al., 2014). The Hegre Group, including Skagerrak Formation, is considered a part of the njl,jm-4 play in the Central Graben (Figure 2.10), but the formation is also encountered in several of the studied wells, implying a somewhat similar distribution as the njm-1 play.

Considering Sub-Triassic reservoirs, the npl-1 play is most relevant for the study areas (Figure 2.10). The play npl-1 target Permian sands of the Rotliegend Group but is yet to be confirmed as a functioning play (NPD, 2017). The high-risk, high-reward, Statoil-operated (now Equinor) Lupin prospect (16/8-3S) targeted Rotliegend sandstones in the Ling Depression as a potential new play opener (Energy-Pedia, 2013). Several risk elements were recognized, including maturity of source rock, migration, timing and reservoir quality. The well was dry. Acceptable and excellent reservoir properties in Permian sandstones have been reported east of Southern Viking Graben and in Dutch sector, respectively, proving the potential of the play (Gaup & Okkerman, 2011; NPD, 2017). Older and deeper reservoirs of Devonian age is being produced e.g. in the Embla field (2/7-20) in the Central Graben, reflecting the beneficial effects of overpressure and hydrocarbon emplacement in decreasing chemical compaction (Bjørlykke, 2015a), proving age and depth (to some extent) is just a number in terms of reservoir quality.

The presence of several proved and unproved plays and sufficient reservoir properties within the study area indicates that the reservoir part of the petroleum system is in place and working.

2.4.3. Cap rocks and traps

The Kimmeridge Clay equivalent Draupne and Tau Formations are the most common cap rocks in the study area and large parts of the Central North Sea. Mechanical testing and sealing capacity analysis has been performed on several cap rock interval cores, including 16/8-3S in the Ling Depression (Skurtveit, et al., 2015). Results show very low permeability in the Draupne shale, with high capillary sealing properties due to small pore throats.

Other cap rocks in the Central North Sea includes the Åsgard Formation locally on Utsira High, Zechstein salts and Smith Bank Formation claystones locally in the Norwegian-Danish Basin. Cenozoic shales cap the reservoir of the Ekofisk Field in Central Graben.

A variety of trap types are present in the various plays; structural traps, rotated fault blocks, sealing faults and stratigraphic traps (NPD, 2017). Salt-dome traps are also present in the Central North Sea parts affected by halokinesis (Nemcok, 2016).

Gautier (2005) sorted seals and traps in the North Sea after the rift setting at the time of deposition. Pre-rift reservoirs are prone to accumulate in tilted fault-block traps overlain with fine-grained deposits acting as seal. Shallow marine syn-rift reservoirs are typically capped by Kimmeridge Clay equivalents, often with additional fine-grained Cretaceous overburden. Fine-grained facies of Tertiary age usually seal post-rift reservoirs (Gautier, 2005).

A trap classification based on how they retain, leak and spill hydrocarbons was proposed by Sales (1993). The relation between seal strength and trap closure gives three possible trap types. A class-1 trap will rather spill than leak gas and finally spill oil by replacement. Class-3 traps do not spill any hydrocarbons but accumulate oil until the pressure surpass the maximum seal strength, resulting in gas and excess oil leakage. The last trap type, Class-2, will leak gas and spill oil with a gas/oil contact within the trap (Figure 2.11). All trap types have been identified in the North Sea, including Gullfaks, Snorre, and most of the Ekofisk group of anticlines are class 3, Oseberg is class 2 and Troll East is class 1. The lack of substantial hydrocarbon discoveries makes this classification inefficient in the study area of this thesis. A general low maturity in the area rules out most gas accumulations and filled-to-spill situations. The correlation between hydrocarbon phases and cap rock quality is shown in Figure 2.11.

2.4.4. Uplift and seal failure

During the late Cenozoic, mainland Norway and the eastern part of the Norwegian Shelf experienced uplift and erosion (Hansen, 1996). When analyzing claystone intervals (mainly V_P and bulk density), the effect of over-compaction can be used for quantification of uplift. Assuming any process of compaction is irreversible, a shale will retain the compaction it gained at maximum burial. In the event of uplift and erosion, a shale will show lower porosity than expected from its present burial depth and thus appear over-compacted (Mondol, 2015). Such shift of V_P/bulk density from expected compaction trend (50:50 silt-kaolinite mixture in this case) is observed in the Egersund Basin, indicating exhumation (Kahlani, et al., 2015). Kahlani (2015) estimated uplift of 700-750 m in well 9/2-2 and approximately 200 m in block 9/4. Calculations by Hansen (1996) indicate an increased amount of net uplift, from 0 to more than 600 m, towards the east in Central North Sea. A similar Late Cenozoic uplift trend is proposed by Doré & Jensen (1996), with a range from 0 to more than 1000 m.

The extensive amounts of uplift in the Barents Sea have been comprehensively studied to constrain paleo maturity states (e.g Theis et al., 1993). Similar methods have been applied to marginal basins in the North Sea, where potential source rocks are generally shallow buried, and considered immature from geothermal gradients (Doré & Jensen, 1996). An example of successful uplift estimation is Jensen and Smith's (1993) model of the Farsund Basin, using limiting cases of 1000m and 1700 m uplift. Results suggested that, prior to late Cenozoic uplift, a narrow strip of source rock in the basin axis entered the "oil-window". Without such estimations, the entire basin would have been considered immature.

A possible negative consequence of uplift is that source rocks that currently appear to be in the "oil window" (mature) may have been in the "gas window" (over mature) prior to uplift (Doré & Jensen, 1996). The trend of immature to early mature source rocks implies this is not a big concern in the study area.

Substantial uplift and erosion may result in seal failure. Watts (1987) defined caprock seals into two categories; membrane seals and hydraulic seals. The names indicate the mechanism by seal failure is most prone to occur. Membrane seals fail when the net buoyancy pressure of the hydrocarbon column exceeds the capillary displacement pressure of the seal, causing capillary leakage. Consequently, the weakest point of any membrane caprock will be the largest interconnected pore throat.

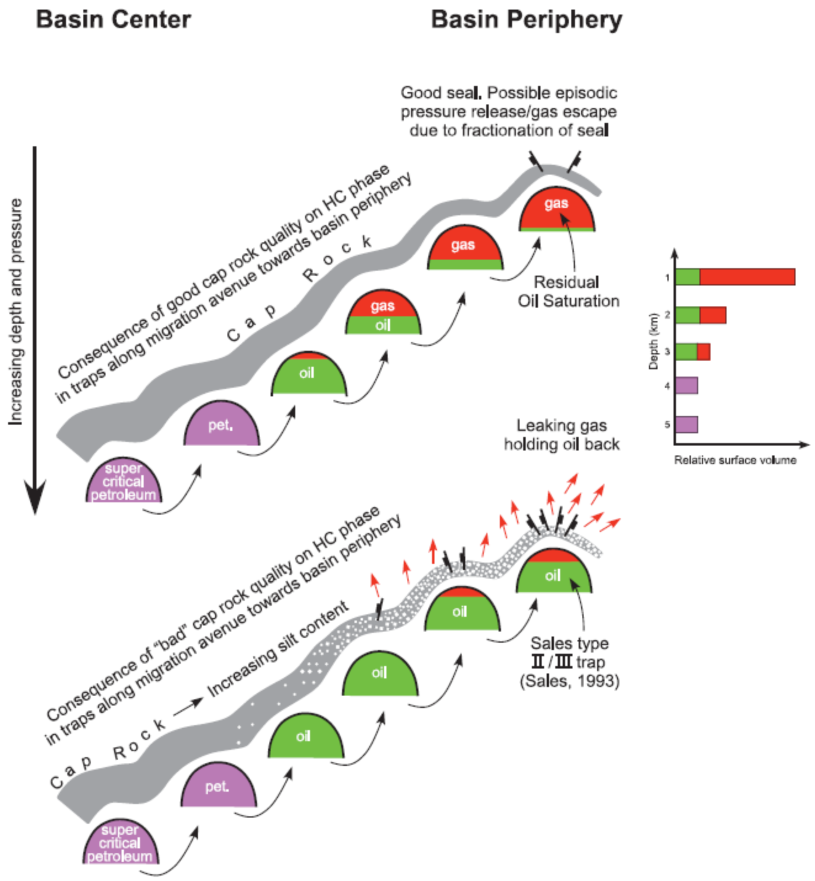

Figure 2.11: Correlation between hydrocarbon phase and caprock quality. Upper figure is typical type 1 trap which will spill oil and only leak gas due to potential fracturing. Type 2/3 trap is shown in lower figure, where gas will leak due to membrane fail, while oil will be retained (Ohm et al., 2008).

Hydraulic seals (e.g. tight shales) have very high capillary entry pressures and capillary failure is therefore not likely (Hillis, 1998). In such cases, leakage will occur due to fracturing/faulting of the caprock (Figure 2.11). A typical hydraulic seal failure is tensile fracturing (or natural hydraulic fracturing), where increased pore fluid pressure (e.g. due to uplift) reduces the minimum effective stress to below the tensile strength of the rock, causing fractures (Watts, 1987; Hillis, 1998).

3. Research methodologies and theoretical background

3.1. Workflow

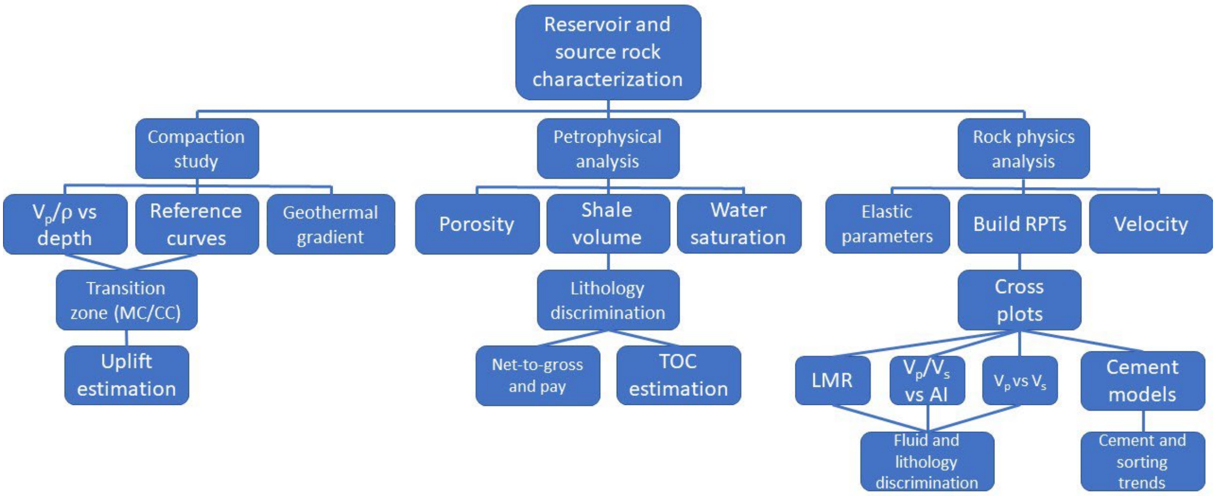

Figure 3.1: Chart of preferred workflow in this study.

3.2. Compaction study and uplift estimation

3.2.1. Compaction

The main lithologies in sedimentary basins, including the North Sea, are shales, sandstones and carbonates. Shales and sandstones will be the focus in this thesis due to their abundancy in the study area. Because of different physical properties these lithologies respond differently to increased stress and temperature during burial. At any given depth these properties are a result of the original composition, as well as temperature and stress history. A general trend is lower porosity with depth, resulting in increased density and velocity. The porosity loss (compaction) varies greatly as each lithology has different compaction curves. Porosity may increase with depth in intervals with certain changes in lithology, but porosities in individual lithologies will almost always decrease with depth. Clastic deposits and their properties continuously change from deposition to present day due to a number of diagenetic processes. The main diagenetic processes are (Bjørlykke, 2015a):

- Near-surface diagenesis
- Mechanical compaction
- Chemical compaction
- Precipitation of cement

3.2.1.1. Mechanical compaction

Mechanical compaction includes packing, deformation and fracturing of grains. This results in increased mechanical stability and reduced porosity. Mineralogy and textural parameters such as grain size, shape, sorting and fabric are controlling factors for mechanical compaction in sands. Fine and rounded sand grains have generally higher strength compared to more coarse and angular grains. Larger grain size and increased angularity will increase crushing and result in a higher porosity loss (Chuhan, et al., 2003; Fawad, et al., 2011). Several physical processes contribute to mechanical compaction, including grain crushing, sliding and reorientation of brittle grains and pseudo-plastic deformation of ductile grains (Bjørlykke, et al., 1989) (Figure 3.2). Mechanical compaction processes are a direct response to increased effective stress, which is the difference between lithostatic pressure and pore pressure. Permeability controls the buildup of pore pressure and therefore acts as a controlling factor for the general rate of compaction, while permeability itself is controlled by the textural parameters mentioned.

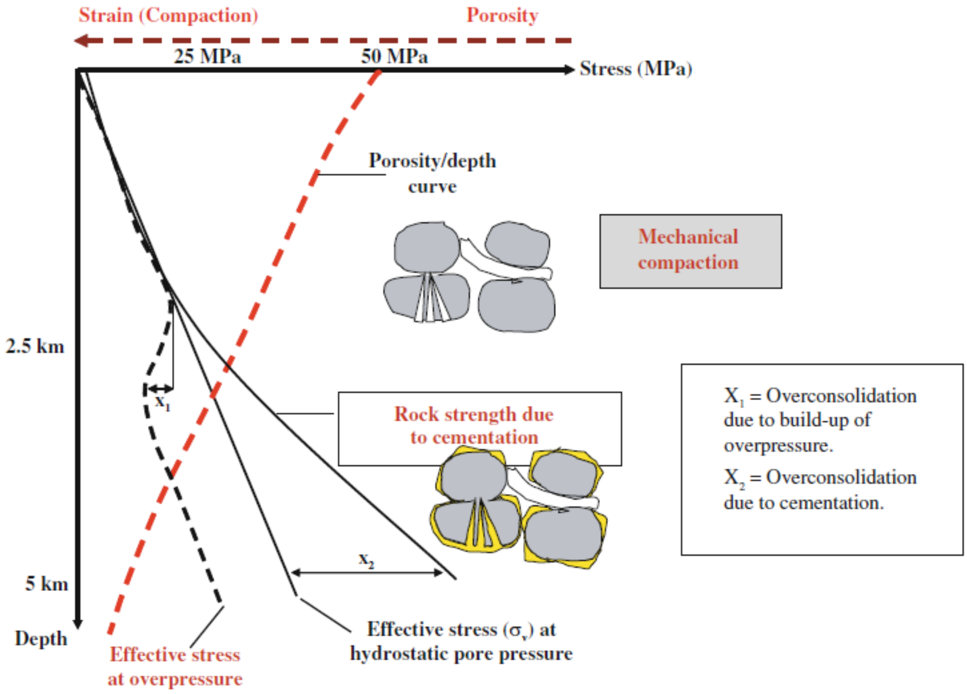

Figure 3.2: Overview of sandstone diagenesis (Bjørlykke and Jahren, 2015).

Mechanical compaction of shales and mudstones, composed of fine-grained silt and clay particles, are mainly controlled by the mineralogical composition of the constituent clay particles (Mondol, et al., 2007; Mondol, et al., 2008; Peltonen, et al., 2008; Marcussen, et al., 2010; Mondol, 2009). In terms of mechanical compaction, kaolinite and smectite act as end member clay minerals. Smectite has a very small grain size resulting in large specific surface area and a high cation change capacity. This allows for large volumes of water to be bound within the smectite structure. Fine-grained particles and high amount of bound water creates high pore pressure and makes smectite the hardest clay mineral to compact. The other end member clay mineral, kaolinite, has a coarser and more blocky texture making it easier to compact.

The compaction of clays can start already after a decimeter to a few meters of burial, while sand require more overburden stress for significant compaction to start. The mechanical compaction will dominate in the shallow part of a basin in both cases typically down to depths of 2-4km, depending on local geothermal gradient (Bjørlykke, 2015a). In a mechanical compaction regime, a vertical principal stress axis is expected as both the overburden sediments and pore fluids produce vertical stress. Lithostatic stress, stress provided by the overburden sediments, can be calculated using the following formula:

$$\sigma_v = \rho_b gh \qquad \text{Eq. 3.1}$$

where σ_v is the average bulk density of all overburden sediments, g is gravitational force and h is the total thickness of the overburden. The most important factor is, however, the effective stress. Effective stress (σ'_v) is defined as the difference between lithostatic stress (σ_v) and pore pressure (P_P):

$$\sigma'_v = \sigma_v - P_p \qquad \text{Eq. 3.2}$$

3.2.1.2. Chemical compaction

Chemical compaction usually follows mechanical compaction at depths of 2-4km (dependent on geothermal gradient) and deeper in sedimentary basins. Controlling factors are time and temperature, while physical processes include dissolution and mineral precipitation (Walderhaug, 1994; Walderhaug, 2000; Walderhaug, et al., 2004). These processes cause a stiffer rock framework, making it insensitive to effective stress (Bjørlykke, 1999; Storvoll, et al., 2005). At temperatures above 70ºC chemical compaction may proceed independently of the effective stress. This initial phase at around 70ºC, where stiffening due to cementation at grain contacts start (Vernik & Landis, 1996), is called the transition zone. Chemical compaction will prevail if temperatures stay below the 70-80ºC threshold, even during episodes of uplift. As temperatures sink during uplift, the compaction rate will sink as well (Bjørlykke & Jahren, 2015). Chemical compaction in sandstones is observed as dissolution along stylolites and as precipitation of cement on quartz grains. The transition from mechanical to chemical compaction in mudstones is more related to the stability of primary minerals than specific temperatures. One of the most important digenetic alteration processes is the transition from smectite to illite (and/or chlorite) at 70-100ºC (Thyberg, et al., 2009):

$$\text{Smectite} + \text{K-feldspar} = \text{Illite} + \text{Quartz} + H_2O \qquad \text{Eq. 3.3}$$

The next important chemical reaction usually occurs at approximately 130ºC when authigenic illite form by the transformation of K-feldspar and kaolinite (Bjørlykke, et al., 1986):

$$\text{K-feldspar} + \text{Kaolinite} = \text{Illite} + \text{Quartz} + H_2O \qquad \text{Eq. 3.4}$$

If the precipitated quartz produces a coating of the sand grains it can prevent cementation of quartz and thus preserve porosity even at great depths. In cases of pore water supersaturated with quartz from dissolved Opal A or Opal CT a similar grain coating may evolve at temperatures as low as 60-80ºC (Bjørlykke & Jahren, 2015). The illitization process of smectite creates a network of smaller and stiffer crystals (micro-quartz) which simultaneously reduces permeability and produce overpressure (Thyberg, et al., 2009).

3.2.1.3. Porosity preservation

As described there are several factors and processes that reduce porosity during burial. However, any universally valid porosity-depth function doesn't exist. There are various porosity preserving mechanisms acting on sediments during burial that may have very local and/or unpredictable occurrence. Bloch et al. (2002) identified four reasons for higher than expected porosities in sandstones at great depths:

1. Grain coating
2. Emplacement of hydrocarbons
3. Fluid overpressure
4. Secondary porosity

Known grain coatings include chlorite, illite, detrital clay, iron oxide and micro-quartz. Effective porosity preservation requires formation of grain coating before substantial quartz cementation starts. The coating itself should be continuous, cover the total grain surface and developed on the majority of grains for effective porosity preservation (Storvoll, et al., 2002). Grain coating allows mechanical compaction to dominate at greater than normal depth, generating fractures and secondary porosity in the process. Oil emplacement may retard the rate of quartz cementation severely. Marchand et al. (2002) reported reduced quartz precipitation rates by two orders of magnitude in oil legs relative to water legs. Fluid overpressure, on the other hand, provide effective porosity preservation when the effective stress is sufficiently decreased.

3.2.1.4. Compaction study

The compaction study in this thesis aims to locate the mechanical and chemical compaction domains, as well as the transition zone between them. More specific deviations from expected compaction trends are also interesting to identify if present, e.g. overpressure, mineral transitions and presence of hydrocarbons. Experimental compaction studies offer important information about how mechanical compaction is affected by sediment composition and sorting (Mondol, et al., 2007; Mondol, et al., 2008), while the effect of chemical compaction on velocity, density and porosity is difficult to simulate in the laboratory due to low kinetic reaction rates in siliciclastic sediments. The outcome of such experimental compaction studies is a set of experimental compaction curves, with specific set of parameters. Five published compaction curves, with different clay compositions, sandstones and mixes of silt, clay and sand, have been utilized in this thesis (Storvoll, et al., 2005; Mondol, et al., 2007; Mondol, 2009; Marcussen, et al., 2010). A natural, log-derived dataset should plot along an experimental compaction curve with similar characteristics, within the mechanical compaction domain. Once the chemical compaction domain is entered, we expect to see the log-derived data deviate from the compaction curve. Velocity, density and porosity are the most applicable logs for this purpose. A geothermal gradient for the dataset is valuable to identify (and later predict) temperatures of the different compaction domains.

3.2.2. Uplift estimation

Compaction studies are very useful for estimation of potential uplift and erosion in sedimentary basins. The assumption behind such an uplift estimation is increased compaction (reduced porosity, increased velocity etc.) with burial and that this process is nearly irreversible. Hence, the observed compaction of a given sediment should represent its deepest burial (Giles, et al., 1998; Mondol, 2015).

The first part of an uplift estimation is to consider relevant experimental compaction trend or establish a normal compaction trend in a normally compacted succession at maximum burial. Once an appropriate compaction trend is chosen, this can be compared with the porosity/velocity versus depth trend from different wells. A higher degree of compaction (lower porosity, higher velocity) at present-day depth compared to the experimental trend indicates over-compaction. An over-compaction achieved at greater burial depth than presently observed. The estimation of uplift can be derived from the displacement of the two trends along the depth axis. The gross exhumation will be equal to the amount of eroded sediments if there are unconformities present. If the sediments have been re-buried post-exhumation, the erosion estimates will be too low (Baig, 2018).

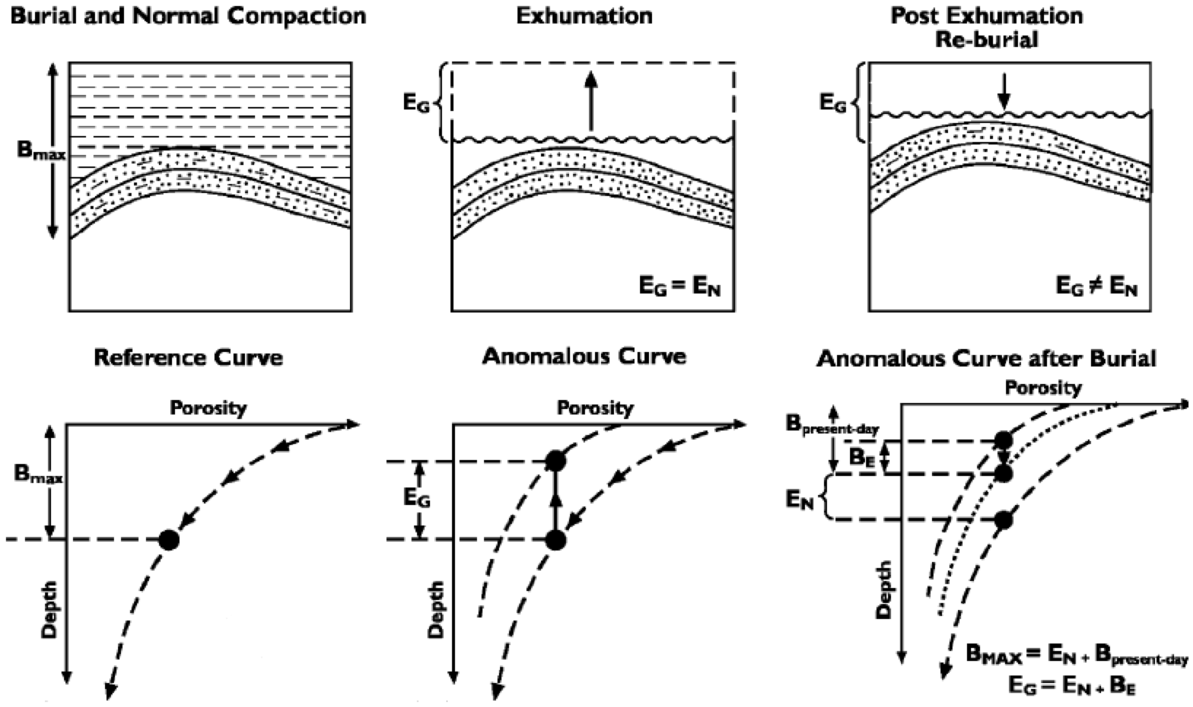

Figure 3.3: Illustration of uplift-estimation workflow. A maximum burial example is showed to the left with an associated porosity/velocity versus depth curve. This curve is typically projected using a suitable normal compaction trend. Uplift, erosion and the resulting curve is depicted in the middle. The difference between the normal compaction curve and the uplifted one equals the gross exhumation. An example of post exhumation re-burial is portrayed to the right. Re-burial will shift the uplifted curve towards the normally compacted one, depending on the amount of re-burial. B_{max} is the maximum burial, E_G is the gross exhumation, B_E is the thickness of post exhumation reburial and E_N is net exhumation (modified from Corcoran and Doré, 2005).

3.3. Petrophysical analysis

Interpretation of petrophysical well logs plays a major role in analysis of sedimentary successions relevant for hydrocarbon exploration. A petrophysical analysis aims to identify source, reservoir and cap rock units and describe their quality parameters, including lithology, porosity, permeability and hydrocarbon saturation. Such parameters are more precisely obtained directly from cuttings or cores. However, cores are only available from a selection of wells and intervals while cuttings often fail to provide reservoir property information. Consequently, most wells and intervals must rely on petrophysical well logs for lithology determination and reservoir properties. Well log data can be analyzed in their original state or used to calculate additional parameters. All well logs have limitations or pitfalls and must therefore also be used in combinations with each other to minimize margin of error and maximize potential and confidence.

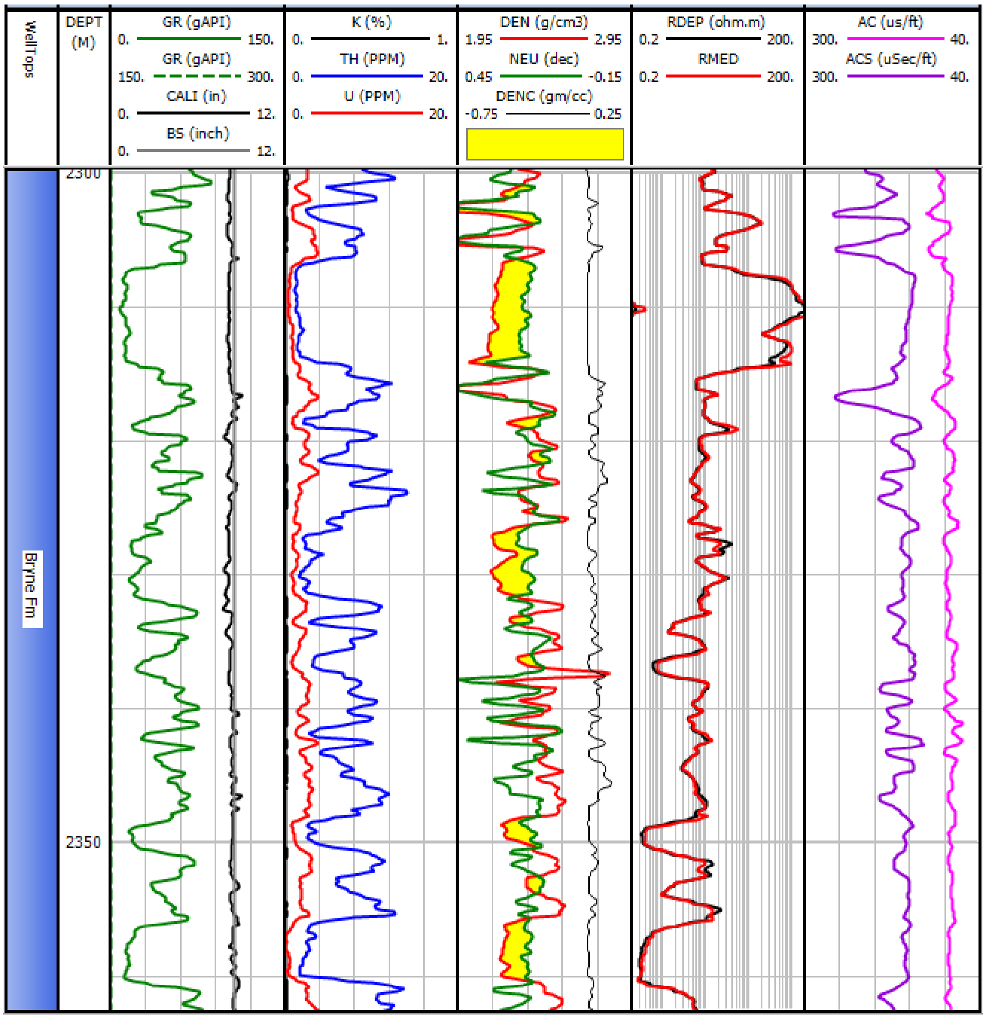

Figure 3.4: Overview of main logs used in petrophysical analysis. Several of these logs are referred to with different names in other wells, e.g. DEN=RHOB and NEU=CN. Example from well 17/12-4.

In a petrophysical analysis of reservoir and source rock units, important parameters include e.g. shale volume, TOC, porosity, water saturation and net-to-gross. Main well logs used in the analysis are shown in Figure 3.4.

3.3.1. Lithology discrimination and net-to-gross estimation

Lithology is primarily determined using gamma ray log (GR) and neutron/density logs. Borehole diameter measured by caliper log may indicate brittle shales (caving) and permeable formations (mudcake). Information on the same parameters can be extracted from Spontaneous Potential (SP) log. The shape and shale baseline deviation of the SP curve can contribute to separate shales from more permeable beds. Oil-based muds in drilling prevent the use of SP log, as the measured electric potential rely on conductive muds. The photoelectric log (PEF), a variation of the density log, measures the return of low energy gamma rays, mostly independent of porosity and density and may therefore help discriminate lithologies. Drilling muds with barite makes a PEF log useless (Mondol, 2015).

The gamma ray log is based on passive recording of the total natural gamma radiation. The radioactive isotopes of potassium (^{40}K), thorium (^{232}Th) and uranium (^{238}U) are the main source of this radiation in rocks. Considering siliciclastic rocks, clean sands display low GR values while more shaly rocks display higher GR values. Very high GR values can be expected from organic-rich shales because of high uranium content. The uranium part of the spectral gamma log is therefore important to confirm the organic richness of high GR lithologies. There is not much research supporting the use of gamma ray log as shale volume indicator (and in extension, lithology indicator), but it is a common, accepted assumption that increased shale volume is represented by higher gamma ray readings (Kennedy, 2015). Gamma ray log provides non-unique solutions, as limestones, dolomite, coal and salt may produce the same low values as a clean quartz sand (Mondol, 2015).

Net-to-gross ratio is a rather unclear term as there are several uses and definitions. The definition used in a study should be specifically stated to avoid misunderstandings. This study uses the sequential approach and definition proposed by Worthington and Cosentino (2005). Different levels of "net" thicknesses (N) and their related "gross" reservoir thickness (G) are presented below:

- *Gross rock*: Total rock volume within the interval of investigation. Typically, a formation.
- *Net sand*: Part of the initial volume that show potential for acceptable reservoir properties. Typically based on a shale volume (V_{sh}) cutoff value.
- *Net reservoir*: The intervals within the net sand that proves to have useful reservoir properties, based on porosity (ϕ) and a defined porosity cutoff value.
- *Net pay*: Net reservoir intervals which contain acceptable amounts of hydrocarbons, predefined by a hydrocarbon (S_h) or water saturation (S_w) cutoff value.

These definitions can be used to express different ratios; net-to-gross sand, net-to-gross reservoir and net-to-gross pay (Worthington & Cosentino, 2005). A pay zone is described as a zone with sufficiently low shale volume and high porosity, in addition to extractable and economic viable hydrocarbon content (Bjørlykke, 2015c). The cutoff values used in this study is based on suggested values from Worthington and Cosentino (2005) and are presented in Table 3.1.

Table 3.1: Utilized cutoff values for calculation of net thicknesses. Values are chosen with inspiration from Worthington and Cosentino (2005).

Cutoff parameter	Cutoff value
Shale volume (V_{sh})	0.4
Porosity (ϕ)	0.1
Water saturation (S_w)	0.6

3.3.2. Shale volume calculation

Assuming a linear relationship, shale volume can be derived directly from the gamma ray log, using Eq. 3.5. This equation assumes a constant value for pure shale in one area, well or zone. Based on this simplification, a subjectively picked maximum average is chosen to represent 100% shale, while a chosen minimum average represents 0% shale (Mondol, 2015):

$$I_{GR} = \frac{GR_{log} - GR_{min}}{GR_{max} - GR_{min}} \qquad \text{Eq. 3.5}$$

where, I_{GR}: gamma ray index, GR_{log}: gamma ray reading, GR_{min}: minimum gamma ray reading (sand line/no shale), GR_{max}: maximum gamma ray reading (shale line/no sand). As previously mentioned, this linear relationship between gamma ray index and shale volume has no scientific basis. The general trend from this relationship is a considerable overestimation (Mondol, 2015). Decreasing depth of investigation with increasing formation density is the main reason for said overestimation. To avoid this overestimation when calculating shale volume, correction by non-linear published trends should be applied (Asquith & Krygowski, 2004; Mondol, 2015):

$$\text{Larinov (older rocks): } V_{sh} = 0.33(2^{2.0 \times IGR} - 1) \qquad \text{Eq. 3.6}$$

$$\text{Clavier (1971): } V_{sh} = 1.7 - [3.38 - (IGR - 0.7)^2]^{1/2} \qquad \text{Eq. 3.7}$$

$$\text{Stieber (1970): } V_{sh} = \frac{IGR}{3 - 2 \times IGR} \qquad \text{Eq. 3.8}$$

$$\text{Larinov (tertiary rocks): } V_{sh} = 0.083(2^{3.7 \times IGR} - 1) \qquad \text{Eq 3.9}$$

When calculating shale volume from neutron-density logs, one considers the separation between these logs. A neutron-density curve combination will identify shale from large positive separations, due to the high hydrogen index of shale matrix. Matrix density of shales and quartz are similar, and the density curve will therefore not change much from shale to sand units. However, the neutron readings will rapidly increase with increased shale volume, resulting in the observed positive separation. The separation will normally decrease with increasing quartz volume and reach a slightly negative separation in formations with clean sand (Mondol, 2015).

A bulk density versus neutron porosity crossplot is commonly used as a part of an additional shale volume calculation (figure 3.6). This crossplot requires a subjective definition of a “clean line” and a “clay point”. The position and distance between these two limits is used in the following equation to determine shale volume from the density versus neutron porosity crossplot:

$$V_{shND} = \frac{(D_{Cl2} - D_{Cl1}) \times (N - N_{Cl1}) - (D - D_{Cl1}) \times (N_{Cl2} - N_{Cl1})}{(D_{Cl2} - D_{Cl1}) \times (N_{Clay} - N_{Cl1}) - (D_{Clay} - D_{Cl1}) \times (N_{Cl2} - N_{Cl1})} \qquad \text{Eq. 3.10}$$

where D_{Cl1}, N_{Cl1} and D_{Cl2}, N_{Cl2}: selected end values of the clean line; D_{Clay}, N_{Clay}: density and neutron values for the shale point; D, N: measured density and neutron values.

This method is, however, dependent on both saturation and mineralogy, providing accurate result for brine-saturated shaly sand formations with a quartz-clay mix. The composition of other sand-forming minerals and low density of hydrocarbons can affect the observed log separation (Mondol, 2015).

3.3.3. Porosity estimation

Porosity is defined as the ratio of pore volume to bulk volume or the volume fraction of fluids within the rock. This definition can be considered somewhat inaccurate as some of the water may be considered a part of the matrix. Especially clay minerals, with their large surface forming morphology, will often bind significant volumes of water. To remove uncertainties regarding definitions of porosity, two extra terms are introduced; *total* and *effective* porosity (Kennedy, 2015). *Total porosity* is defined as the total non-solid space in a rock. *Effective porosity* includes only the connected porosity of a rock.

From wireline logging, four logs are generally used to provide information about porosity:

- Density log (RHOB) [g/cm^3 or kg/m^3]
- Neutron log (NPHI) [fraction or %]
- Sonic log (Δt) (acoustic measurement) [µs/ft]
- Nuclear Magnetic Resonance (NMR) (not available in studied wells)

3.3.3.1. Density porosity

The density logging tool measures the attenuation of induced gamma radiation (decreases with increasing porosity) and uses this to calculate bulk density (ρ_b). The bulk density is a function of fluid density and matrix density and these are together applied to estimate the porosity (Mondol, 2015):

$$\phi_D = \frac{(\rho_{matrix} - \rho_{log})}{(\rho_{matrix} - \rho_{fluid})} \qquad \text{Eq. 3.11}$$

where ϕ_D: calculated density porosity, ρ_{matrix}: grain density, ρ_{fluid}: fluid density, ρ_{log}: bulk density measurement. Thus, an accurate porosity estimation requires control on matrix mineralogy and present fluids. The presence of oil and/or (especially) gas can cause significant porosity overestimations from the density log. Density logs are accompanied by a density correction curve (DRHO) to indicate the amount of correction applied to counteract borehole effects. Asquith and Krygowski (2004) proposes that a correction of more than 0.20 g/cm^3 indicate an incorrect bulk density reading.

The in-built porosity calculation tool of the Interactive Petrophysics software features a more complex equation based on density. The complexity of the equation includes several parameters and constants, as well as new uncertainties. The help manual states that if a density porosity model is selected in Interactive Petrophysics, then porosity is calculated as follows:

$$\phi_D = \frac{\rho_{ma} - \rho_b - Vcl \times (\rho_{ma} - \rho_{cl})}{\rho_{ma} - \rho_{fl} \times Sxo - \rho_{HyAp} \times (1 - Sxo)} \qquad \text{Eq. 3.12}$$

Where ρ_{ma}: matrix density, ρ_b: input bulk density log, Vcl: wet clay volume, ρ_{cl}:wet clay density, ρ_{fl}:filtrate density, Sxo: flushed zone water saturation and ρ_{HyAp}: apparent HC density.

3.3.3.2. Neutron porosity

Another indirect measurement of porosity can be derived from the neutron log. The neutron log is a measure of formation hydrogen content. Assuming all hydrogen is fluid bound, the log gives a water content estimate and consequently an estimate of the porosity. Hydrogen-rich clay minerals as smectite and kaolinite may cause higher porosity in clay-rich formations. This is known as the shale effect. To eliminate such effects, the neutron tool is commonly calibrated against limestone. Due to the low hydrogen content in limestone, more accurate porosity estimations are possible in such intervals. The low density of hydrocarbons (oil and gas) also affects the neutron log due to low hydrogen content per volume. This is a typical cause of porosity underestimation in neutron logs. In combination with a density log, such underestimations help identify gas zones (Asquith & Krygowski, 2004; Mondol, 2015).

Interactive Petrophysics software is used for this calculation. The in-built neutron porosity model is based on the following formula:

$$\phi_N = \frac{(\phi_{neu} - Vcl \times NeuCl + NeuMatrix + Exfact + NeuSal)}{(Sxo + (1 - Sxo) \times NeuHyHI)} \qquad \text{Eq. 3.13}$$

Where ϕ_{neu}: input neutron log, Vcl: wet clay volume, NeuCl: neutron wet clay value, NeuMatrix: neutron matrix correction, Exfact: neutron excavation factor, NeuSal: neutron formation salinity correction, Sxo: flushed zone water saturation, NeuHyHI: neutron HC apparent hydrogen index.

3.3.3.3. Combined neutron and density porosity

To avoid lithology effects and most accurately estimate porosity, a combination of logs can be utilized. The combination of neutron and density porosity logs is most common. Several ways to exploit this combination exists. The relative relationship of the curves can be compared directly, or the values can be crossplotted with an overlay with pure sandstone, limestone and dolomite lines (Figure 3.6). In a sand and shale dominated basin (like the North Sea), the scales should preferably use the sandstone line as reference (Asquith & Krygowski, 2004).

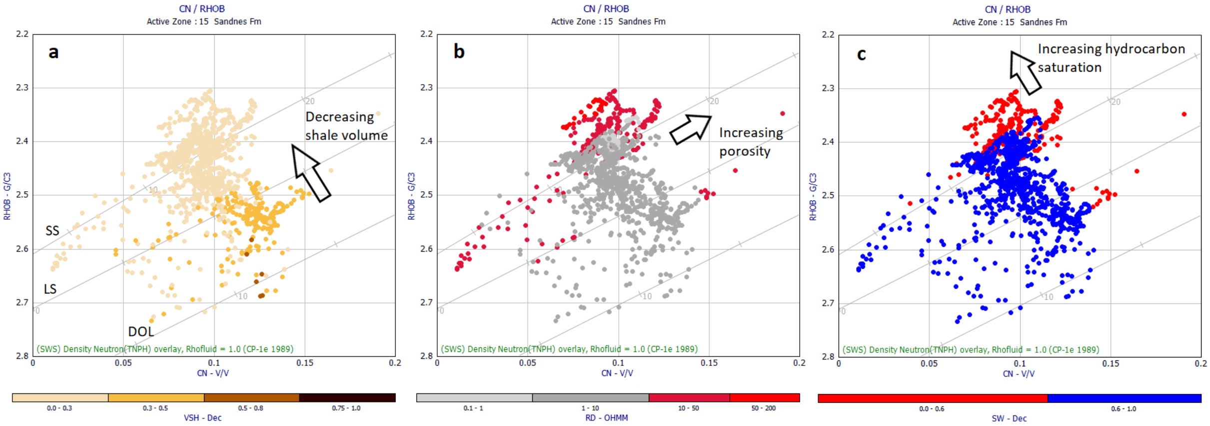

Figure 3.6: Neutron versus density crossplots of the Sandnes Fm in well 9/2-1. A) Color coded by shale volume showing decreasing shale volume towards the sandstone line. B) Color coded by deep resistivity to identify hydrocarbons with direct measurements. Also note how increasing density and neutron readings is indicative of increasing porosities. C) Color coded by calculated water saturation. As expected in a sandstone reservoir, hydrocarbon accumulations plot from the sandstone line towards lower densities. SS: sandstone, LS: limestone, DOL: dolomite.

A third option is to calculate the average of the two porosity estimates, aiming to even out lithology or fluid effects. This is especially effective in a gas-filled reservoir, where density porosity is overestimated due to lowered bulk density and neutron porosity is underestimated due to low hydrogen concentration. A more accurate porosity of a gas-bearing formation can therefore be calculated using the following equation (Asquith & Krygowski, 2004):

$$\phi_{ND} = \sqrt{\frac{\phi_N^2 - \phi_D^2}{2}} \qquad \text{Eq. 3.14}$$

where ϕ_{ND}: average neutron and density porosity, ϕ_N: neutron porosity, and ϕ_D: density porosity.

3.3.3.4. Sonic porosity

The velocity of elastic waves through a given lithology is a function of porosity. A sonic logging tool produces compressional sound waves and measures the slowness of these as they travel through the surrounding rocks. An interval transit time (Δt or DT) reading is produced, most commonly with µs/ft as unit. This reading represents the inverse velocity but is easily converted to velocity as m/s or km/s. The velocity of a rock is affected by both lithology and porosity. A porosity estimation from sonic log therefore requires correct velocity values for both the rock matrix and the formation fluid. Wyllie (1958) proposed the following *time average equation* for estimation of porosity from sonic log (Asquith & Krygowski, 2004; Mondol, 2015):

$$\phi_S = \frac{\Delta t_{log} - \Delta t_{matrix}}{\Delta t_{fluid} - \Delta t_{matrix}} \qquad \text{Eq. 3.15}$$

where ϕ_S: sonic porosity, Δt_{log}: sonic transit time in formation of interest, Δt_{matrix}: transit time of matrix, and Δt_{fluid}: transit time of fluid.

The Raymer-Hunt-Gardener equation (1980)is an alternative for sonic porosity estimation:

$$\phi_S = \frac{5}{8} \times \frac{\Delta t_{log} - \Delta t_{matrix}}{\Delta t_{log}} \qquad \text{Eq. 3.16}$$

A number of standard values exist for the matrix and formation fluid parameters, including; 55.5 and 56 µs/ft as sandstone matrix value for Wyllie and RHG equation respectively, and 189 µs/ft for brine as formation fluid.

3.3.3.5. Effective porosity

Total porosity includes the water bound in clay minerals, while only the connected porosity of a rock is regarded as effective porosity (Figure 3.7). Estimates like neutron porosity are affected by mineral-bound water and effective porosity is therefore desirable (Ellis & Singer, 2007). This relationship can be theoretically represented by the following equation (Hook, 2003):

$$\phi_E = \frac{V_{pt} - V_{cbw}}{V_b} \qquad \text{Eq. 3.17}$$

where ϕ_E: effective porosity, V_{pt}: total pore volume, V_{cbw}: volume of clay bound water and V_b: bulk rock volume.

The Hampson-Russel software suggests another approach utilizing calculated shale volume:

$$\phi_E = (1 - V_{sh}) \times \phi_T \qquad \text{Eq. 3.18}$$

where V_{sh}: estimated shale volume and ϕ_T: total porosity (i.e. the average of neutron porosity and density porosity.

Interactive Petrophysics proposed another equation, based on wet clay volume:

$$V_{sh} = V_{cl} + V_{silt} \qquad \text{Eq. 3.19}$$

and

$$V_{silt} = 1 - \frac{\phi_E}{\phi_{max}} - V_{cl} \qquad \text{Eq. 3.20}$$

where V_{cl}: wet clay volume, V_{silt}: silt volume and ϕ_{max}: maximum porosity in clean sand.

Shale volume and clay volume are not the same, and these relations assume a similar amount of clay in the calculated shale volume and the shale of interest (Ellis & Singer, 2007). For effective porosity estimations, a clay fraction of 0.7 is used. This is within the average range of clay in shale from Bhuyan and Passey (1994), which is suggested to be 0.5-0.7.

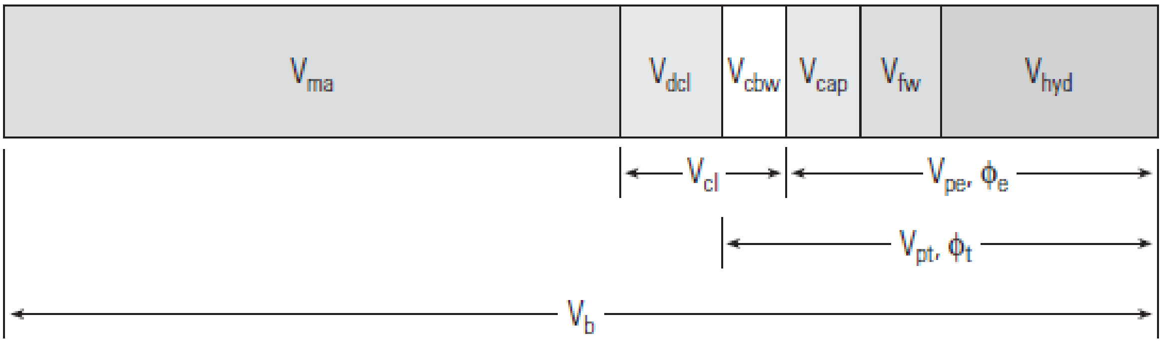

Figure 3.7: Different definitions of formation volumes. The subscripts ma: matrix, dcl: dry clay, cl: wet clay, cbw: clay bound water, cap: capillary bound water, fw: free water, hyd: hydrocarbon, b: bulk, p: porosity, e: effective and t: total (Ellis & Singer, 2007).

3.3.4. Water saturation and pay zone identification

Most rock forming minerals act as insulators while enclosed fluids act as conductors. Since most of the conduction takes place through the fluid phase, resistivity is controlled by the pore fluid and its properties. Hydrocarbons are almost infinitely resistive while brine conducts well (depending on salt content). This difference makes resistivity logs a powerful tool for detecting hydrocarbon-filled formations and separating those from brine-filled formations. Presence of hydrocarbons results in high formation resistivity, captured by deep (and possibly medium) resistivity logs. Resistivity reading are instrumental for determining water saturation, and consequently hydrocarbon saturation, using Archie's law (intended for clean, consolidated sandstones) (Asquith & Krygowski, 2004; Mondol, 2015):

$$S_w = (\frac{a \times R_w}{R_t \times \phi^m})^{\frac{1}{n}} \qquad \text{Eq. 3.21}$$

where

- S_w: calculated water saturation
- a: tortuosity factor
- m: cementation exponent (1.8-2.0 are typical sandstone values)
- n: saturation exponent (usually set to 2)
- R_w: formation water resistivity
- ϕ: porosity (neutron-density average is used in this study)
- R_t: true formation resistivity (from deep resistivity log)

As seen in Eq. 3.21, an accurate water saturation estimation require control on formation water resistivity (R_w). This parameter is typically calculated from SP log, when available. Alternatively, it can be estimated from resistivity logs in water-filled zones. Assuming 100% water saturation, the bulk resistivity (R_0) should be equal to true formation resistivity (R_t), and the formation water resistivity can be derived from Archie's equation (Ellis & Singer, 2007):

$$R_w = R_t \times \phi^m \qquad \text{Eq. 3.22}$$

With three different depth sensitive resistivity logs (micro/shallow, medium, deep), a full transitional resistivity-profile can be measured. The micro resistivity (most common in new wells) will give the resistivity of the flushed zone (R_{xo}), the medium log will measure resistivity of the invaded zone (R_i), while the deep provide measurements from the uninvaded zone. If the mud filtrate resistivity is known (or guessed), flushed zone saturation (S_{xo}) can be calculated (Mondol, 2015).

Resistivity logs, and ultimately saturation calculations, have multiple uncertainties and limitations. Clay can have an influence on formation conductivity and therefore potentially overestimate water saturation (Ellis & Singer, 2007). The logging tool can only be used in intervals drilled with conductive mud. Resistivity of both formation fluids and drilling muds varies with temperature. Temperature and the constants used in Archie's equation are all uncertainties that need to be assessed. Unless a temperature log is available, the geothermal gradient can be estimated for a well using the following equation (Mondol, 2015):

$$G = \left(\frac{BHT - T_{ms}}{TD}\right) \times 100 \qquad \text{Eq. 3.23}$$

where G: temperature gradient in $^{O}C/100m$, BHT: bottom hole temperature (^{O}C), T_{ms}: mean surface temperature (normally considered to be 4 ^{O}C at sea floor), and TD: total depth (m BSF).

3.3.5. Permeability estimation

Permeability, the measure of resistance to the fluid flow through a rock, is an important reservoir parameter. The unit of measure for permeability is Darcy, and typically ranges from several millidarcies to several darcys. Ideally, permeability is measured directly on core samples, or alternatively sidewall cores or from a drill stem test. To estimate the permeability from well log data is difficult and will only result in an approximation. Three relationships between permeability, porosity and irreducible water saturation are used in this study:

$$k = \frac{10^4 \Phi_e^{4.5}}{S_w^2} \text{ (Timur equation)} \qquad \text{Eq. 3.24}$$

$$k = \frac{3400 \Phi_e^{4.4}}{S_w^2} \text{ (Wylie-Rose formula with Timur parameters) Eq. 3.25}$$

$$k = \frac{62500 \Phi_e^{6}}{S_w^2} \text{ (Wylie-Rose formula with Morris-Biggs parameters) Eq. 3.26}$$

where k is the calculated permeability, ϕ_e is effective porosity and S_w is irreducible water saturation. These equations are used for permeability estimations in the Interactive Petrophysics software.

3.3.6. Source rock identification and TOC prediction

Organic-rich shales with source rock potential are usually recognizable in logs by increased gamma ray, high neutron porosity, low bulk density and high sonic transit time. However, a more quantitative approach requires for thorough investigations. Most accurate results are normally achieved with analytical techniques used on cores. The advantages using petrophysics compared to cuttings analysis include continuous sampling, improved depth control, enhanced vertical resolution and elimination of sampling bias and contamination. Essential parameters for source rock evaluation are total organic content (TOC) and maturity. V_p (sonic log) and resistivity logs have proved to be most effective in reflecting organic carbon richness and thermal maturity (Passey, et al., 1990). The level of maturity will influence the resistivity log significantly. Organic matter has a high resistivity, but if it remains solid and the pore space is water-filled, formation resistivity will experience little effects. As the source rock matures and hydrocarbons are generated, water is replaced by oil in pores, and resistivity consequently increases. A V_p versus formation resistivity crossplot is effective to eliminate lithology effects, for example carbonates and highly compacted shales (Mondol, 2015).

The combination of resistivity and sonic logs allows for calculation of TOC in a source rock. First, the sonic log is plotted on a normalized scale with the resistivity log (Figure 3.8). When the normalized scales are correct, the sonic and resistivity logs follow each other close, regardless of compaction and compositional changes. Curve separation occurs with presence of source rock and relates to both maturity and TOC% (Passey, et al., 1990). If the maturity is known, TOC% can be calculated using the following formula:

$$\mathrm{TOC\%} = (\Delta\log\mathrm{R}) \times 10^{(2.297-0.1688\times\mathrm{LOM})} \qquad \text{Eq. 3.27}$$

where TOC%: total organic carbon (%), LOM: level of maturity, and ΔlogR: curve separation in resistivity unit.

This method requires the user to know or at least guess the maturity, in level of organic metamorphism units (LOM) (Hood, et al., 1975). LOM is usually acquired from sample analysis, including vitrinite reflectance, thermal alteration index or T_{max}, or thermal history estimates. An incorrect estimate of LOM will give inaccurate prediction of absolute TOC values. However, the vertical variability in TOC will be correct. The use of LOM, a much less commonly used measure of source rock maturity, is one of several weaknesses with this method. The method also fails to pick up petrophysical properties of organic-rich shales which may vary significantly between different formations. Despite its flaws, the equation of Passey et al. (1990) is used in the TOC calculation tool of the Interactive Petrophysics software which is utilized in this thesis.

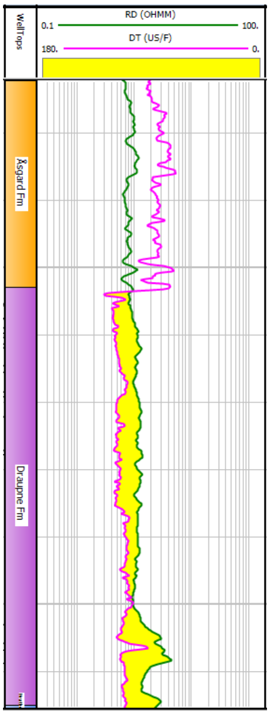

Figure 3.8: Deep Resistivity (RD) and sonic (DT) log separation example from well 15/12-2. The curves follow each other close in the organic-lean Åsgard Fm, while showing significant negative separation in the organic-rich Draupne Fm. The lack of response of the resistivity log suggests immature source rock.

Another equation for prediction of TOC was proposed by Vernik & Landis (1996). The equation is based how TOC is related to densities of both minerals and kerogen in different lithologies:

$$\mathrm{TOC\%} = 67\,\frac{\rho_k(\rho_m-\rho_s)}{\rho_s(\rho_m-\rho_k)} \qquad \text{Eq. 3.28}$$

where ρ_k is the kerogen density, ρ_m is average solid matrix density, ρ_s is grain density and a constant (67) is used for the assumed organic content in kerogen (Tissot & Welte, 1978).

The solid matrix density is given by the density log. Kerogen density is normally in the range of 1.0-1.4 g/cm^3, dependent on maturity. The grain density will vary significantly with lithology and mineralogy. Consequently, this method also requires knowledge or educated guesswork of mineralogy and kerogen. In both cases the desired solution is measured values from analyzed samples, providing calibration points to your estimation.

3.4. Rock physics

Rock physics act as a bridge between elastic properties (e.g. V_P, V_S, V_P/V_S ratio, acoustic impedance) and geological parameters (e.g. shale volume, lithology, porosity, sorting) of a rock (Avseth, 2015). Today, rock physics is a key technology in petroleum geophysics as an important part of quantitative seismic interpretation. The overall goal of the application of rock physics is reduction of exploration risk and improved reservoir predictions by extracting information that is hidden from conventional seismic interpretation. A typical rock physics analysis is performed utilizing crossplots of elastic parameters versus a given geological parameter (or two by color-coding). In this thesis both the elastic parameters and most of the geological parameters are derived from well log data. Together with a rock physics model, the data can shed light on how the geology is controlling the elastic parameters. Different models and crossplots are utilized in the compaction study and the petrophysical analysis to understand how the geological parameters affect elastic properties.

3.4.1. Cement models

As highlighted in the compaction study, cementation of a rock has an impact on stiffness and velocity. Velocity-porosity trends are drastically changed by the onset of such pore scale solids. In the case of a reservoir sandstone, three theoretical models exist to describe the possible velocity-porosity trends; contact-cement model, constant-cement model and friable sand model (Figure 3.9).

3.4.1.1. Friable sand model

Dvorkin and Nur (1996) introduced the concept of a friable sand model. This model assumes that the decreasing porosity is due to deposition of solid matter in the pore space of the rock and away from the grain contacts. This is effectively deteriorating the grain sorting while only weakly affecting the stiffness of the rock. The model has two end members; a point with well sorted packing of grains with critical porosity (typically 40%) and a zero-porosity point (i.e. elastic moduli). Critical porosity is where a sediment transitions from being fluid-suspended (grains not in contact) to being load-bearing.

Avseth et al. (2005) describes the procedure of producing the friable sand model for varying effective pressures. First, the elastic moduli of the well-sorted end member are calculated using Hertz-Mindlin theory, assuming an elastic sphere pack exposed to confining pressure (Mindlin, 1949):

$$K_{HM} = \left[\frac{n^2(1-\phi_c)^2\mu^2}{18\pi^2(1-\vartheta)^2}P\right]^{\frac{1}{3}} \qquad \text{Eq. 3.29}$$

$$\mu_{HM} = \frac{5-4\vartheta}{5(2-\vartheta)}\left[\frac{3n^2(1-\phi_c)^2\mu^2}{2\pi^2(1-\vartheta)^2}P\right]^{\frac{1}{3}} \qquad \text{Eq. 3.30}$$

Where K_{HM}: dry rock bulk moduli, μ_{HM}: dry rock shear moduli, P: effective pressure, ϕ_c: critical porosity, μ: shear modulus of the solid phase, ϑ: Poisson's ratio of the solid phase, and n is the coordination number (number of grain contacts), estimated using the following formula (Avseth, et al., 2005):

$$n = 20 - 34\phi + 14\phi^2 \qquad \text{Eq. 3.31}$$

meaning that at a critical porosity of 40%, the average number of grain contacts are 8.6.

The Poisson's ratio can be expressed by a combination of bulk (K) and shear (μ) modulus (Avseth, et al., 2005):

$$\vartheta = \frac{3K-2\mu}{2(3K+\mu)} \qquad \text{Eq. 3.32}$$

The other end member of the friable sand model, which is at zero porosity, will have similar elastic properties as the corresponding mineral. An interpolation of the moduli between 0 and ϕ_c is calculated using the Hashin-Shtrikman bounds. To model the friable sand model, the lower bound is used (Avseth, et al., 2005):

$$K_{dry} = \left[\frac{\phi/\phi_c}{K_{HM}+4\mu_{HM}/3} + \frac{1-\phi/\phi_c}{K+4\mu_{HM}/3}\right]^{-1} - \frac{4}{3}\mu_{HM} \qquad \text{Eq. 3.33}$$

$$\mu_{dry} = \left[\frac{\phi/\phi_c}{\mu_{HM}+z} + \frac{1-\phi/\phi_c}{\mu+z}\right]^{-1} - z \qquad \text{Eq. 3.34}$$

where

$$z = \frac{\mu_{HM}}{6}\left(\frac{9K_{HM}+8\mu_{HM}}{K_{HM}+2\mu_{HM}}\right) \qquad \text{Eq. 3.35}$$

After computing the dry elastic moduli of the friable sand model end members, fluid substitution can be utilized to calculate the saturated elastic moduli. Fluid substitution is performed using Gassmann's equation:

$$\mu_{dry} = \mu_{sat} \qquad \text{Eq. 3.36}$$

$$K * = K_d + \frac{\left(1-\frac{K_d}{K_s}\right)^2}{\frac{\Phi}{K_f}+\frac{1-\Phi}{K_s}+\frac{K_d}{K_s^2}} \qquad \text{Eq. 3.37}$$

Where μ_{dry}: shear modulus of dry rock, μ_{sat}: shear modulus of fluid saturated rock, K*: effective bulk modulus of saturated rock, K_d: dry rock bulk modulus, K_f: fluid bulk modulus, K_s: solid (mineral) bulk modulus and ϕ: porosity.

Ultimately, the seismic velocities of the different porosities along the friable sand model can be calculated by the following equations:

$$V_p = \sqrt{\frac{K+4/3\times\mu}{\rho}} \qquad \text{Eq. 3.38}$$

$$V_s = \sqrt{\frac{\mu}{\rho}} \qquad \text{Eq. 3.39}$$

Where ρ: bulk density.

A properly calculated friable sand model will visualize the velocity-porosity relationship of an unconsolidated sandstone as a function of sorting at specific pressure levels. The degree of sorting decides where on the modeled line (for a specific pressure value) the data will fall (Avseth, et al., 2005). An effective example on how geophysical parameters can provide insights to geological parameters.

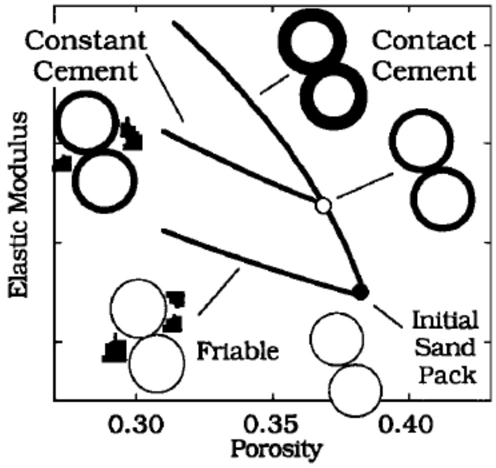

Figure 3.9: Three effective medium models for high-porosity sands in the elastic-modulus-porosity plane (Avseth, et al., 2000).

3.4.1.2. Contact-cement model

The theory behind the compaction study illustrated that sands are likely to become cemented sandstones after sufficient burial. In the contact-cement model this cementation is assumed to be uniform layers progressively deposited around grains, “gluing” grain contacts together. A drastically increase of stiffness is experienced due to such contact cement. Consequently, a large velocity increase is observed, with only a minor decrease of porosity (Avseth, et al., 2005). The equations used to calculate this model are given and explained in Dvorkin and Nur (1996).

3.4.1.3. Constant-cement model

The last cement model studied in this thesis is the constant-cement model, introduced by Avseth et al. (2000). Acting as a combination of the friable sand model and the contact-cement model, the constant-cement model assumes equal amounts of contact-cement for sands with varying porosity. Presence of non-contact pore-filling material is the controlling factor of the porosity factor in this model. The constant-cement model provides a good representation of a constrained reservoir, where cementation is mostly depth-dependent, and sorting may vary significant laterally due to depositional factors (Avseth, et al., 2005).

3.4.2. Rock physics templates

The rock physics template (RPT), first introduced by Ødegaard and Avseth (2004), combine depositional and diagenetic models (e.g. cement models) with Gassmann fluid substitution in charts/templates for prediction of lithology and presence of hydrocarbons (Avseth, et al., 2005). RPTs are not universal and geological parameters, including lithology, burial depth, diagenesis and pore pressure, must be constrained to local geology (e.g. basin). Lithology is particularly important, and only expected lithologies should be included. This thesis includes wellbores that penetrated mainly siliciclastic successions and shale, shaly sand and clean sands are therefore expected lithologies. Utilized mineral parameters are presented in Table 3.2:

Table 3.2: Mineral parameters utilized for rock physics diagnostics. Based on Mavko et al. (2009).

Mineral	V_p (km/s)	V_s (km/s)	Density (g/cm^3)	Bulk (K) modulus (GPa)	Shear (μ) modulus (GPa)	Poisson's ratio
Quartz	6.05	4.09	2.65	37.0	44.0	0.08
Quartz with clay	5.59	3.52	2.65	39.0	33.0	0.17
Clay	3.81	1.88	2.6	21.0	7.0	0.35

Avseth et al. (2005) emphasize that using generalized values for clay is a simplification and must be done with caution.

3.4.2.1. V_p / V_s versus AI

The introduction of rock physics templates by Ødegaard and Avseth (2003) was on a cross plot of V_p/V_s ratio versus acoustic impedance (AI) (Figure 3.10). The V_p/V_s ratio is useful discriminate hydrocarbon bearing sands from brine-filled sands and mature source rocks from immature source rocks. Additional information from AI enables this cross plot to describe lithology, porosity and possibly TOC content of shales. Fluid separation is most noticeable in unconsolidated, homogeneous sands and decreases with increasing cementation. Cementation is a weakness of this template, as increased cementation often lowers the V_p/V_s ratio of brine sand to similar levels as oil-bearing unconsolidated sands. Sensitivity to net-to-gross is also low. This could result in a low net-to-gross oil-sand plotting at high V_p/V_s ratio, where brine sands are expected (Avseth, et al., 2005).

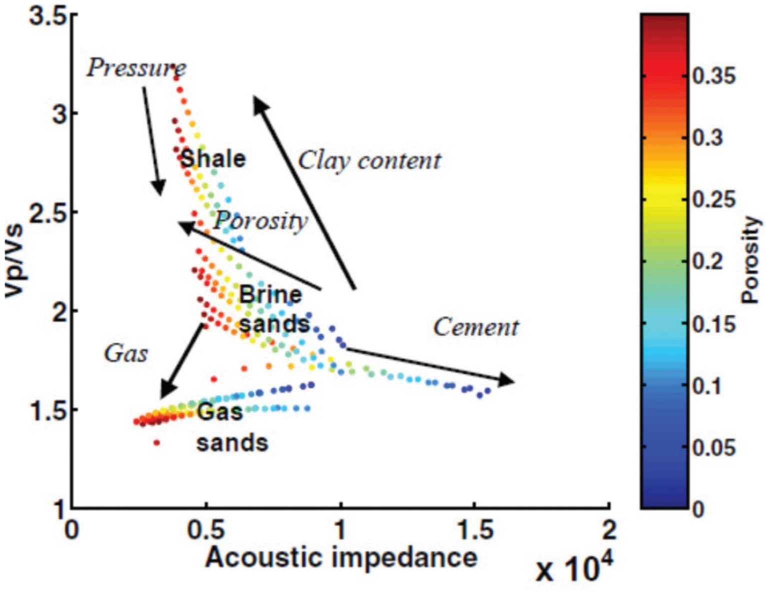

Figure 3.10: Interpretation of a rock physics template in terms of shale/clay volume, fluid content, compaction/cementation. Increasing TOC and maturation of source rock are expected to have similar effects on the shale trend as the increasing gas saturation has on a brine sand (Ødegaard and Avseth, 2003).

A site-specific rock physics template may be created using the following steps:

- Applying Hertz-Mindlin theory to estimate dry bulk and shear modulus at initial porosity ($\phi_c = 40\%$).
- Defining the zero-porosity mineral point based on the quartz bulk and shear modulus from Carmichael (1989).
- Using Hashin- Shtrikman upper bound at different porosities to interpolate and create a model between the two end-members.
- Calculating effective moduli at various fluid saturations using Gassmann fluid substitution.
- Performing similar procedures for shale/clay and various TOC content and maturity.
- Calculating V_p, V_s and density for each scenario.
- Cross plot V_p/V_s ratio and acoustic impedance on the template for interpretation.

3.4.2.2. LambdaRho versus MuRho

The theory behind a Lambda-Mu-Rho (LMR) cross plot is the Lamé parameters; rigidity (μ) and pure incompressibility (λ). The combination of each of these parameters and density are called the Lamé impedances. The following equations, from Goodway (2001), show how these impedances are related to velocities:

$$\lambda\rho = \mathrm{Ip}^2 - 2\mathrm{Is}^2 \qquad \text{Eq. 3.40}$$

$$\mu\rho = \mathrm{Is}^2 \qquad \text{Eq. 3.41}$$

where Ip: P-impedance ($\rho * V_P$), Is: S-impedance ($\rho * V_S$), λρ: LambdaRho and μρ: MuRho.

Gray and Andersen (2000) demonstrated the value of LMR cross plot analysis and their model can work as a rock physics template (Figure 3.11). The model includes threshold cutoffs for better discrimination of pore fluids and lithology. This discrimination is based on the ratio between incompressibility (λ) and rigidity (μ) and how the organization of grain in a sedimentary rock affects the distribution of effective stress. A gas sand often shows low λρ value (<20 GPa) and high μρ response (>20 GPa) due high compressibility of gas combined with the high rigidity of spherical sand grains (Gray & Andersen, 2000). Higher incompressibility than rigidity ($\lambda > \mu$) is more likely to be associated with shales, as anisotropy leads to elongated grains with very little effective porosity.

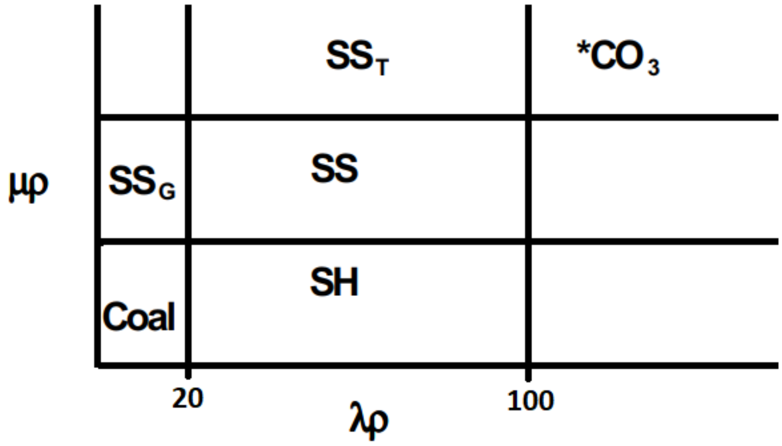

Figure 3.11: Lambda-Mu-Rho cross plot with lithology separation. Lambba-Rho values are GPa*g/cm^3. SH: Shale, SS: sandstone, SS_G: gas sand, SS_T: cemented sandstone, CO_3: carbonate (modified from Gray & Andersen, 2000).

4. Compaction Study

4.1. Results

4.1.1. Geothermal gradient

Temperature becomes an increasingly important factor to the compaction of sediments with depth. Thus, an understanding of the geothermal gradient in the study area is of high importance. The acquisition and calculation of geothermal gradients are described in subchapter 3.3.4. Although the calculations are based only on the base sea floor temperature (assumed to be 4°C) and the individual bottom hole temperatures, they provide a useful description of how the temperature evolves with increasing depth. As one of the controlling factors for chemical compaction, temperature may severely impact reservoir quality. Geothermal gradient may also be used to indicate areas where source rocks are within the temperature-dependent oil window. Figure 4.1 shows a map of the geothermal gradient in the study area, based on calculations from each well and interpolation between them. The low data-point density is sufficient to highlight trends in the area but should be treated with caution.

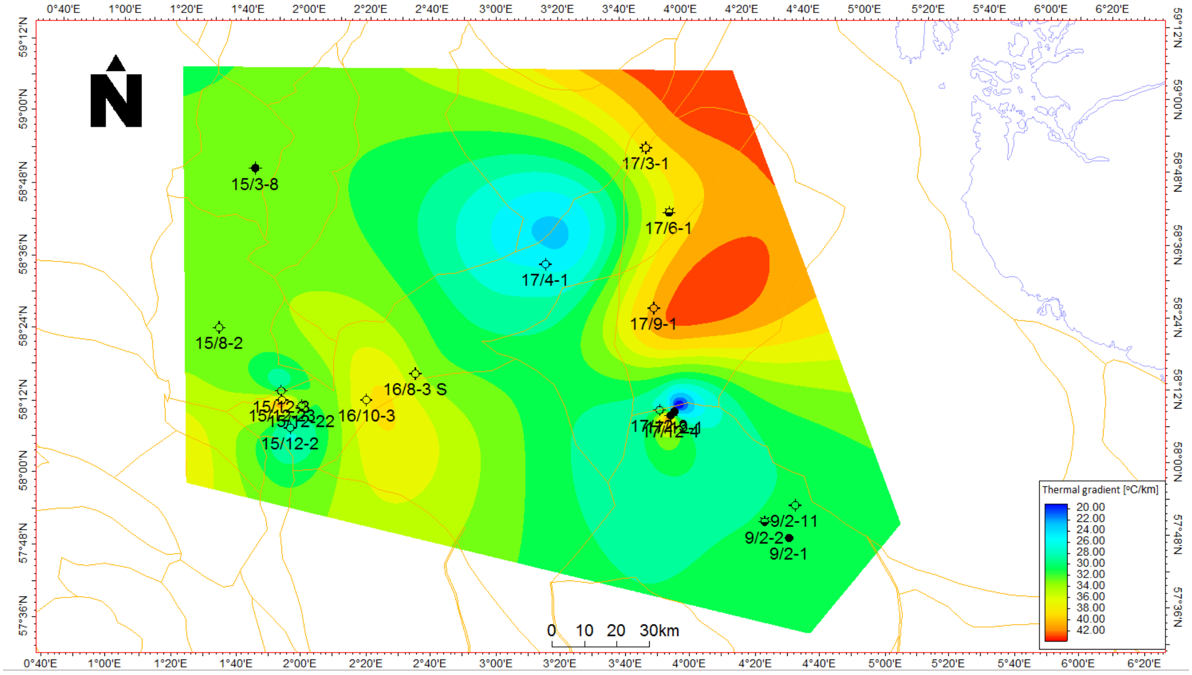

Figure 4.1: Present day geothermal gradient in the study area based on bottom hole temperatures reported by NPD (2018).

4.1.2. Compaction trends

The depth trends for V_p and density are presented in Figure 4.2. Both the V_p-depth and density-depth plots include all available wells, except 15/3-8 and 15/8-2. All depths are adjusted to represent depths below sea floor (BSF). Three distinctive features are marked in the Figure 4.2. The amount of data points and data scatter make it difficult to interpret trends. However, linear trends above and below about 2200 m BSF are possible to deduce in both plots.

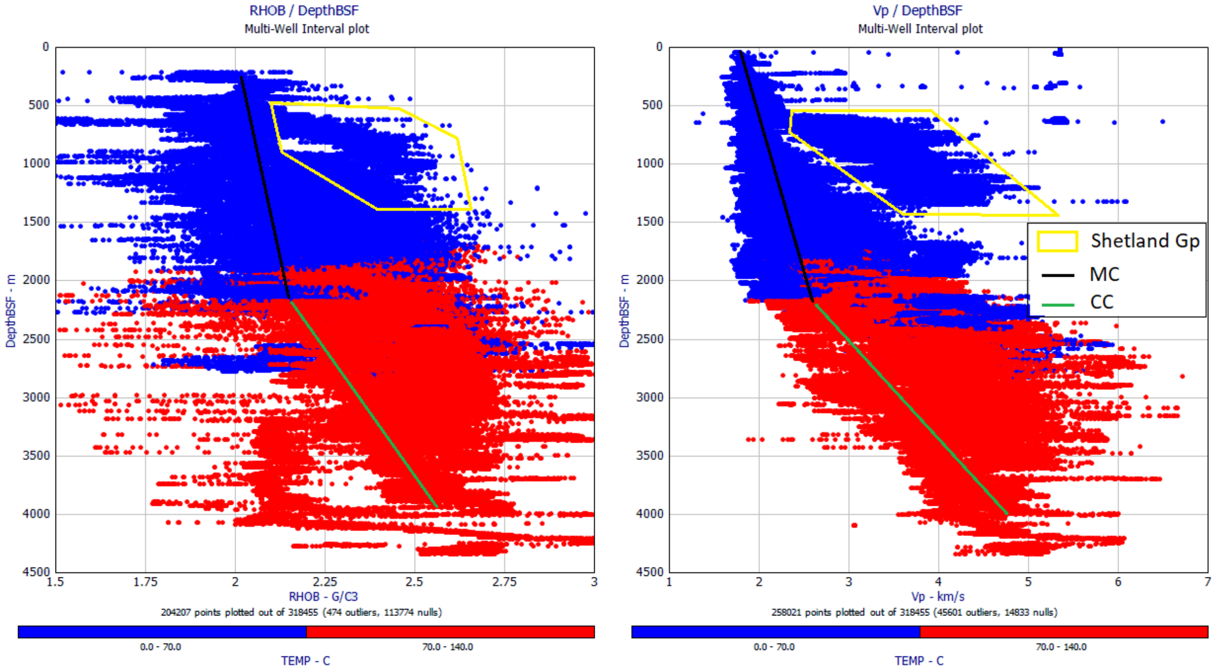

Figure 4.2: Density versus depth (left) and V_p versus depth (right) plots. All wells (except 15/3-8 and 15/8-2) included in the plots. All depths in meters below sea floor (m BSF). The color code is temperature. MC=mechanical compaction, CC=chemical compaction.

Above 1500 m BSF an area of higher velocities stands out. This anomaly is identified as data points primarily from the Shetland Group. High carbonate content within this group results in the increased velocity. Such anomalies are important to identify as they can alter interpretations of different compaction regimes. The general trend of both plots is increasing density and velocity with increasing depth. Within this higher order trend, two different trends can be observed for both density and velocity. While somewhat harder to identify in the density plot, the two trends show the same behavior in both plots. The black and green lines represent the mechanical and chemical compaction trends, respectively. Such trends in density and velocity plots illustrates the difference in subsurface compaction regimes. At about 2200 m BSF a significant increase of velocity is observed. Local velocity variations are typically related to lithology (e.g carbonates in Shetland Group), while the observed higher order change of trend indicate an increased stiffness of the rock.

A third option for identification of compaction regimes is density-velocity crossplots, as presented in Figure 4.3. The first plot includes all data points from the studied wells. The amount of data from a relatively large area and different lithologies makes it hard to identify the trends. However, a rapid increase in density is observed at low velocities while the velocity rapidly increases at higher densities. This is expected behavior of the mechanical and chemical compaction regimes, respectively.

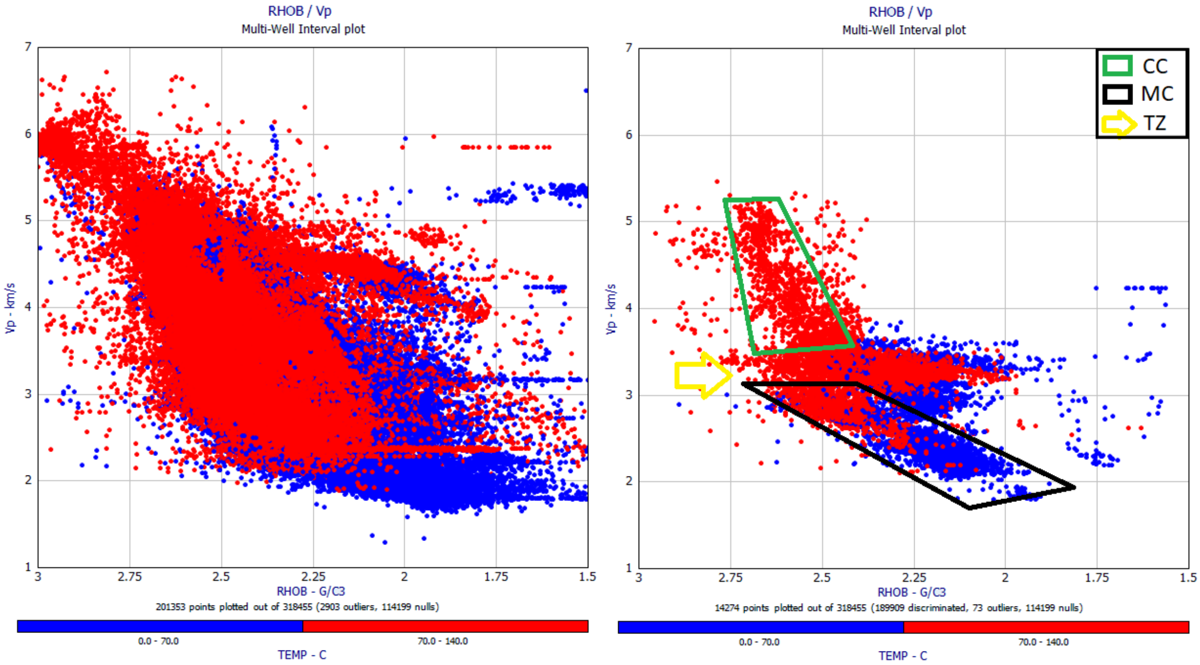

Figure 4.3: Density versus V_P crossplots including all data (left) and shale only ($V_{sh}>0.67$) (right) color coded by temperature. CC=chemical compaction, MC=mechanical compaction, TZ=transition zone.

By only plotting data points with shale volume above 67% (Figure 4.3), most lithologies, including sandstone and carbonates, are taken out of the plot. This discrimination allows for further analysis of the compaction regimes and transition zone between them. Plotting only shale data reveal the same trends as with all data included, but each compaction regime is significantly easier to separate and mark. Chemical compaction is marked with green box and mechanical compaction is marked with black box in Figure 4.3. The observed change of velocity within the chemical compaction zone seems to coincide with the change in temperature. Chemical compaction processes start between 70-100 °C. Both plots show distinct chance in velocity from 70 °C and above.

In Figure 4.4, all relevant wells are again presented in a velocity versus depth plot. They are plotted together with five different published compaction trends for comparison. Data from the studied wells has some degree of correlation with all the compaction trends down to about 2200 m BSF. Below this point even the best fitting compaction trends show decreasing correlation with the data. Again, this deviation coincides well with a temperature of about 70^{O}C and consequently the onset of chemical compaction.

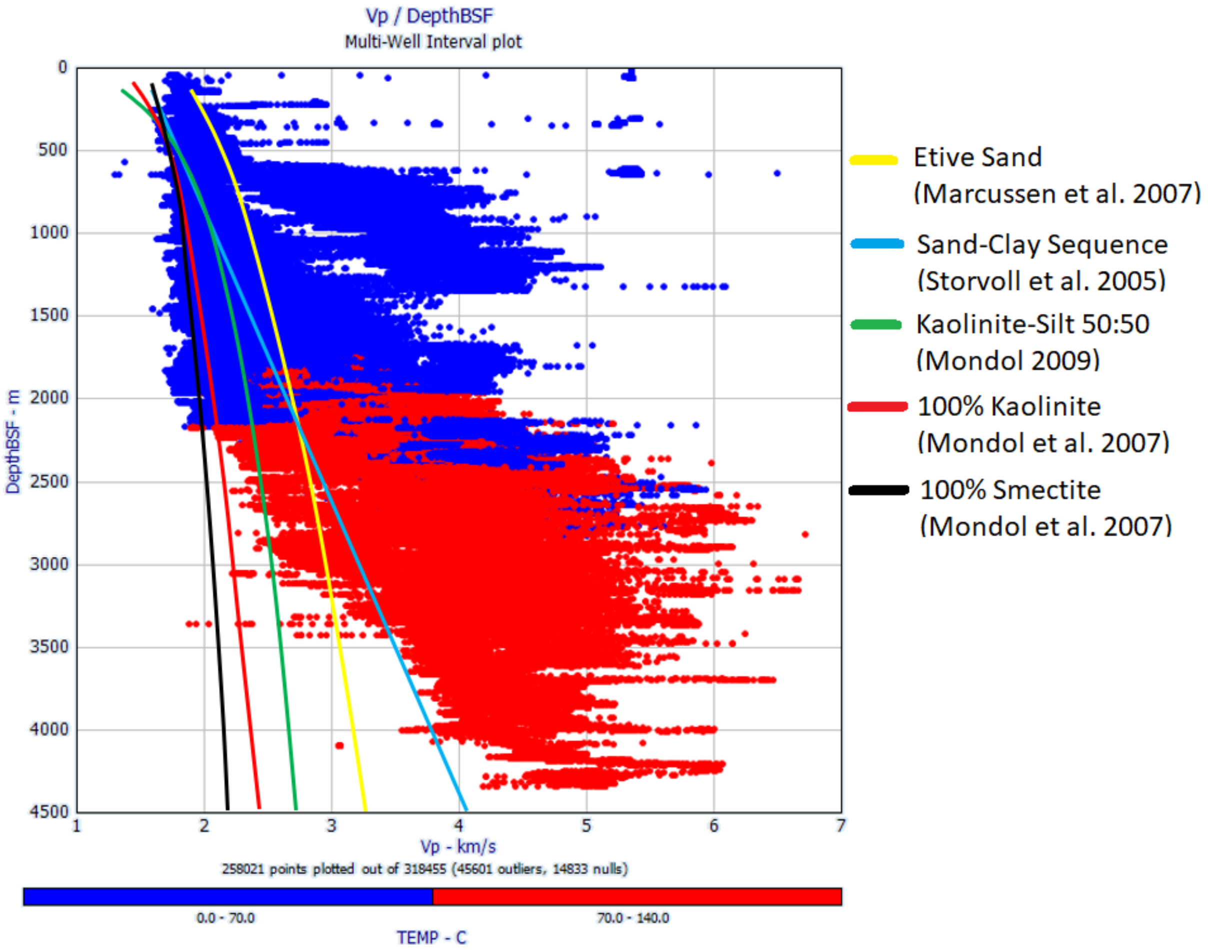

Figure 4.4: V_P versus depth plot including all wells (except 15/3-8 and 15/8-2) color coded by temperature. Published compaction trends (see legend) are plotted on top of the data for comparison.

4.1.3. Shale compaction

It is obvious that different lithologies compact differently with depth. Therefore, any compaction trend analysis is more effectively performed on separate lithologies.

Figure 4.5 contains only shale points within the $V_{sh}>0.67$ cutoff. Three published clay compaction trends are used for comparison. The depths of these shale points are not corrected for uplift and data with origin in uplifted parts of the study area show higher velocities than expected at uncorrected depths. Still, the shallow buried shales correlates well with the published clay compaction trends, especially the Kaolinite-Silt combination, down to approximately 2100 m BSF. Sub 70°C temperatures in this interval supports mechanical compaction and therefore good correlation to published compaction trends, particularly for non-uplifted shale. Below 2100 m BSF all data deviate from the compaction trends. The only exceptions are short intervals at about 2550 and 2900 m BSF, which correlates with the

Kaolinite-Silt trend. These intervals represent organic-rich shales of the Tau and Draupne Formations, and possibly shales and/or coals of Bryne Formation.

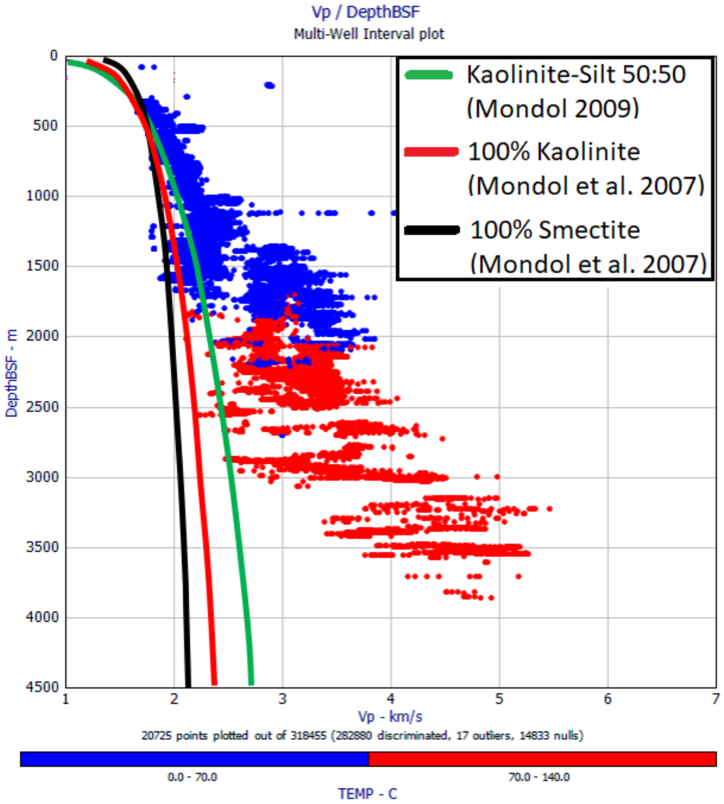

Figure 4.5: V_p versus depth plot of shale data (V_{sh}>0.67 cutoff) color coded by temperature. Published clay compaction trend added for comparison (see legend for detail).

Shale compaction is closely analyzed in well 15/12-2 and 16/10-3 in Figure 4.6 c) and f), respectively. Both wells are located in the westernmost part of the Ling Depression, which has experienced very little to none exhumation (see subchapter 4.1.6). A great variation in the amount of shale points is observed between the two wells. In well 15/12-2 the shale points between 800 and 1700 m BSF correlates well with the Kaolinite-Silt compaction trend. Consequently, these points are assumed to be within the mechanical compaction domain. The same assumption is made for the shale points in well 16/10-3 between 300 and 1800 m BSF.

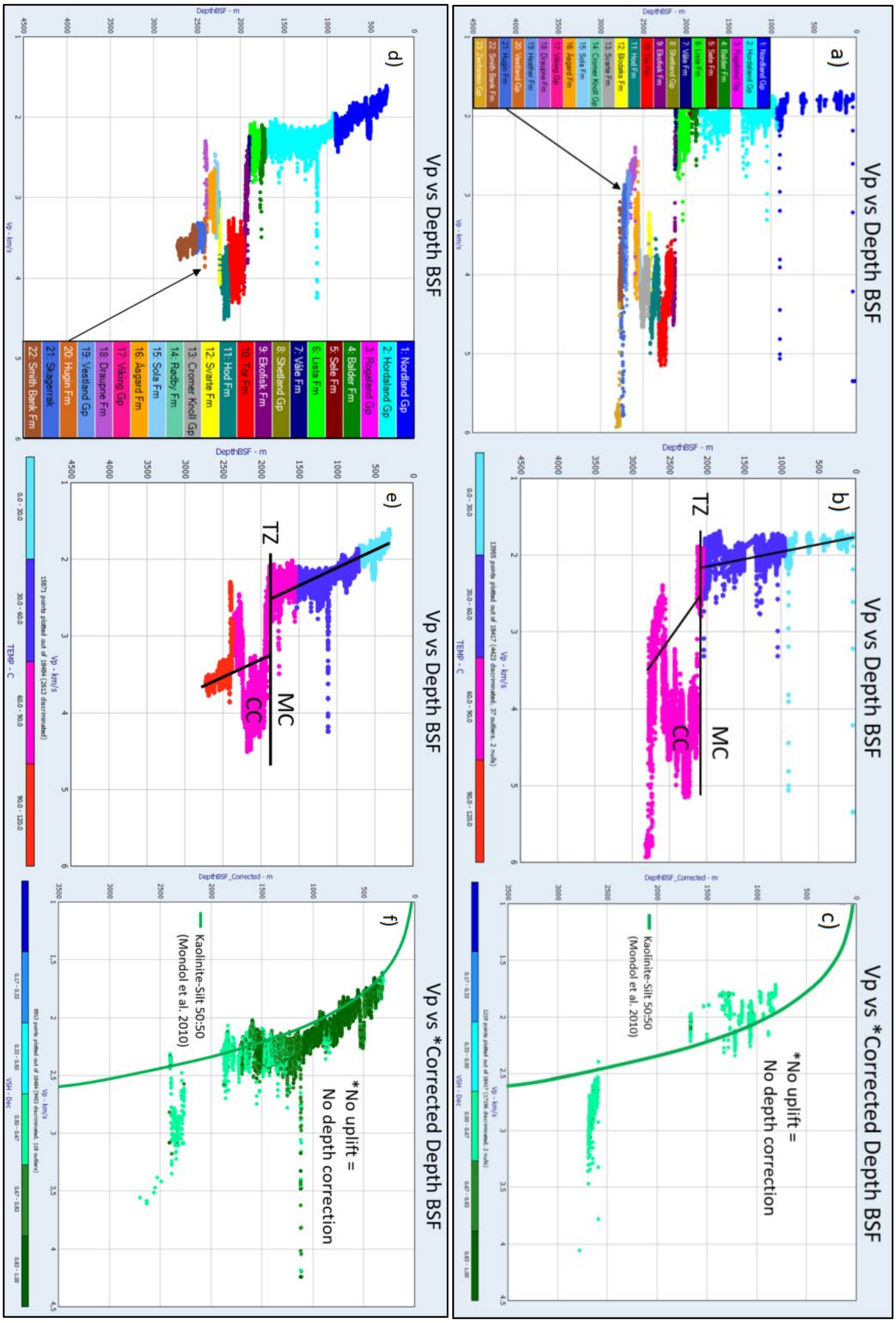

Figure 4.6: Well 15/12-2 V_P versus depth crossplots color coded with formation names (a), temperature (b) and lithology (c). Well 16/10-3 V_P versus depth crossplots color coded with formation names (d), temperature (e) and lithology (f). c) and f) includes shale points only with V_{sh}>0.5 cutoff. MC=mechanical compaction, CC=chemical compaction, TZ=transition zone.

Both plots fail to reveal exactly where the chemical compaction-related deviation from the compaction trend takes place, due to lack of shale data in this interval. In well 15/12-2, a shale interval plots away from the compaction trend at 2600-2700 m BSF. From Figure 4.6a, this interval corresponds to the shales of Draupne and Heather Formations. The temperature observed in Figure 4.6b indicates temperatures above 70^{O}C in this interval which justify a chemical compaction regime. The clear deviation from the published compaction trend at this depth implies that the onset of chemical compaction takes place at a shallower depth, between 1700 and 2600 m BSF where no shale data is present. In well 16/10-3, most of the shale interval between 2250-2400 m BSF deviates from the Kaolinite-Silt compaction trend. Only a highly organic part of the Draupne Formation plots on the compaction trend at this depth. The rest of the interval corresponds to shales from Draupne, Åsgard and Sola Formations (Figure 4.6e). Chemical compaction is assumed based on the deviation and the temperature of +/- 90 °C.

The Tau Formation shales reveal an interesting observation (Figure 4.7). The plot includes shale points of the Tau Formation only from the available wells that penetrated the Tau Formation. Close to all data points deviate from all three clay-relevant published compaction trends, even after being uplift-corrected. In addition, all data show temperatures close to or above 70 °C. Thus, available data indicates a chemical compaction regime for the Tau Formation throughout the study area.

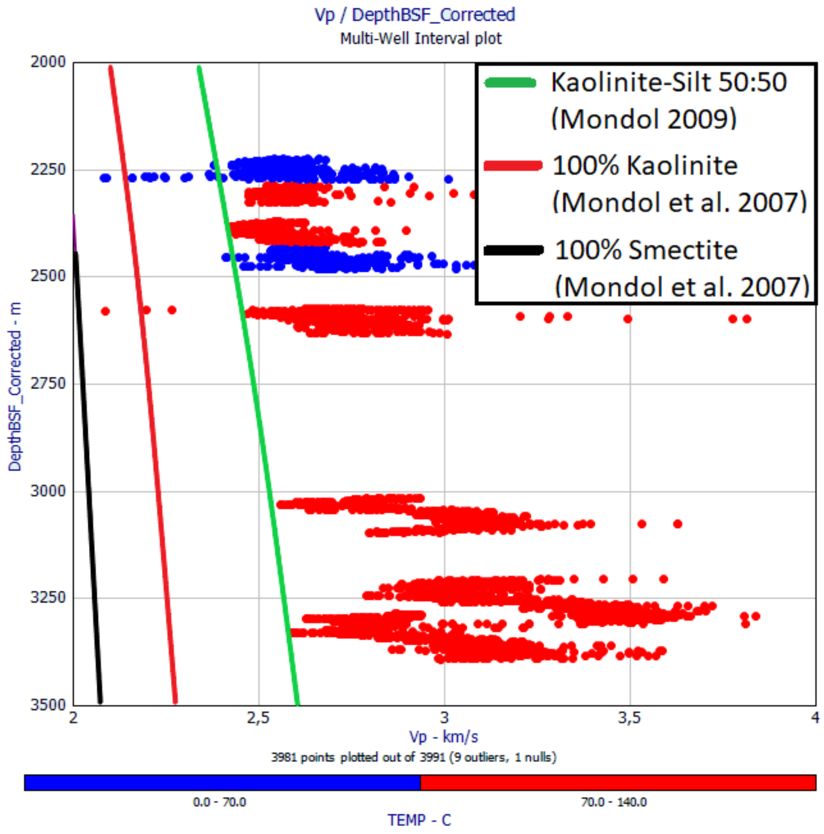

Figure 4.7: Velocity-Depth plot of only shale points from Tau Formation in the studied wells. The color bar is temperature. Published clay compaction trends (see legend) are added for comparison.

4.1.4. Sandstone compaction

Published compaction trends for different sands from Marcussen et al. (2010) and Storvoll et al. (2005) are utilized for sandstone compaction analysis. Figure 4.8 includes sandstone data (V_{sh}<0.33 cutoff) from all the wells in the compaction study. The data are rather ambiguous due to the cutoff not excluding carbonates from the Shetland Group (deviating data between 500-1500 m BSF) and because uplift is not corrected for in this plot. Generally, a good correlation with the compaction trends is identified down to about 2300 m BSF. This depth coincides well with temperatures of 70 °C and below. Thus, highlighting that the deviation from compaction trends is due to the change from mechanical to chemical compaction regime. The ambiguity of the sandstone data makes exact transition zone depth-identification hard. Still, the suggested depth from the sandstone data matches rather well with the suggested depth from the shale data (Figure 4.5). Depths of 2100 and 2300 m BSF are suggested as transition from mechanical to chemical compaction from the full dataset of shale and sandstone, respectively, indicating a local change of compaction regime within this interval in the study area.

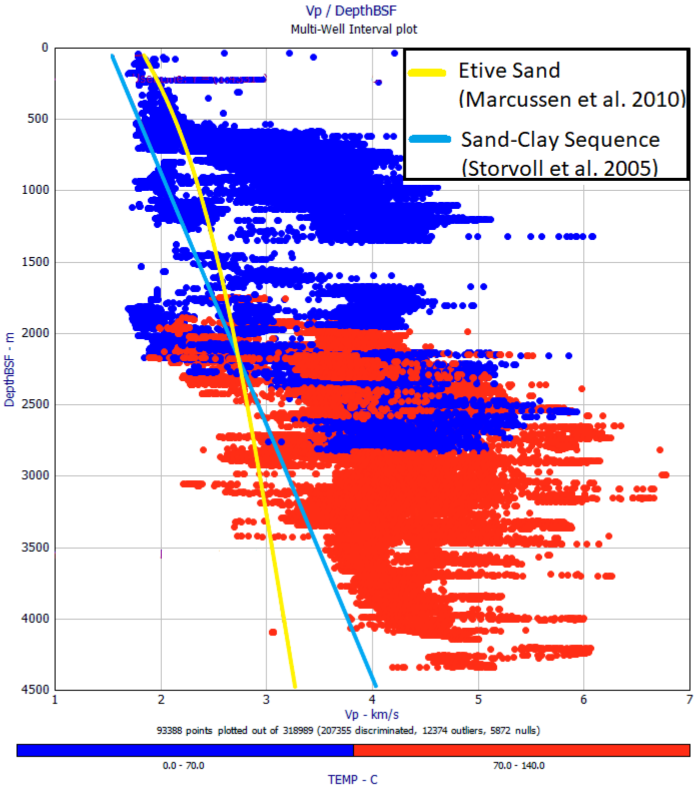

Figure 4.8: V_P versus depth plot of sandstone data (V_{sh}<0.33 cutoff) for all wells (excluding 15/3-8 and 15/8-2), color coded by temperature. Sandstone-relevant compaction trends (see legend) plotted for comparison.

Transition zone identification for individual wells is further explored and presented in subchapter 4.1.5. Sandstone compaction in well 17/3-1 and 17/12-1 is further evaluated and presented in Figure 4.9. Both plots use depths corrected for uplift (see subchapter 4.1.6) to better show compliance to and deviation from the relevant published mechanical compaction trends. In well 17/3-1 (Figure 4.9), there is a good match between the sandstone data and the published trends, arguably best with the Etive Sand trend, down to 2650 m corrected depth BSF. At this point a substantial shift in velocity is observed. From this depth the velocity increases at a higher rate with depth then at shallower levels. The more continuous set of sandstone data in well 17/12-1 (Figure 4.9) helps to identify the onset of chemical compaction even easier. After plotting with a good fit to the Etive Sand trend down to 2350 m corrected depth BSF, a sharp deviation is observed at this depth. As opposed to the change of rate observed in well 17/3-1, the rate remains similar in well 17/12-1 but is sharply shifted to about 1 km/s higher velocity. Temperature data fail to support the observed change in well 17/12-1, which could indicate that a wrong or unrepresentative bottom hole temperature is provided for geothermal gradient in this well. Temperatures above 70ºC at the observed deviation in well 17/3-1 supports chemical compaction as cause.

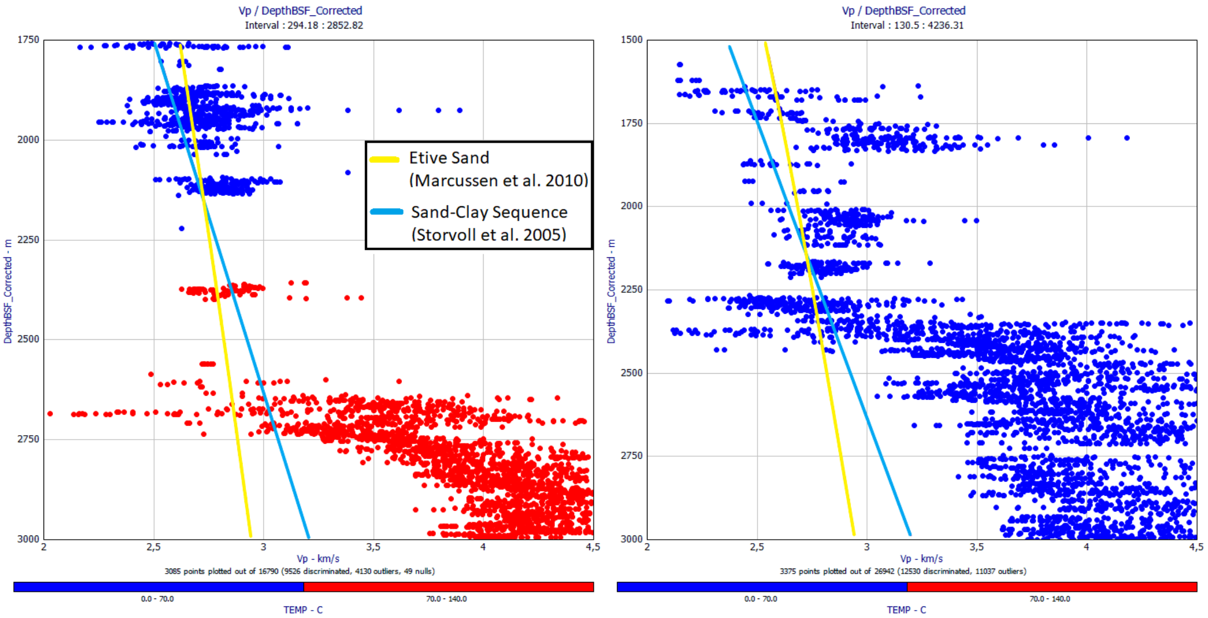

Figure 4.9: V_p versus depth plots of well 17/3-1 (left) and 17/12-1 (right) only showing sandstone points ($V_{sh}<0.33$) color coded by temperature. Published sand compaction trends (see legend) plotted for comparison.

4.1.5. Transition zone identification

The results from the individual transition zone identification from each well is presented in Table 4.1. The transition zone is estimated from significant shifts in velocity that relates to deviation from published compaction trends for mechanical compaction regime. Lithostratigraphic intervals dominated by high-velocity carbonates and evaporites, like Shetland and Zechstein Groups, are excluded to avoid misinterpretation. Low-velocity intervals as the organic-rich Tau and Draupne Formations are removed for the same reason. Interpretation is performed on depth data not corrected for any uplift because present-day depths of the transition zone are more relevant from an exploration point of view. Two examples are provided in Figure 4.12. In well 15/12-2 the transition zone is suggested at 2160 m BSF. This corresponds to a temperature of 68 °C, basically on the lower limit of the temperature window for onset of chemical compaction and quartz cementation. The transition zone is followed by an abruptly increasing velocity gradient. Continuously low V_{sh} during this shift gives confidence that it is not due to changing lithology. Similar trends are observed in well 17/4-1. Increased velocity gradient within an interval of similar V_{sh} suggests a transition zone at 1700 m BSF. Uplift-corrected temperature at this depth equals 49 °C. This is lower than expected and, if the geothermal gradient is correct, not enough to initiate any chemical compaction. Additional shifts in velocity is observed deeper, e.g. at ~2150 m BSF. V_{sh} data at this level indicate a shift to a sandier interval with higher velocities. As this level would equal an uplift-corrected temperature of 60 °C, the change of lithology may camouflage any potential onset of chemical compaction at this level.

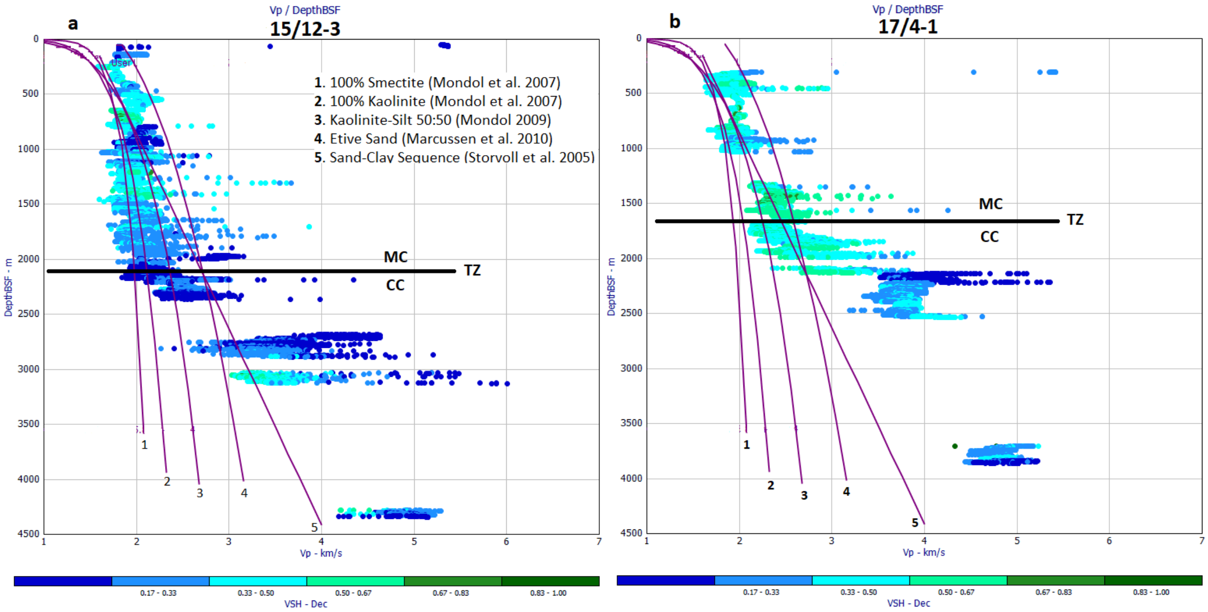

Figure 4.12: V_p versus depth plot of a) well 15/12-3 and b) well 17/4-1 color coded by shale volume. MC=mechanical compaction, CC=chemical compaction, TZ=transition zone.

The second approach to transition zone estimation utilizes the S-wave velocity data available in six of the studied wells. All data from these wells are used in the V_s-density crossplot (Figure 4.13). The shale volume color coding reveal different trends in the compaction of shaly and sandy lithologies. Shades of green (indicating shale) are more continuous while the sandy data in blue are more widespread. A majority of the shaly data plots towards lower V_s and density, indicating shallow burial. This is expected due to the general dominance of clay in the shallow sedimentary succession within the study area. Only the shale-dominated fraction ($V_{sh}>0.5$ cutoff) is used for further examination.

Figure 4.14 shows the shear modulus, derived from V_s, versus density and color coded by temperature. By analyzing how the shear modulus changes with increasing density (indication of decreasing porosity), different behaviors in the upper and lower part of the plot are observed. Increased shear modulus indicate increased stiffness, and an increased shear modulus gradient is most likely caused by cementation. In the 2.2-2.5 g/cm^3 density interval shear modulus is increased by ~5 GPa. From 2.5-2.7 g/cm^3 the increase in shear modulus is

~10 GPa. This shift is observed to happen at approximately 5-6 GPa. A shear modulus of 5-6 GPa consequently represents initial cementation and a transition zone in the area. This corresponds to temperatures between 60-90 ºC (color coding), which should be sufficient for quartz cementation in shales.

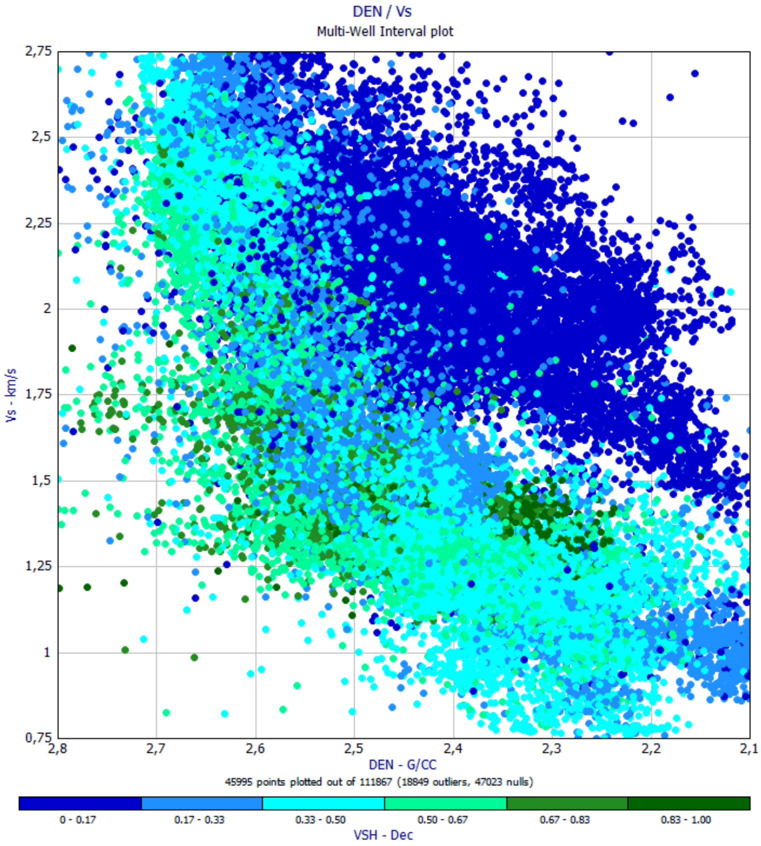

Figure 4.13: Density versus V_s plot including all wells with V_s data available. Color coded by shale volume.

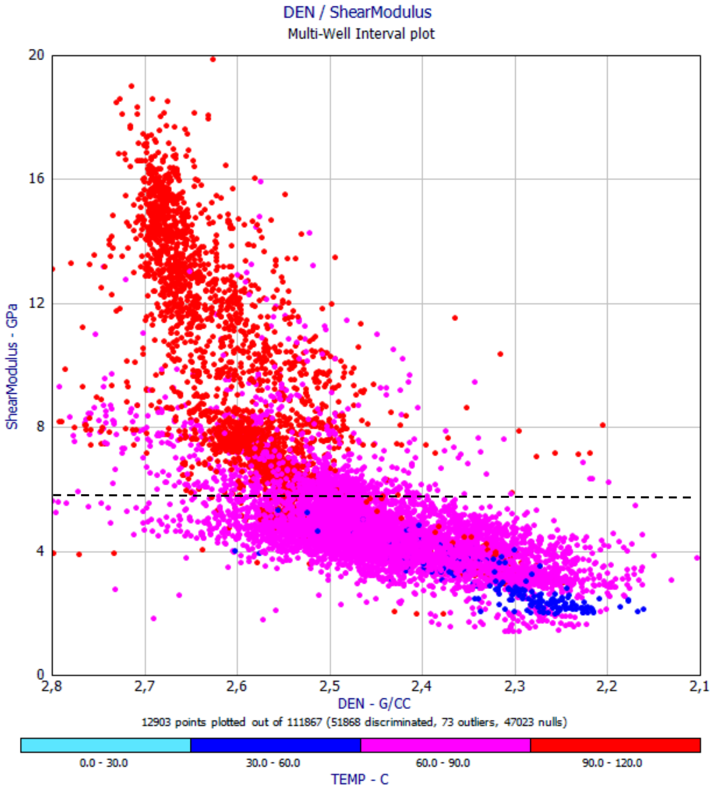

Figure 4.14: Density versus shear modulus plot of all wells with V_s data available. Color coded by temperature. Shaly lithologies only (V_{sh}>0.5 cutoff). Stippled line indicates estimated transition zone.

The same trend is observed in Figure 4.15, a V_s-density crossplot color coded by shear modulus. Using the shear modulus value for transition zone acquired from the previous plot, a Vs value for the transition zone is found. A change of velocity gradient is observed at Vs=1.45 km/s (stippled line), which corresponds μ=5-6 GPa. Below this line the velocity is increased with approximately 0.45 km/s (1-1.45 km/s) within a denity interval of 2.2-2.6 g/cm^3. V_s is increased with 1.1 km/s (1.45-2.55 km/s) between density values of 2.5 and 2.7 g/cm^3.

Furthermore, the same data (V_{sh}>0.5) are color coded with cement volume, using the relationship between velocity and cement volume suggested by Marcussen et al. (2010), in Figure 4.16. The relation from Marcussen et al. (2010) is based on sandstones but also predicts initial cementation in the transition zone estimated for the shaly lithologies in this study. Initial cementation in the tranisition zone is causing increased rock stiffness (observed by increased V_s and μ) while only causing minor effects to porosity (observed by small changes of density). Figure 4.16a include a linear regression best fit line for all the data. This line provide a decent fit to the overall trend. In Figure 4.16b, a significantely better fit for each compaction regime is achieved by applying linear regression to data above and below the transition zone (V_s=1.45 km/s), separately. An additional observation is made from the dashed lines in Figure 4.16a, indicating less scatter of data as the velocity and cement volume increase within the chemical compaction domain. Compared to the similar plot in Figure 4.3, which utilizes V_p data versus density, Figure 4.16b is significantly less ambigous at the knee-point, making transition zone estimation easier.

A transition zone range purely based on temperature is estimated for each well and presented in Table 4.1. Onset of chemical compaction (i.e tranistion zone) generally occur between 70-100 ºC (around 70-80 ºC for sandstones and around 70-100 ºC for mudrocks) (Mondol, et al., 2007; Thyberg, et al., 2009). By multiplying the local geothermal gradient of each well with the temperature end members, a range of depth where transition zone is expected to occcur is established. The size of this range is directly dependant on the geothermal gradient. Constant geothermal gradient is assumed both pre- and post-uplift, and uplift-corrected estimates should therefore be compared to the suggested range. The average estimated present day transition zone is 1706 m BSF. Corrected for uplift, the average transition zone shifts to 1942 m BSF. Most of the wells affected by uplift have a below-average transition zone estimate, while the remaining wells generally are estimated above average. Only eight estimates are within the suggested range based on temperature, mainly from non-uplifted wells. Shallower transition zone in wells with high geothermal gradients is a general trend.

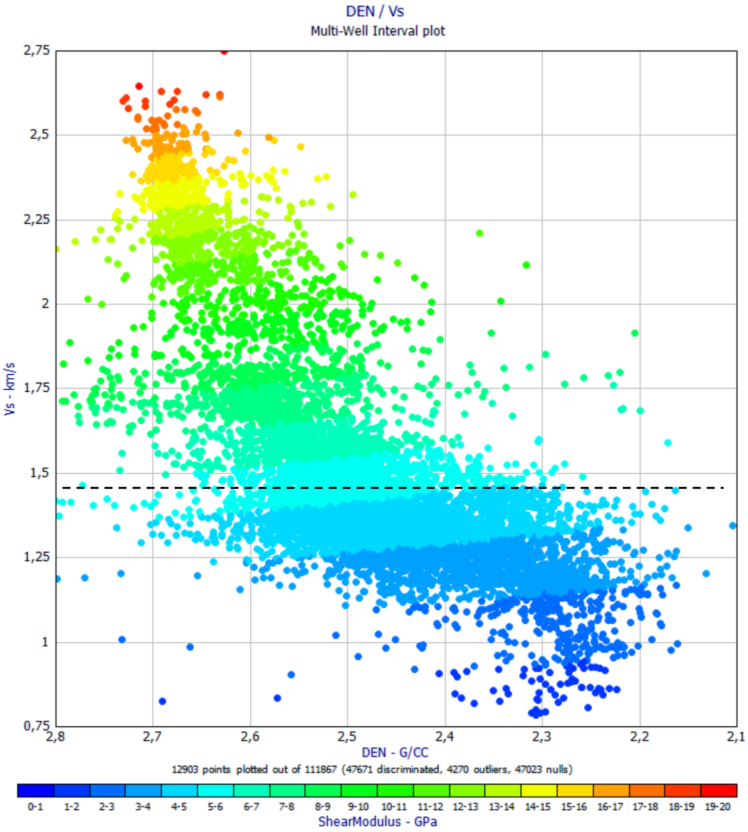

Figure 4.15: Density versus V_s crossplot, color coded with shear modulus. Stippled line indicate estimated transition zone.

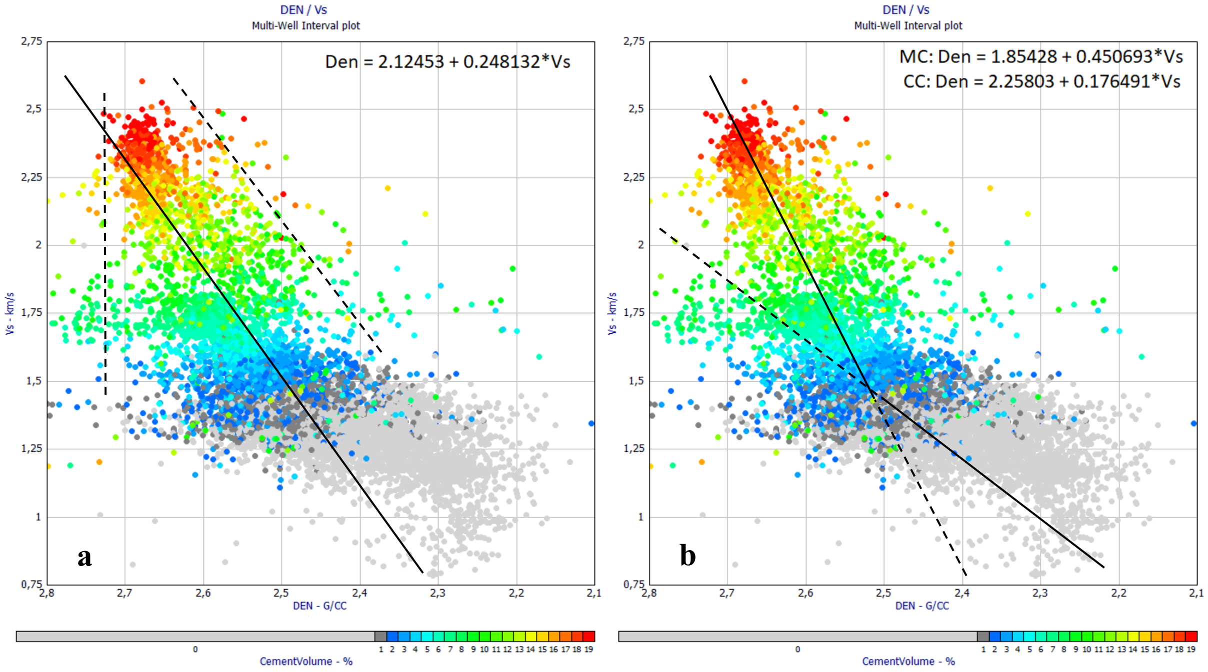

Figure 4.16: Density versusV_s crossplots color coded with cement volume. a) Linear regression line based on all data (solid), and approximate min/max density in the chemical compaction domain (stippled line). b) Separate regression lines (solid part of lines) and equations based on data above and below V_s=1.45 km/s.

Table 4.1: Results from uplift and transition zone estimation using P-wave velocities and temperature.

Well	Uplift [m]	Geothermal gradient [°C/km]	Transition zone current [m]	Transition zone adjusted [m]	Estimated range of transition zone [m]
9/2-1	340	31.9	1380	1720	2068-3094
9/2-2	450	30.3	1320	1770	2178-3168
9/2-11	650	30.5*	1410	2060	2163-3147
15/12-2	0	28.8	2090	2090	2291-3333
15/12-3	0	31.4	2160	2160	2101-3057
15/12-22	0	32.7*	2080	2080	2018-2936
15/12-23	0	38.0	2260	2260	1736-2526
16/8-3 S	0	34.6	1950	1950	1907-2774
16/10-3	0	37.7	1900	1900	1750-2546
17/3-1	560	38.4	1280	1840	1718-2500
17/4-1	230	25.4	1700	1930	2598-3779
17/6-1	380	37.5*	1410	1790	1760-2560
17/9-1	290	40.4	1410	1700	1622-2376
17/12-1	200	24.3	2020	2220	2716-3950
17/12-3	330	29.3	1500	1830	2252-3276
17/12-4	350	35.8	1420	1770	1843-2681

*Geothermal gradient estimated using interpolation

4.1.6. Uplift estimation

The results from the uplift estimation are presented in Table 4.1. All V_P-data in each well are initially screened against the five utilized published compaction trends. Generally, the shallow buried, shaly lithologies in the study area correlate well with the Kaolinite-Silt trend (Mondol, 2009). By using a $V_{sh}>0.5$ cutoff and adjusting the depth of the velocity data to give the best fit to the Kaolinite-Silt line, an uplift estimate is achieved. In Figure 4.17, only shale data are plotted, and an additional 230 m are added to the depth BSF to simulate maximum burial depth and optimal fit to the Kaolinite-Silt trend line. The additional depth required to give the best fit is equal to the uplift. Similar procedures are performed for all wells, and presented in Appendix A. A gradient map is made using uplift estimations in each well location and interpolation between them (Figure 4.18). Low well density equals uncertain interpolation, but the map provides useful trends. The most obvious trend is an increase of uplift towards the mainland.

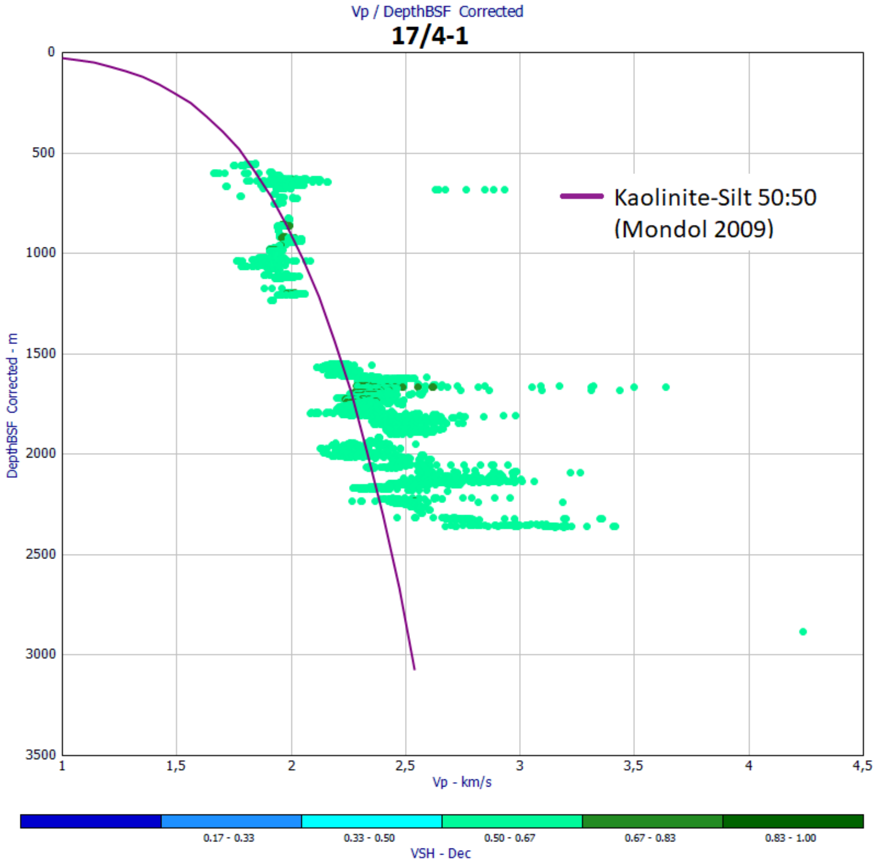

Figure 4.17: V_P versus depth plot of well 17/3-1 showing uplift estimation. Depth is adjusted to provide best fit with trend (see legend) and hence simulate maximum burial.

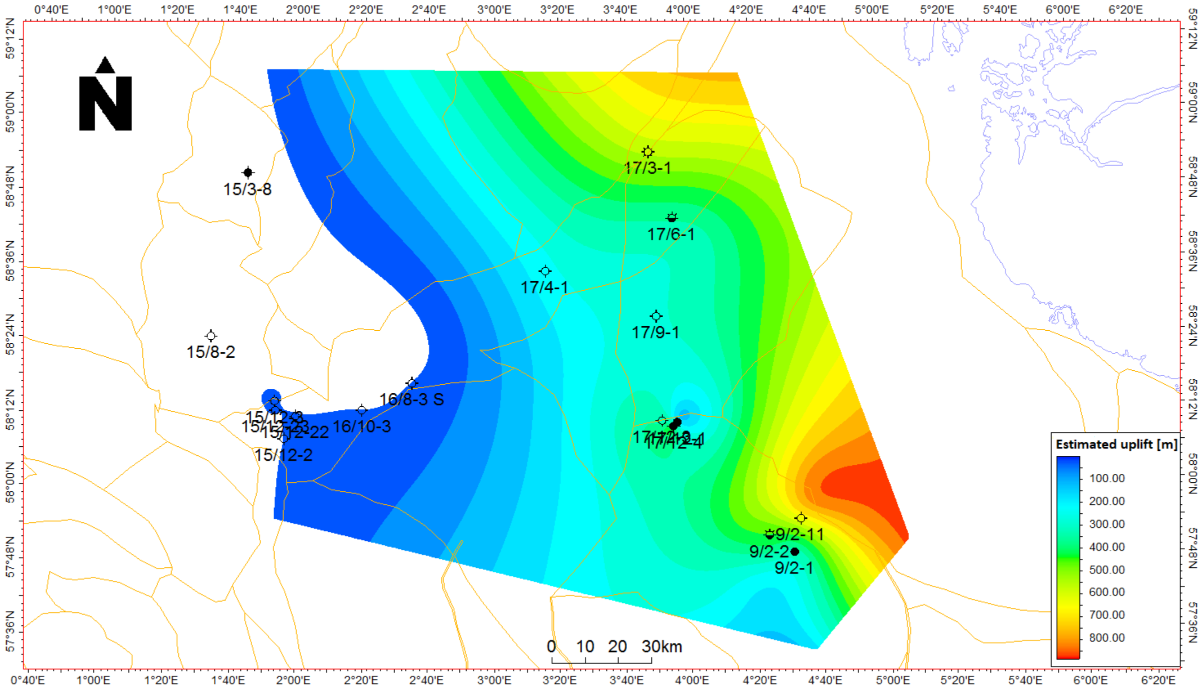

Figure 4.18: Uplift estimation gradient map of the study area. Western border of dark blue indicates zero uplift.

4.1.7. Reservoir rock analysis

4.1.7.1. Burial and cementation relative to transition zone

In an exploration point of view, it is of great interest to know how reservoirs are situated and affected by transition zones and uplift. This study provides two depth estimates where quartz cementation could affect reservoirs. The first is the estimated current transition zone presented in Tables 4.1 and 4.2. Interpretation of well data suggests that quartz cementation is likely below depths of each individually estimated transition zone. A more theoretical approach is to use the start of the temperature-based range of transition zone (also presented in Table 4.1) and subtract the estimated uplift. This theoretical transition zone after uplift correction is shown in Table 4.2. By comparing top reservoir depths with these estimates, it is possible to deduce the relative time formations have been situated below the transition zone and consequently how extensive the cementation is. Results are presented in Table 4.2.

Table 4.2: Top reservoir depths compared with two different transition zone estimates.

Well	Top main reservoir depth (m BSF)	Theoretical transition zone after uplift (m BSF)	Reservoir depth below theoretical transition zone	Estimated current transition zone (m BSF)	Reservoir depth below estimated transition zone
9/2-1	3034	1728	1306	1380	1654
9/2-2	3002	1728	1274	1320	1682
9/2-11	2502	1513	989	1410	1092
15/12-2	2707	2291	416	2090	617
15/12-22	2723	2018	705	2080	643
16/10-3	2406	1750	656	1900	506
17/3-1	2090	1158	932	1280	810
17/4-1	2133	2368	-235	1700	433
17/6-1	2340	1380	960	1410	930
17/9-1	2052	1332	720	1410	642
17/12-1	2148	2516	-368	2020	128
17/12-3	2234	1922	312	1500	734
17/12-4	2149	1493	656	1420	729

The reservoirs of well 9/2-1 and 9/2-2 are buried significantly deeper relative to the transition zone than other wells analyzed in this study. Deep reservoir burial compared to the transition zone is also observed in well 9/2-11, 17/3-1 and 17/6-1. Reservoirs in these wells have likely been buried for a longer time below the transition zone than other wells, experienced higher temperatures and are expected to have higher cement volume. On the contrary, reservoirs in well 17/4-1 and 17/12-1 have been buried shallow compared to estimated transition zone and lower actually above the theoretical transition zone. Thus, lower temperature exposure and amount of cement volume is expected. It is interesting to note that these two wells have the lowest geothermal gradients in this study. After uplift, top reservoir is still located below the estimated transition zone for all wells, except 17/12-1. Reservoirs in well 17/4-1, 17/12-1 and 17/12-3 are located above theoretical transition zone when corrected for uplift.

By using the relation between cement volume and P-wave velocity for sandstones by Marcussen et al. (2010), cement volume is estimated for all reservoir formations analyzed in this study. The results are presented in Table 4.3.

Table 4.3: Average cement volume of reservoir formations calculated using the relation from Marcussen et al. (2010). Red indicating formation not present in well.

Average Calculated Cement volume (%)			
Well	Sandnes Fm	Bryne Fm	Hugin Fm
9/2-1	21.8	20.3	🟥
9/2-2	17.5	15.5	🟥
9/2-11	13.5	13.1	🟥
15/12-2	🟥	🟥	10.7
15/12-22	🟥	🟥	9.7
16/10-3	🟥	🟥	8.4
17/3-1	8.3	8.7	🟥
17/4-1	🟥	🟥	14.8
17/6-1	13.0	13.5	🟥
17/9-1	3.9	10.6	🟥
17/12-1	11.8	8.2	🟥
17/12-3	9.9	8.4	🟥
17/12-4	7.6	9.7	🟥

The calculated cement volumes correlate well with the expectations from burial depths compared to transition zone estimates. Generally, relatively high cement volume values are predicted for Jurassic reservoirs in the study area. More than eight percent cement volume are predicted in all reservoir formations, except the Sandnes Formation in well 17/9-1. As expected, highest cement volume is predicted in reservoirs of block 9/2, especially in the deeply buried reservoirs of well 9/2-1 and 9/2-2. Particularly high values are also predicted for reservoirs in wells 17/4-1 and 17/6-1.

4.1.7.2. V_p versus depth trends

Figure 4.19 shows the P-wave velocity data from the Hugin and Sandnes Formations from the 13 wells which penetrate the formations. These formations are typical drilling targets when present and have proven reservoir potential on the NCS, and in the study area (see chapter 5). Figure 4.19a shows present day depths BSF while Figure 4.19b is plotted against depths BSF corrected for uplift (which is presented in subchapter 4.1.6). Generally, the present-day depth plot shows a clear deviation from both compaction trends but is unable to provide one suitable trend for all data. When looking at the uplift-corrected plot the data appear less random and display a clearer trend. These reservoir data display, arguably, a similar trend as both the utilized compaction trends. However, this trend appears at a significantly higher velocity.

This trend similarity is clear between 2300-2900 m BSF in the uplift-corrected plot where the published trends plot mainly below 3 km/s and the reservoir data at about 3.5 km/s. Similar trend, but higher velocity indicate early chemical compaction regime, also supported by temperatures +/- 70ºC. Below 3000 m BSF, an increased rate of velocity per depth is observed with a velocity trend reaching more than 4.5 km/s. The reservoir data at this depth belongs to the Sandnes Formation in the block 9/2 wells in Egersund Basin. Greater burial depths in this basin results in higher temperatures and evidently more quartz cementation within the sandstone.

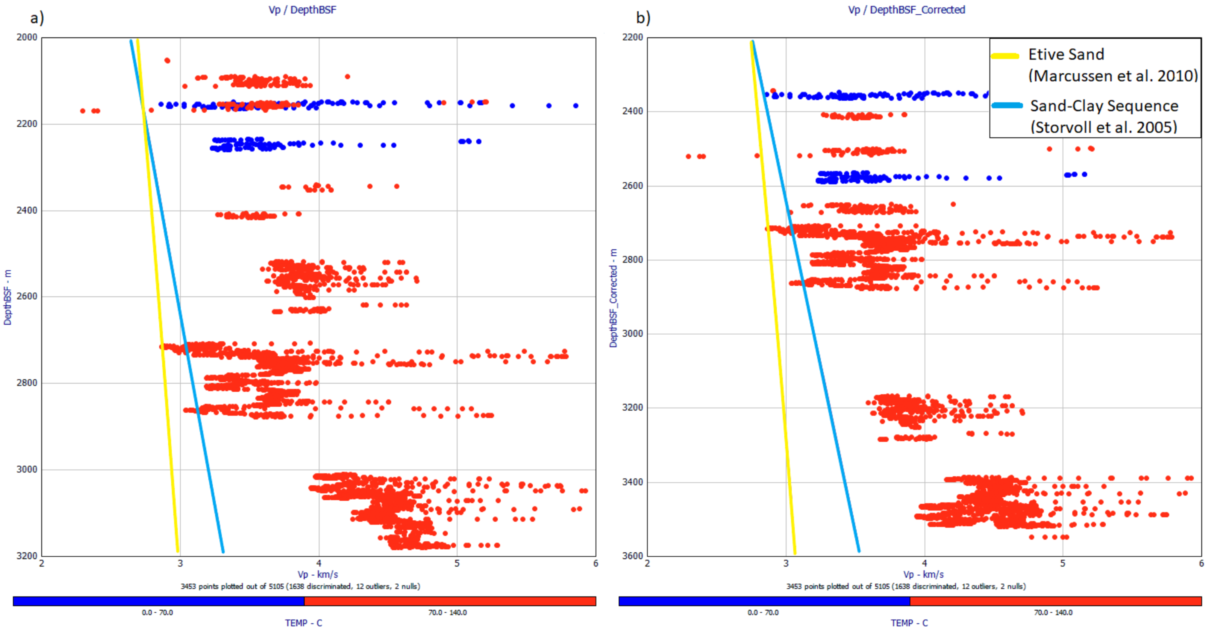

Figure 4.19: V_P versus depth plots of the Hugin and Sandnes Formations color coded by temperature. a) Present day depth BSF, b) depth BSF corrected for uplift. Published sand compaction trends (see legend) plotted for comparison.

Throughout the two plots several short intervals with great velocity spikes is observed, possibly indicating highly cemented local intervals. This is particularly expected where the temperature exceeds 70 ºC. From these plots it is evident that the main reservoir intervals in the study area span a depth interval of about 1100 meter. Compaction is shown to vary greatly within this depth interval and constraints of both transition zone and uplift are consequently of great importance. Visual interpretation of velocity-depth trend correlate well with the cement volume estimates. Distinct features of Hugin, Sandnes and Bryne Formations can be observed in Figure 4.20.

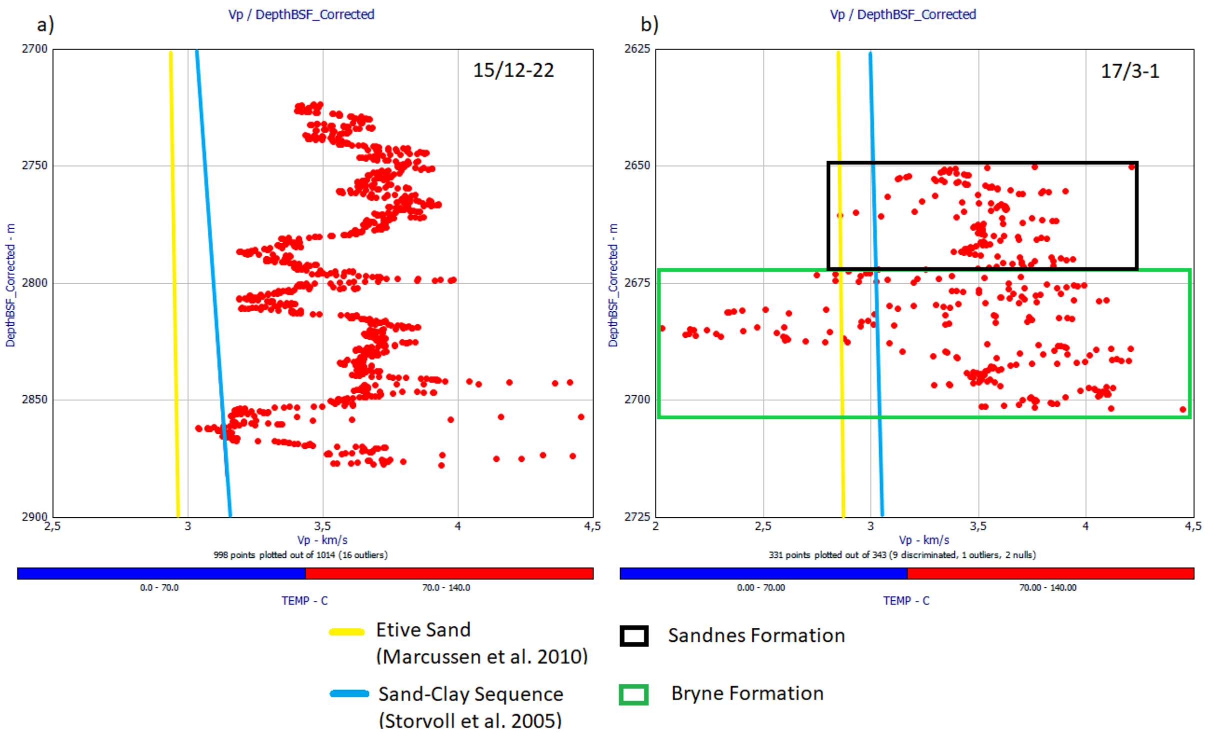

Figure 4.20: V_p versus depth plots (corrected for uplift) of the a) Hugin Formation in well 15/12-22 and b) the Sandnes and Bryne Formations in well 17/3-1.

4.1.7.3. Cement models

As shown in the transition zone estimation subchapter (4.1.5), velocity versus density/porosity crossplots effectively highlights trends related to diagenesis and sorting. In this subchapter, reservoir formations are analyzed in V_s versus total porosity crossplots overlain by digitized sandstone trends from Avseth et al. (2010). These trends are known as cement models and are introduced in chapter 3.4. The cement models include a friable sand model (uncemented sand trend) related to sorting, the Dvorkin-Nur contact cement model (Dvorkin & Nur, 1996) related to cementation and several constant cement lines. The constant cement lines indicate a constant value of cement and variations related to sorting along the line. Sandstone trends related to cementation and sorting are expected to have somewhat similar behavior to shale data seen in subchapter 4.1.5. Similar to a shale, a cemented sandstone is expected to be stiffer than a non-cemented sandstone, assuming equal porosity and mineralogy. Sorting related trends (e.g. variations in shale/clay volume) will generally result in small effects on the velocity as the porosity is reduced. Continuously poorer sorting is expected from the contact cement model line and towards zero porosity as the amount of pore-filling material increases. Trends related to cementation have a steeper increase of velocity as the porosity is reduced. The increase of velocity is most noticeable at the onset of cementation at early stage chemical compaction regime.

Sandnes/Hugin Formations:

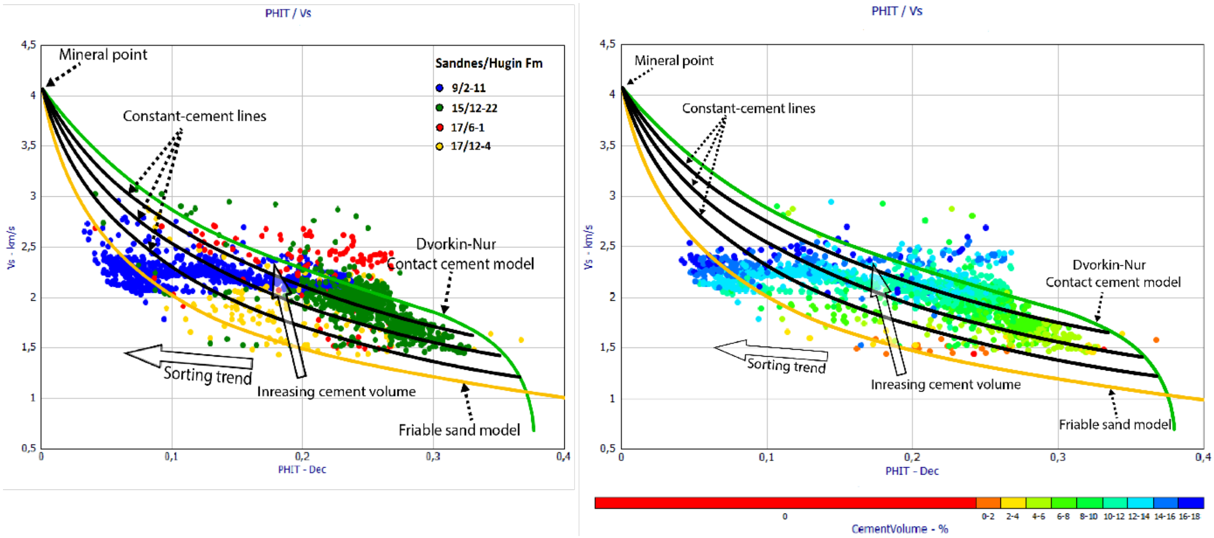

Figure 4.21: Sandnes Formation (9/2-11, 17/6-1, 17/12-4) and Hugin Formation (15/12-22) in V_s versus total porosity crossplot (left). The same data color-coded with calculated cement volume (right).

Figure 4.21 shows the Sandnes and time-equivalent Hugin Formation in the four wells with available V_s data, in a V_s versus porosity crossplot. Cement volume in the Hugin Formation range from ~8-12% at the contact cement line for well 15/12-22. This well has a noticeable limited sorting trend, which suggests low shale volume and relatively clean sand. More distinct sorting trends are observed in the other wells. The Sandnes Formation in well 9/2-11 and 17/6-1 are significantly more cemented than the two other wells, with cement volumes ranging roughly between 10-18%. The Sandnes Formation in well 17/12-4 has a slightly less distinct sorting trend than the Sandnes Formation in the two other wells. In addition, large variations in cementation is observed, ranging from data points below 1% constant cement line to about 10% estimated cement volume.

<u>Bryne Formation</u>:

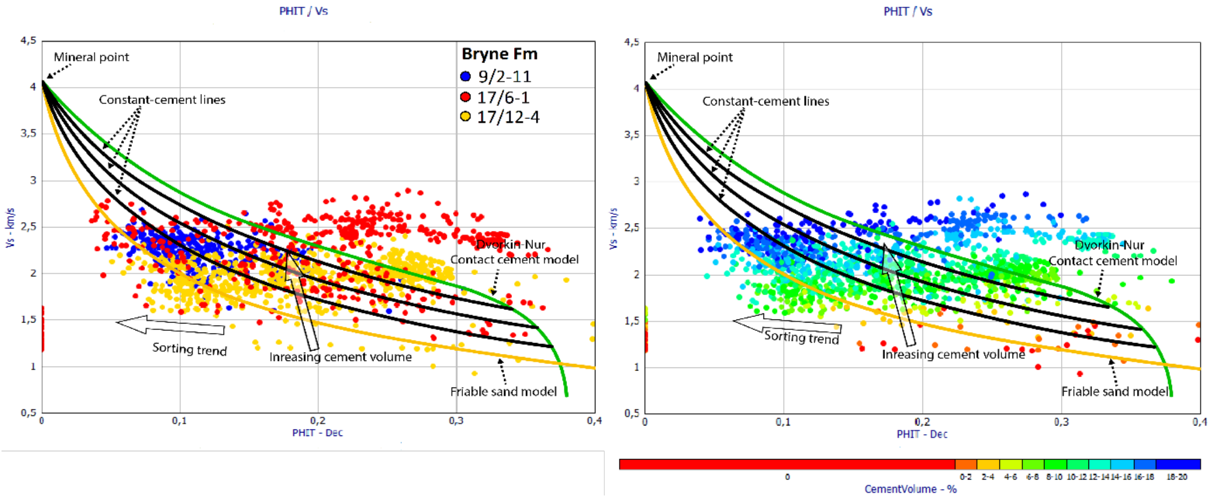

Figure 4.22: V_s versus total porosity crossplot Bryne Formation (from well 9/2-11, 17/6-1 and 17/12-4) (left). The same data color-coded with calculated cement volume (right).

Figure 4.22 shows the Bryne Formations from the three wells with available V_s data. Compared to Sandnes/Hugin Formations, data points are dragged towards higher cement values, mainly due to deeper burial. The heterogeneity of the Bryne Formation is reflected in pronounced sorting trends in all three wells, especially 17/6-1 and 17/12-4. These two wells have significant amount of data plotting above/right of the contact cement model at high porosities, indicating that despite large variations in sorting and shale volume intervals with very good reservoir quality are expected.

4.1.7.4. LMR crossplot

The relatively deep buried Sandnes Formation in well 9/2-11 and the shallower buried Hugin Formation in well 15/12-22 are plotted in the LMR (Lambda-Rho versus Mu-Rho) rock physics template with an additional cutoff line suggested by Goodway et al. (1997). This crossplot is an effective lithology and fluid indicator. Rigidity is not affected by fluid type or saturation and should therefore separate different lithologies. Incompressibility is largely affected by gas saturation, as gas is easily compressible compared to rock and fluids. However, significant gas saturations are not encountered in this study and the LMR crossplot is instead utilized to compare effects of compaction.

The result is shown in Figure 4.23. The Sandnes Formation in well 9/2-11, buried between 3152-3284 m BSF corrected for uplift, is color coded in green. The Hugin Formation in well 15/12-22, buried between 2723-2879 m BSF (no uplift), is color coded in blue. The deeper buried Sandnes Formation is situated at both higher values of rigidity and incompressibility, especially rigidity, compared to the Hugin Formation. This trend correlates well with the calculated cement volume for both formations, seen in Figure 4.22. Cement volume in Sandnes Formation range from ~10-20% while cement volume in Hugin Formation range from ~0-12%. Based on individual geothermal gradients top Sandnes Formation has been exposed to temperatures of ~96 ºC at maximum burial in well 9/2-11. Hugin Formation in well 15/12-22 are expected to have been exposed to temperatures of 89 ºC at maximum burial. Results in Table 4.2 indicate that Sandnes Formation has been significantly deeper buried relative to the transition zone compared to Hugin Formation. All of this is reflected in the calculated cement volume. High rigidity values for cemented sandstones fits the rock physics model (Goodway, 2001). The general idea is that precipitation of cement on and in between grains in a sandstone leads to increased stiffness. In the LMR model this is reflected by increased rigidity and incompressibility with increasing depth and cementation. Increasing depth and cementation is strongly linked to decreasing porosity and density. Relatively low cement volume and high porosities in Hugin Formation result in lower rigidity and incompressibility. Very few data points plot to the left of the porous gas sand cutoff line. The low density and high compressibility of gas leads to significantly lower incompressibility than any fully water-saturated rock. Significant accumulations of hydrocarbon are encountered in neither of these wells. It is however noted that the low cement volume/high porosity data plots closest to the cutoff line, as expected.

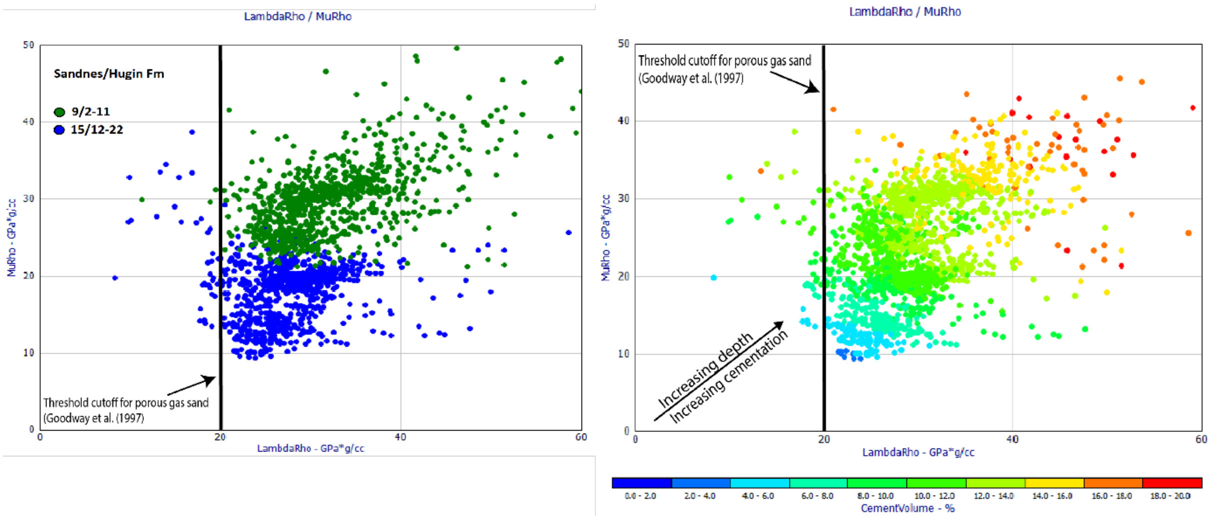

Figure 4.23: Sandnes Formation from well 9/2-11 and Hugin Formation from well 15/12-22 in the LMR crossplot (left) color coded by cement volume (right).

4.1.8. Source rock analysis

Known organic-rich shale formations have mostly been ignored in this compaction study since their elastic parameters differ significantly from normal shales and thus deviate from general compaction trends. However, compaction and burial history largely control the maturation and hydrocarbon generation of potential source rocks. How maturation is affected by compaction and burial depth is investigated using rock physics crossplots techniques.

4.1.8.1. V_p/V_s versus AI crossplot

Figure 4.24 show the Kimmeridge Clay equivalent Tau and Draupne Formations in the V_p/V_s versus AI crossplot of well 9/2-11, 15/3-8, 17/6-1 and 17/12-4. These wells are utilized because V_s data are available and since they represent four different stages of maximum burial. From Figure 4.24 it is observed that maximum burial for the source rock is between 2000-2500 m BSF in well 17/12-4, between 2500-3000 m BSF in well 17/6-1, between 3000-3500 m BSF in well 9/2-11 and between 3500-4500 m BSF in well 15/3-8. Increasing burial depth leads to increasing compaction. Increasing compaction in organic-rich shales results in increasing anisotropy, hence, the decreasing V_p/V_s-ratio with increasing burial depth observed in the data. Increasing density and cementation are also a general response to increasing compaction and porosity reduction, evident from the high AI in the deeply buried Draupne Formation (well 15/3-8).

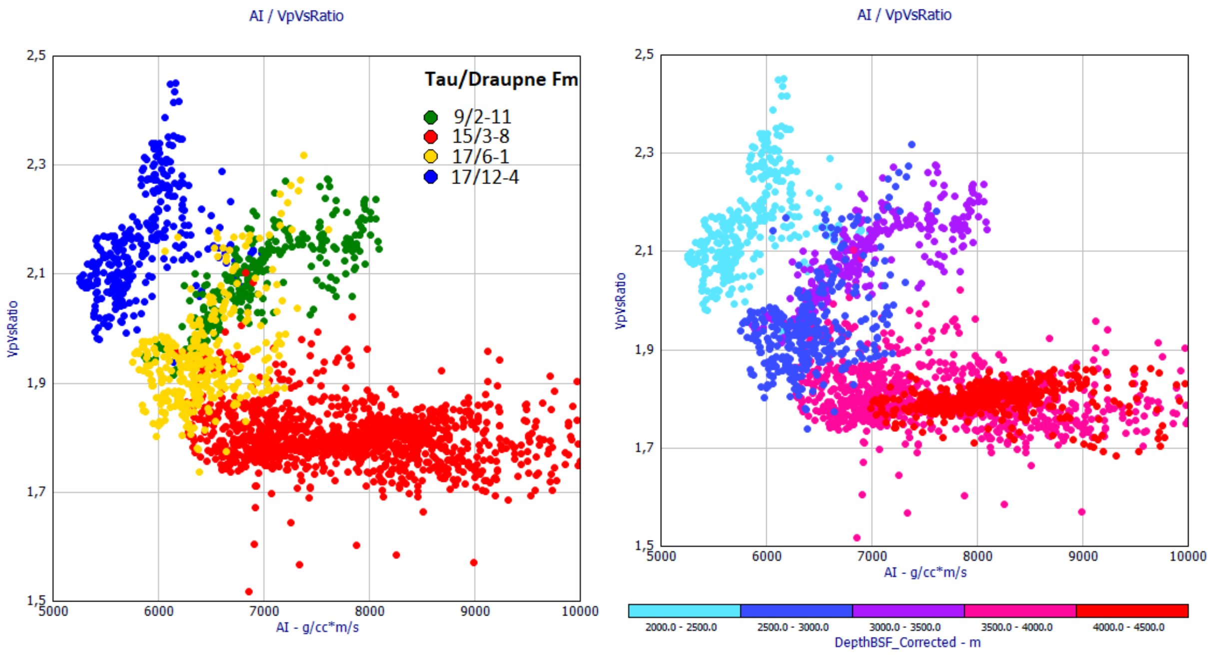

Figure 4.24: Comparison of source rock formations at four different levels of maximum burial in a V_p/V_s versus AI crossplot color coded by well (left) and uplift-corrected depth BSF (right).

Figure 4.25 shows the same data and crossplot as the previous figure but is now color-coded with estimated TOC percent and measurements from deep resistivity logs. TOC percent is estimated using the Passey method (Passey et al.,1990), and the methods and results of this estimation is discussed in subchapter 3.3 and 5.1, respectively. Individual trends of increasing TOC and increasing resistivity are marked with an arrow for each well. From organic-lean parts of the shallow buried Tau Formation to parts with higher TOC, a clear decrease in V_p/V_s-ratio and acoustic impedance is observed. In well 17/12-4, AI values vary from ~6200 to 5200 g/cm^3*m/s with increasing TOC, while also V_p/V_s ratio varies from ~2.35 to 2.1 with increasing TOC. A very different signature is observed in well 15/3-8, where AI values vary from ~9000 to 6300 g/cm^3*m/s with increasing TOC, while the V_p/V_s ratio remains similar for all TOC levels. It is evident that the effects of increasing TOC on seismic parameters changes with burial depth. Each arrow qualitatively represents the rate of changing seismic parameters with increasing TOC. The two shallowest formations have the steepest rate while the deepest buried formation has an almost horizontal rate. High resistivities show correlation with the estimated TOC values and good correlation with deep burial depth.

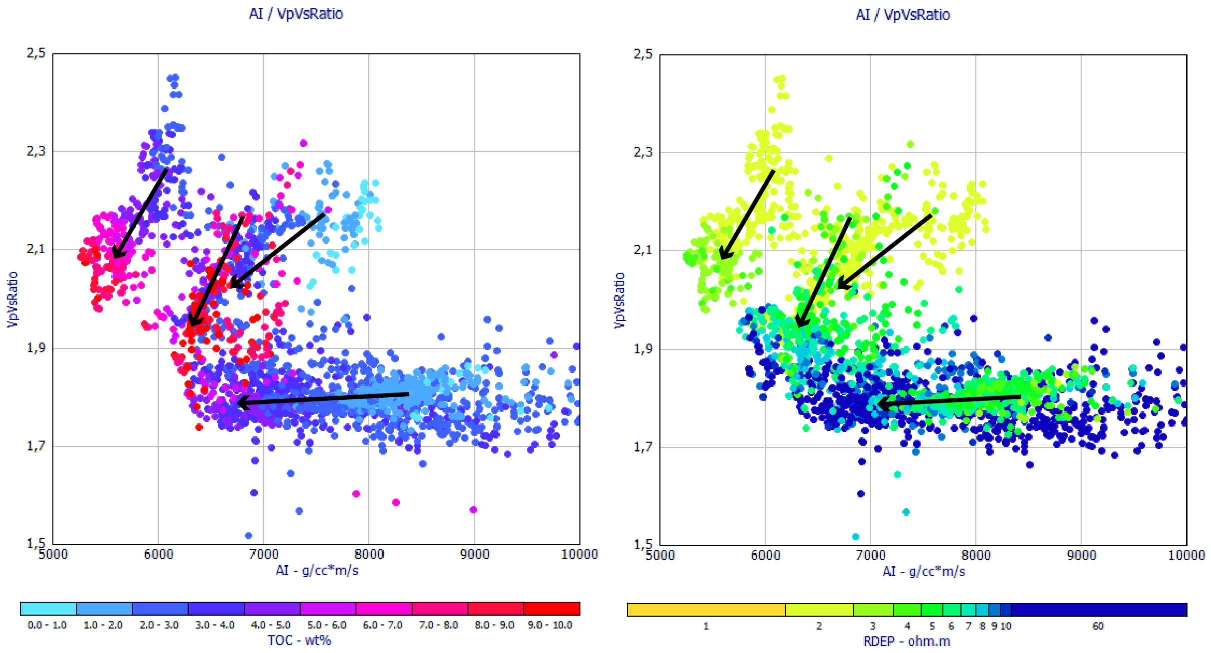

Figure 4.25: Comparison of source rock formations at four different levels of maximum burial in a V_p/V_s versus AI crossplot color coded by estimated TOC (left) and deep resistivity (right).

4.1.8.2. LMR crossplot

From the LMR crossplots in Figure 4.26, different compaction trends are observed based on burial and maturation. The low resistivity data (orange and yellow) represent the compaction trend for organic-lean and immature source rock. Increased burial and maturation, represented by high resistivity data, display a different trend with steadily increasing Mu-Rho and rather low Lambda-Rho. There is very little difference in Lambda-Rho values for the immature and mature source rock units. It is also noted that somewhat similar elastic property signatures are observed for organic-rich shales (Figure 4.26) and high-porosity clean sandstones (Figure 4.23).

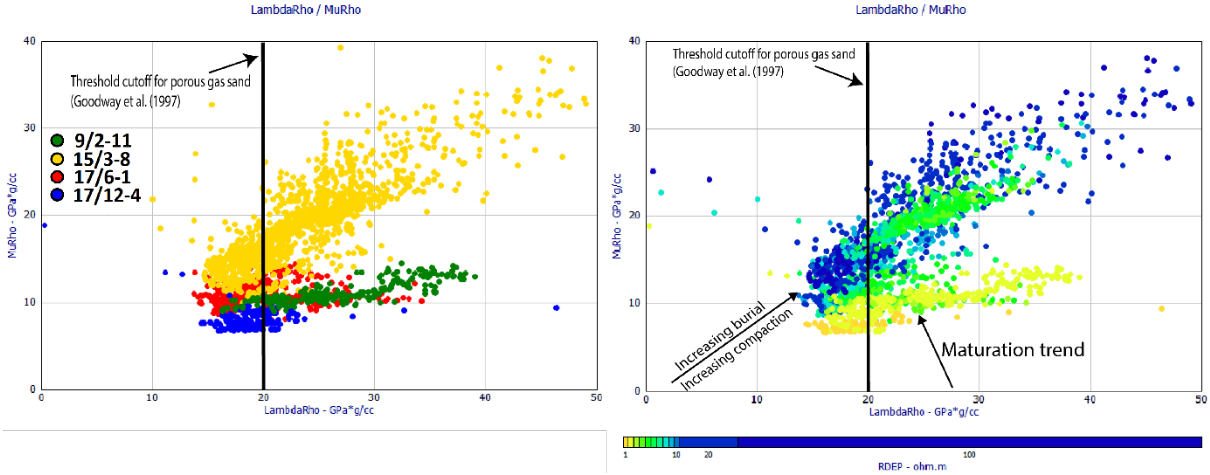

Figure 4.26: Comparison of source rock formations at four different levels of maximum burial in a LMR crossplot color coded by wells (left) and deep resistivity data (right).

4.2. Discussion

4.2.1. Temperature

The mean geothermal gradient of the study area, calculated from bottom hole temperatures, is 31.5 °C/km. This is noticeably lower than the overall North Sea average of 35-40 °C/km, suggested by Bjørlykke (2015b). Geothermal gradients are strongly influenced by heat flow. Sedimentary basins as the North Sea have an upward heat flow from the basement and into the overlying sediments. Radioactive basement rocks, such as granite, generate more heat. Basement rocks is an important controlling factor for the heat flow on the NCS (Bjørlykke, 2015b). Wells from the Johan Sverdrup field on the Utsira High (adjacent to the Ling Depression) show an average geothermal gradient of about 42 °C/km (Kaspersen, 2016). Maast et al. (2011) argue that such variations can be explained by distance to high-conductivity basement rock (structural highs) and the thickness of low-conductivity post-rift sedimentary successions (grabens/basins). The influence of layers or domes of salt on geothermal gradients is also acknowledged. Evaporites of the Zechstein Group are present south of the Ling Depression and especially in the Egersund Basin. High conductivity of salt equals low thermal gradient, resulting in relatively high temperature at the top of the salt and low at the bottom (Bjørlykke, 2015b).

One important reaction within the chemical compaction domain is the dissolution of smectite by reacting with available K^+ at about 70-100 °C/km and precipitation of illite and micro-quartz as a result. Because the kinetics of chemical reactions is highly temperature- and time-dependent, the depth of the transition zone between mechanical compaction and chemical compaction is mainly controlled by the local geothermal gradient. However, availability of K^+ reactants may in some cases be equally important to the transformation of smectite to illite and quartz in shales (Bjørlykke, 1998). In well 15/12-1 (in the study area but not availible in the study), XRD results from Berstad and Dypvik (1982) reveal lack of K-feldspar and generally low K^+ levels in Eocene sediments with temperatures exceeding 70 ºC (Figure 4.27), sufficient for illitization (i.e chemical compaction) to take place. Koochak Zadeh et al. (2014) concludes that chemical compaction has been restricted and moved to a deeper level of Paleocene aged sediments where sufficient K^+ was available, in addition to temperature. From Figure 4.27 one can easily observe the deviation from compaction trend due to onset of chemical compaction at 85 ºC.

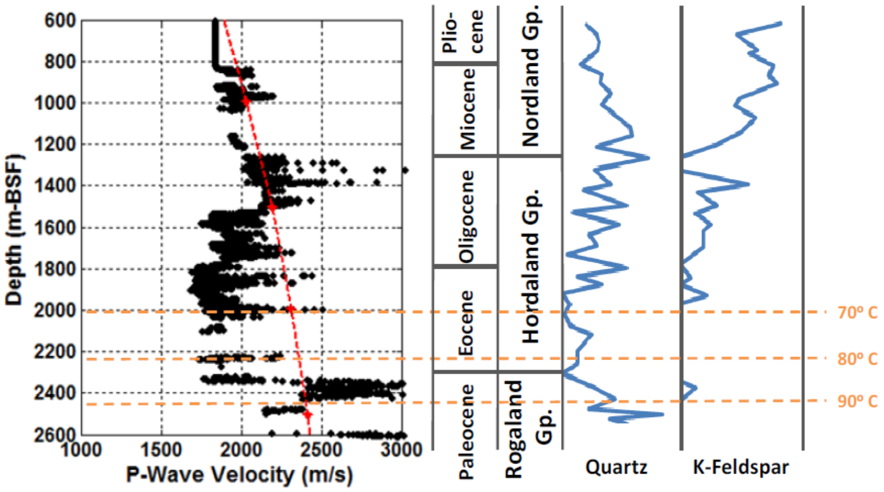

Figure 4.27: Velocity versus depth plot for shales in well 15/12-1 overlain by the Kaolinite-Silt compaction curve from Mondol (2009), and corresponding compositions of quartz and K-feldspar and quartz from Berstad and Dypvik (1982) (Koochak Zadeh, et al., 2014).

4.2.2. Compaction

The primarily used published compaction trend for uplift and transition zone estimation in this study represents mechanical compaction of 50:50 kaolinite-silt (Mondol, 2009) aggregates under progressive compression at hydrostatic pressure. This trend has shown to act as a good model for mechanically compacted shaly lithologies on the NCS (Kahlani, et al., 2015; Hansen, et al., 2017). XRD-analysis by Kalani et al. (2015) identified kaolinite as the dominating clay mineral in the shaly overburden intervals in the Egersund Basin. Mudstones have previously been considered as one single lithology. However, there are significant variations in physical properties of different clay minerals resulting in different compaction behaviors. Through experimental mechanical compaction tests of smectite and kaolinite aggregates by Mondol et al. (2007), considerable variations in compaction trends for different clay minerals were revealed. In Figure 4.6 one can observe how the smectite-rich mudstones of Hordaland Group plot with lower velocities than the applied reference trend, as this curve is based on the more compactable mix of kaolinite and silt. Similar to how Mondol et al. (2007) recognized the importance of mineralogy in clay compaction, Chuhan et al. (2003) and (Fawad, et al., 2011) shed light on how mineralogy, grain size, sorting and grain shape affects compaction of sands. All these parameters are results of provenance and depositional environment.

4.2.3. Transition zone

Experimental compaction trends are effective in reproducing mechanical compaction conditions. The elements of time and temperature in chemical compaction are very hard to reproduce. Thus, deviated V_P (and density) trends compared to published compaction trends may indicate onset of chemical compaction. Deviations from mechanical compaction trends due to time- and temperature-dependent chemical compaction can to some degree be quality controlled by mineralogical data and SEM analysis. For well 9/2-1 (Figure 4.28) and 9/2-2 in the Egersund Basin, Kalani et al. (2015) reported that increase of quartz and illite coincide with decrease of K-feldspar and smectite at 1500 and 2000 m BSF, respectively. Considering the geothermal gradients this would correspond to present day temperatures just below 50 ºC.

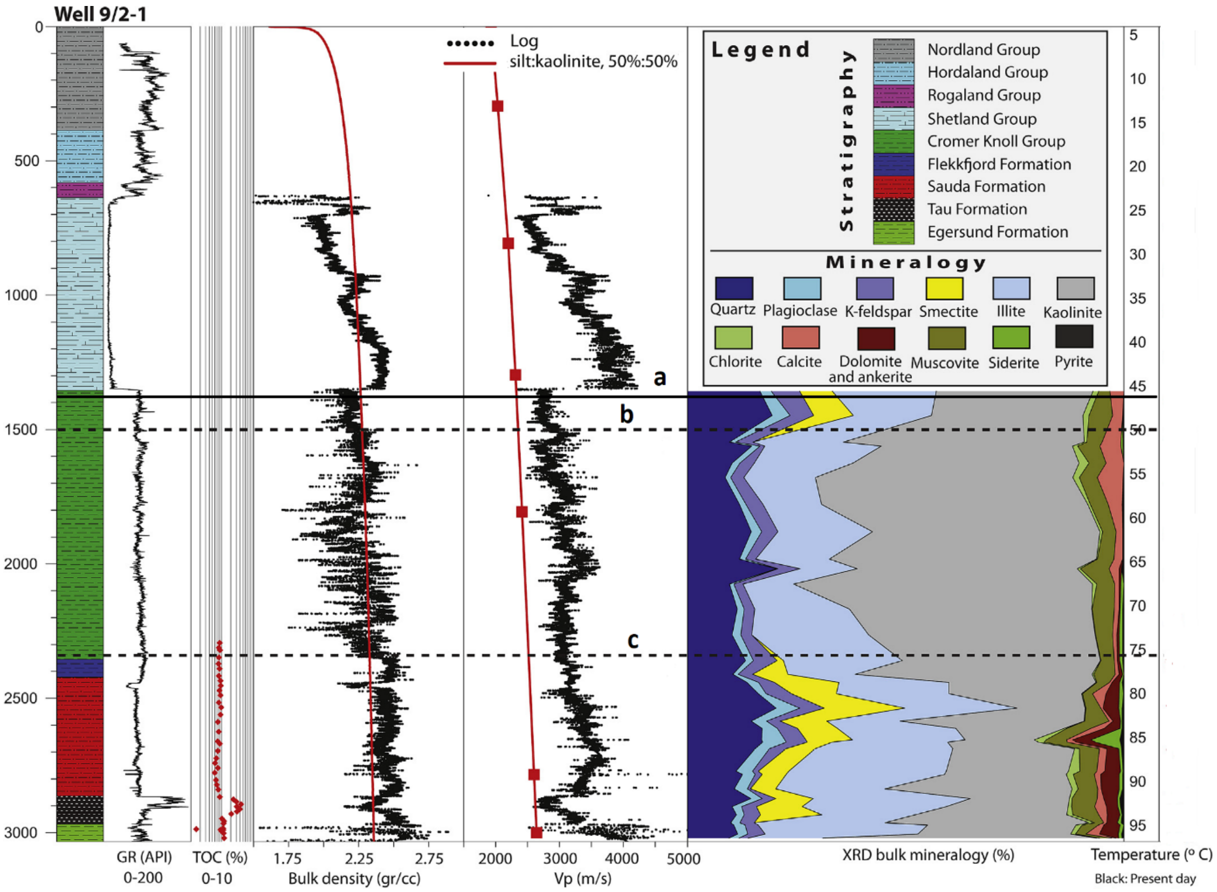

Figure 4.28: Stratigraphy, gamma ray, TOC, density and V_P plots with compaction trend from Mondol (2009) and quantitative mineralogy from well 9/2-1. Labels represent (a) transition zone suggested in this study, (b) onset of and (c) intense chemical compaction suggested by Kalani et al. (2015).

Adjusted for exhumation temperatures above 60 ºC is expected at 1500 m BSF and considering the mineralogical changes this seems to be sufficient to start the illitization process. Higher uplift estimates (e.g. Kalani et al., 2015 and Hansen et al., 2017) will indicate even higher temperatures. Illitization of smectite is believed to be the main chemical compaction process in the area due to the occurrence and increase of micro-quartz coinciding with increasing illite, albitization and presence of K-feldspar. An example of illitization is seen in thin section from Hugin Fm in well 15/12-2 (Figure 4.29), underlining the importance of this process throughout the study area.

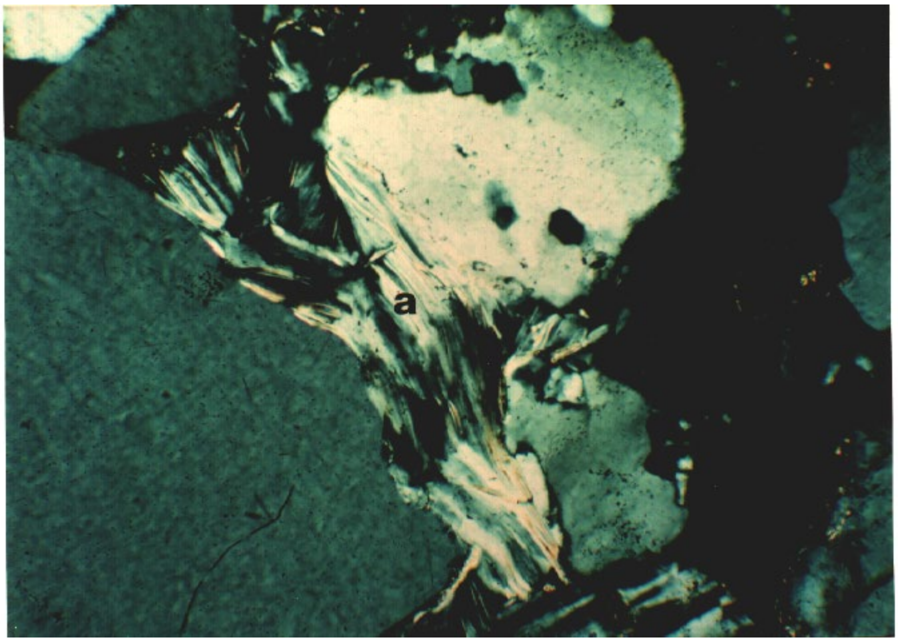

Figure 4.29: Thin section of core sample from 2831.8 m BSF in Hugin Formation from well 15/12-2. Label a) indicate illitizated kaolinite. From petrographic study of well 15/12-2 available from NPD (2018).

Kalani et al. (2015) divides the chemical compaction domain into “onset of chemical compaction” and “intense chemical compaction” (Figure 4.28). Transition zone estimates proposed in this study is mostly based on an assumption similar to “onset of chemical compaction”. A westward increase of current transition zone depths is shown in this study (Table 4.1). This correlates well with the eastward increase of estimated exhumation. A continuous transition zone at a constant depth is expected pre-exhumation within an area, assuming similar geothermal gradients and equal deposition. A subsequent tilting of the area due to progressive exhumation and erosion towards the east (as observed in the study area) would lead to shallower transition zones to the east. By this assumption the estimated transition zones adjusted for uplift should be equal. This is not the case this study, and not expected due to a relatively large study area with large variations in geothermal gradients, basin elements and evolution. However, an inconsistency between non-uplifted and uplifted area is observed. The non-uplifted wells of quadrants 15 and 16 show a difference of 360 meters between highest and lowest estimate and an average depth of 2073 m BSF. Uplifted wells in quadrants 9 and 17 show a difference of 520 meters and an average of 1863 m BSF. This implies that the estimation of uplift (further discussed in the following subchapter) introduce more uncertainty to the already difficult act of interpreting transition zones.

By utilizing V_s and density data (Figures 4.13-4.16), a transition zone represented by a shear wave velocity of 1.45 km/s is proposed. Additionally, individual regression lines for mechanical and chemical compaction regime are produced. Both show low correlation, but effectively mimics the individual trends, compared to one single best-fit line. Consequently, two density-velocity-relations are suggested to represent the mechanical and chemical compaction trends for shales in the study area:

$$\text{MC: } \rho = 1.854 + 0.4507V_s \qquad \text{Eq. 4.1}$$

$$\text{CC: } \rho = 2.258 + 0.1765V_s \qquad \text{Eq. 4.2}$$

V_s and density data proves very useful for this purpose. Both are direct measurements of elastic properties, which eliminate several uncertainties. Density is preferred over porosity estimations, even though porosity may be easier to comprehend. Porosity can be estimated from density, but this includes uncertainty related to lithology-dependent matrix density and fluid density dependent on fluid type and salinity. Alternatively, neutron porosity can be applied, but this estimation is also highly influenced by lithology, shaliness and gas (Mondol, 2015). V_s data is preferred, when available, over V_p due to being unaffected by pore fluids (Avseth, et al., 2005). Insensitivity to pore fluids is equal to increased sensitivity to cementation and rock stiffness. This is an important parameter for identification of transition zone as the initial few percent of cementation are predicted to yield biggest change in physical properties (e.g. V_s and shear moduli). V_p data was tested (Figure 4.3) but yielded more data scatter and uncertainties, especially close to assumed transition zone. A similar study is performed by Hansen et al. (2017) roughly within the same study area. This study utilized a greater number of wells and within a more limited area, resulting in differences in the proposed relations for compaction trends. A transition zone at V_s: 1.35 km/s was proposed, an acceptable deviation of 0.1 km/s compared to this study.

4.2.4. Uplift estimates

The western part of the study area, mainly including Southern Viking graben and the western part of Ling Depression, are currently at maximum burial depth, indicated by the lack of observable exhumation. More marginal part of the study area, including Egersund Basin, Åsta Graben and eastern part of the Ling Depression, experienced maximum burial in early Miocene (Japsen, et al., 2011). The late Neogene exhumation episode (Baig, 2018) had a significant effect on these areas and exhumation estimates show an increasing trend towards east (Table 4.1). Erosion of sediments from the overburden most likely caused isostatic uplift of the ground to achieve isostatic balance. Presumably, isostatic rebound only restored 60-70% of erosion-reduced surface levels in most areas. Subaerial exposure is indicated in the Norwegian-Danish Basin by pre-erosion restoration of surface elevations. Coastal/deltaic depositional environments in the Norwegian-Danish Basin during the late Neogene support this.

Table 4.4: Comparison of uplift estimation from this study and other published studies, for a selection of wells in the study area.

Comparison of uplift estimation [m]								
Well	This study	Average from Baig et al. (2018)	Vitrinite reflectance from Baig et al. (2018)	Kalani et al. (2015)	Hansen et al. (2017)	Hansen (1996)	Average from other studies	Discrepancy from this study
9/2-1	340	-	-	600	-	390	495	155
9/2-2	450	565	482	750	650	235	536	86
9/2-11	650	565	-	-	620	-	593	59
15/12-23	0	-	-	-	0	-	0	0
17/3-1	560	566	618	-	750	-	645	85
17/4-1	230	193	217	-	250	-	220	10
17/9-1	290	495	466	-	300	-	420	130

Uplift estimates from several studies are presented in Table 4.4. Most estimates are based on the same trend fitting technique as used in this study. Both experimental compaction trends and area-specific normal compaction trends are used. The average values from Baig et al. (2018) are a result of combining exhumation estimates based on individual lithostratigraphic units. Estimates from vitrinite reflectance are included because such data is highly sensitive to the temperature gradient and maximum burial temperatures, which can be related to uplift. An average uplift from the other studies is computed and compared to estimates from this study. The discrepancy ranges from 0, in presumably non-uplifted area, to 155 m in well 9/2-1 in the Egersund Basin. These variations emphasize how difficult precise uplift estimation is and the importance of it. The highest and lowest estimates in well 9/2-2 vary with 525 meters, which would equal a 16 °C temperature difference. Such differences could highly impact interpretations of source rock maturity and onset of porosity-reducing chemical compaction. An ideal uplift estimation would include a high well-density dataset with continuous V_P coverage, vitrinite reflectance and also utilize seismic sequence stratigraphic techniques.

4.2.5. Effects on elastic properties of source rocks

Comparison of source rock formations with different levels of maximum burial depths (Figures 4.22 and 4.23) show that increasing compaction and diagenesis are the primary cause of changing elastic parameters in organic-rich shales. TOC content is also observed to have substantial influence due to the low density and velocity of kerogen. Increasing TOC is observed to shift the data towards lower V_P/V_S and AI compared to organic-lean shales, which is noticeably different than expected from only increasing burial and compaction. This deviation from normal shale compaction trend is the reason for exclusion of organic-rich shales in the rest of the compaction study.

Geochemical data, presented in subchapter 5.1.6, reveal maturities from immature (well 9/2-11 and 17/12-4) to possibly early oil window (well 17/6-1) and peak/late oil window in well 15/3-8 (Isaksen & Ledje, 2001), used for comparison. The low resistivity values in well 9/2-

11 and 17/12-4 are representative for immature source rock and no hydrocarbon generation. Observed differences in elastic properties are therefore credited to increased compaction due to deeper maximum burial depth. In addition to compaction, data from well 15/3-8 is affected by organic content and hydrocarbon generation. Effects of hydrocarbon generation are observed as additionally lowered V_p/V_s ratio and acoustic impedance compared to the trends of increasing compaction and TOC. A rather weak example of the similar effect is observed in the high resistivity part of well 17/6-1, but the shallower burial has resulted in only weak hydrocarbon effects on elastic properties.

4.2.6. Implications

Understanding compaction, burial and thermal history are essential to understand the geological development of an area or a basin. This development is in turn vital to understand local hydrocarbon prospectivity. Both positive and negative effects on prospectivity may arise from compaction processes, uplift and erosion, as seen in Figure 4.30.

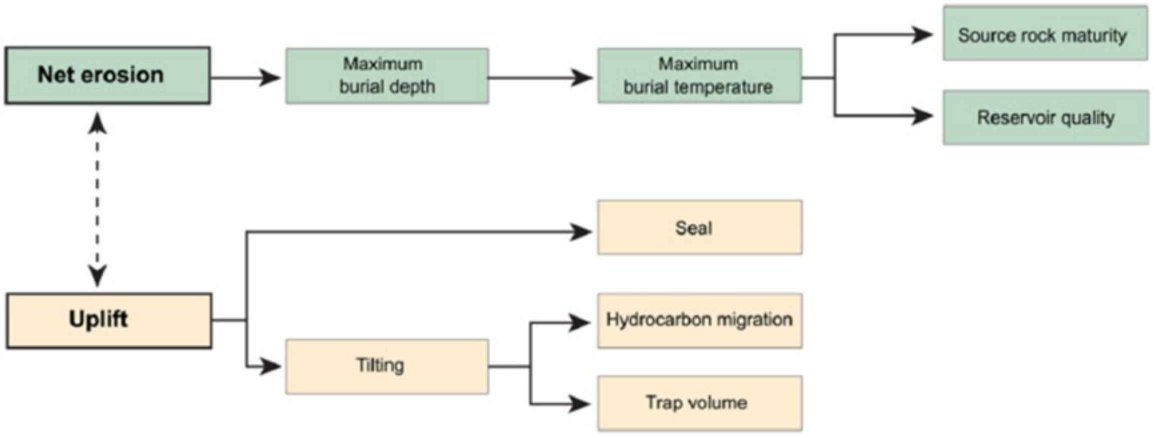

Figure 4.30: The role of uplift and erosion on processes affecting hydrocarbon prospectivity (modified from Henriksen et al., 2011).

The following is mainly based on Doré and Jensen (1996), Bjørlykke and Jahren (2015) and Baig et al. (2018):

Positive effects on prospectivity

Reservoir quality: Overpressure reduces the effective stress from the overburden and consequently preserves porosity due to reduced mechanical compaction. In highly oil-saturated reservoirs silica transportation efficiency is minimized and thus preventing quartz cementation with oil or bitumen acting as coating. Grain coatings, such as chlorite, may also effectively shut down quartz cementation and prevent large porosity reductions.

Source rock maturation: Source rocks located in uplifted areas will prove more mature than present day temperatures would imply, due to previously deeper burial. This is the case in Egersund Basin and eastern Ling Depression, where present day temperatures imply immature source-rocks and uplift-correction gives a more optimistic maturity indication locally. Therefore, a good control on uplift and erosion in areas with shallow buried source rock can be very important.

Release of methane gas: Formation water is known to have methane-producing potential during extensive uplift. Dissolved methane is a result of highly mature organic matter. Since the solubility of methane in water increase with pressure, a decrease of pressure due to extensive uplift may produce free methane.

Fractured reservoirs: A chemically compacted reservoir is able to withstand far less strain than a typical caprock. A fractured reservoir may show higher porosity and permeability. If the caprock still inhabits its sealing properties it will be positive for prospectivity.

Remigration: Exhumation and subsequent erosion will generally cause release and reduction of pressure, also within reservoirs. Any liquid hydrocarbons present will experience gas exsolution and expansion, potentially resulting in spilling. Spilling also occur due to differential uplift (Figure 4.31). Spillage, seal failure, overpressure and fractures are all processes that may lead to remigration. In such cases hydrocarbons from deeper horizons may migrate upwards and in the direction of differential uplift, and hopefully be trapped in a shallower or adjacent trap.

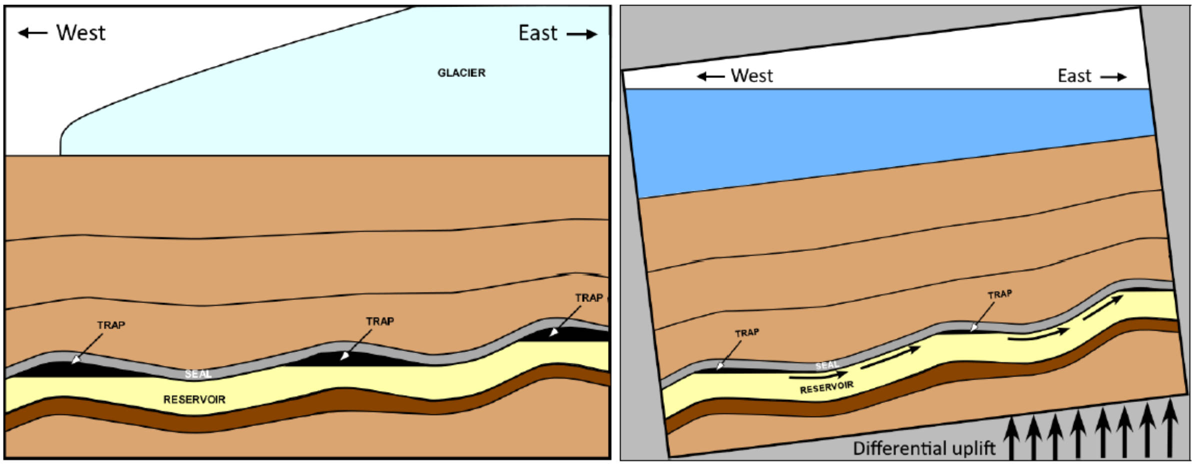

Figure 4.31: Illustration of how remigration may occur due to differential uplift as a result of isostatic rebound (Wesenlund, 2016).

Wesenlund (2016) suggests tilting due to differential uplift in the Central North Sea is a possible part of the migration route to the Johan Sverdrup discovery and also the small gas discovery in well 17/3-1. Oils of the Yme discovery (9/2-1) in the Egersund Basin does not show a good match with underlying source rocks in terms of maturity (Ritter, et al., 1987). Hence, hydrocarbons most likely have migrated from the deeper basin areas southwest of the discovery, possibly due to differential uplift and tilting.

Negative effects on prospectivity

Reservoir quality: Diagenetic processes are effectively irreversible and will prevail during uplift, as long as the temperature is sufficient. Thus, compaction will reflect the maximum burial of a rock and will typically inhabit lower porosity and permeability than expected at current depth. This effect is relevant in this study as onset of chemical compaction is observed at shallower depth in uplifted areas.

Seal integrity: Overpressure or hydrocarbon expansion may lead to fracturing and leakage through caprocks during uplift. The thermal history of the Tau Formation (both source and seal) in the Egersund Basin indicate sufficient time-exposure to temperatures suitable for chemical compaction. This includes smectite transformation which may have resulted in increased brittleness. It is also likely that Quaternary unloading have caused fracturing and hydrocarbon leakage due to the already increased brittleness.

Petroleum generation and migration: Maturation of source rocks is irreversible. Areas with extensive uplift may contain overmature source rocks at relatively shallow current depths, as the maturity of the source rock reflects its maximum temperature. If uplift occurred during generation of hydrocarbon, the generation may have ceased and led to underfilled traps. The latter is most likely within the study area, as no source intervals show signs of high maturity.

4.3. **Uncertainties**

Uncertainties related to the compaction study includes:

- Calculation of geothermal gradient is based on available bottom hole temperatures and the assumption of a temperature average of 4 °C at sea bottom. The temperature gradient may not reflect local changes in the subsurface. Measured borehole temperature may not reflect the temperature representative for that depth.

- Transition zones are estimated qualitatively and may be interpreter biased. Geothermal gradient and lithology discrimination is used to minimize uncertainties.

- Transition zone and uplift estimations utilize shale volume cutoffs to discriminate between sandy and shaly lithologies. Uncertainties related to shale volume estimation are discussed in chapter 5.

- Cement volume is estimated using a relation developed specifically for the Etive sandstones in the North Sea (Marcussen, et al., 2010). Using this relation for sands and shales in this study area may cause inaccuracies but should effectively reproduce relative cement volumes.

5. Petrophysical Analysis

5.1. Results

The study area, and the North Sea in general, contains several formations with reservoir and/or source rock potential. Three formations (Sandnes, Bryne, Hugin) stood out as all wells were screened for reservoir potential and they were chosen for reservoir characterization. Their reservoir potential was identified during lithology discrimination of all wells. Information from NPD (2018) confirm these formations as the main targets for several of the studied wells in the Central North Sea. Sandnes and Bryne Formations are mainly found in the eastern part of the study area (Table 2.1). They are penetrated by well 9/2-1, 9/2-2, 9/2-11, 17/12-1, 17/12-3 and 17/12-4 in the Egersund Basin, 17/9-1 in the Åsta Graben and 17/3-1 and 17/6-1 in the Ling Depression. The Hugin Formation is mainly found in the western part of this study area (Table 2.2). It is penetrated by well 15/12-2, 15/12-22 and 16/10-3 in the Ling Depression and 15/8-2 in the Southern Viking Graben. The reservoir potential from wells containing at least one of these formations are presented in Table 5.1. Each formation is discussed separately. The methods used for reservoir interpretation and analysis are discussed in chapter 3.3.

Lithology discrimination and literature study identified the Tau, Draupne, Bryne and Fjerritslev Formation as successions with source rock potential. These are assessed with both available measured data (NPD, 2018) and well log data. The methods used are discussed in chapter 3.3.6.

During lithology discrimination the complete Jurassic succession is assessed to locate different petroleum system constituents. Potential non-Jurassic petroleum systems and components were ignored in this study. Obvious shale intervals are investigated for source or cap rock potential, while sandy intervals are investigated for reservoir potential. A typical reservoir formation rarely has reservoir potential throughout and therefore any productive intervals must be identified. Interpretation of gamma ray logs can identify sandy intervals and neutron/density-crossplots will separate lithologies and plot sands along the sandstone line (Figure 3.6). The gamma ray log with Larinov's (old rocks) calibration is used for shale volume (V_{sh}) estimation. The chosen cutoff value of V_{sh} is 40%. Shale volume calculation from the neutron-density log is used for quality control. The neutron-density combination is used for effective porosity estimation, with 10% as cutoff value. Archie's equation is utilized for water saturation (S_w) calculation. The S_w cutoff value is set to 60%.

General information about reservoir and source rock intervals is to some extent available in well summaries submitted by the oil companies to the Norwegian Petroleum Directorate (NPD, 2018).

To minimize ambiguity regarding reservoir property terminology, a set of terms are utilized. Assuming only presence of shale and sand, the shale volume terminology is:

- 0-25% shale equals sand
- 25-50% shale equals shaly sand
- 50-75% shale equals sandy shale
- 75-100% shale equals shale

For formations with reservoir potential the following porosity terminology is used:

- 0-5% porosity is considered insignificant
- 5-10% porosity is considered poor
- 10-15% porosity is considered fair
- 15-20% porosity is considered good
- <20% porosity is considered excellent

In terms of permeability the following nomenclature is used:

- 1-10 mD is considered poor
- 10-100 mD is considered good
- <100 mD is considered excellent

5.1.1. Evaluation of reservoir potential

Results from the evaluation of overall reservoir potential of the Sandnes, Bryne and Hugin Formations are presented in Table 5.1.

Table 5.1: Results from evaluation of the overall reservoir potential of the Sandnes, Bryne and Hugin Formations. Only wells penetrating the formations are included. Evaluations from well 17/12-1 is missing due to insufficient well data. Well 9/2-11 was drilled to TD at 2861 m MDKB within the Bryne Formation and thickness of the formation is therefore not known in this well.

Formation Evaluation								
Formation	Well	Formation depth (m RKB)	Formation thickness [m]	GR_{min}-GR_{max} [API]	V_{sh}	Eff. Porosity	N/G reservoir	Net res. [m]
Sandnes	9/2-1	3162-3309	147	25-98	0.137	0.09	0.51	75.31
Sandnes	9/2-2	3123-3230	107	28-100	0.205	0.08	0.37	39.38
Sandnes	9/2-11	2629-2761	132	25-120	0.191	0.10	0.45	59.89
Sandnes	17/3-1	2388-2410	22	20-105	0.060	0.18	0.91	19.94
Sandnes	17/6-1	2630-2647	17	35-150	0.334	0.13	0.60	10.18
Sandnes	17/9-1	2220-2237	17	20-103	0.273	0.24	0.22	3.79
Sandnes	17/12-3	2370-2396	26	15-95	0.178	0.16	0.78	20.21
Sandnes	17/12-4	2277-2298	21	25-118	0.172	0.14	0.57	11.91
Bryne	9/2-1	3309-3601	292.00	25-98	0.49	0.07	0.17	50.81
Bryne	9/2-2	3230-3475	245.00	28-100	0.33	0.11	0.38	92.63
Bryne	9/2-11	2761-2861*	100+	25-120	0.41	0.07	0.21	21.00
Bryne	17/3-1	2410-2440	30.00	20-105	0.19	0.21	0.81	24.41
Bryne	17/6-1	2647-2726	79.00	35-150	0.30	0.15	0.49	38.30
Bryne	17/9-1	2237-2835	598.00	20-103	0.39	0.15	0.07	43.43
Bryne	17/12-3	2396-2617	221.00	15-95	0.24	0.20	0.92	202.41
Bryne	17/12-4	2298-2398	100.00	25-118	0.15	0.15	0.62	61.50
Hugin	15/8-2	3882-4238	356.00	15-140	0.11	0.15	0.76	268.74
Hugin	15/12-2	2818-2868	50.00	20-130	0.03	0.20	0.872	43.59
Hugin	15/12-22	2831-2985	154.00	30-120	0.06	0.24	0.982	152.19
Hugin	16/10-3	2521-2532	11.00	45-135	0.19	0.15	0.905	9.96
Hugin	17/4-1	2265-2352	87	12-100	0.132	0.053	0.014	1.22

5.1.2. Sandnes Formation

A thickness map and a depth map of Sandnes Formation are shown in Figure 5.1. These are constructed using convergent interpolation between the studied wells in Petrel. The thickness map indicates a relatively thin succession of the Sandnes Formation in quadrant 17, which includes the NE Ling Depression, Åsta Graben and the northern part of the Egersund Basin. The thickness ranges from 16 to 26 meters. Towards the more central part of the Egersund Basin and quadrant 9, the thickness increases to a maximum of 147 meters. A similar trend is observed in the depth map. In quadrant 17, the top of Sandnes Formation ranges from 2220 to 2630 m MDKB. An increasingly deeper burial is observed in in the Egersund Basin and quadrant 9 where top of Sandnes Formation reaches 3162 m MDKB.

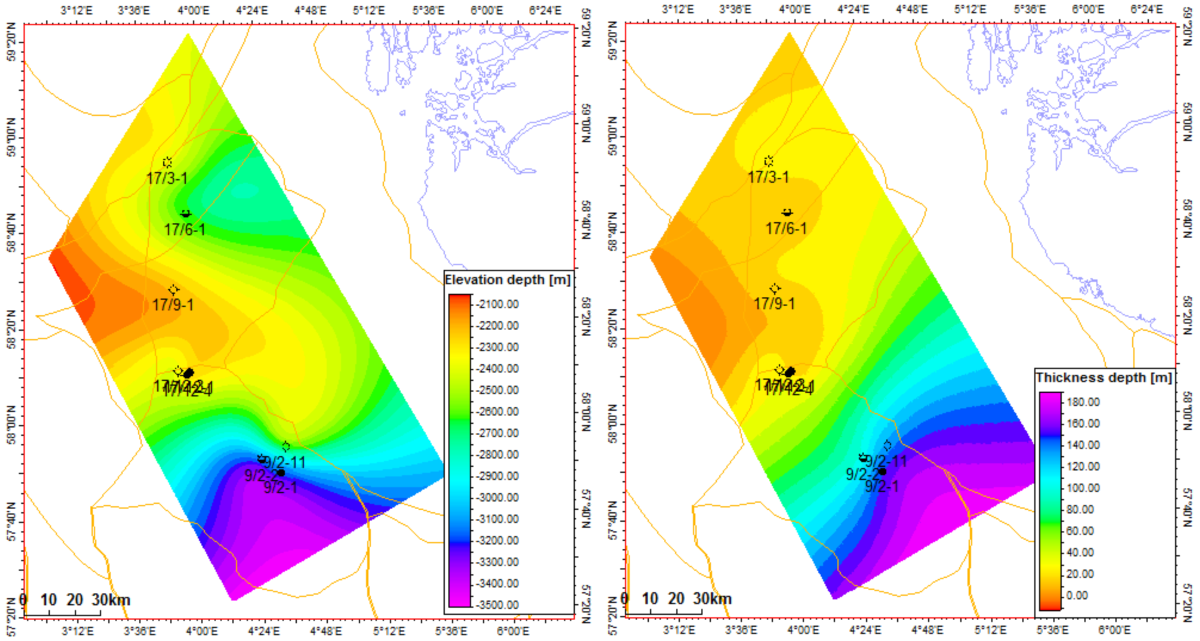

Figure 5.1: Left: Top Sandnes Formation depth map. Depth in m MDKB. Right: Thickness map of the Sandnes Formation based on interpolation between wells. Yellow lines represent structural elements. Mainland Norway is situated in the upper right corner.

An evaluation of the reservoir potential of the Sandnes Formation is presented in Table 5.1. The results of the petrophysical analysis of reservoir intervals within the Sandnes Formation is compiled in Table 5.2. The well log intervals of wells 9/2-1 and 17/6-1 are shown in Figures 5.2 and 5.3, respectively. The shale volume of the Sandnes Formation ranges from 6.0 to 33.4% within the studied wells. Both the lowest value (17/3-1) and the highest value (17/6-1) are located in the NE Ling Depression. The average shale volume of the Sandnes Formation in the analyzed wells is 19.3%, well within the “sand” classification. An average shale volume of 17.7% and 20.3% is observed in quadrants 9 and 17, respectively. A similar trend is evident for the net/gross ratio with 0.44 and 0.61 in quadrant 9 and 17, respectively. When considering the proposed reservoir intervals within the Sandnes Formation, more difference is evident. Clean reservoirs with an average shale volume of 5.0% are estimated in the Sandnes Formation reservoirs in quadrant 9. For quadrant 17, the same estimate is 22.0%.

Calculation of effective porosity reveals the opposite pattern with average of 16.8% in the relatively deep reservoirs in quadrant 9, while the shallower reservoirs of quadrant 17 average at 20.4%. The net/gross ratio within the Sandnes Formation reservoirs in quadrant 9 is at an average of 0.86.

Table 5.2: Petrophysical analysis of reservoir intervals of the Sandnes Formation.

Sandnes Formation									
Well	Reservoir depth (m RKB)	Gross reservoir [m]	GR_{min}-GR_{max} [API]	V_{sh}	Eff. Porosity	N/G reservoir	Net res. [m]	S_w in pay	Net pay [m]
9/2-1	3174-3263	89	25-98	0.029	0.131	0.858	76.38	0.384	31.88
9/2-2	3134-3187	53	28-100	0.051	0.146	0.730	38.69	-	-
9/2-11	2648-2663	15	25-120	0.066	0.195	1.000	15.00	0.532	0.15
	2670-2685	15	25-120	0.056	0.202	0.919	13.78	-	-
17/3-1	2388-2410	22	20-105	0.152	0.178	0.906	19.94	0.583	0.15
17/6-1	2630-2647	17	35-150	0.285	0.168	0.599	10.18	0.537	2.58
17/9-1	2220-2237	17	20-103	0.356	0.289	0.223	3.79	0.510	3.79
17/12-3	2370-2396	26	15-95	0.165	0.190	0.777	20.21	-	-
17/12-4	2277-2298	21	25-118	0.145	0.195	0.567	11.91	0.347	1.12

The following wells have estimated pay zones in the Sandnes Formation:

- 9/2-1 (Yme): 31.88 m with 38.4% average water saturation (Figure 5.3)
- 17/6-1 (Svaneøgle): 2.58 m with 53.7 average water saturation (Figure 5.2)
- 17/9-1: 3.79 m with 51.0% average water saturation
- 17/12-4 (Vette): 1.12 m with 34.7% average water saturation

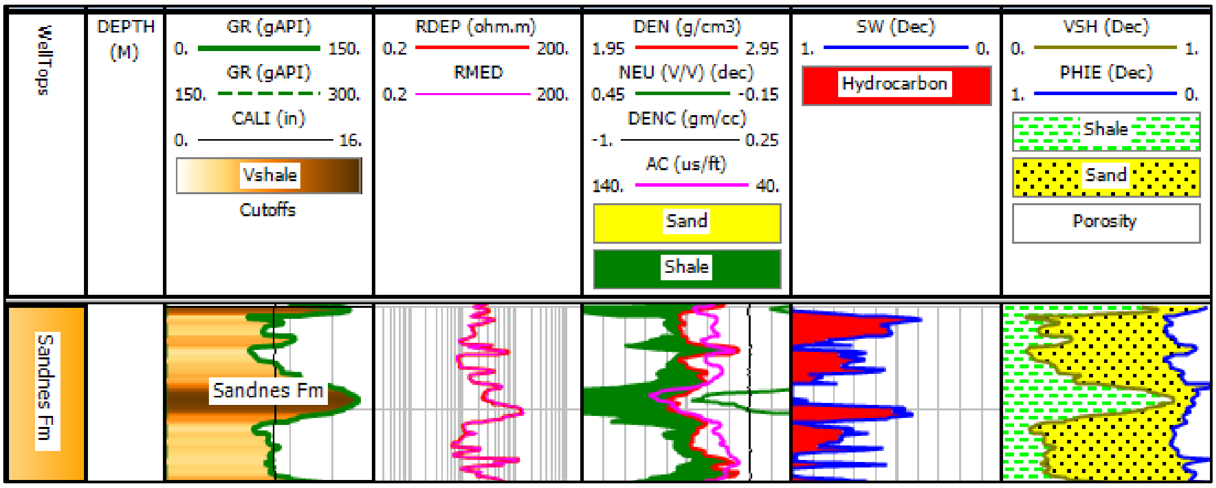

Figure 5.2: Sandnes Formation in well 17/6-1 (Svaneøgle). The whole formation is considered a reservoir in this well. The depth interval is 2630-2647 m MDKB.

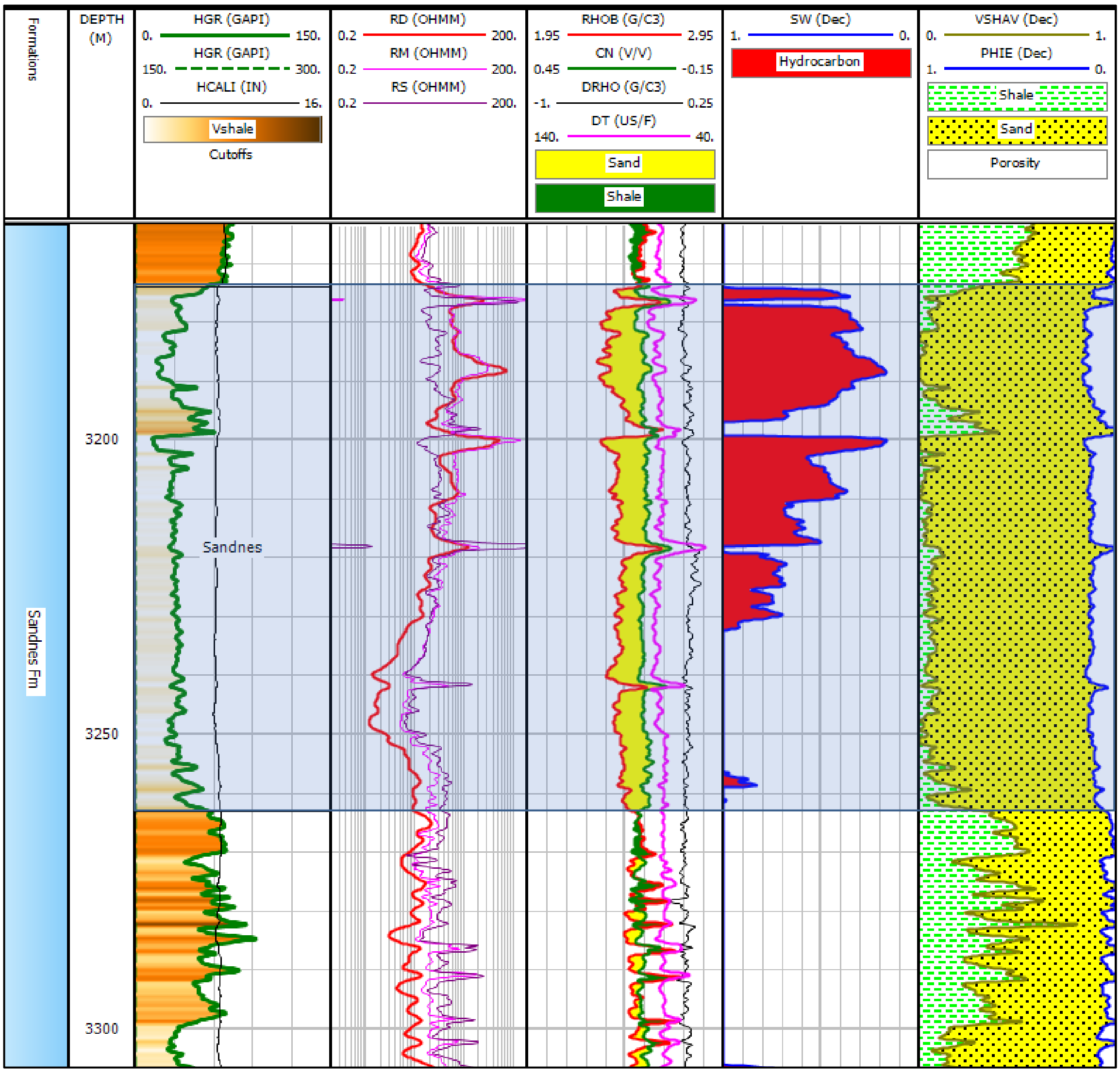

Figure 5.3: The Sandnes Formation in well 9/2-1 (Yme). Reservoir interval in blue shading.

5.1.3. Bryne Formation

The Top Bryne Formation depth map (Figure 5.4) shows a similar trend as seen in the depth map of Top Sandnes Formation. Quadrant 17 hosts nine of the studied wells which penetrates the Bryne Formation in the NE Ling Depression, Åsta Graben or the northern Egersund Basin. These are all relatively shallow buried, between 2237 and 2647 m MDKB. Further into the Egersund Basin, the Bryne Formation is progressively deepening to a maximum of 3309 m MDKB (9/2-1). In the NE Ling Depression, the thickness reaches 79 m, while it reaches several hundred meters locally in the Åsta Graben and Egersund Basin.

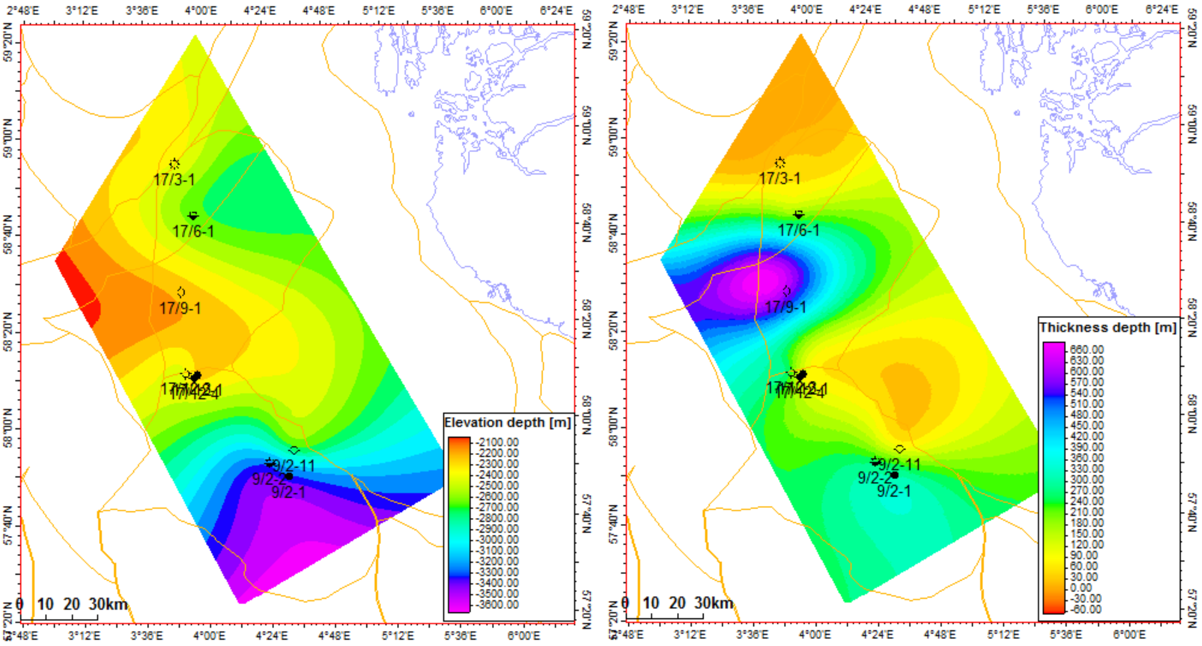

Figure 5.4: Top Bryne Formation depth map (left) and thickness map (right). Depths in MDKB.

An evaluation of the reservoir potential of the Bryne Formation is presented in Table 5.1. The results of the petrophysical analysis of reservoir intervals within the Bryne Formation is compiled in Table 5.3. The well log interval of well 17/12-4 is shown in Figure 5.5. Average shale volume estimates for the Bryne Formation ranges from a minimum 15.2% (well 17/12-1) to a maximum 49.3% (well 9/2-1). There is a general trend of increasing shale volume from quadrant 17 in the north towards quadrant 9 in the south. The same trend is evident for both effective porosity and net/gross ratio. However, evaluating reservoir intervals only reduces the average shale volume and increases the effective porosity of the quadrant 9 wells significantly. The upper reservoir interval of 9/2-1 only shows 2.8% shale and 13.1% effective porosity, which reflects a significantly higher reservoir quality than the average of the whole formation. Heterogeneities result in very clean reservoir intervals, but only 0.17 net/gross ratio for the full formation.

Table 5.3: Petrophysical analysis of reservoir intervals in the Bryne Formation.

Bryne Formation									
Well	Reservoir depth (m RKB)	Gross reservoir [m]	GR_{min}-GR_{max} [API]	V_{sh}	Eff. Porosity	N/G reservoir	Net res. [m]	S_w in pay	Net pay [m]
9/2-1	3448-3480	32	25-98	0.028	0.131	0.410	13.13	0.227	0.38
	3549-3601	52	25-98	0.081	0.128	0.498	25.88	0.224	9.38
9/2-2	3252-3338	86	28-100	0.115	0.146	0.506	43.50	0.370	10.44
	3442-3468	24	28-100	0.051	0.149	0.779	20.25	-	-
9/2-11	2761-2777	16	25-120	0.209	0.265	0.493	8.38	0.178	5.33
17/3-1	2410-2440	30	20-105	0.157	0.230	0.814	24.41	0.270	9.45
17/6-1	2683-2704	21	35-150	0.181	0.256	1.000	21.00	-	-
17/9-1	2237-2550	313	20-103	0.383	0.229	0.071	22.10	0.536	11.28
17/12-3	2396-2617	221	15-95	0.174	0.214	0.916	202.41	0.414	10.06
17/12-4	2298-2398	100	25-118	0.095	0.219	0.615	61.50	0.285	27.00

The petrophysical analysis suggests the following pay zones in the Bryne Formation:

- 9/2-1 (Yme): 9.38 m with 22.4% average water saturation in the lower reservoir.
- 9/2-2: 10.44 m with 37% average water saturation in the upper reservoir.
- 9/2-11: 5.33 m with 17.8% average water saturation.
- 17/3-1 (Bark): 9.45 m with 27% water saturation.
- 17/9-1: 11.28 m with 53.6% average water saturation.
- 17/12-3: 10.06 m with 42.2% average water saturation.
- 17/12-4 (Vette): 27.00 m with 28.5% average water saturation.

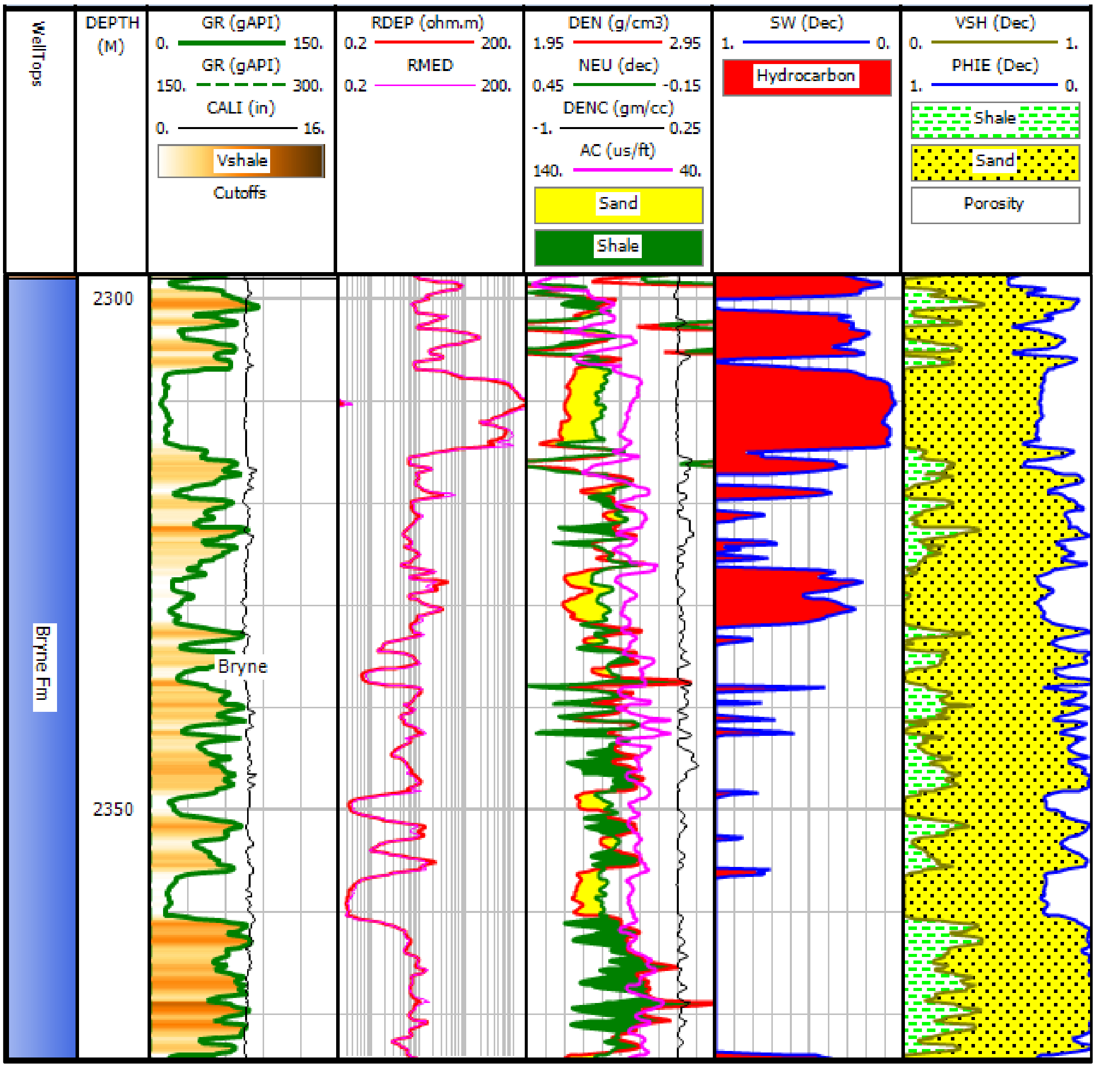

Figure 5.5: The Bryne Formation in well 17/12-4 (Vette).

5.1.4. Hugin Formation

A Top Hugin Formation depth map is presented in Figure 5.6. While it is based on well tops only, and incorporates no structural information, a general trend in evident. Within the Ling Depression, an increasing burial depth is observed from NE towards SW for the Hugin Formation. In the NE Ling Depression, Top Hugin Formation is reached at 2265 m MDKB in well 17/4-1, while in the SW Ling Depression, the equivalent depth reaches a maximum of 2831 m MDKB. 15/8-2 is the only studied well penetrating the Hugin Formation in the Southern Viking Graben. Here, the Hugin Formation is reached at 3882 m MDKB. This significant increase of depth into the Southern Viking Graben is easily observed in Figure 5.6. The two thickest successions of the Hugin Formation are found in wells 15/8-2 and 15/12-22 with a thickness of 356 and 154 m, respectively. Well 16/10-3 hosts the thinnest interval with its 11 m Hugin Formation succession. This implies a trend of increased thickness towards the west and basinward.

An evaluation of the reservoir potential of the Hugin Formation is presented in Table 5.1. The results of the petrophysical analysis of reservoir intervals within the Hugin Formation are compiled in Table 5.4. The well log interval in well 16/10-3 is shown in Figure 5.7.

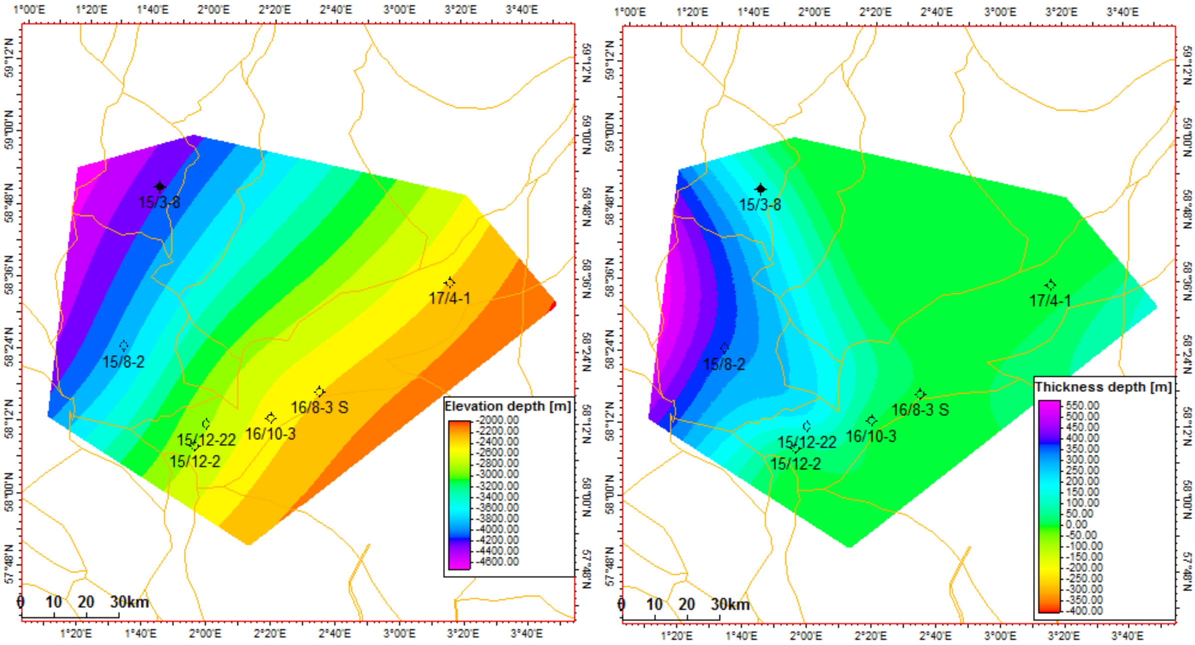

Figure 5.6: Top Hugin Formation depth map (left) and thickness map (right). Depth in MDRKB.

When considering potential reservoir zones within the Hugin Formation, the homogeneity of the gamma ray log made zonation difficult. Great variability in thickness between wells makes any potential zone correlation difficult. Thus, the complete formation has been considered as reservoir for the petrophysical analysis. The formation evaluation reveals relatively low shale volume in all the studied wells, ranging from 18.8% in well 16/10-3 to only 2.5% in well 15/12-2, all well within the sand definition cutoff. Good to excellent porosities is present in four of the studied wells, with a maximum porosity of 23.6% in well 15/12-22. Poor porosity of only 5.3% was estimated in 17/4-1, resulting in very low net-to-gross. Disregarding this outlier, the net-to-gross values are higher in the Ling Depression than in the Southern Viking Graben wells. From the most south-western part of the Ling Depression (15/12-2 and 15/12-22) into the Southern Viking Graben (15/8-2), a noticeable drop in effective porosity and net-to-gross is observed in the cutoff intervals, without a trend in shale volume supporting this.

Table 5.4: Petrophysical analysis of reservoir cutoff intervals in the Hugin Formation.

Hugin Formation									
Well	Reservoir depth (m RKB)	Gross reservoir [m]	GR_{min}-GR_{max} [API]	V_{sh}	Eff. Porosity	N/G reservoir	Net res. [m]	S_w in pay	Net pay [m]
15/8-2	3882-4238	356	15-140	0.060	0.171	0.755	268.74	0.204	7.16
15/12-2	2818-2868	50	20-130	0.112	0.219	0.872	43.59	-	-
15/12-22	2831-2985	154	40-130	0.044	0.239	0.982	152.19	-	-
16/10-3	2521-2532	11	45-135	0.177	0.159	0.905	9.96	-	-
17/4-1	2265-2352	87	12-100	0.115	0.106	0.014	1.22	-	-

The petrophysical analysis estimates only one pay zone, a total of 7.16 m with an average water saturation of 20.4% in well 15/8-2. All remaining wells are considered water-bearing. Figure 5.7 illustrates the lack of hydrocarbon saturation in the Hugin Formation in well 16/10-3.

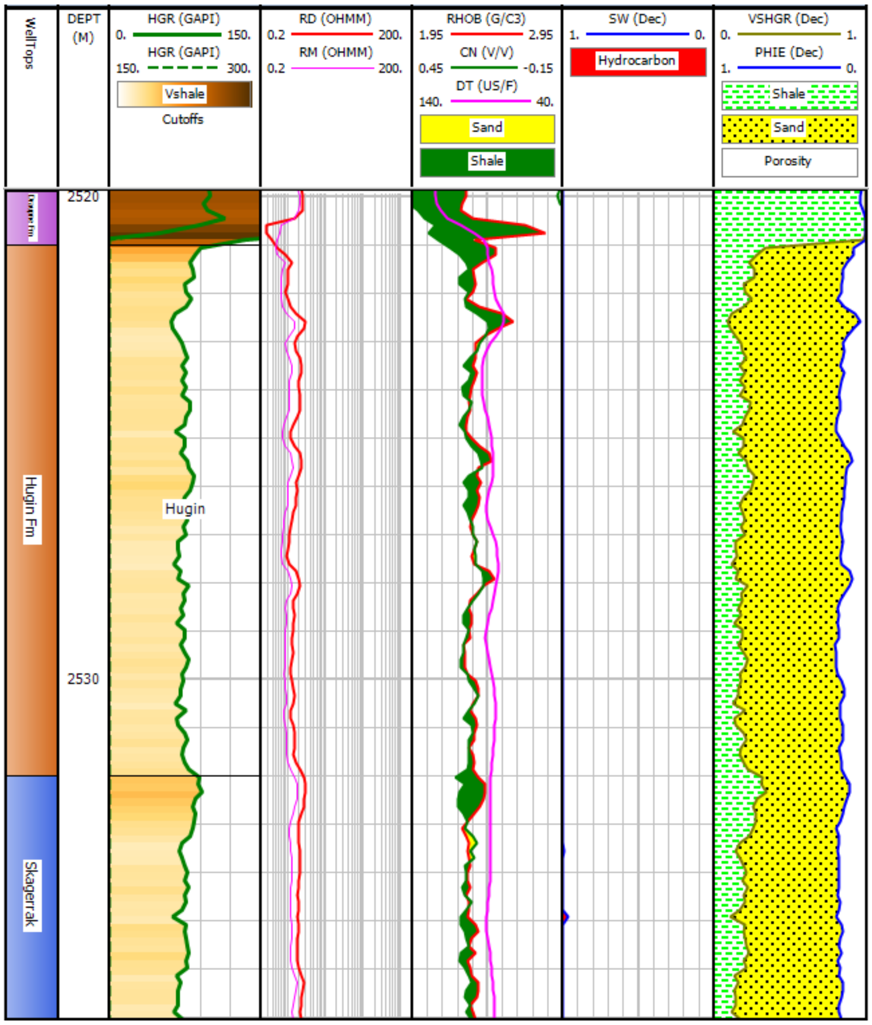

Figure 5.7: Hugin Formation in well 16/10-3. Draupne Formation is above, and Skagerrak Formation is below.

5.1.5. Permeability

Permeability has indirectly been quantified using the relationships introduced in subchapter 3.3.5. 17/3-1 is the only well with directly measured permeability data available. Measured porosity and permeability are available from a 20-meter interval from the top of Sandnes Formation. The operator reports a ~2m gas column at the top of the formation (NPD, 2018), while the petrophysical analysis in this study predicts less than a meter of net pay zone in the same interval. Figure 5.8 compares the directly measured data with the estimates from petrophysical analysis.

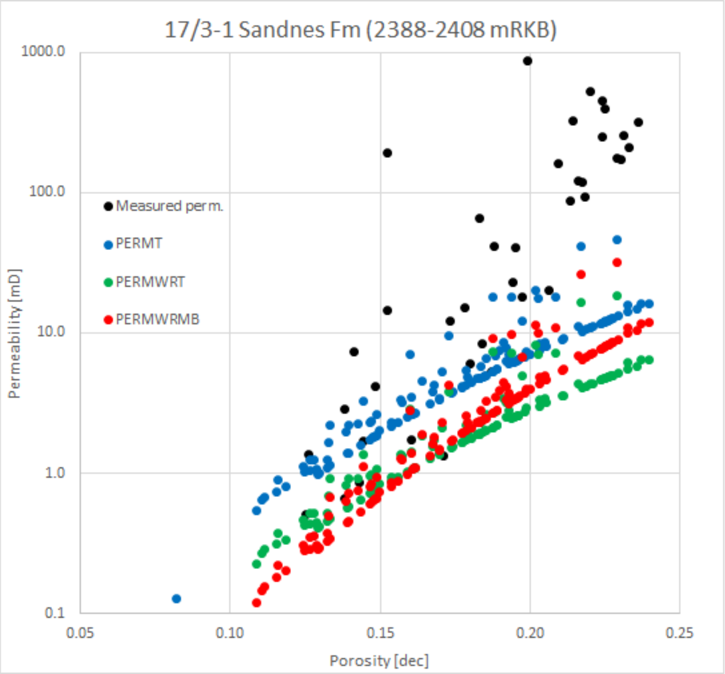

Figure 5.8: Comparison of measured and estimated porosity- and permeability data from well 17/3-1. PERMT: Timur equation, PERMWRT: Wylie-Rose equation with Timur parameters, PERMWRMB: Wylie-Rose equation with Morris-Biggs parameters.

The petrophysical analysis includes far more data points than the measured dataset. As the aim is to compare different permeability estimates, it must be noted that the measured and estimated porosity in this interval does not perfectly coincide, making the comparison less precise. As expected, both measured and estimated data show an increasing trend in permeability with increasing porosity. Measured permeability increases significantly with increasing porosity, with most of the data points indicating excellent to good permeability. Neither of the estimates manage to predict similar high values. The Timur equation produces the highest estimate, and therefore the best correlation with measured data. However, the discrepancy is large and only poor to good permeability is estimated. The fact that all three estimation relationships are highly affected by saturation seems to be the major contributing factor to the miscorrelation. The measured data are from a core sample with very limited hydrocarbon saturation. As all three relationships yield too low estimates, these relationships are not recommended in reservoir intervals with low hydrocarbon saturation.

The same relationships are used to estimate permeability in the example from Sandnes Formation in well 9/2-1, in Figure 5.9, with greater success.

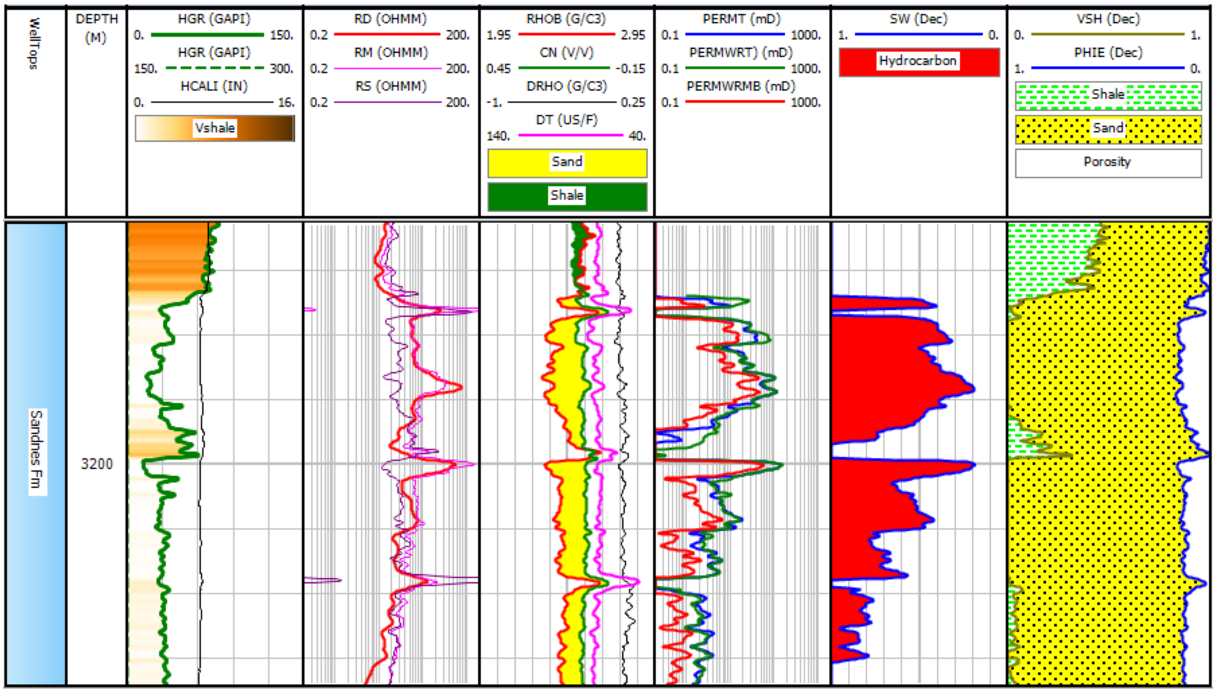

Figure 5.9: Example of permeability prediction from well 9/2-1 (Yme). PERMT: Timur equation, PERMWRT: Wylie-Rose equation with Timur parameters, PERMWRMB: Wylie-Rose equation with Morris-Biggs parameters.

Good to fair and poor permeabilities are observed with a general decrease with depth. The hydrocarbon saturated part of the reservoir indicates the possibility of compartmentalization based on very low permeability estimates where interbedded shales appear. Relatively high hydrocarbon saturation is expected to provide more accurate estimations compared to the previous example. The two relationships based on the Timur parameters are most applicable in oil-filled reservoirs and yield the highest permeability estimates. Permeability estimates compare well with the low reported permeability from the operator (NPD, 2018), especially in the deeper part of the reservoir.

5.1.6. TOC estimation

The Total Organic Carbon (TOC) of four shale rich formations in the study area has been estimated using two different petrophysical methods and also by utilizing measurements from samples. The methods are based on Passey et al. (1990) and Vernik and Landis (1996) and these are described in chapter 3.3.6. The method from Vernik and Landis (1996) utilizes the density log and constant values for kerogen density, matrix density and fraction of carbon in organic matter. For simplicity, 1.1g/cm^3 is used for kerogen density, 2.6 g/cm^3 is used for matrix density and 67 (constant) is used as the fraction of carbon in organic matter. TOC estimation using the methods from Passey et al. (1990) utilizes the sonic log and the deep resistivity log, in addition to a constant value indicating level of maturity (LOM). According to Passey et al. (1990), a LOM of 7 corresponds to the onset of maturity for oil-prone kerogen, while a LOM of 12 will correspond to the onset of overmaturity for oil-prone kerogen. The available measured data from NPD (2018) often include Hydrogen Index and T$_{max}$, which are parameters useful for identifying kerogen types and maturity. Crossplots between the two parameters are presented in Figure 5.10 and 5.11 and used to identify kerogen type and maturity.

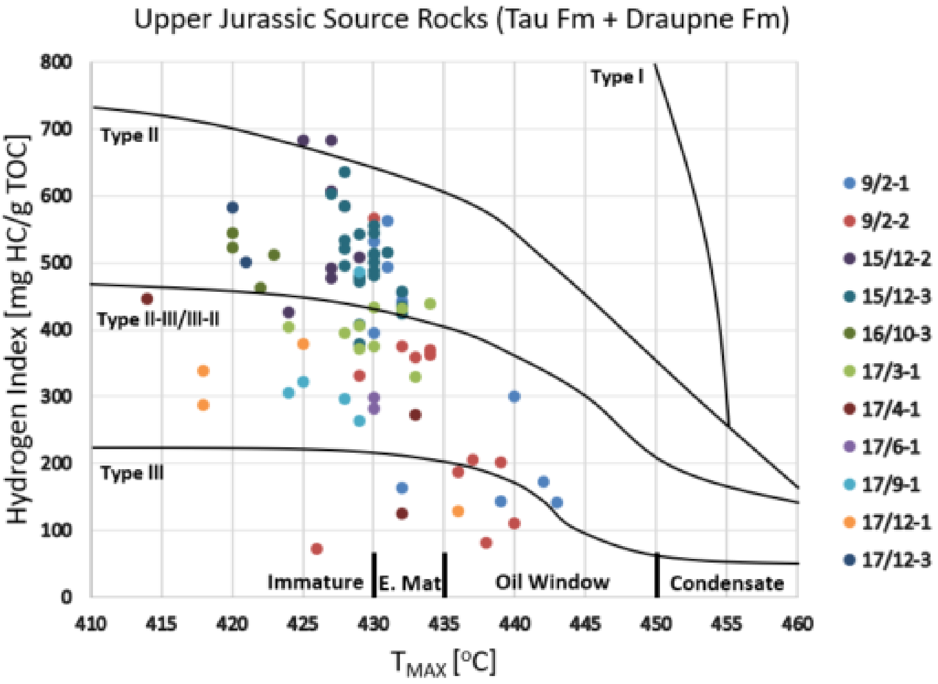

Figure 5.10: T$_{max}$ versus HI plot with samples from Draupne and Tau Formations. The four lines indicate where the different types of kerogen should plot. The areas at the bottom indicate where samples should plot with respect to maturity.

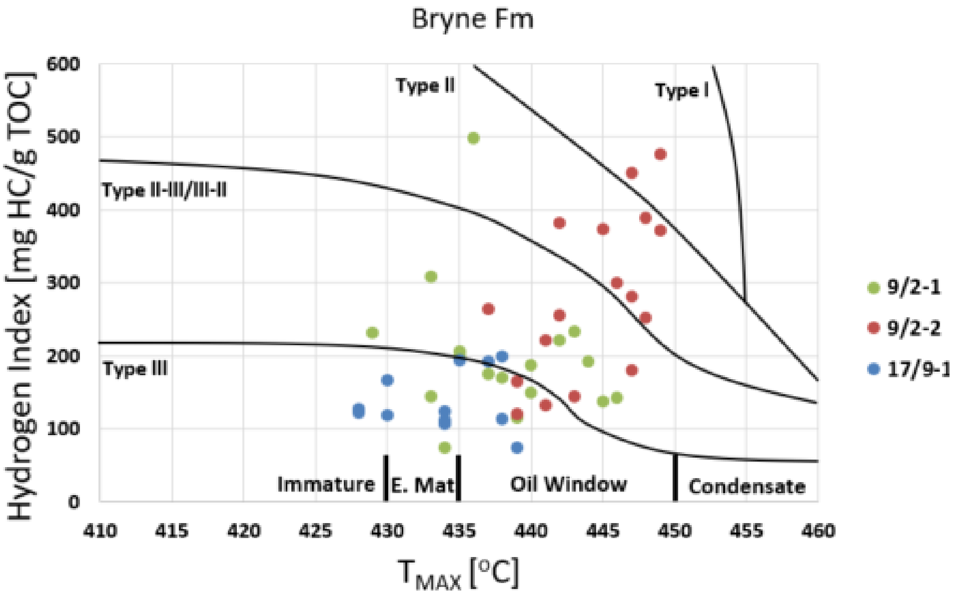

Figure 5.11: T_{max} versus HI plot with samples from Bryne Fm. The four lines indicate where the different types of kerogen should plot. The areas at the bottom indicate where samples should plot with respect to maturity.

The crossplots above are used to constrain LOM used for TOC estimation. All Draupne and Tau Formation intervals are assigned a LOM of 8, due to plotting mainly within the immature and early mature area. The only exceptions are the two wells in Southern Viking Graben (15/3-8 and 15/8-2). These are not plotted due to lack of available data, but due to deep burial and reports indicating oil window (NPD, 2018), a LOM of 11 is applied. For the Bryne and Fjerritslev Formations a LOM of 8 is chosen for all intervals except in well 9/2-1 and 9/2-2. From both the Bryne Formation crossplot (Figure 5.11) and the actual burial depths a higher maturity is indicated in this part of the Egersund Basin, and consequently a LOM of 10 is applied here. A significantly lower maturity in the other wells is justified by the T_{max} values from 17/9-1, along with the relatively shallow burial outside of the Egersund Basin.

In terms of TOC richness and consequently kerogen quality, the following terminology is used in this assessment (Schlumberger, 2018):

- 0.5-1 wt.% is considered poor
- 1-2 wt.% is considered fair
- 2-4 wt.% is considered good
- 4-12 wt.% is considered very good

The results from the two estimation methods and the available measured data are presented in table 5.5. Both methods and the measured data are shown in the well log example from Tau Formation in well 9/2-1 (Figure 5.12).

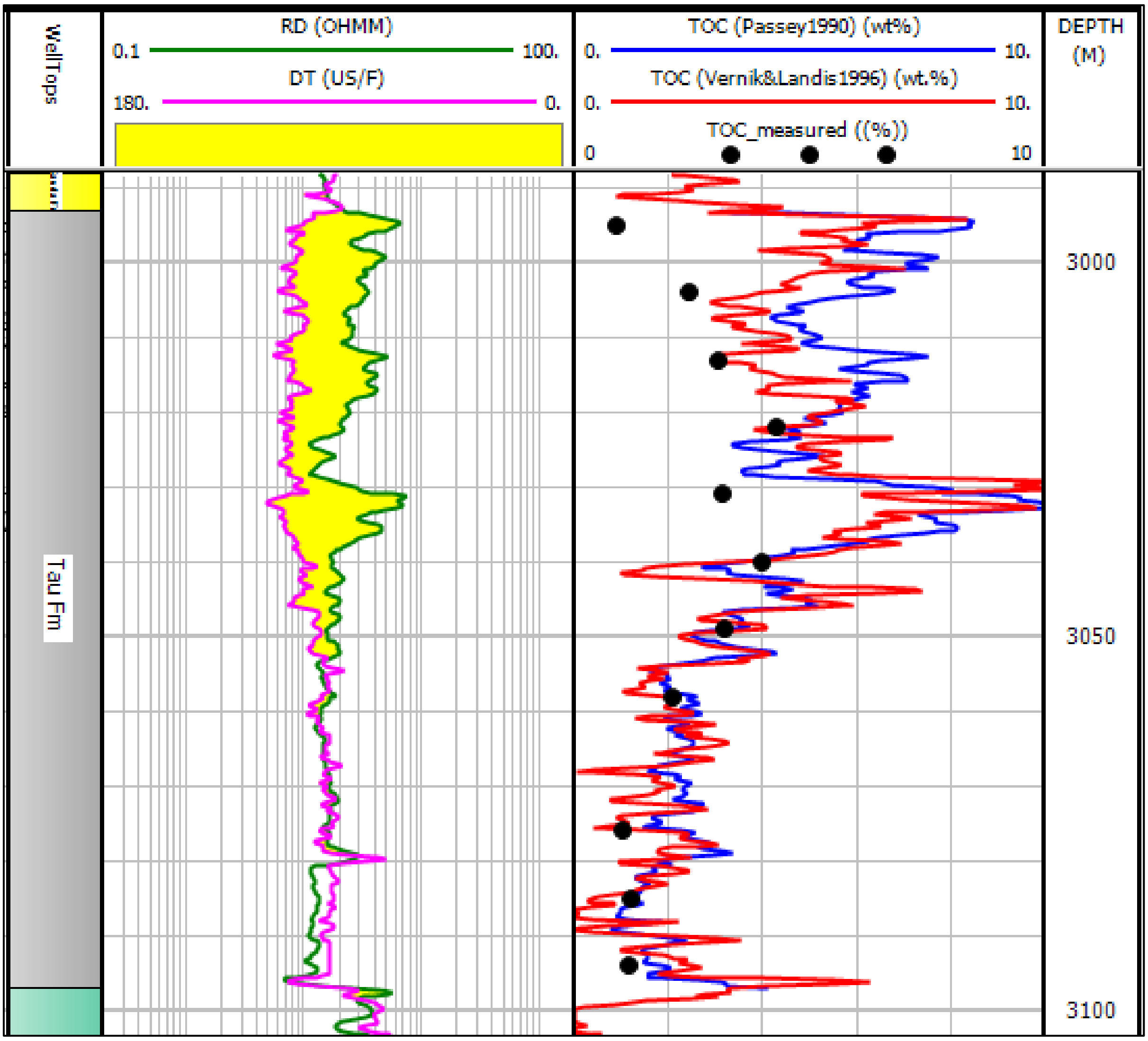

Figure 5.12: Well panel from Tau Formation of well 9/2-1 showing separation between the deep resistivity and velocity curves in the organic-rich part. The estimated TOC using the Passey et al. (Passey, et al., 1990) and Vernik and Landis (Vernik & Landis, 1996) methods are also shown in a panel with measured TOC.

Table 5.5: Results from TOC estimation using methods from Passey et al. (1990) and Vernik and Landis (1996) and comparison with measured data from samples made available by NPD (2018). All TOC values in weight percent. Depths in m MDKB.

Well	Depth	Avg. TOC (wt.%) (Passey et al, 1990)	Avg. TOC (wt.%) (Vernik and Landis, 1996)	Avg. Measured TOC (wt.%) (NPD, 2018)
Draupne Formation				
15/12-2	2703-2765	6.65	8.05	8.12
15/12-3	2998-3142	7.65	5.59	8.65
15/12-22	2764-2799	2.66	5.72	-
15/12-23	2966-3013	1.79	4.49	-
16/8-3 S	2570-2656	4.79	7.28	-
16/10-3	2501-2521	4.58	5.88	4.55
17/4-1	2122-2217	4.85	5.78	4.21
15/3-8	3933-4073	3.23	3.76	-
15/8-2	3763-3839	1.86	2.69	-
Tau Formation				
9/2-1	2993-3097	3.98	3.66	2.40
9/2-2	2957-3062	3.69	4.26	4.35
9/2-11	2492-2574	1.97	1.68	-
17/3-1	2311-2339	10.06	7.85	7.87
17/6-1	2489-2542	10.31	5.05	7.24
17/9-1	2135-2205	8.88	9.61	7.01
17/12-1	2167-2215	8.72	12.16	6.81
17/12-3	2236-2288	7.14	8.54	5.61
17/12-4	2149-2198	5.21	6.68	-
Bryne Formation				
9/2-1	3309-3601	3.02	3.16	3.21
9/2-2	3230-3475	2.34	3.86	6.98
9/2-11	2761-2861	1.68	2.70	-
17/3-1	2410-2440	6.34	8.92	-
17/6-1	2647-2726	4.81	3.45	-
17/9-1	2237-2835	3.22	2.24	1.12
17/12-1	2306-2410	5.76	10.20	-
17/12-3	2396-2617	2.84	6.77	4.29
17/12-4	2298-2398	4.16	5.79	-
Fjerritslev Formation				
9/2-1	3601-3685	2.16	2.39	1.43
9/2-2	3475-3551	1.21	0.4	-
17/6-1	2726-2800	4.24	0	-
17/9-1	2835-2992	4.30	4.86	0.76
17/12-4	2398-2439	1.15	2.30	-

There are great variations in availability of measured TOC data for the studied wells, making comparison and quality control with the two estimation methods difficult. The individual average values for measured TOC are also based on different number of data points. Generally, average measured values for Bryne and Fjerritslev Formations contain fewer data point compared to Tau and Draupne Formations. The two well log estimation methods are based on a totally different level of data point density, with about six data points of every meter interval.

Using the introduced TOC richness and kerogen quality terminology an effective comparison can be done. Among the 11 wells with available measured data from Draupne and Tau Formations all estimates fall into the same classification as the measured average. The only exception is the estimate from the Passey method in well 9/2-2 (Tau Formation) which estimate "good" quality compared to "very good" from measurements. For Bryne and Fjerritslev Formations only one of six intervals yield estimates with similar classification as the measured values. Compared to the 17 measured average values, the Passey method overestimates in eleven and underestimates in six intervals. Using the method from Vernik and Landis, the result is overestimation in ten and underestimation in seven intervals.

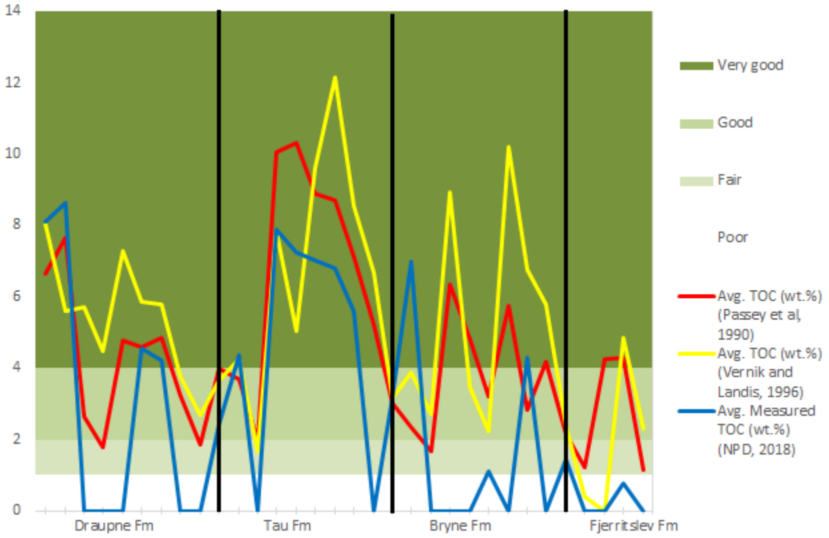

Figure 5.13: Diagram with measured TOC and TOC estimates for each of the four relevant formations. Template with shades of green indicates TOC richness classification. All value in wt.%. No measurement available is indicated by the value 0.

Figures 5.12 and 5.13 illustrate how the methods predict TOC relative to measured data. Excellent correlation is observed for both methods in the less organic-rich lower part of Tau Formation in well 9/2-1 (Figure 5.12). In the organic-rich upper part both methods overestimate significantly. However, both methods efficiently mimic the relative trends in the data. Similar conclusion can be drawn from Figure 5.13, where data from each formation in each well are averaged. The Passey method shows a better correlation, but both methods quite efficiently recreate the trends observed in the measured data.

5.2. Discussion

This subchapter discusses the reservoir quality, depositional environment and hydrocarbon potential of individual formations of Jurassic age. Reservoir potential parameters for three reservoir units are presented in Figure 5.14.

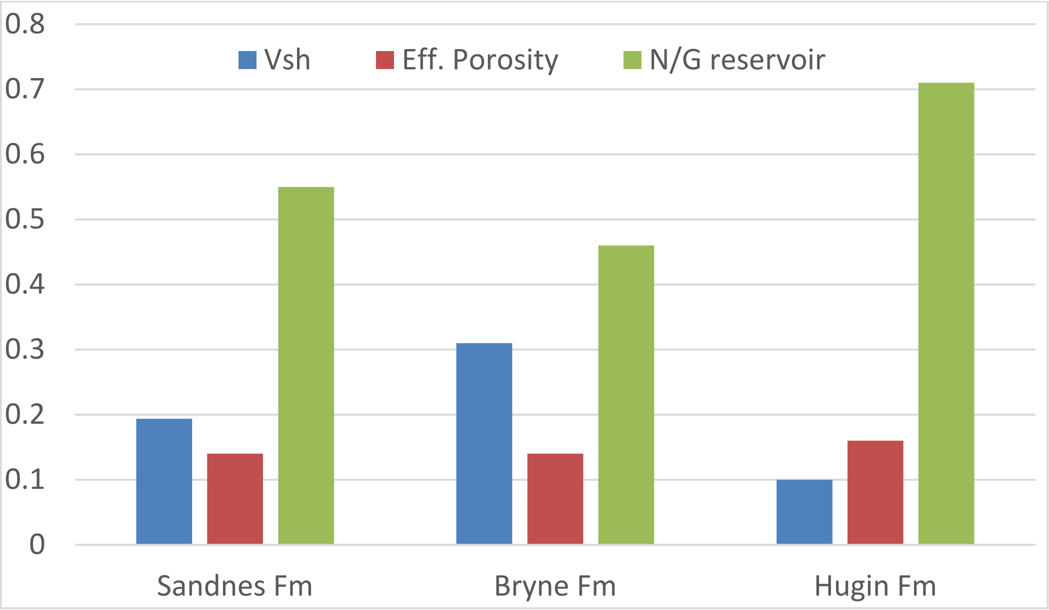

Figure 5.14: Average reservoir properties for the three formations with reservoir potential in this study.

5.2.1. Jurassic reservoirs

Within the Jurassic succession of the main study area (excluding Southern Viking Graben), main reservoir targets and discoveries are found in the Sandnes Formation. Different reservoir formation combinations, consisting of Sandnes and Bryne Formations, are found in block 17/12. Cores from both Sandnes and Bryne Formations are shown in Figure 2.6. The initial observation is that the Sandnes Formation is cleaner than the Bryne Formation. A similar observation can be made from the Hugin Formation (Figure 2.7). The reservoir potential is considered best in the Hugin Formation, closely followed by Sandnes Formation and lowest in Bryne Formation, based on the main parameters (Figure 5.14). However, as the results from the analysis of Bryne Formation reservoirs showed, excellent reservoir properties are found in sands interbedded in shales locally in the Bryne Formation. Despite sufficient reservoir potential in the Jurassic succession, most wells disappoint in terms of hydrocarbon saturation.

5.2.1.1. Sandnes and Hugin Formations

The Sandnes and Hugin Formations are roughly time equivalent successions deposited during Bathonian-Oxfordian times. Both are transgressive units deposited during eustatic sea-level rise and rift-related subsidence and subsequent flooding of the Southern Viking Graben (Hugin Formation) and Egersund Basin/Ling Depression (Sandnes Formation). The net-transgressive Jurassic succession resulted in a change from continental (Skagerrak Formation) to fluvio-deltaic and floodplain environments (Bryne/Sleipner Formations) to prograding coastal environments (Sandnes/Hugin Formations) and eventually open marine settings (Tau/Draupne Formations), visualized in Figure 5.15. Both Sandnes and Hugin Formation are generally composed of stacked shoreface deposits (Kieft, et al., 2010; Mannie, et al., 2016).

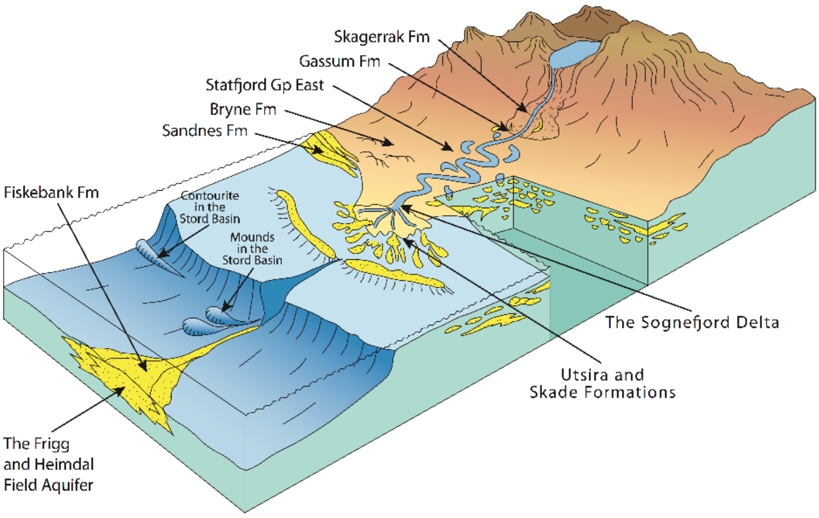

Figure 5.15: Depositional environments of selected formations found in the North Sea. From Halland et al. (2014).

The overall clean nature of both formations yields low and continuous blocky responses from the gamma ray log. The Sandnes Formation generally has its highest gamma ray responses in the lowest part and gradually decreasing upwards with lowest responses in the upper part. This type of funnel shape should indicate an upward decrease of shale content from the lower part and most likely an upwards coarsening succession. Shallow marine sandstones are often recognized by their upward coarsening character (Bjørlykke & Jahren, 2015). Mannie et al. (2014) studied the Sandnes Formation and describes an upwards coarsening trend, ranging from the offshore transition zone near the base to upper shoreface deposits near the top, in well 9/2-1 (Figure 5.16b).

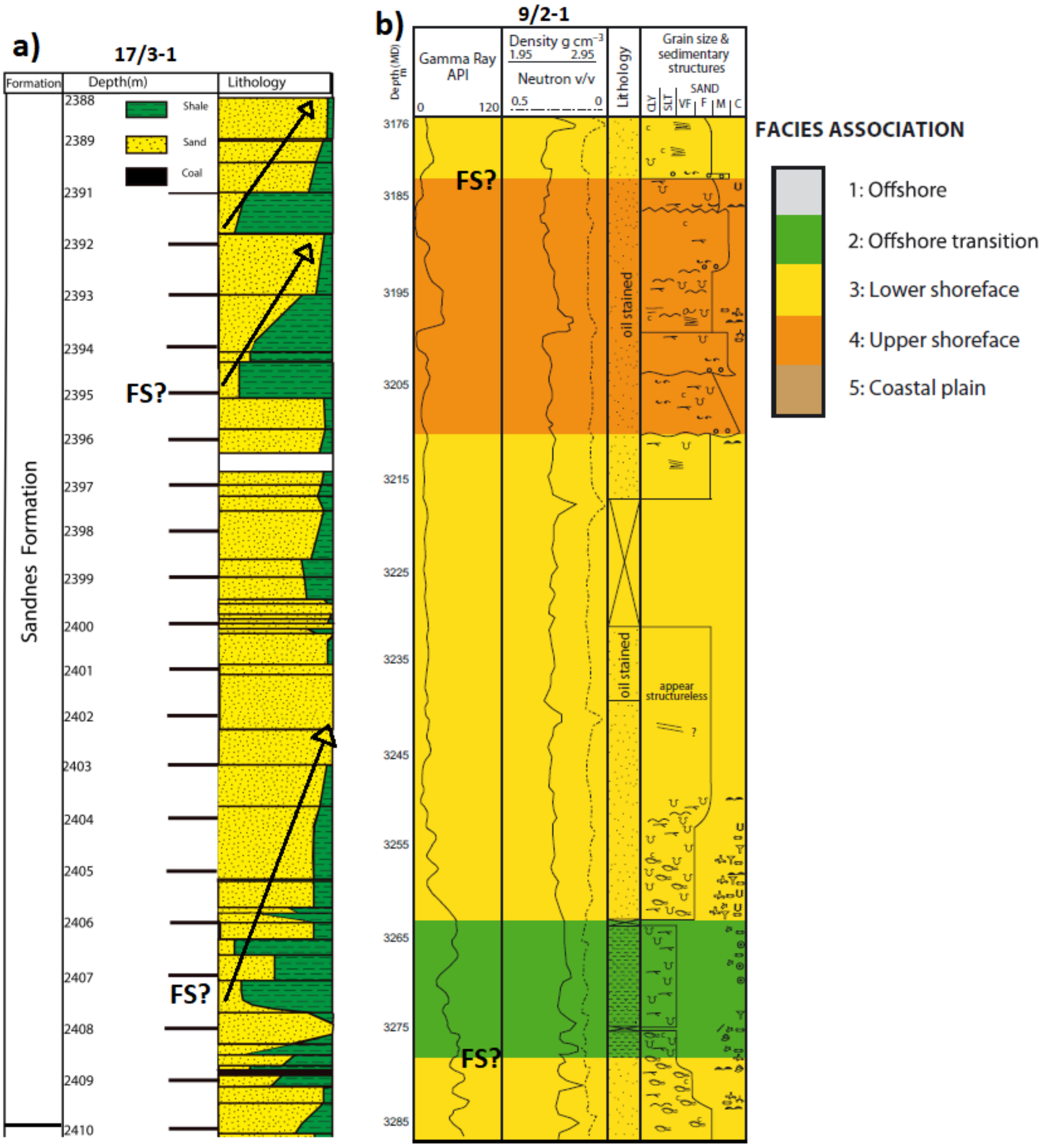

Figure 5.16: A) Lithology log of Sandnes Formation, well 17/3-1 (modified from Javed, 2013). B) Core and well logs with facies associations of Sandnes Formation, well 9/2-1 (modified from Mannie et al., 2014). FS: possible flooding surface.

The offshore transition zone in the Sandnes Formation is described as a bioturbated, carbonaceous siltstone with thin hummocky cross-stratification, indicating low rates of deposition in a low-energy environment, with episodic input from storm action. Lower shoreface is the dominating facies association in the Sandnes Formation. It is recognized by hummocky cross-stratified and bioturbated sandstones evolving into well-sorted massive sandstone units. These signatures are indicative of deposition during storm events, bioturbation between storms, and eventually extensive reworking, sorting and deposition above fair-weather wave base. Following the lower shoreface are deposits indicating upper shoreface. Depositional signatures include upward-fining, erosion-based, poorly sorted sandstone evolving into a medium-grained, cross-stratified sandstone. Variabilities in both sorting and energy conditions point to a combination of fair-weather wave reworking and fluvial input, possibly also channel migration and abandonment (Mannie, et al., 2014). Transitions from higher to lower energy conditions (e.g. lower shoreface to offshore transition or upper shoreface to lower shoreface) should represent flooding surfaces in transgressive successions such as the Sandnes Formation. The facies association and associated depositional environment shows good correlation with the results from petrophysical analysis. Shale volume is increasing, while porosity and permeability is decreasing with depth in well 9/2-1 as a result of sorting and grain sizes controlled by the depositional environment. Higher porosity and permeability would be expected if not for the deep burial and sufficient temperature resulting in cementation.

Some similar trends are observed in the Sandnes Formation of well 17/3-1 (Figure 5.16a; Figure B.4). The base of the formation is dominated by coastal/tidal facies with alternating shale and sand rich intervals, and occasional presence of coal. The subsequent erosional base and well-sorted massive sandstone shows a clearly upwards coarsening trend, as the formation transitions into upper/lower shoreface environments. Javed (2013) identified glauconite in the formation, supporting a shallow water shelf environment. Two abrupt changes from medium sand to poorly-sorted shaley sand follows. This is indicative of a new period of fluvial input in an upper shoreface/coastal environment. The uppermost two meters show a clean sandstone. This correlates with the neutron/density crossover and the estimated gas column from the petrophysical analysis. Shoreface dominated deposition, with only minor influence of shaley tidal deposits, yield a net-to-gross above 0.9 and good to excellent porosities and permeability from both measured data and petrophysical analysis.

Kieft et al. (2010) reports similar shoreface-dominated deposition for the Hugin Formation. Evidence include funnel shaped gamma ray log intervals, indicating upwards coarsening sequences (Figure B.10). Minimum three upwards coarsening sequence can be interpreted from the gamma ray log of well 15/12-2 (Figure B.10). They are identified by distinct spikes which are assumed to represent transgressive event. Such transgressive event-related gamma ray peaks are identified in both Hugin and Sandnes Formations in several wells. They often coincide with neutron-density shale crossover and porosities towards zero, possibly resulting in reservoir compartmentalization. The following decrease in gamma ray is believed to be a response to a shift towards higher energy environment with better sorting and larger grain sizes (e.g. transition from offshore transition to lower shoreface). Such transgressional surfaces are expected in a prograding coastal environment. The more continuous low gamma ray response and neutron-density negative separation (sand crossover) in well 15/12-22 (Figure B.11) indicate that only deposits from an upper/lower shoreface environment is preserved. The continuous log responses indicate clean, massive sandstone which has been extensively reworked and well-sorted during deposition in a high energy environment, e.g. above fair-weather wave base (Kieft, et al., 2010). Kieft et al. (2010) concludes that the most prospective reservoir intervals in the Hugin Formation are likely to be in the upper part where the shallow marine deposits are best developed.

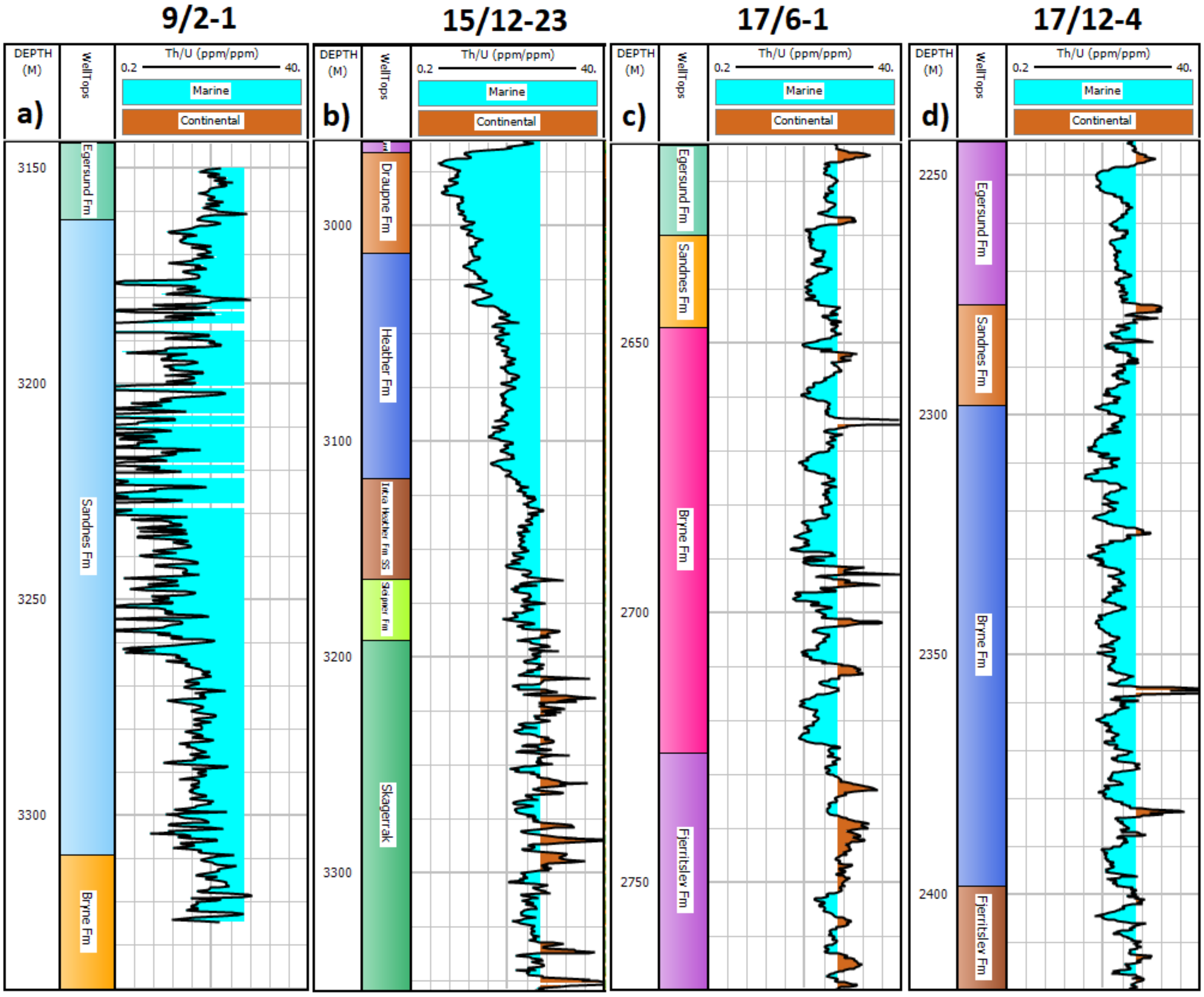

Figure 5.17: Thorium/Uranium-ratio from spectral gamma log in well a) 9/2-1, b) 15/12-23, c) 17/6-1 and d) 17/12-4. Note that different formations are included in each plot. Note also different colors for similar formations.

The spectral gamma logs, and especially the Th/U ratio derived from them, are used for additional indication of depositional environment (Figure 5.15). Klaja and Dudek (2016) proposed a Th/U ratio of 7 as a suitable separation between marine and continental conditions. Figure 5.17b clearly replicate the net-transgressive trend from Triassic continental deposition (Skagerrak Formation) to open-marine deposition in Upper Jurassic (e.g. Tau/Draupne Formations). Ratios observed in wells 9/2-1, 17/6-1 and 17/12-4 support deposition in more or less marine environments throughout the Sandnes Formation. Low ratios in well 9/2-1 indicate marine-dominated deposition, while the increasing ratio towards the top of the formation correlates with the landwards shift from lower to upper shoreface. Similar upwards increasing Th/U trend is observed in well 17/12-4, but with significantly higher values. High ratios (but still below 7) are observed in well 17/6-1. These relatively high ratios would place the deposition of Sandnes Formation in these two wells more towards a transition zone between marine and continental conditions. However, this contradict the south-eastward transgression trend observed in this area (Kieft et al., 2011; Mannie et al., 2014). The transgression was diachronous and thus, the Sandnes Formation generally becomes younger from northwest to southeast. Hence, more offshore dominated depositional environments are present towards northwest. Some contradicting trends are expected as a single depositional model are unable replicate the complete study area. The rift- and salt-basin settings observed in the study area controls the local development of accommodation, topography and sediment routing, which in turn are major influencers on facies distribution, reservoir architecture and character (Kieft, et al., 2010; Gawthorpe & Leeder, 2000).

The Sandnes and Hugin Formations show good reservoir properties in all wells, except in well 17/4-1 where the porosity estimates for Hugin Formation are low. Higher reservoir potential and more continuous distribution of reservoirs and pay zones in the upper part of the formation is observed. Compartmentalization is predicted in some wells. Higher gamma ray values and shale volume are typical for the lower part of the formations. This is very much in line with the literature (Kieft, et al., 2010; Mannie, et al., 2014).

Only one significant discovery is made in the Sandnes Formation among the studied wells. This discovery, named Yme, was made in well 9/2-1. No gas was present in this discovery. Top of oil is recognized by a drop in the density log (negative neutron-density separation) and rapidly increasing deep resistivity at 3174 m MDKB. This depth coincides with a sharp reduction of shale volume and consequently a sharp increase of porosity, indicating top of reservoir. The exact same depth for top Jurassic sand (reservoir) and top oil in reported by NPD (2018). A large fall in deep resistivity at 3233 m MDKB is interpreted to represent the OWC (oil-water contact). NPD (2018) reports that an exact OWC is not determined but believed to situated between 3230 and 3239. Thus, a minimum oil-column of 56 meter is expected. The petrophysical analysis predicts a ~32m pay zone in the reservoir. This is less than the total oil-column due to the maximum 60% water saturation cutoff used in this study. 1-2 m spikes in gamma ray, density and neutron logs are observed at 3177, 3197, 3218 and 3242 m MDKB. Zero porosity and permeability are predicted in the middle two of these zones, dividing the reservoir (and oil column) into at least three compartments. Reservoir properties and oil saturation are predicted and reported to decline for each compartment. Two drill stem tests in the lowermost compartment failed to produce reservoir fluids due to low permeabilities. A third drill stem test in the uppermost compartment was successful due to sufficient permeability (NPD, 2018).

5.2.1.2. Bryne Formation

The coastal plain depositional environment of the Bryne Formation is complex and heterogeneous. Mannie et al. (2016) reports the presence of fine- to medium grained rooted sandstone, coal, bioturbated organic-rich mudstones, fissile shales and interbedded, cross-stratified sandstones. These different facies are recognized by a combination of well log signatures. Coal layers are represented by very low readings on the density log ($<2 g/cm^3$). Sandstone facies are generally recognized by low gamma ray values and often a funnel-shaped log curve (e.g. Figure B.5). A negative separation between neutron and density log (sand crossover) is also typical. The organic-rich silt- and mudstones found in the Bryne Formation show higher gamma ray and density reading than the associated sands and coals

(Mannie et al., 2014). The Bryne Formation succession penetrated by well 17/6-1 (Figure B.5) contains good examples of the discussed well log signatures. Low density, interpreted to be coal, is observed at 2650, 2655-2658, 2674 m MDKB. Low value, funnel-shaped gamma ray log signatures together with negative neutron-density separation (or overlap) are recognized at several depths. Most noticeable are the intervals at 2664-2667 and 2683-2704 m MDKB. Very low gamma ray indexes are assigned to these intervals, resulting in very low shale volume and also high porosity estimates. The petrophysical analysis predict excellent reservoir properties in the second interval, with a net/gross ratio of 1. Compared to the overlying shallow marine Sandnes Formation reservoir, lower shale volumes and higher porosities are predicted in the Bryne Formation reservoir. NPD (2018) confirms better reservoir sand development in Bryne Formation compared to Sandnes Formation in well 17/6-1. The rooted sandstones present in the Bryne Formation are interpreted as coastal-plain deposits. Best reservoir properties are encountered in the cross-bedded sandstone, with ripples and occasional erosive base, indicating deposition in fluvial or deltaic distributary channels (Mannie, et al., 2014). A continental depositional environment interpretation for the Bryne Formation sandstones in wells 17/6-1 and 17/12-4 is supported by high Th/U ratios observed in these intervals (Figure 5.17c and 5.17d). The vertical permeability in Bryne Formation successions are expected to be significantly lowered by the presence of coaly layers. Potential low connectivity between reservoir sands deposited in distributary channels lower the prospectivity of the formation, regardless of excellent reservoir properties locally. Overall, the Bryne Formation sequence comprises a transgressive succession, with increasing marine influence and sandstone development upwards. Hence, the highest hydrocarbon prospectivity is expected in the upper part of the formation.

Among the studied wells, one significant discovery is encountered in the Bryne Formation, namely well 17/12-4 (Vette) (Figure 5.5). Top of the oil column is identified at Top Bryne Formation (2298 m MDKB) by increasing deep resistivity response and low densities. Good quality sands are predicted at 2307-2314, 2327-2332, 2348-2360 and 2374-2389 m MDKB, due to low gamma ray readings and clear negative separation of the neutron-density log (sand crossover). Petrophysical analysis performed in this study predicts a more or less continuous oil column down to a proposed oil-water contact (OWC) at 2332 m MDKB. This correlates well with the reported main OWC by the operator at 2334.5 m MDKB (NPD, 2018). Oil-bearing sands with possibly three OWC’s are reported below the main OWC, but inconclusive pressure data could not propose exact OWC’s. The petrophysical analysis similarly predict the presence of hydrocarbons in these sands, but high water saturation means they are not included in the predicted 27 meters pay zone.

5.2.2. CO_2 storage potential

Halland et al. (2014) provide a detailed overview of the work being done on CO_2 storage in Norway and aims to identify safe and effective areas for long-term storage of CO_2. Concepts and results relevant for this study are presented below.

A typical evaluation process for CO_2 storage sites is shown in Figure 5.18. Depending on many of the same geological properties as for an oil/gas reservoir, several types of geological formations may provide CO_2 storage opportunities. CO_2 is injected as a supercritical fluid (high temperature and high pressure) and will migrate within interconnected pore spaces, similar to other fluids (oil, gas, brine). Different combinations of five main trapping mechanisms are expected to store CO_2 within a reservoir. Stratigraphic traps or structural traps, or a combination, are the main initial trapping mechanisms, similar to classic hydrocarbon traps. Trapping mechanisms on smaller scales includes residual, dissolution and mineral trapping. Residual trapping means that the capillary pressure of water traps CO_2 in small pores. Increasing pressure from water after injection will immobilize, and eventually dissolve the CO_2 in the brine or oil present in the reservoir. Mineral trapping may occur, depending on reservoir rock mineralogy, when dissolved CO_2 react chemically with adjacent rocks to form stable minerals. This is considered the most secure CO_2 trapping mechanism, but it is a very slow process as mineral formation may take thousands of years.

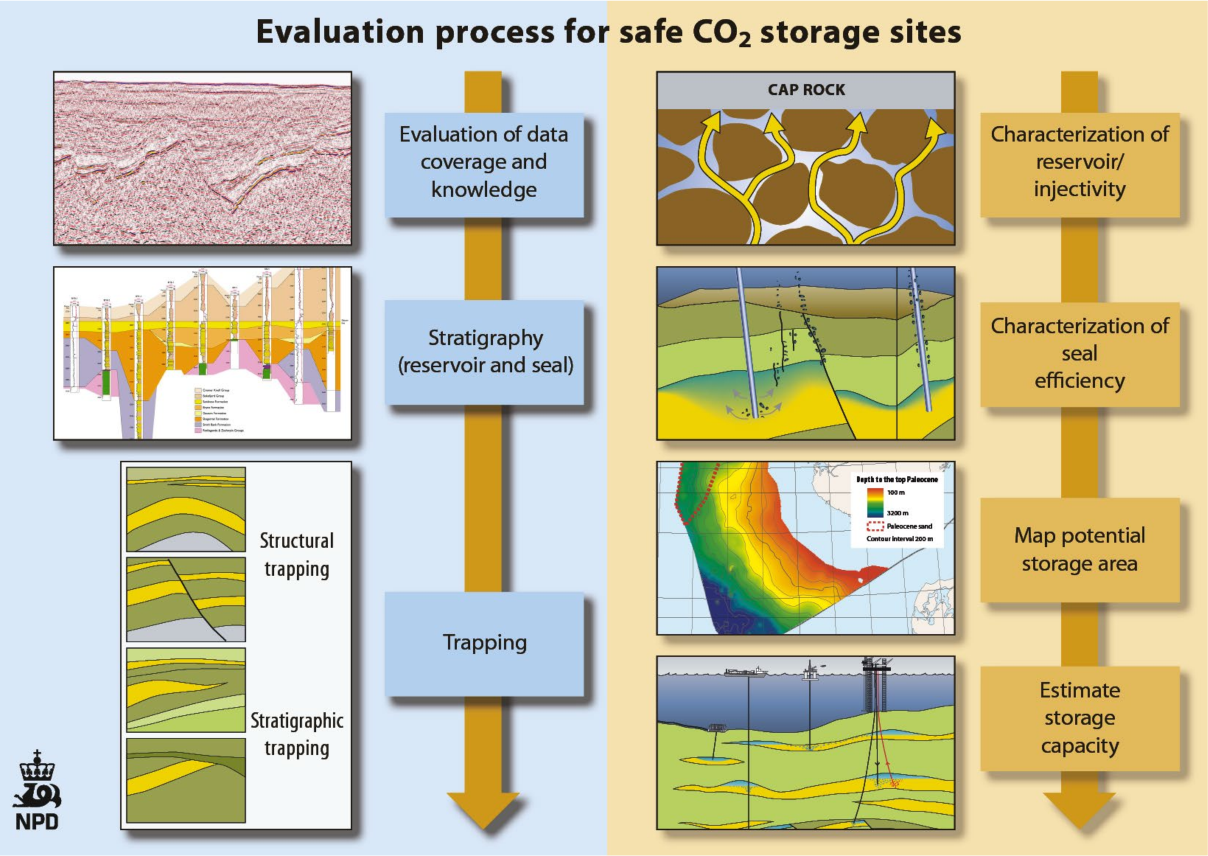

Figure 5.18: Typical approach for assessing the suitability of geological formations for CO_2 storage (Halland, et al., 2014).

Characterization of aquifers and structures with potential for CO_2 storage is based on the following criteria:

- Reservoir quality

  - Capacity: based on parameters as rock volume, structuring, traps, pore pressure, depth and porosity.
  - Injectivity: based on parameters as pore pressure, depth, reservoir heterogeneity, thickness and permeability.

- Sealing quality
  - Seal: based on number of sealing layers, properties of seals (pressure barrier, thickness) and composition of seal (clay content, homogeneity)
  - Fracture of seal: based on presence and magnitude of faults (throw distance, tectonic activity) and other seal breaks as sand injections, slumps or gas chimneys.

Storage capacity is calculated using the following formula (beyond the scope of this thesis):

$$\mathrm{M_{CO_2}} = \mathrm{V_b} \times \Phi \times \mathrm{N/G} \times \rho_{\mathrm{CO_2}} \times \mathrm{S_{eff}} \qquad \text{Eq. 5.1}$$

Where M_{CO2}: mass of CO_2, V_b: bulk volume, Φ: porosity, N/G: net-to-gross ratio, ρ_{CO2}: density of CO_2 and S_{eff}: storage efficiency factor.

The workflow used for assessing CO_2 storage potential acknowledges the importance of reservoir characterization studies, as performed in this study. Porosity and permeability predictions from petrophysical analysis, along with regional compaction trend predictions, prove very useful for evaluating reservoir capacity and injectivity. Discoveries/predictions of oil and gas reservoirs are indirect proof of seal integrity, as the present hydrocarbons have been kept within the reservoir for a long time.

Halland et al. (2014) introduces the Bryne and Sandnes Formations aquifer as the sandy sequence made up of the Jurassic Bryne and Sandnes Formations with occasional contact with the sands of the Triassic Gassum and Skagerrak Formations. Permeability in the Sandnes Formation and lateral and vertical communication in the Bryne Formation are parameters considered to be uncertain, similar to the conclusions of this study. Still, sufficient reservoir capacity and injectivity are predicted, and the Bryne Formation and some of the Triassic sands are expected to contribute to the active aquifer volume. The total aquifer capacity is calculated with an estimated 440 Gm^3 total pore volume, 1700m average depth, 150 mD average permeability and a storage efficiency of 4.5%. This yields an aquifer storage capacity of 14 Gt, and a range of 0.5-2 Gt for individual prospects.

An Egersund Basin specific case study was performed on the Bryne and Sandnes Formation aquifer by Halland et al. (2014). A reservoir simulation was run on a segment (48km x 62km) within the Egersund Basin to test the estimated storage capacity and reveal migration paths. Variations of 1-3 injection wells and injection rates from 2-10 MSm^2 CO_2/year over 50 years were simulated along with permeable/impermeable fault scenarios. Model and relative permeability curves from the Frigg field was used with residual CO_2 saturation of 0.3. The reservoir simulation estimated the following storage capacities (Halland, et al., 2014):

- 9 bar reservoir pressure buildup by 1 injector: 180 GSm^3 or 0.36 Gigatons.
- 26 bar reservoir pressure buildup by 3 injectors: 546 GSm^3 or 1.1 Gigatons.

The study concludes that open/closed faults only affect the distribution of the CO_2 plume, and not the volume of CO_2 injected.

5.2.3. Jurassic source rocks

5.2.3.1. Tau and Draupne Formations

The Tau and Draupne Formations are roughly time equivalent successions deposited during Oxfordian-Tithonian times. Both are deposited in marine environments during high eustatic sea-level present in the transgression observed throughout the Jurassic. Marine origin is supported by low Th/U ratios (Figure 5.17b). The high organic content is initially formed by photosynthesis producing algae in the photic zone and higher organisms which feed on algae. The organic-rich nature of Tau and Draupne Formations prove very limited deposition of clastic material, which is an important requirement for formation of a rich source rock. Additional requirements include stagnant water and lack of oxygen (anoxia/dysoxia) (figure 5.19). Such conditions will exclude most life forms and hence bioturbation. Therefore, net accumulation of organic matter in sediments is dependent of the relationship between productivity and bionic breakdown and oxidation (Bjørlykke, 2015d).

This relationship is highly affected by local differences and parameters as water depth, currents, distance from shoreline and locally high productivity (e.g. upwelling). Optimal preservation of marine organic matter is expected to result in oil-prone kerogen type II. Kerogen type zonation in Figure 5.10 indicates that conditions for optimal preservation were not present all over the study area, resulting in a mixture of type II and III kerogen, also within the Tau Formation in individual wells. High quality kerogen type II is most prominent in wells located in the Egersund Basin and Southern Viking Graben and in the upper part of the formations, which probably indicate stagnant and anoxic bottom water due to large water depths associated with rift-related subsidence.

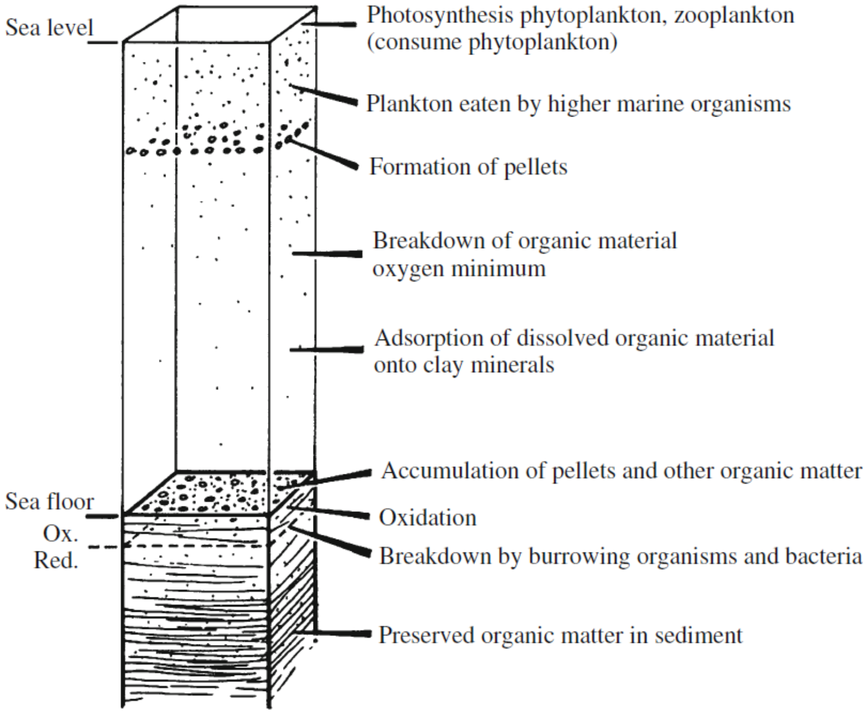

Figure 5.19: Formation of marine source rocks. Note how only a small fraction of the organic matter is preserved (Bjørlykke, 2015d).

Although almost all Tau and Draupne Formation data yield “very good” TOC richness values, a correlation between highest TOC and kerogen type II is hard to see. This would indicate that source rock quality assessments must include proper kerogen type analysis and can not only be based on TOC richness. Demaison (1984) proposed variations can be related to the past degree of oxygenation of the water column, the sedimentation rate and the type of organic matter input.

Compared to surrounding low-organic shales/claystones, the main difference in a source rock is not the mineralogy but the high organic matter content. Well preserved marine organic matter absorbs dissolved uranium from the ocean water which yield high (>~150 API) gamma ray readings (Figure 5.20a). Passey et al. (2010) states the volume of organic matter is roughly twice the TOC percent in a rich source rock since the density of kerogen (1.1-1.4 g/cm^3) is approximately half of a typical clay mineral density (2.6 g/cm^3).

High percentages of organic matter highly affect the acoustic parameters of the rock, including compressional velocity (V_P), shear velocity (V_S), bulk density (ρ) and anisotropy. Velocities tend to drop compared to deep resistivity (ΔlogR), and this deviation proves effective in recognizing intervals with source rock potential (e.g. Figure 5.20a). Densities are observed to drop significantly in the Upper Jurassic organic rich shales in the study area, due to the low density of the present kerogen. V_P of the Tau and Draupne Formations is generally observed to be low and clearly deviates from shale compaction trends (e.g. Draupne Formation in Figure 4.6). Acoustic impedance, the product of compressional velocity and density, shows a nonlinear correlation with increasing TOC (Figure 5.20b). Thus, organic rich source rock yield lower AI than otherwise similar organic-lean claystones and most other rock types. Significant reduction and increase in AI is expected at top and base of organic-rich source rocks, respectively (Løseth, et al., 2011). The example from well 17/6-1 (Figure 5.20a) clearly shows the drop in AI at the top of Tau Formation.

An upwards-increasing profile for the estimated TOC is observed in the Tau Formation in well 17/6-1 (Figure 5.20a). This is a general trend observed for the Upper Jurassic source rock formations in the North and Norwegian Sea (Tau, Draupne and Spekk Formations) (Løseth, et al., 2011).

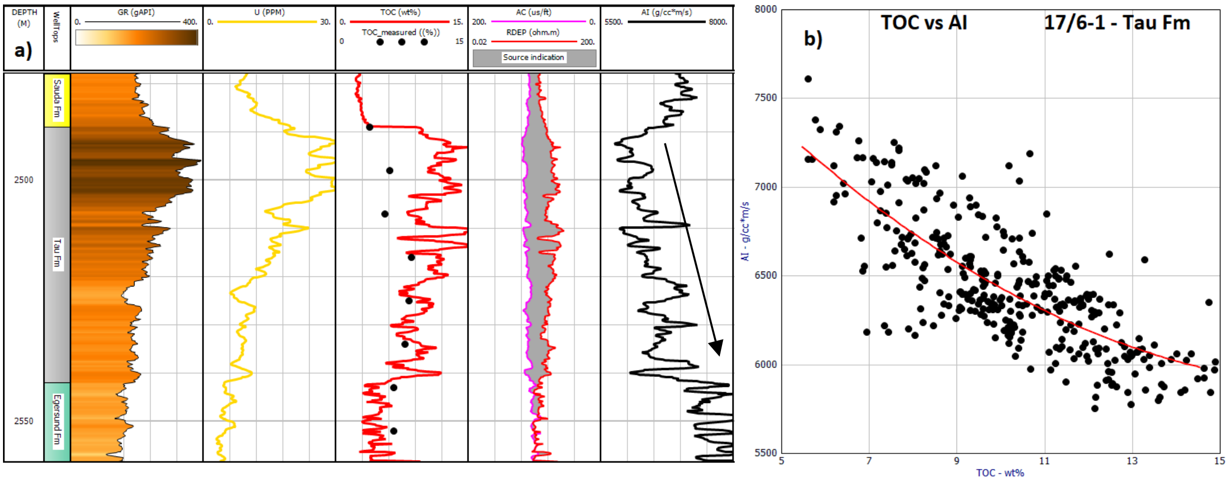

Figure 5.20: a) 17/6-1 well log data b) TOC versus AI crossplot of Tau Formation from 17/6-1.

Variations in TOC profile and content have significant implications for the seismic signature of a source rock. Figure 5.21 demonstrates the expected seismic response of the general TOC profile observed in the Tau/Draupne Formation in this study area.

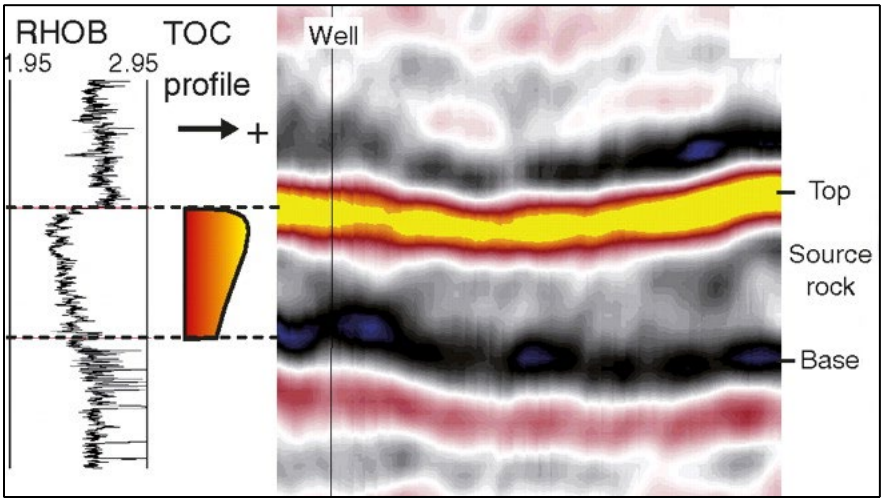

Figure 5.21: Example of density log (g/cm^3), TOC profile and associated near trace seismic section of an Upper Jurassic organic-rich shale (Spekk Formation) (modified from Løseth et al., 2011).

The observed upwards-increasing TOC profile results in an upwards-decreasing AI trend (Figure 5.20). Consequently, the highest seismic amplitude will appear at the top of formation (Figure 5.21). Out of the Draupne Formation penetrating wells in this study (Figure 2.9), the upwards-increasing TOC/gamma ray profile is observed in all wells, except 17/4-1 and 15/3-8. Thus, highest amplitude of the Draupne (and Tau) Formation will generally occur at the top in the study area. This understanding is important to include in a seismic interpretation workflow. This bright amplitude is typically recognized as the Base Cretaceous Unconformity (BCU) in North Sea and Norwegian Sea. Another recognizable feature of top organic-rich source rock units is the distinct AVO Class 4 reflection, characterized by significant drop in AI together with a clear dimming of amplitude with increasing reflection angle (Castagna & Swan, 1997). Dimming with offset is related to the intrinsic anisotropy of organic-rich shales. Increasing TOC and fissility in shales result in significantly higher velocities parallel to the bedding than perpendicular to the bedding (Vernik & Landis, 1996). TOC values estimated for Tau/Draupne Formations in this study can be used to predict where the strongest AVO Class 4 responses will occur. These would include well 15/12-2, 15/12-3, 17/3-1, 17/6-1, 17/9-1, 17/12-1, 17/12-3 and 17/12-4, based on estimated and measured TOC values. However, the assumption of increasing organic content leading to increased amplitudes at source rock interfaces and dimming with increasing offset is only valid for source rock successions thicker than tuning thickness. Løseth et al. (2011) shows that top source rock amplitude dimming occur when thickness decreases to <~20 meter. Hence, nonuniform source rock formation thickness is expected to cause lateral amplitude variations. Most wells included in this study contain Tau/Draupne Formation intervals with thicknesses well above the typical tuning thickness (20m) (Table 4.5). Still, dimming of top source rock reflection is expected in well 16/10-3 (20m), and possibly 17/3-1 (28m) and 15/12-22 (35m).

5.2.3.2. Bryne and Fjerritslev Formations

An assessment of the hydrocarbon potential of the Bryne and Fjerritslev Formations is of interest because very little data from the available wells support oil generation in Tau/Draupne Formation. Some hydrocarbon potential is acknowledged in formations including Sauda, Flekkefjord and Egersund, but they are expected to have similar or lower maturity than Tau/Draupne. Since the major issue is maturity (Figure 5.10), mainly controlled by temperature and depth (geothermal gradient), an evaluation of deeper buried formations with source rock potential is performed.

The complex and heterogeneous Bryne Formation is reported to include various sandstone units, coals and organic-rich mudstones from variety of coastal plain associated facies and depositional environments (Mannie, et al., 2014; Mannie, et al., 2016; NPD, 2018). Consequently, the hydrocarbon generation potential of the formation will be highly facies dependent. The sparse availability of TOC measurements for Bryne and Fjerritslev Formations may provide an average value that is not representative for the full formation. Especially, the heterogenous Bryne Formation is exposed to sampling bias. How the samples are spread in organic-rich shales/coals or sandstones has significant implications. The average estimated Bryne Formation TOC values in this study is therefore expected to be more representative than the measured values. However, it is unknown how precise the estimation of TOC-rich coal layers is and how this affects the estimated average values.

T_{max}-data from Bryne Formation are only available from three wells within the Egersund Basin and Åsta Graben (Figure 5.11). Generally, higher maturities are observed compared to data from Tau/Draupne Formation. The two wells from the Egersund Basin represent the deepest burial of the Bryne Formation in the study area. Shallower buried coals from Bryne Formation in well 17/3-1 are reported to be immature (Wesenlund, 2016). This underlines the importance of depth and temperature in maturity prediction of source rocks. However, in terms of hydrocarbon generation the kerogen type plays an important role. The Bryne and Fjerritslev Formations plot mainly with kerogen type II-III/III-II and type III. This is expected based on the interpreted depositional environments of the coals and organic-rich mudstones. These facies originate from coastal, onshore environments as mire, abandoned fluvial channels and dysoxic lakes/lagoons for Bryne Formation and shallow marine for Fjerritslev Formation. Kerogen derived from continental plants and vegetal debris in similar environments is trademark kerogen type III. Kerogen type III is characterized by low initial hydrogen index (and high initial oxygen index). Kerogen type largely controls what type of hydrocarbon has generation potential in that rock. Low hydrogen index in kerogen type III is less favorable for oil generation compared to type I and II, but generally adequate for gas generation, if buried at sufficient depth (Tissot & Welte, 1978). This means that even though Bryne and Fjerritslev Formations are vertically deeper buried and more thermally mature, even higher thermal maturity is required due to the shift in hydrocarbon type generation potential in kerogen type III compared to the kerogen type II found in Tau/Draupne Formation. Consequently, low thermal maturity and shallow burial depth is the main limiting factor for hydrocarbon generation in Tau/Draupne, Bryne and Fjerritslev Formations in this study area. Significant generation of hydrocarbons from Bryne and Fjerritslev Formations are proved in the Danish part of the Norwegian-Danish Basin (Petersen, et al., 2008) and possibly in the Egersund Basin (Ritter, et al., 1987), where burial depths are sufficient locally. Substantial hydrocarbon contributions from the Bryne Formation-equivalent Sleipner Formation in the Southern Viking Graben are also known (Isaksen, et al., 2002), proving the potential of nonmarine source rock at sufficient burial depths.

Sharp shifts in lithology within the Bryne Formation results in sharp shifts in elastic parameters. Coal layers are identified by very low readings on the density log (<2g/cm^3), low velocities and high estimated TOC in the example from well 17/6-1 (Appendix B.5 and Figure 5.20). Low density, interpreted to be coal, is observed at 2650, 2655-2658, 2674 m MDKB. These intervals correlate more or less with velocity-resistivity deviation (ΔlogR), indicating organic matter/source rock potential. The acoustic impedance of coals and organic-rich mudstones of Bryne Formation is in sharp contrast to overlying sands of the Sandnes Formation and also intra-formation sands. A clear trend of decreasing AI with increasing TOC percent is observed in Figure 5.22b. The AI log in Figure 5.22a similarly show close inverse correlation with the predicted TOC curve. Coal layers are often present at the top of Bryne Formation and the time-equivalent Sleipner Formation and used to differentiate Middle

Jurassic marine sandstones from underlying coastal plain deposits. This creates a somewhat similar upwards-increasing TOC profile as discussed for the Upper Jurassic organic-rich shales. The result is again a sharp contrast in AI which may produce a positive reflection coefficient and a bright reflection observable in seismic. Since Bryne Formation in many cases host clean sandstones in addition to shales and coal, strong reflections can be expected within the formation, given individual facies intervals exceed tuning thickness. This is however hard to decide from the example in Figure 5.22a, since the main sandstone interval is just below tuning thickness and does not produce a large shift in AI. The more homogenous trend in elastic parameters and TOC in the Fjerritslev Formation will result in a less distinct seismic signature. Whether or not the top Fjerritslev Formation is easily recognized in seismic data will generally depend on the facies and elastic parameters at base Bryne Formation.

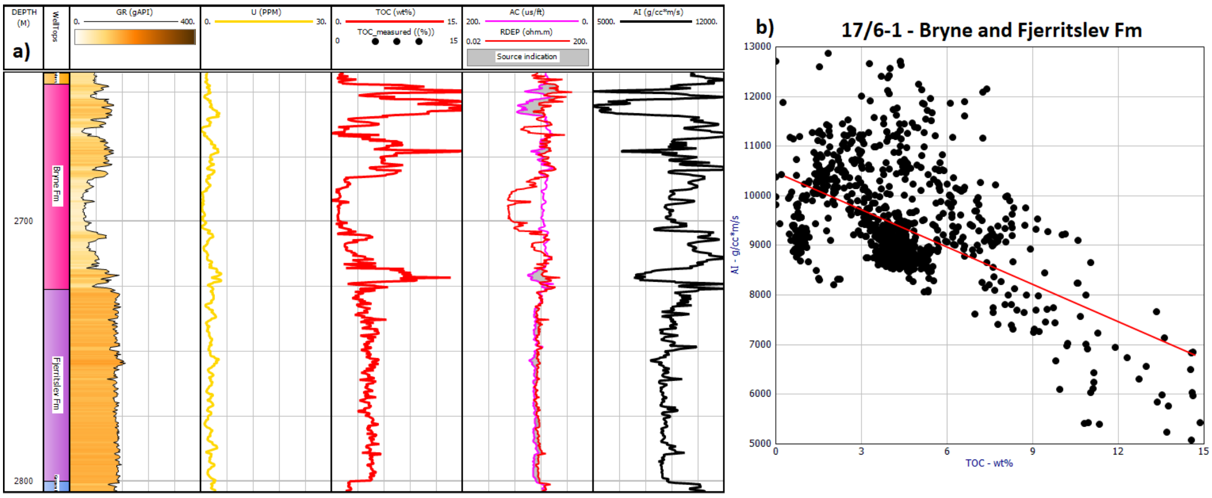

Figure 5.22: a) 17/6-1 well log data b) TOC versus AI crossplot of Bryne and Fjerritslev Formations of well 17/6-1.

Exploration wells tend to be drilled near the top of structures. If there are sufficient depth variations for a potential source rock, it may prove immature at well site and mature in deeper parts down-flank. The generally shallow burial encountered in wells from the study area indicates that local deeper burial of the potential source rocks is required to reach sufficient thermal maturity for oil generation. Such potential kitchen areas are more effectively mapped with seismic data than only a few wellbores. This exploration strategy should be applied to locate mature parts of the Tau, Draupne, Bryne and Fjerritslev Formations in the Central North Sea. Well log and seismic signatures discussed in this chapter should lead to efficient seismic well ties and subsequent mapping of deeper buried parts of the area.

5.3. Uncertainties

A petrophysical analysis heavily relies on different relations and simplifications to predict geological parameters, as directly measured data is scarce. Identified sources for errors and uncertainties in the petrophysical analysis is discussed below:

Acquisition

Aspects of drilling operations and resulting boreholes conditions may result in erroneous well log data. Mechanical damage from the drill bit, such as fractures and holes in the borehole walls. Chemical damage from interactions between drilling fluid and the surrounding rocks (e.g. swelling of smectite as is absorb water from water-based mud). Uneven borehole walls (mainly due to caving in shales) may lead to disconnection between logging tools and the formation. Caliper logs are useful to identify such conditions, but they are not easily corrected for and therefore a potential major uncertainty. This is observed to by an issue in shaly parts of the Bryne Formation, where e.g. hydrocarbon saturation is overestimated due to log reading affected by cavings. Another important source of error is the drilling mud used during drilling, especially oil-based muds which may severely affect density and resistivity logs and complicate identification of oil-water-contact and shows (Mondol, 2015).

Shale volume

Calculation of gamma ray index, and consequently shale volume, is heavily biased by the subjective interpretation of gamma ray baselines for sand and shale. Abnormally high readings from organic-rich shales make determination of shale line difficult. Radioactive sandstones will complicate sand line interpretation. Baseline values are important to include in a study to increase reproducibility. The chosen relation between gamma ray index and shale volume will always be a simplification but a good relation assessment will minimize errors. Comparison with neutron-density log will also minimize errors.

Porosity

Errors and uncertainties from shale volume estimation will be brought into porosity calculation. The neutron-density combination used for estimation of porosity requires a wet clay neutron value and shale density value which may cause inaccurate results.

Water saturation

Water saturation is calculated using Archie’s equation, which relies on several different parameters that may introduce uncertainty individually. Water resistivity is estimated from a brine-saturated interval, but as only minor hydrocarbon saturation may seriously affect resistivity, this parameter may be inaccurate. Cementation exponent, saturation exponent and tortuosity factor usually rely on generalized values based on lithology. This is a major simplification that will provide uncertainties. Formations with high shale volume requires corrections for clay bound water, which may be inaccurate and hence produce uncertainties (Ellis & Singer, 2007).

Permeability

The permeability relations used in this study are highly simplified. Propagation of errors from the porosity and water saturation calculation results in additional uncertainties in permeability calculation. All utilized relationships heavily rely on water saturation, and useless results are expected in fully brine-saturated reservoirs. Parameters as grain surface area, pore shape and pore size are ignored due to no available data.

TOC

Estimation of TOC from well log data is associated with large uncertainties and simplification related to level of maturity, grain density and kerogen density. Still, the methods used should yield correct relative results.

6. Summary and conclusions

This study aims to describe the reservoir and source rocks quality of selected Jurassic formations in the Central North Sea. The Central North Sea has been explored for commercial hydrocarbon accumulations since the 1960s, but large parts of the study area remain immature regarding density exploration wells. Decreasing exploration activity is a result of a several dry wells and noncommercial discoveries. However, most wells prove existing petroleum system constituents, such as cap, reservoir and source rock units.

The maturity of source rocks due to their shallow burial proves to be a critical factor in the Central North Sea. Discoveries, such as Yme, are mainly restricted to areas where the source rock are buried deepest. The Norwegian Petroleum Directorate (NPD) has identified that source rock presence, maturity and migration are the reasons for 46% of the dry or underperforming wells in the North Sea.

The study area comprises the Ling Depression and parts of the Åsta Graben and Egersund Basin, in terms of structural elements. Well log data from 18 exploration wells have been examined and utilized in different geophysical workflows: Comparison of elastic parameters with published compaction trends, rock physics diagnostics, petrophysical analysis and TOC estimation. Geochemical information from 11 wells, available from NPD, has been used to assess kerogen type and maturity and to quality control TOC estimates.

A compaction study is performed to identify and understand zones of mechanical and chemical compaction. By utilizing published depth trends, the transition zones are constrained, and regional uplift estimated. Rock physics relations improve transition zone delineation and cement volume estimation. Information on compaction and uplift is considered when petrophysical analysis is conducted. The petrophysical analysis is carried out to estimate reservoir properties and identify net reservoir and net pay zones in Sandnes, Hugin and Bryne Formations when present. Combinations of well log data is used to estimate TOC in Tau, Draupne, Bryne and Fjerritslev Formations, which are potential source rocks in the area. Trends linked to well locations and corresponding uplift history and depositional environments are observed for several parameters.

The following conclusions are made from this study:

- The mean geothermal gradient of the study area, calculated from available bottom hole temperatures, is 31.5 °C/km. This is noticeably lower than the overall North Sea average of 35-40 °C/km and may have significant implications for source rock maturity and onset of chemical compaction.

- An increase in exhumation towards east and north east is observed. Uplift estimations range from 0 m in quadrants 15 and 16 to maximum 560 m in quadrant 17 and 650 m in block 9/2. Estimations are within acceptable range of published estimates, but increased discrepancy is observed where uplift is assumed to be most extensive.

- Mechanical and chemical compaction regimes are identified in all wells by observing changes of elastic parameters with increasing depth. Current transition zone estimates range from 1320-2260 m BSF with an average of 1706 m BSF. Transition zone estimates adjusted for uplift range from 1700-2260 m BSF with an average of 1942 m BSF. The lowest estimates are generally located in areas with most uplift. About half of the transition zone estimates are within the estimated range of transition zone based on individual geothermal gradients. Wells with low geothermal gradients tend to predict transition zone shallower than the estimated range.

- By utilizing V_s from six wells and density data, a more general transition zone is proposed, represented by a shear wave velocity of 1.45 km/s and shear modulus of 5-6 GPa. Shear wave velocity and shear modulus show a distinct change compared to density at these values. This indication of increasing stiffness correlate with predicted onset of cementation and thus, chemical compaction. Based on individual regression lines two density-velocity-relations are suggested to represent the mechanical and chemical compaction trends for shales in the study area: MC: $\rho = 1.854 + 0.4507V_s$ and CC: $\rho = 2.258 + 0.1765V_s$.

- Reservoir potential is identified in Hugin, Sandnes and Bryne Formations in all wells they were present and sufficient well log data were available. Full formation interval analysis reveals superior reservoir potential in Hugin Formation, with lowest shale volume, highest porosity and highest net-to-gross. Sandnes and Bryne Formations show excellent reservoir potential in some wells (e.g. 17/3-1 and 17/12-3) but generally have a higher shale volume and lower porosities than Hugin Formation. Despite superior reservoir potential, Hugin Formation is water-bearing in all the studied wells (small pay zone is wrongly predicted in 15/8-2).

- Sandnes and Bryne Formations contain one well with a significant discovery each. Well 9/2-1 is one of the Yme Field discovery wells. Well 17/12-4 is one of several discovery wells for the currently noncommercial Vette discovery. Hydrocarbons are trapped by younger impermeable shales and intra-formation coal and shale in the two discoveries, respectively. Reported oil-water contacts are accurately predicted by the petrophysical analysis in both cases. Small pay zones are predicted in both Sandnes and Bryne Formation in several wells, without any reported hydrocarbon accumulations. This is likely a result of high water saturation cutoff values or inaccurate estimation of water saturation.

- Hugin Formation shows relatively large variations in thickness with 356 meters outside the main study area in well 15/8-2 and a range of 11-154 meter in the SW Ling Depression. Low shale volume (<18%) is calculated in all wells. High effective porosity (>15%) and high N/G (>0.75) are also calculated in all wells, except 17/4-1. The reservoir in well 17/4-1 has an average effective porosity just above the cutoff value of 10% and consequently yield very low net reservoir.

- Sandnes Formation has a thickness of 17-26 meter in Quadrant 17 (NE Ling depression and Åsta Graben) and a thickness of 107-147 meter in Block 9/2 (Egersund Basin). Net reservoir intervals vary from 4 to 76 meters. Calculated effective porosity is noticeably lower in the deeper buried reservoirs of well 9/2-1 and 9/2-2, due to considerable cementation. The reservoirs of Block 9/2 still yield highest net/gross reservoir ratio with 0.73-1.

- Bryne Formation is the thickest formation encountered with a gross thickness of maximum 598 meter (17/9-1, Åsta Graben) but with a minimum gross thickness as low as 30 meters (17/3-1, NE Ling Depression). Large gross thickness yield relatively large net reservoirs, up to 202 meters in well 17/12-3. Bryne Formation is complex and heterogenous with facies ranging from clean sandstones to impermeable shales and coal. This lowers vertical permeability and the reservoir potential of the formation as a whole. Still, sandstone intervals encountered in this formation are calculated to host some of the best reservoir quality of this study. Great examples are 2.8% shale volume in upper reservoir in 9/2-1 and 25.6% porosity and N/G of 1 in 17/6-1. All Bryne Formation reservoirs in Quadrant 17 have calculated effective porosities above 21%.

- The Kimmeridge Clay equivalent Tau and Draupne Formations contain mainly organic-rich marine shales. Available geochemical data indicate mainly oil-prone kerogen type II and immature, except early mature in deeper buried part of the Egersund Basin. TOC estimations show best correlation with measured values when using the ΔlogR method. Estimates range from ~2-10 wt.% and an average of 6.6 wt.% using this method. As acoustic impedance is observed to decrease with increasing TOC, and the calculated TOC profile is upwards-increasing, top Tau/Draupne Formation is expected to have a high amplitude seismic reflection. High organic content is associated with high anisotropy and therefore a Class 4 AVO signature is expected at top Tau/Draupne Formation.

- The Middle Jurassic Bryne Formation include layers of coal and organic-rich mudstones of coastal plain-related origin. These facies contain mainly gas-prone type III kerogen. Its younger age result in deeper burial and a greater amount of available geochemical data indicate oil-window. Uncertainty is linked to whether this increased maturity is sufficient for significant hydrocarbon generation from the lower quality kerogen type III. TOC estimation using the ΔlogR method yield a range from ~2-6 wt.% and an average of 3.8 wt.%. Layers of coal and organic-rich facies are generally situated at the top of the formation producing a clear change of AI compared to the overlying the initially shaly sands of Sandnes Formation. Consequently, top Bryne Formation may yield a positive reflection coefficient and distinctive amplitude seismic reflection.

- The Lower Jurassic shallow marine shales of the Fjerritslev Formation have similar kerogen and maturity as the Bryne Formation. TOC estimates range from ~1-4 wt.%

and an average of 2.6 wt.%. Homogenous lithology yields low variations in AI. The deeper burial of the formation compared to Tau/Draupne Formations is most likely not sufficient to generate significant amounts of hydrocarbons due to less organic content and lower-quality kerogen.

References

Asquith, G. & Krygowski, D., 2004. *AAPG Methods in Exploration, No. 16: Basic Well Log Analysis.* 2 ed. s.l.:AAPG Special Publications.

Avseth, P., 2015. Explorational Rock Physics: The Link between Geological Processes and Geophysical Observables. In: *Petroleum Geoscience: From Sedimentary Environments to Rock Physics.* 2 ed. Berlin: Springer, pp. 455-488.

Avseth, P., Dvorkin, J., Mavko, G. & Rykkje, J., 2000. Rock physics diagnostics of North Sea sands: Link between microstructures and seismic properties. *Geophysical Research Letters*, 27(17), pp. 2761-2764.

Avseth, P., Mukerji, T. & Mavko, G., 2005. *Quantitative Seismic Interpretation: Applying rock physics tools to reduce interpretation risk.* Cambridge: Cambridge University Press.

Avseth, P., Mukerji, T., Mavko, G. & Dvorkin, J., 2010. Rock-physics diagnostics of depositional texture, diagenetic alterations, and reservoir heterogeneity in high-porosity siliciclastic sediments and rocks - A review of selected models and suggested work flows. *Geophysics*, 75(5), pp. 75A31-75A47.

Avseth, P. & Ødegaard, E., 2004. Well log and seismic data analysis using rock physics templates. *First Break*, 22(10), pp. 37-43.

Baig, I., 2018. *Burial and thermal histories of sediments in the southwestern Barents Sea and North Sea areas: evidence from integrated compaction, thermal maturity and seismic stratigraphic analysis.* Oslo: University of Oslo. PhD Thesis.

Berstad, S. & Dypvik, H., 1982. Sedimentological evolution and natural radioactivity of tertiary sediments from the Central North Sea. *Journal of Petroleum Geology*, 5(1), pp. 77-88.

Bhuyan, K. & Passey, Q. R., 1994. *Clay Estimation from GR and Neutron-Density Porosity Logs.* Tulsa, Society of Petrophysicists and Well-Log Analysts.

Bjørlykke, K., 1998. Clay mineral diagenesis in sedimentary basins - a key to the prediction of rock properties. Examples from the North Sea Basin. *Clay minerals*, 33(1), pp. 15-34.

Bjørlykke, K., 1999. Principal aspects of compaction and fluid flow in mudstones. *Geological Society, London, Special Publications,* 158(1), pp. 73-78.

Bjørlykke, K., 2015a. Compaction of Sedimentary Rocks Including Shales, Sandstones and Carbonates. In: *Petroleum Geoscience: From Sedimentary Environments to Rock Physics.* 2 ed. Berlin: Springer, pp. 329-337.

Bjørlykke, K., 2015b. Heat Transport in Sedimentary Basins. In: *Petroleum Geoscience: From Sedimentary Environments to Rock Physics.* 2 ed. Berlin: Springer, pp. 273-277.

Bjørlykke, K., 2015c. Production Geology. In: *Petroleum Geoscience: From Sedimentary Environments to Rock Physics.* 2 ed. Berlin: Springer, pp. 545-558.

Bjørlykke, K., 2015d. Source Rocks and Petroleum Geochemistry. In: *Petroleum Geoscience: From Sedimentary Environments to Rock Physics.* 2 ed. Berlin: Springer, pp. 361-371.

Bjørlykke, K. et al., 1986. Diagenesis and reservoir properties of Jurassic sandstones from the Haltenbanken area, offshore mid-Norway. *Habitat of hydrocarbons on the Norwegian Continental Shelf,* pp. 275-286.

Bjørlykke, K. & Jahren, J., 2015. Sandstone and Sandstone Reservoirs. In: *Petroleum Geoscience: From Sedimentary Environments to Rock Physics.* 2 ed. Berlin: Springer, pp. 113-140.

Bjørlykke, K., Ramm, M. & Saigal, G. C., 1989. Sandstone diagenesis and porosity modification during basin evolution. *Geologische rundschau*, 78(1), pp. 243-268.

Bloch, S., Lander, R. & Bonnell, L., 2002. Anomalously high porosity and permeability in deeply buried sandstone reservoirs: Origin and predictability. *AAPG Bulletin*, 86(2), pp. 301-328.

Carmichael, R. S., 1989. *Practical handbook of physical properties of rocks and minerals.* Boca Raton: CRC press.

Castagna, J. P. & Swan, H. W., 1997. Principles of AVO crossplotting. *The Leading Edge*, 16(4), pp. 337-344.

Chuhan, F. A., Kjeldstad, A., Bjørlykke, K. & Høeg, K., 2003. Experimental compression of loose sands: relevance to porosity reduction during burial in sedimentary basins. *Canadian Geotechnical Journal*, 40(5), pp. 995-1011.

Corcoran, D. V. & Doré, A. G., 2005. A review of techniques for the estimation of magnitude and timing of exhumation in offshore basins. *Earth-Science Reviews*, 72(3-4), pp. 129-168.

Cornford, C., 1998. Chapter 11: Source Rocks and Hydrocarbons of the North Sea. In: K. W. Glennie, ed. *Petroleum Geology of the North Sea: Basic concepts and recent advances.* Hoboken: Blackwell Science, pp. 376-462.

Deegan, C. E. & Scull, B. J., 1977. *A standard lithostratigraphic nomenclature for the central and northern North Sea,* London: HMSO.

Demaison, G., 1984. The Generative Basin Concept. In: *Petroleum Geochemistry and Basin Evaluation. AAPG Memoir 35.* s.l.:American Association of Petroleum Geologists.

Demaison, G. J. & Moore, G. T., 1980. Anoxic Environments and Oil Source Bed Genesis. *AAPG Bulletin*, August, 64(8), pp. 1179-1209.

Doré, A. G. & Jensen, L. N., 1996. The impact of late Cenozoic uplift and erosion on hydrocarbon exporation: offshore Norway and some other uplifted basins. *Global and Planetary Change*, 12(1-4), pp. 415-436.

Dvorkin, J. & Nur, A., 1996. Elasticity of high-porosity sandstones: Theory for two North Sea data sets. *Geophysics*, 61(5), pp. 1363-1370.

Ellis, D. V. & Singer, J. M., 2007. *Well Logging for Earth Scientists.* 2 ed. s.l.:Springer.

Energy-Pedia, 2013. *Norway: Statoil drills dry hole on the Lupin Prospect in PL360.* [Online] Available at: https://www.energy-pedia.com/news/norway/new-154346
[Accessed 10 February 2018].

Faleide, J. I., Bjørlykke, K. & Gabrielsen, R. H., 2015. Geology of the Norwegian Continetal Shelf. In: *Petroleum Geoscience: From Sedimentary Environments to Rock Physics.* 2 ed. Berlin: Springer, pp. 603-637.

Fawad, M., Mondol, N. H., Jahren, J. & Bjørlykke, K., 2011. Mechanical compaction and ultrasonic velocity of sands with different texture and mineral composition. *Geophysical Prospecting*, 59(4), pp. 697-720.

Fjeldskaar, W. et al., 2004. Numerical simulation of rifting in the northern Viking Graben: the mutual effect of modelling parameters. *Tectonophysics*, 382(3-4), pp. 189-212.

Fossen, H., 1992. The role of extensional tectonics in the Caledonides of South Norway. *Journal of Structural Geology*, 14(8-9), pp. 1033-1046.

Fossen, H. & Hurich, C. A., 2005. The Hardangerfjord Shear Zone in SW Norway and the North Sea: a large-scale low-angle shear zone in the Caledonian crust. *Journal of the Geological Society*, 162(4), pp. 675-687.

Færseth, R. B., Gabrielsen, R. H. & Hurich, C. A., 1995. Influence of basement in structuring of the North Sea Basin, offshore southwest Norway. *Norsk Geologisk Tidsskrift*, 75(2-3), pp. 105-119.

Gaup, R. & Okkerman, J. A., 2011. Diagenesis and reservoir quality of Rotliegend Sandstones in the Northern Netherlands, a review.. *SEPM Special Publication,* Issue 98, pp. 193-226.

Gautier, D. L., 2005. Kimmeridgian Shales Petroleum System of the North Sea Graben Province. *USGS Bulletin,* Issue 2204-C, p. 24.

Gawthorpe, R. L. & Leeder, M. R., 2000. Tectono-sedimentary evolution of active extensional basins. *Basin Research*, 12(3-4), pp. 195-218.

Giles, M. R., Indrelid, S. L. & James, D. M. D., 1998. Compaction - the great unknown in basin modelling. *Geological Society, London, Special Publications*, 141(1), pp. 15-43.

Glennie, K. W., 1972. Permian Rotliegendes of Northwest Europe Interpreted in LIght of Modern Desert Sedimentation Studies. *AAPG Bulletin*, 56(6), pp. 1048-1071.

Goodway , B., Chen, T. & Downton, J., 1997. Improved AVO fluid detection and lithology discrimination using Lamé petrophysical parameters;"λρ","μρ", & "λ/μ fluid stack", from P and S inversions. *SEG Technical Program Expanded Abstracts 1997*, pp. 183-186.

Goodway, B., 2001. AVO and Lamé constants for rock parameterization and fluid detection. *CSEG Recorder,* 26(6), pp. 39-60.

Gray, D. & Andersen, E., 2000. The application of AVO and inversion to the estimation of rock properties. *SEG Technical Program Expanded Abstracts 2000*, pp. 549-552.

Halland, E. K., Mujezinovic, J. & Riis, F., 2014. *CO2 Storage Atlas: Norwegian Continental Shelf.* Stavanger: Norwegian Petroleum Directorate.

Hansen, J. A., Mondol, N. H., Tsikalas, F. & Doering, S., 2017. Improved Transition Zone Identification using Relations Between Shear Wave Velocity and Density. *Fourth EAGE Workshop on Rock Physics Extended Abstracts*.

Hansen, J. A., Yenwongfai, H. D., Fawad, M. & Mondol, N. H., 2017. Estimating exhumation using experimental compaction trends and rock physics relations, with continuation into analysis of source and reservoir rocks: Central North Sea, offshore Norway. *SEG Technical Program Expanded Abstracts 2017*, pp. 3971-3975.

Hansen, S., 1996. Quantification of net uplift and erosion on the Norwegian Shelf south of 66 N from sonic transit times of shales. *Norsk Geologisk Tidsskrift*, Volume 76, pp. 245-252.

Heeremans, M. & Faleide, J. I., 2004. Late Carboniferous-Permian tectonics and magmatic activity in the Skagerrak, Kattegat and the North Sea. *Geological Society, London, Special Publications*, 223(1), pp. 157-176.

Hermanrud, C. et al., 1990. On the accuracy of modelling hydrocarbon generation and migration: The Egersund Basin oil find, Norway. *Organic Geochemistry*, 16(1-3), pp. 389-399.

Hillis, R. R., 1998. Mechanisms of Dynamic Seal Failure in the Timor Sea and Central North Sea Basins. In: P. G. Purcell & R. R. Purcell, eds. *The Sedimentary Basins of Western Australia 2.* Perth: Proceedings of the Petroleum Exploration Society of Australia, pp. 313-324.

Hood, A., Gutjahr, C. C. M. & Heacock, R. L., 1975. Organic Metamorphism and the Generation of Petroleum. *AAPG Bulletin*, 59(6), pp. 986-996.

Hook, J. R., 2003. An Introduction to Porosity. *Petrophysics*, 44(03).

Hospers, J. et al., 1988. Salt tectonics in the Norwegian-Danish Basin. *Tectonophysics*, 149(1-2), pp. 35-60.

Isaksen, G. H. & Ledje, H. I., 2001. Source rock quality and hydrocarbon migration pathways within the greater Utsira High area, Viking Graben, Norwegian North Sea. *AAPG Bulletin*, 85(5), pp. 861-884.

Isaksen, G. H., Patience, R., Van Grass, G. & Jenssen , A. I., 2002. Hydrocarbon system analysis in a rift basin with mixed marine and nonmarine source rocks: The South Viking Graben. *AAPG Bulletin*, 86(4), pp. 557-592.

Japsen, P. et al., 2011. Episodic uplift and exhumation along North Atlantic passive argins: implications for hydrocarbon prospectivity. *Geological Society, London, Petroleum Conference series*, 7(1), pp. 979-1004.

Jarsve, E. M. et al., 2014. Seismic stratigraphic subdivision of the Triassic succession in the Central Northe Sea; integrating seismic reflection and well data. *Journal of the Geological Society*, pp. 353-374.

Javed, K., 2013. *Sedimentological and reservoir geological developments of Triassic/Jurassic formations in Åsta Graben (well 17/3-1),* Master Thesis: University of Oslo.

Jensen, L. N. & Schmidt, B. J., 1993. Neogene uplift and erosion offshore South Norway; magnitude and consequences for hydrocarbon exploration in the Farsund Basin. In: A. M. Spencer, ed. *Generation, Accumulation, and Production of Europe's Hydrocarbons; III.* Berlin: Springer, pp. 79-88.

Justwan, H., Dahl, B., Isaksen, G. H. & Meisingset, I., 2006. Late to Middle Jurassic source facies and quality variations, South Viking Graben, North Sea. *Journal of Petroleum Geology*, 28(3), pp. 241-268.

Kahlani, M., Jahren, J., Mondol, N. H. & Faleide, J. I., 2015. Compaction processes and rock properties in uplifted clay dominated units - The Egersund Basin, Norwegian North Sea. *Marine and Petroleum Geology*, Volume 68, pp. 596-613.

Kaspersen, H. M., 2016. *Reservoir Characterization of Jurassic Sandstones of the Johan Sverdrup Field, Central North Sea,* Master Thesis: University of Oslo.

Kennedy, M., 2015. *Practical Petrophysics.* s.l.:Elsevier B. V.

Kieft, R. L., Jackson, C. L., Hampson, G. J. & Larsen , E., 2010. Sedimentology and sequence stratigraphy of the Hugin Formation, quadrant 15, Norwegian Sector, South Viking Graben. *Geological Society, London, Petroleum Geology Confernece Series,* 7(1), pp. 157-176.

Klaja, J. & Dudek, L., 2016. Geological interpretation of spectral gamma ray (SGR) logging in selected boreholes. *Nafta-Gaz*, 72(1), pp. 3-14.

Koochak Zadeh, M., Mondol, N. H. & Jahren, J., 2014. Compation and Rock Properties of Cenozoic Mudstones in the Quadrant 15, Offshore Norway. *Fourth EAGE Shale Workshop Extended Abstracts.*

Lyngsie, S. B., Thybo, H. & Rasmussen, T. M., 2006. Regional geological and tectonic structures of the North Sea area from potential field modelling. *Tectonophysics*, 413(3-4), pp. 147-170.

Løseth, H. et al., 2011. Can hydrocarbon source rocks be identified on seismic data?. *Geology*, 39(12), pp. 1167-1170.

Maast, T. E., Jahren, J. & Bjørlykke, K., 2011. Diagenetic control on reservoir quality in Middle to Upper Jurassic sandstones in the South Viking Graben, North Sea. *AAPG Bulletin*, 95(11), pp. 1937-1958.

Magoon, L. B. & Dow, W. G., 1994. The Petroleum System: Chapter 1: Part I. Introduction. In: *The Petroleum System - From Source to Trap.* s.l.:AAPG, pp. 3-24.

Mannie, A. S., Jackson, C. A. L. & Hampson, G. J., 2014. Structural controls on the stratigraphic architecture of net-trensgressive shallow-marine strata in a salt-influenced rift basin: Middle-to-upper Jurassic Egersund Basin, Norwegian North Sea. *Basin Research*, 26(5), pp. 675-700.

Mannie, A. S., Jackson, C. . A. L., Hampson, G. J. & Fraser, A. J., 2016. Tectonic controls on the spatial distribution and stratigraphic architecture of a net-transgressive shallow-marine synrift seccession in a salt-influenced basin: Middle to Upper Jurassic, Norwegian Central North Sea. *Journal of the Geological Society*, 173(6), pp. 901-915.

Marchand, A. M. E., Macaulay, C. I., Stuart Haszeldine, R. & Fallicj, A., 2002. Pore water evolution in oilfield sandstones: contraints from oxygen isotope microanalysis of quartz cement. *Chemical Geology*, 191(4), pp. 285-304.

Marcussen, Ø. et al., 2010. Changes in physical properties of reservoir sandstone as a function of burial depth - The Etive Formation, northern North Sea. *Marine and Petroleum Geology*, 27(8), pp. 1725-1735.

Mavko, G., Mukerji, T. & Dvorkin, J., 2009. *The rock physics handbook: Tools for seismic analysis of porous media.* Cambridge: Cambridge University Press.

Mindlin, R. D., 1949. Compliance of Elastic Bodies in Contact. *Journal of Applied Mechanics*, Volume 16, pp. 265-268.

Mondol, N. H., 2009. Porosity and permeability development in mechanically compacted silt-kaolinite mixtures. *SEG Technical Program Expanded Abstracts 2009*, pp. 2139-2143.

Mondol, N. H., 2015. Well Logging: Principles, Applications and Uncertainties. In: *Petroleum Geoscience: From Sedimentary Environments to Rock Physics.* 2 ed. Berlin: Springer, pp. 385-425.

Mondol, N. H., Bjørlykke, K., Jahren, J. & Høeg, K., 2007. Experimental mechanical compaction of clay mineral aggregates - Changes in physical properties of mudstones during burial. *Marine and Petroleum Geology*, 24(5), pp. 289-311.

Mondol, N. H., Jahren, J., Bjørlykke, K. & Brevik, I., 2008. Elastic properties of clay minerals. *The Leading Edge*, 27(6), pp. 758-770.

Nemcok, M., 2016. *Rifts and passive margins: Structural architecture, thermal regimes, and petroleum systems.* Cambridge: Cambridge University Press.

NPD, 2017. *Geological plays.* [Online]
Available at: http://www.npd.no/en/Topics/Geology/Geological-plays/
[Accessed 2 February 2018].

NPD, 2018. *FactPages. Norwegian Petroleum Directorate.* [Online]
Available at: http://factpages.npd.no/FactPages/Default.aspx?culture=en
[Accessed 30 Januar 2018].

Ohm, S. E., Karlsen, D. A. & Austin, T. J. F., 2008. Geochemically driven exploration models in uplifted areas: Examples from the Norwegian Barents Sea. *AAPG Bulletin*, 92(99), pp. 1191-1223.

Passey, Q. R. et al., 2010. From Oil-Prone Source Rock to Gas-Producing Shale Reservoir - Geologic and Petrophysical Characterization of Unconventional Shale Gas Reservoirs. *International oil and gas conference and exhibition in China.*

Passey, Q. R. et al., 1990. A Practical Model for Organic Richness from Porosity and Resitivity Logs. *AAPG Bulletin*, 74(12), pp. 1777-1794.

Pedersen, J. H. et al., 2006. The geochemistry of two unusual oils from the Norwegian North Sea: implications for new source rock and play scenario. *Petroleum Geoscience*, 12(1), pp. 85-96.

Peltonen, C., Marcussen, Ø., Bjørlykke, K. & Jahren, J., 2008. Minerlogical control on mudstone compaction: a study of Late Cretaceous to Early Tertiary mudstones of the Vøring and Møre Basins, Norwegian Sea. *Petroleum Geoscience*, 14(12), pp. 127-138.

Petersen, H. I. et al., 2008. Evaluation of the quality, thermal maturity and distribution of potential source rocks in the Danish part of the Norwegian-Danish Basin. *Geological Survey of Denmark and Greenland Bulletin*, Volume 16, pp. 1-27.

Rawson, P. F. & Riley, L. A., 1982. Latest Jurassic - Early Cretaceous Events and the "Late Cimmerian Unconformity" in North Sea Area. *AAPG Bulletin*, 66(12), pp. 2628-2648.

Raymer, L. L., Hunt, E. R. & Gardner, J., 1980. An Improved Sonic Transit Time-To-Porosity Transform. *SPWLA 21st annual logging symposium*.

Ritter, U., Leslie Leith, T., Griffiths, C. M. & Schou, L., 1987. Hydrocarbon generation and thermal evolution in parts of the Egersund Basin, Northern North Sea. In: A. J. Tankard & C. Beaumont, eds. *Sedimentary Basins and Basin-Forming Mechanisms.* Calgary: Canadian Society of Petroleum Geologists, pp. 75-85.

Rose, P. R., 1992. Chance of Success and Its Use in Petroleum Exploration: Chapter 7: Part II. Nature of the Business. In: *The Business of Petroleum Exploration.* s.l.:AAPG, pp. 71-86.

Sales, J. K., 1993. Closure vs. seal capacity - A fundamental control on the distribution of oil and gas. *Basin Modeling: Advances and application: Norwegian Petroleum Society (NPF) Special Publication,* Issue 3, pp. 399-414.

Schlumberger, 2018. *Oilfield Glossary: TOC.* [Online]
Available at: https://www.glossary.oilfield.slb.com/en/Terms/t/toc.aspx
[Accessed 10 October 2018].

Skurtveit, E. et al., 2015. Mechanical testing and sealing capacity of the Upper Jurassic Draupne Formation, North Sea. *49th US Rock Mechanics/Geomechanics Symposium*.

Storvoll, V., Bjørlykke, K., Karlsen, D. A. & Saigal, G., 2002. Porosity preservation in reservoir sandstones due to grain-coating illite: a study of the Jurassic Garn Formation from the Kristin and Lavrans fields, offshore Mid-Norway. *Marine and Petroleum Geology*, 19(6), pp. 767-781.

Storvoll, V., Bjørlykke, K. & Mondol, N. H., 2005. Velocity-depth trends in Mesozoic and Cenozoic sediments from the Norwegian Shelf. *AAPG Bulletin*, 89(3), pp. 359-381.

Sørensen, S. & Tangen, O. H., 1995. Exploration trends in marginal basins from Skagerrak to Stord. *Norwegian Petroleum Society Special Publications*, Volume 4, pp. 97-114.

Theis, N. J., Nielsen, H. H., Sales, J. K. & Gail, G. J., 1993. Impact of data integration on basin modeling in the Barents Sea. *Basin modeling: Advances and applications: Norwegian Petroleum Society (NPF) Special Publication*, Volume 3, pp. 433-444.

Thomas, B. M., Møller-Pedersen, P., Whitaker, M. F. & Shaw, N. D., 1985. Organic facies and hydrocarbon distributions in the Norwegian Sea. In: *Petroleum Geochemistry in Exploration of the Norwegian Shelf.* Dordrecht: Springer, pp. 3-26.

Thyberg, B. et al., 2009. From mud to shale: rock stiffening by micro-quartz cementation. *First Break*, Volume 2, pp. 53-59.

Tissot, B. P. & Welte, D. H., 1978. *Petroleum Formation and Occurence: A New Approach to Oil and Gas Exploration.* s.l.:Springer.

Vernik, L. & Landis, C., 1996. Elastic Anisotropy of Source Rocks: Implications for Hydrocarbon Generation and Primary Migration. *AAPG Bulletin*, 80(4), pp. 531-544.

Vollset, J. & Doré, A. G., 1984. *A revised Triassic and Jurassic lithostratigraphic nomenclature for the Norwegian North Sea.* Stavanger: Norwegian Petroleum Directorate.

Walderhaug, O., 1994. Precipitation rates for quartz cement in sandstones determined by fluid-inclusion microthermometry and temperature-history modeling. *Journal of Sedimentary Research*, 64(2a), pp. 324-333.

Walderhaug, O., 2000. Modeling Quartz Cementation and Porosity in Middle Jurassic Brent Group Sandstones of the Kvitebjørn Field, Northern North Sea. *AAPG Bulletin*, 84(9), pp. 1325-1339.

Walderhaug, O., Oelkers, E. H. & Bjørkum, P. A., 2004. An Analysis of the Roles of Stress, Temperature, and pH in Chemical Compaction of Sandstones. *Journal of Sedimentary Research*, 74(3), pp. 447-449.

Watts, N. L., 1987. Theroretical aspects of cap-rock and fault seals for single- and two-phase hydrocarbon columns. *Marine and Petroleum Geology*, Volume 4, pp. 274-307.

Wesenlund, F., 2016. *The Petroleum Geochemistry of the Johan Sverdrup Field, Southern Utsira High, Norwegian North Sea,* Master Thesis.: University of Oslo.

Worthington, P. F. & Cosentino, L., 2005. The Role of Cutoffs in Integrated Reservoir Studies. *SPEREE 8,* Issue 4, pp. 276-290.

Wyllie, M. R. J., Gregory, A. R. & Gardner, G. H. F., 1958. An experimental investigation of factors affecting elastic wave velocities in porous media. *Geophysics*, 23(3), pp. 459-493.

Ziegler, P. A., 1982. Triassic rifts and facies patterns in Western and Central Europe. *Geologische Rundshau*, October, 71(3), pp. 747-772.

Ziegler, P. A., 1990. *Geological Atlas of Western and Central Europe.* Hague: Shell International Petroleum Maatschappij B.V..

Ødegaard, E. & Avseth, P., 2003. Interpretation of Elastic Inversion results Using Rock Physics Templates. *65th EAGE Conference & Exhibition.*

Appendix A – Uplift corrections

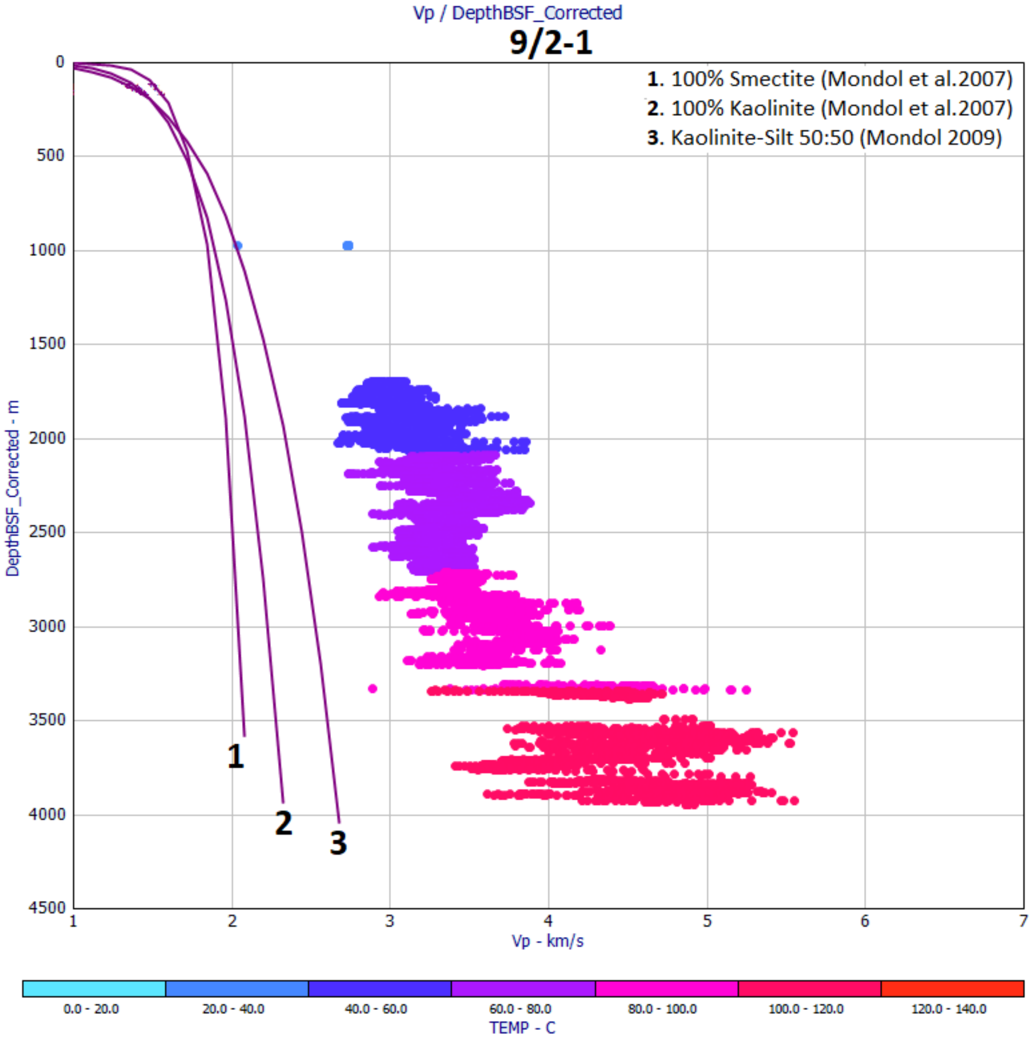

Figure A.1: V_P-depth plot showing shale data from well 9/2-1 corrected for uplift. Depth is adjusted to provide best fit with Kaolinite-Silt 50:50 trend (see legend) above assumed transition zone and hence simulate maximum burial.

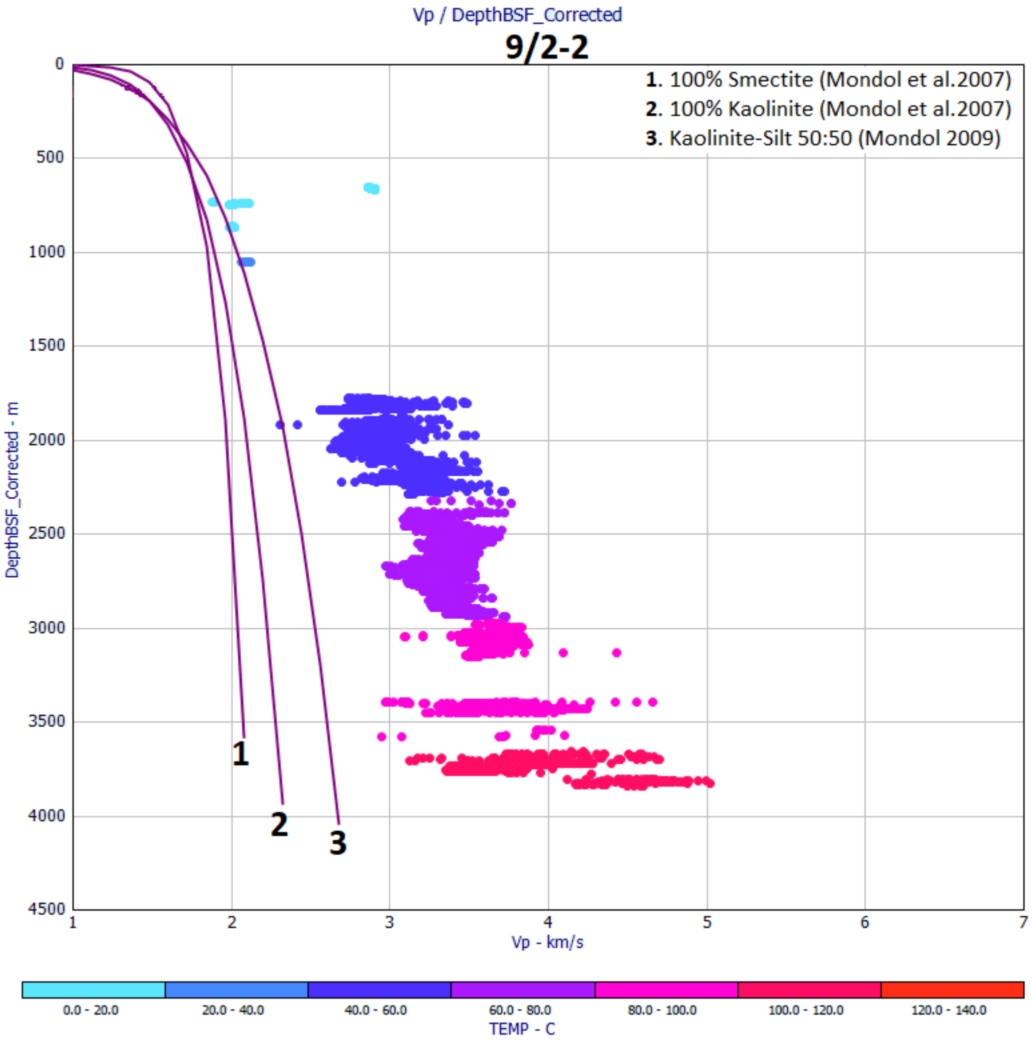

Figure A.2: V_P-depth plot showing shale data from well 9/2-2 corrected for uplift. Depth is adjusted to provide best fit with Kaolinite-Silt 50:50 trend (see legend) above assumed transition zone and hence simulate maximum burial.

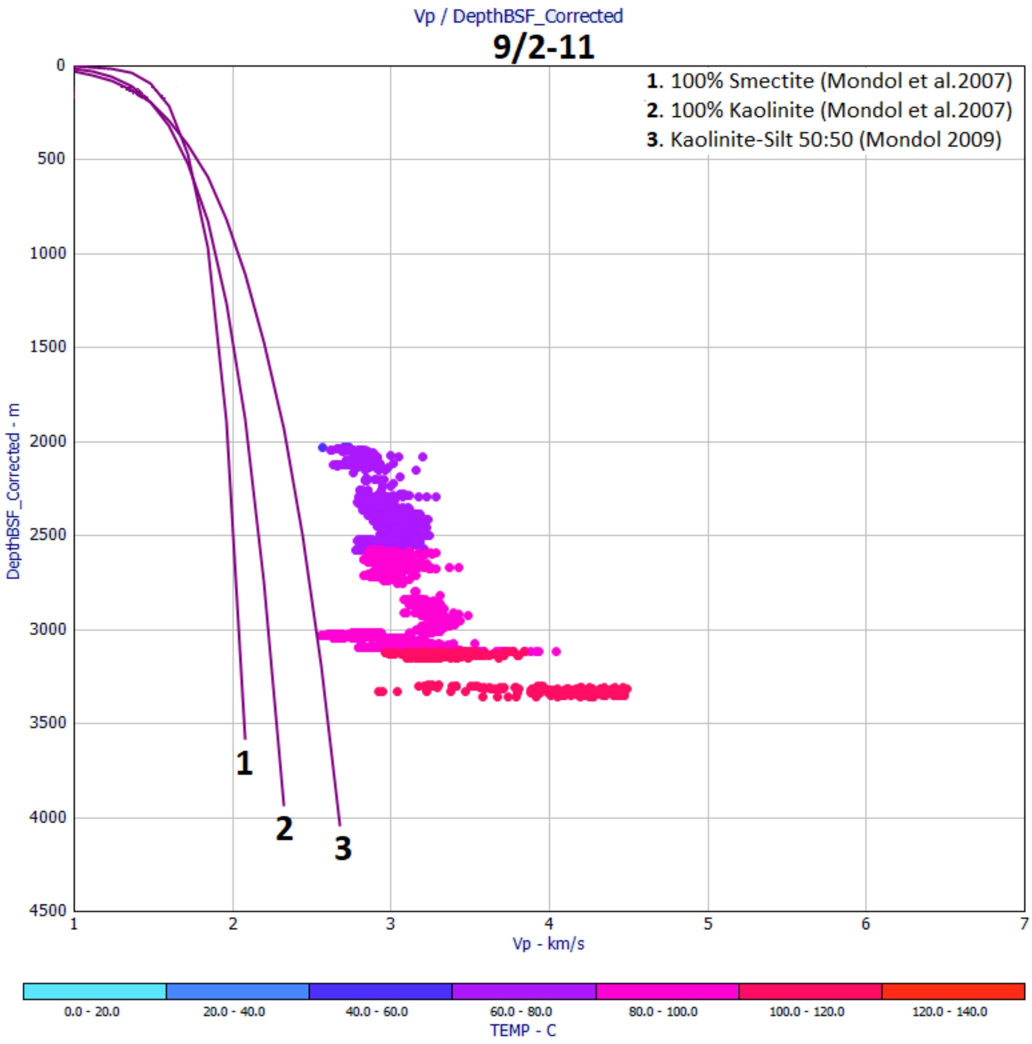

Figure A.3: V_p-depth plot showing shale data from well 9/2-11 corrected for uplift. Depth is adjusted to provide best fit with Kaolinite-Silt 50:50 trend (see legend) above assumed transition zone and hence simulate maximum burial.

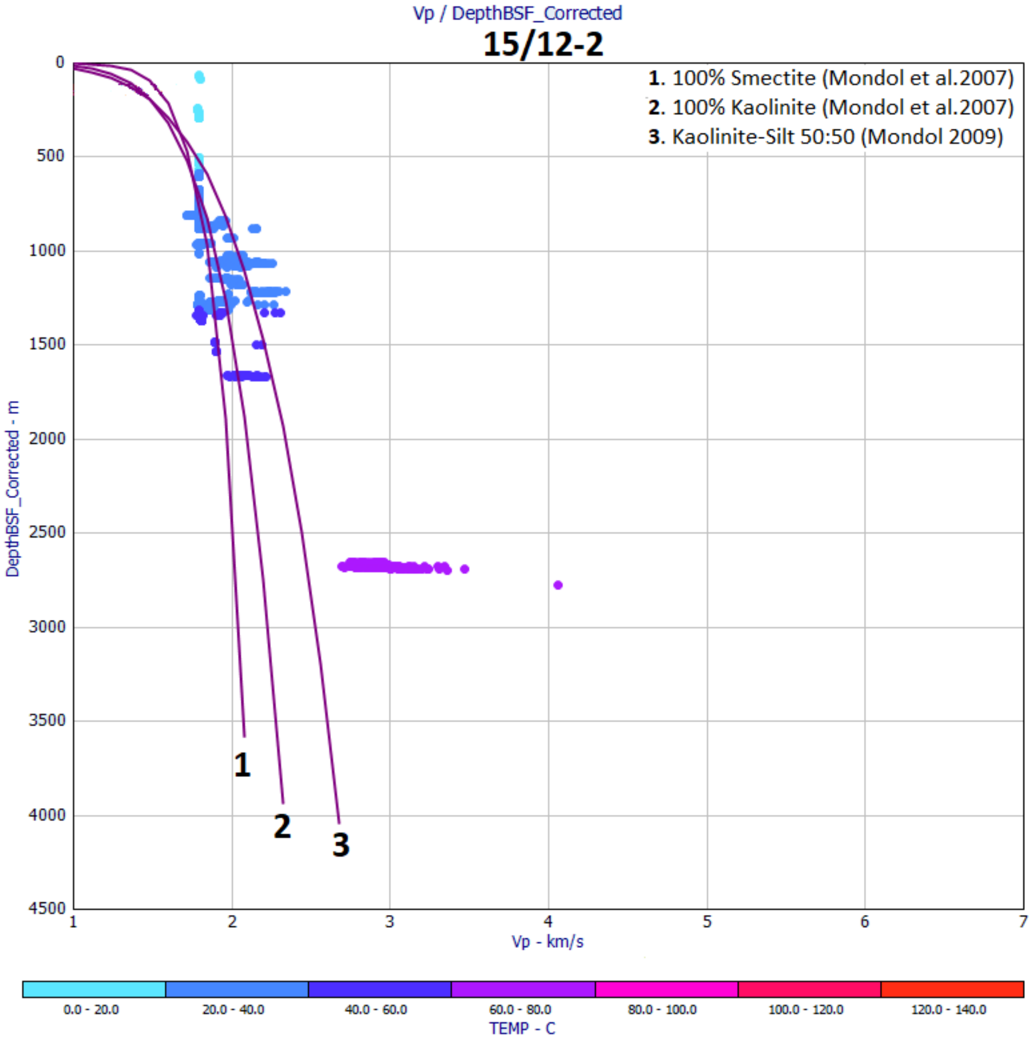

Figure A.4: V_p-depth plot showing shale data from well 15/12-2 corrected for uplift. Depth is adjusted to provide best fit with Kaolinite-Silt 50:50 trend (see legend) above assumed transition zone and hence simulate maximum burial.

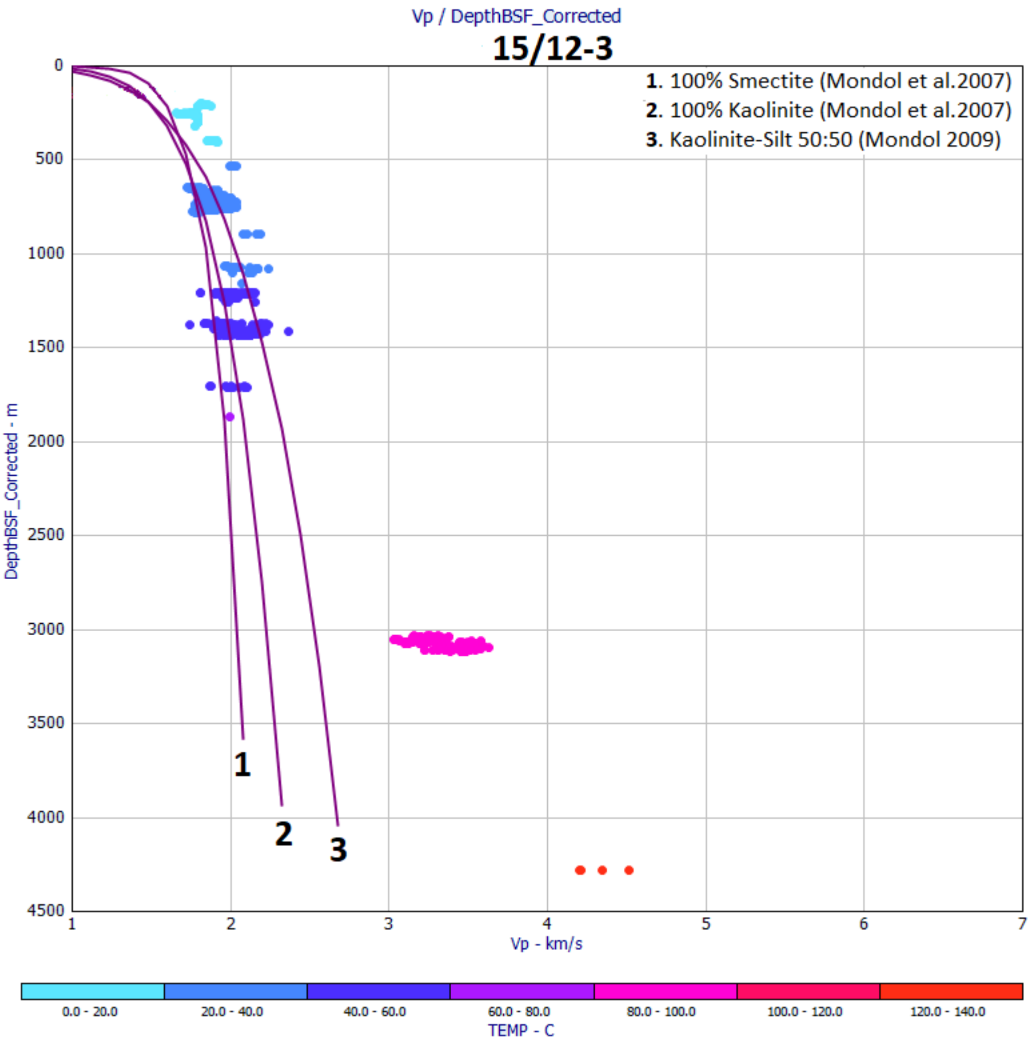

Figure A.5: V_P-depth plot showing shale data from well 15/12-3 corrected for uplift. Depth is adjusted to provide best fit with Kaolinite-Silt 50:50 trend (see legend) above assumed transition zone and hence simulate maximum burial.

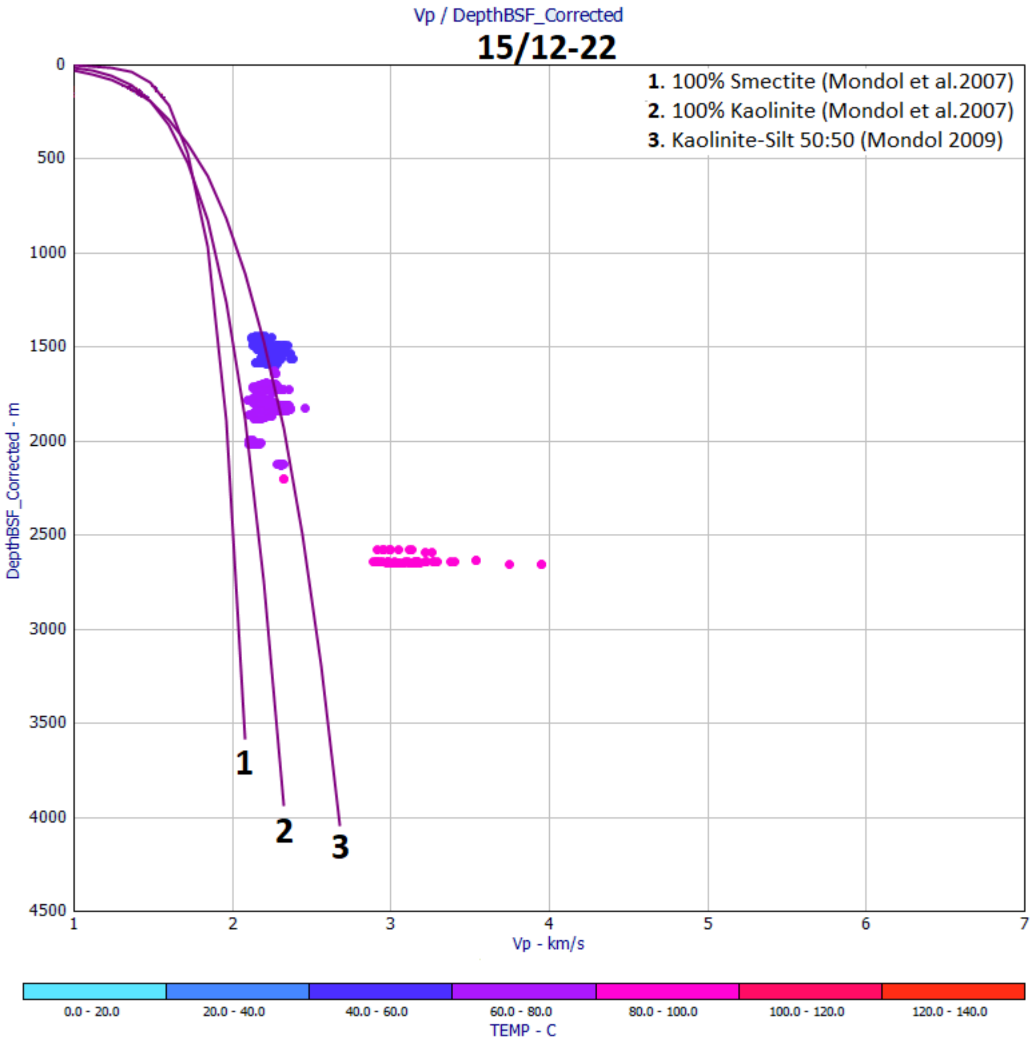

Figure A.6: V_p-depth plot showing shale data from well 915/12-22 corrected for uplift. Depth is adjusted to provide best fit with Kaolinite-Silt 50:50 trend (see legend) above assumed transition zone and hence simulate maximum burial.

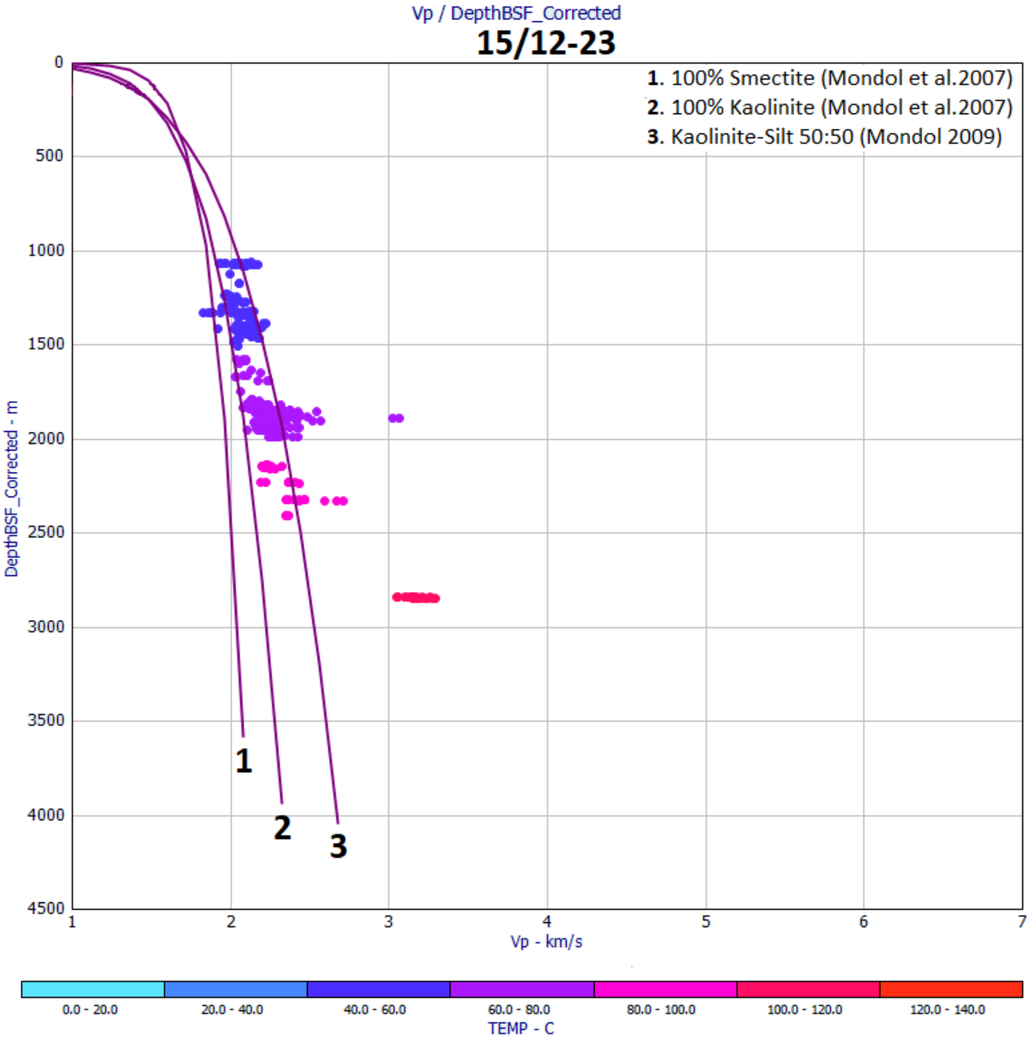

Figure A.7: V_P-depth plot showing shale data from well 15/12-23 corrected for uplift. Depth is adjusted to provide best fit with Kaolinite-Silt 50:50 trend (see legend) above assumed transition zone and hence simulate maximum burial.

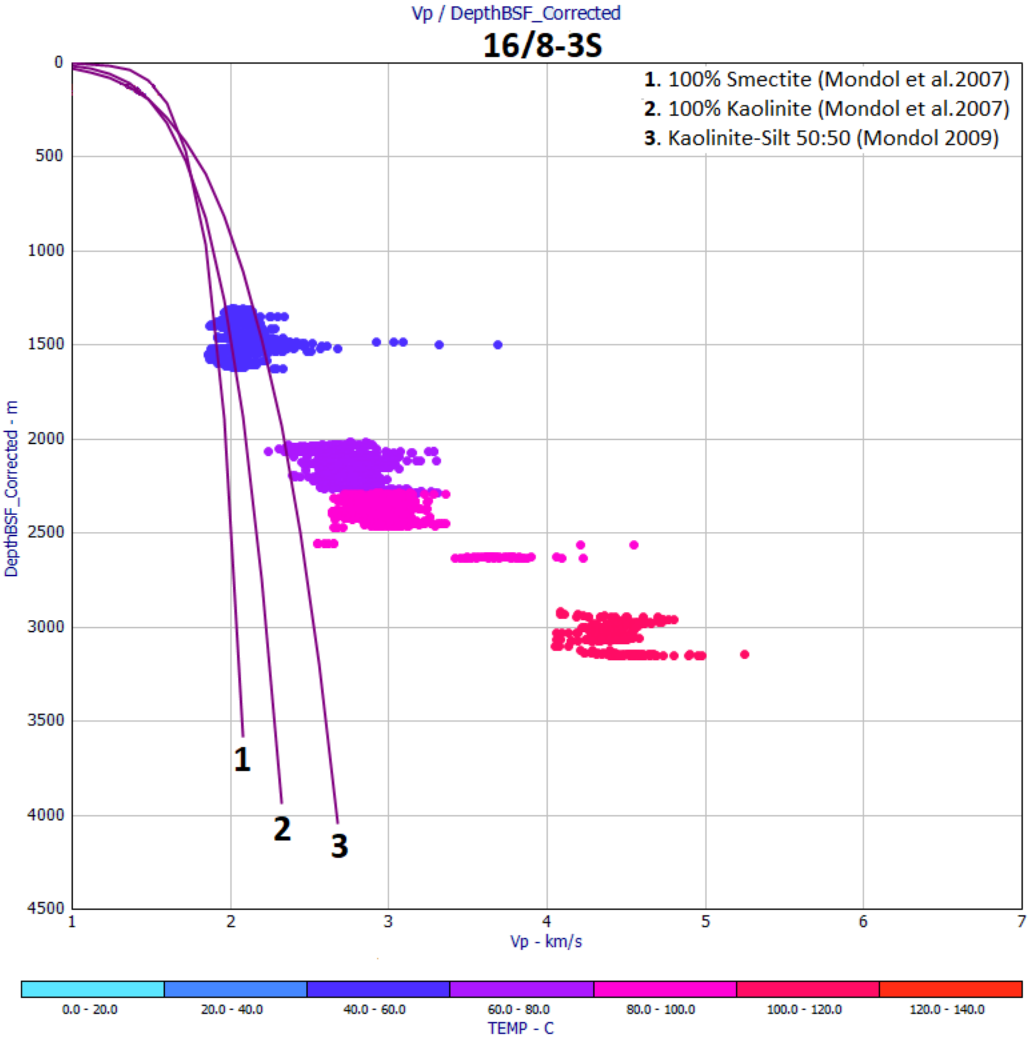

Figure A.8: V_p-depth plot showing shale data from well 16/8-3S corrected for uplift. Depth is adjusted to provide best fit with Kaolinite-Silt 50:50 trend (see legend) above assumed transition zone and hence simulate maximum burial.

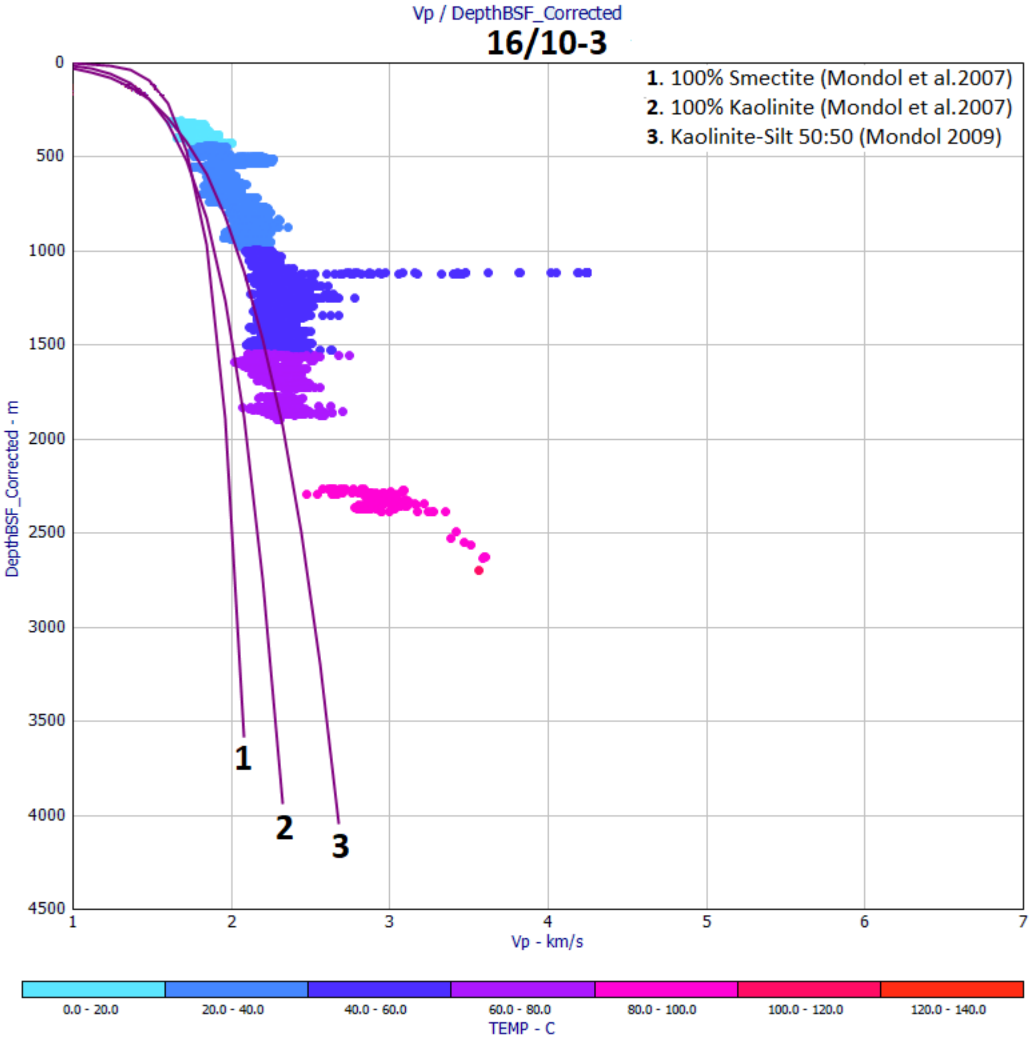

Figure A.9: V_p-depth plot showing shale data from well 16/10-3 corrected for uplift. Depth is adjusted to provide best fit with Kaolinite-Silt 50:50 trend (see legend) above assumed transition zone and hence simulate maximum burial.

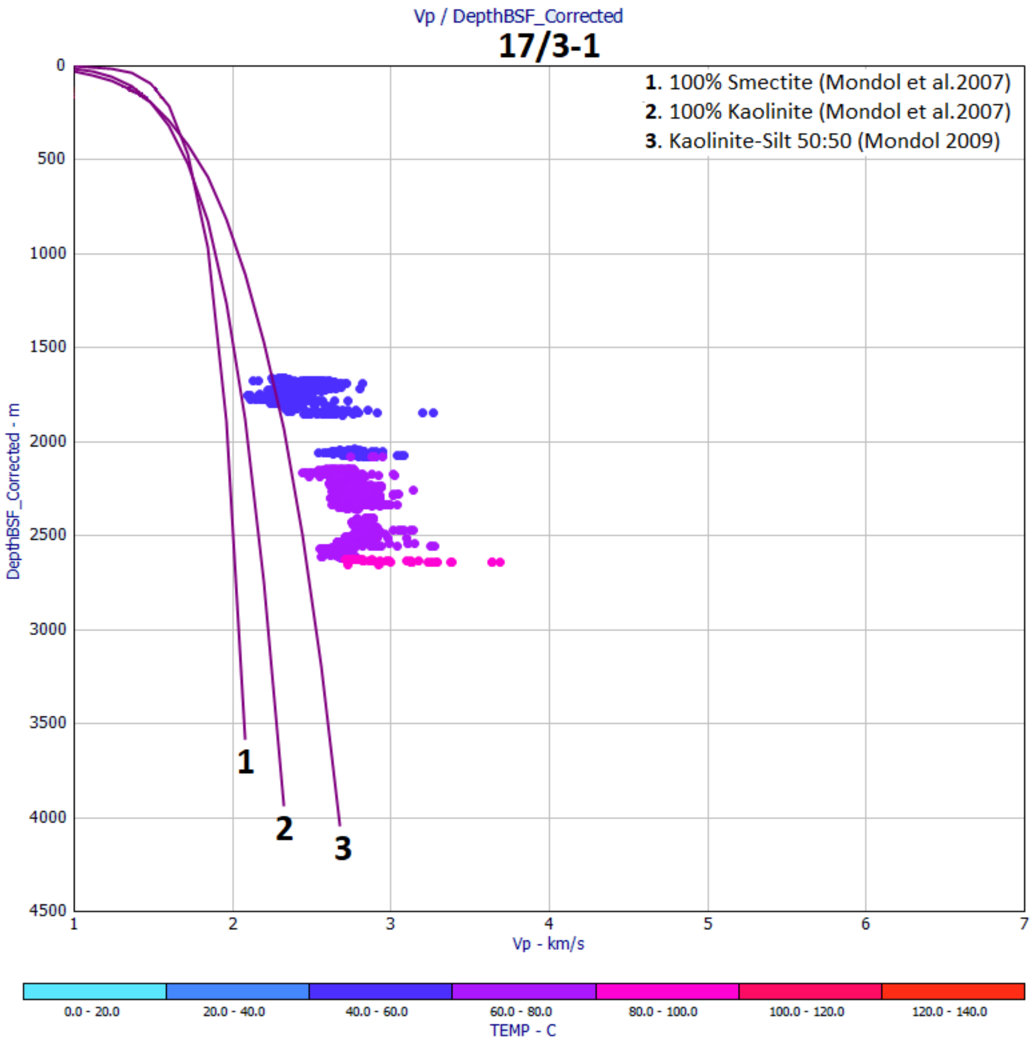

Figure A.10: V_P-depth plot showing shale data from well 17/3-1 corrected for uplift. Depth is adjusted to provide best fit with Kaolinite-Silt 50:50 trend (see legend) above assumed transition zone and hence simulate maximum burial.

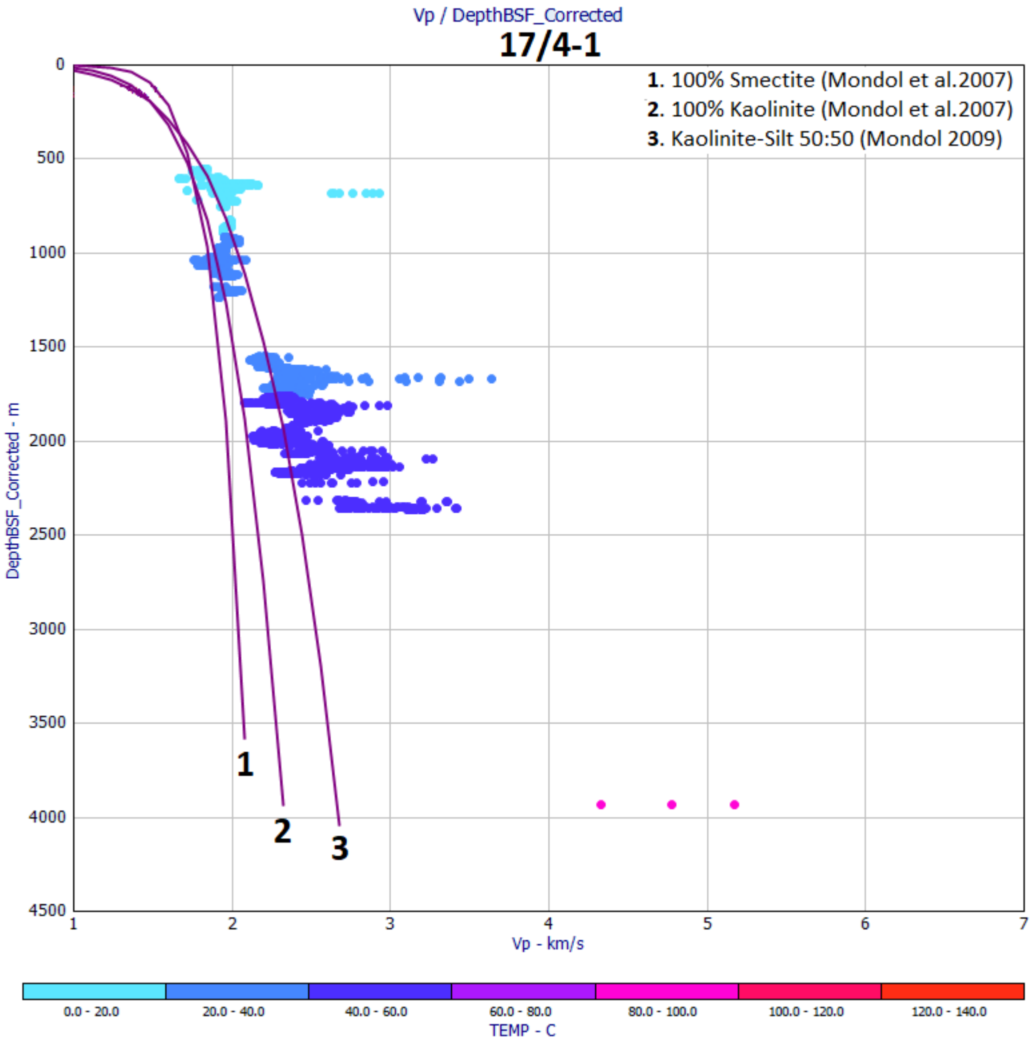

Figure A.11: V_P-depth plot showing shale data from well 17/4-1 corrected for uplift. Depth is adjusted to provide best fit with Kaolinite-Silt 50:50 trend (see legend) above assumed transition zone and hence simulate maximum burial.

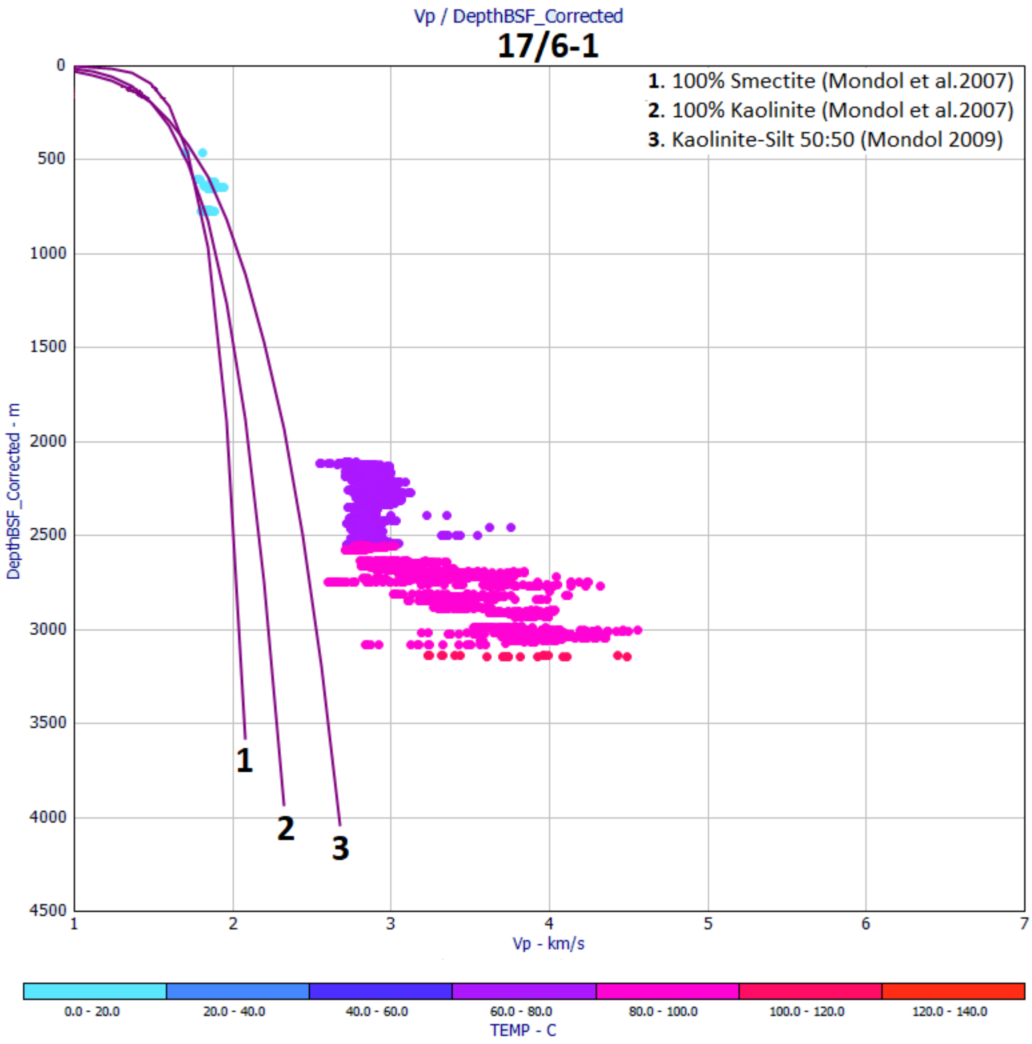

Figure A.12: V_P-depth plot showing shale data from well 17/6-1 corrected for uplift. Depth is adjusted to provide best fit with Kaolinite-Silt 50:50 trend (see legend) above assumed transition zone and hence simulate maximum burial.

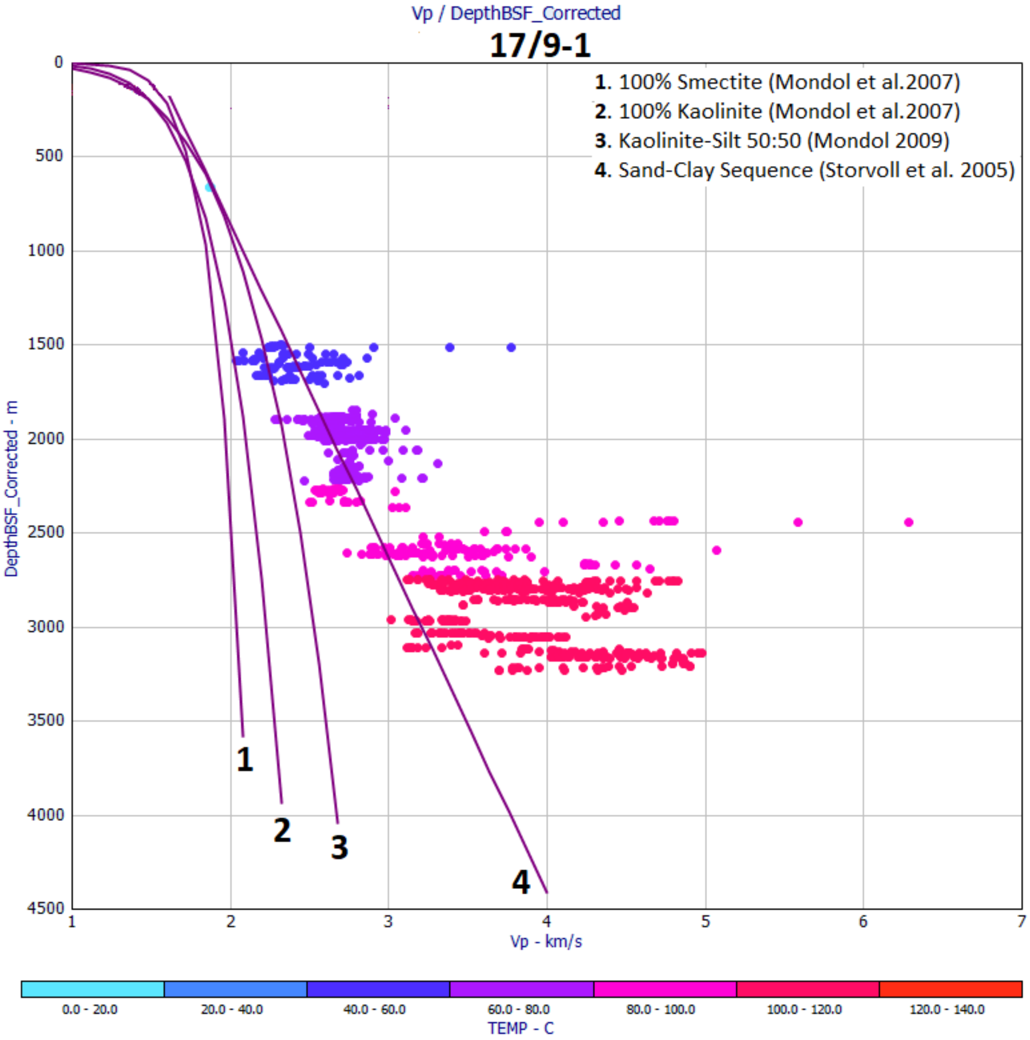

Figure A.13: V_P-depth plot showing shale data from well 17/9-1 corrected for uplift. Depth is adjusted to provide best fit with Kaolinite-Silt 50:50 trend (see legend) above assumed transition zone and hence simulate maximum burial.

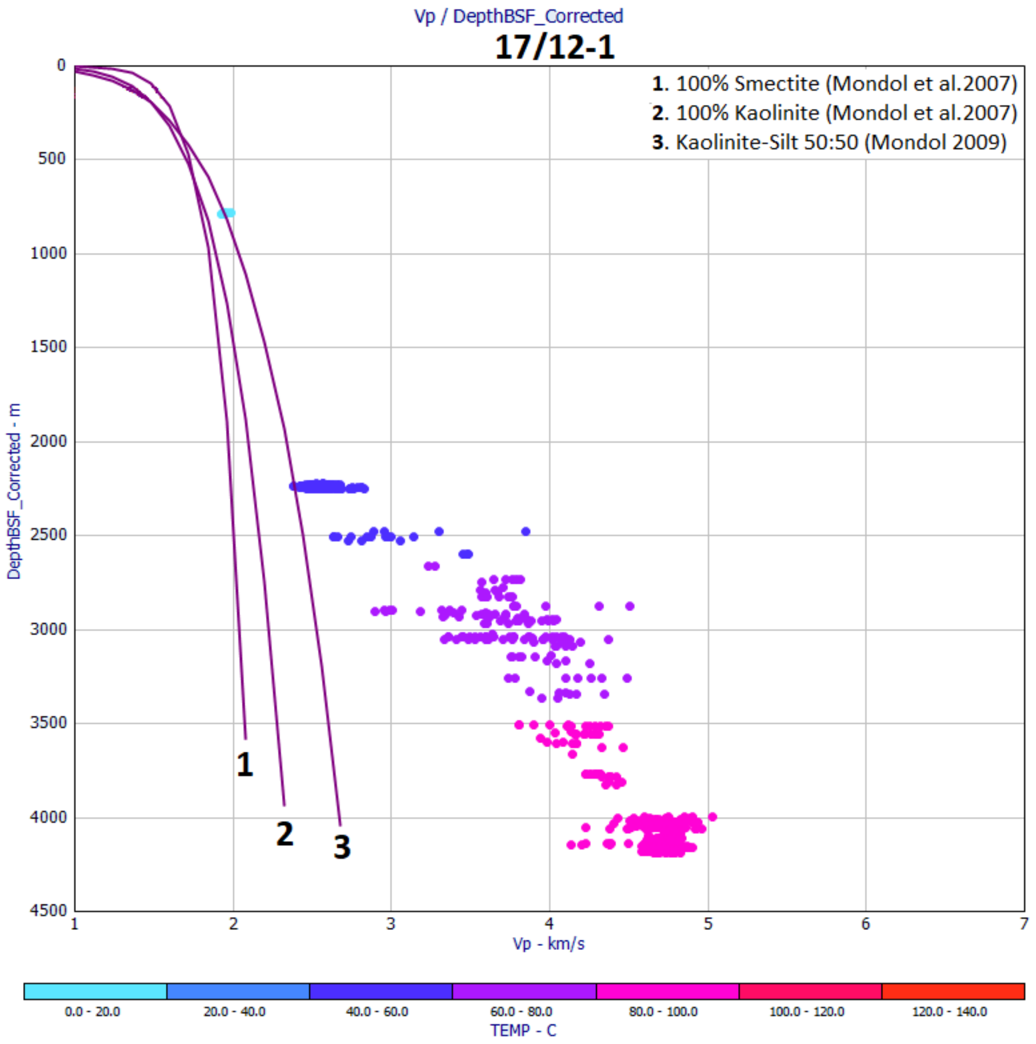

Figure A.14: V_P-depth plot showing shale data from well 17/12-1 corrected for uplift. Depth is adjusted to provide best fit with Kaolinite-Silt 50:50 trend (see legend) above assumed transition zone and hence simulate maximum burial.

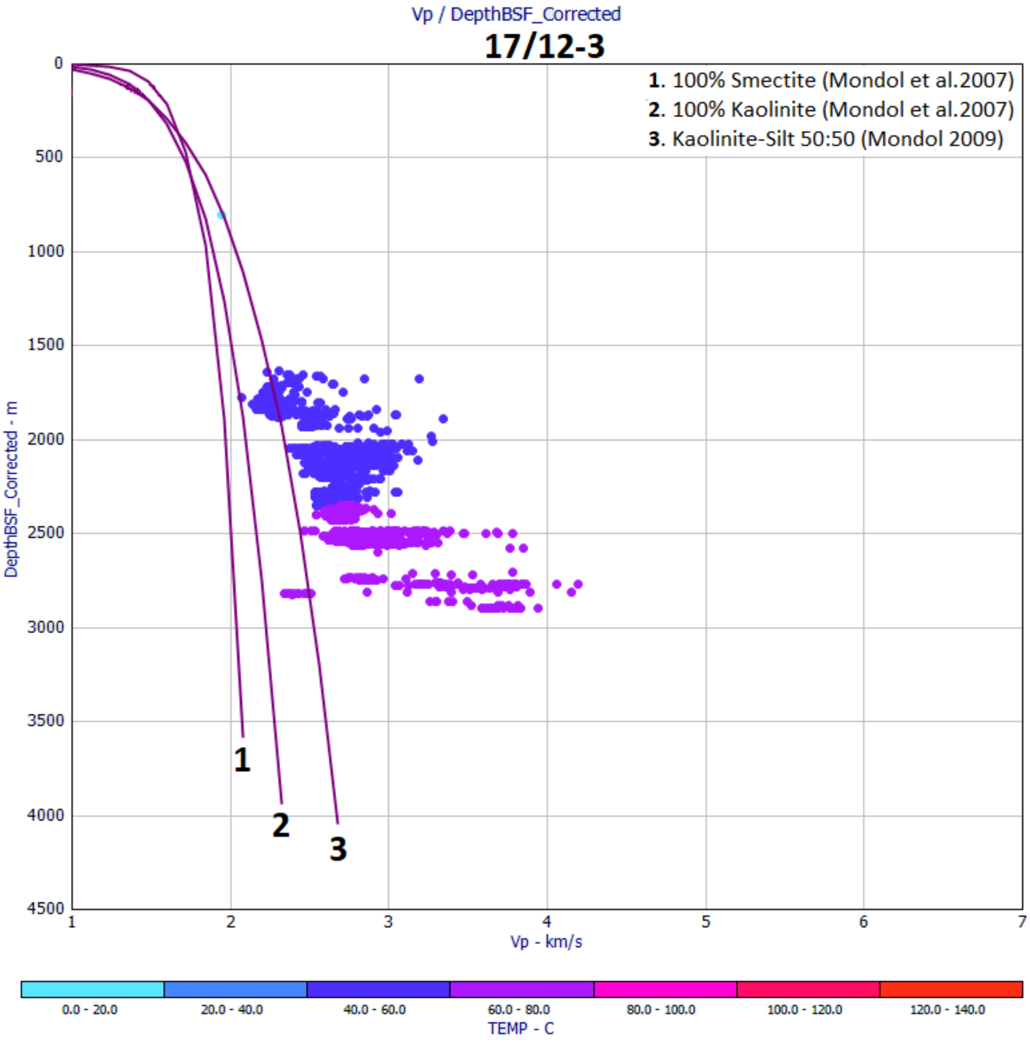

Figure A.15: V_P-depth plot showing shale data from well 17/12-3 corrected for uplift. Depth is adjusted to provide best fit with Kaolinite-Silt 50:50 trend (see legend) above assumed transition zone and hence simulate maximum burial.

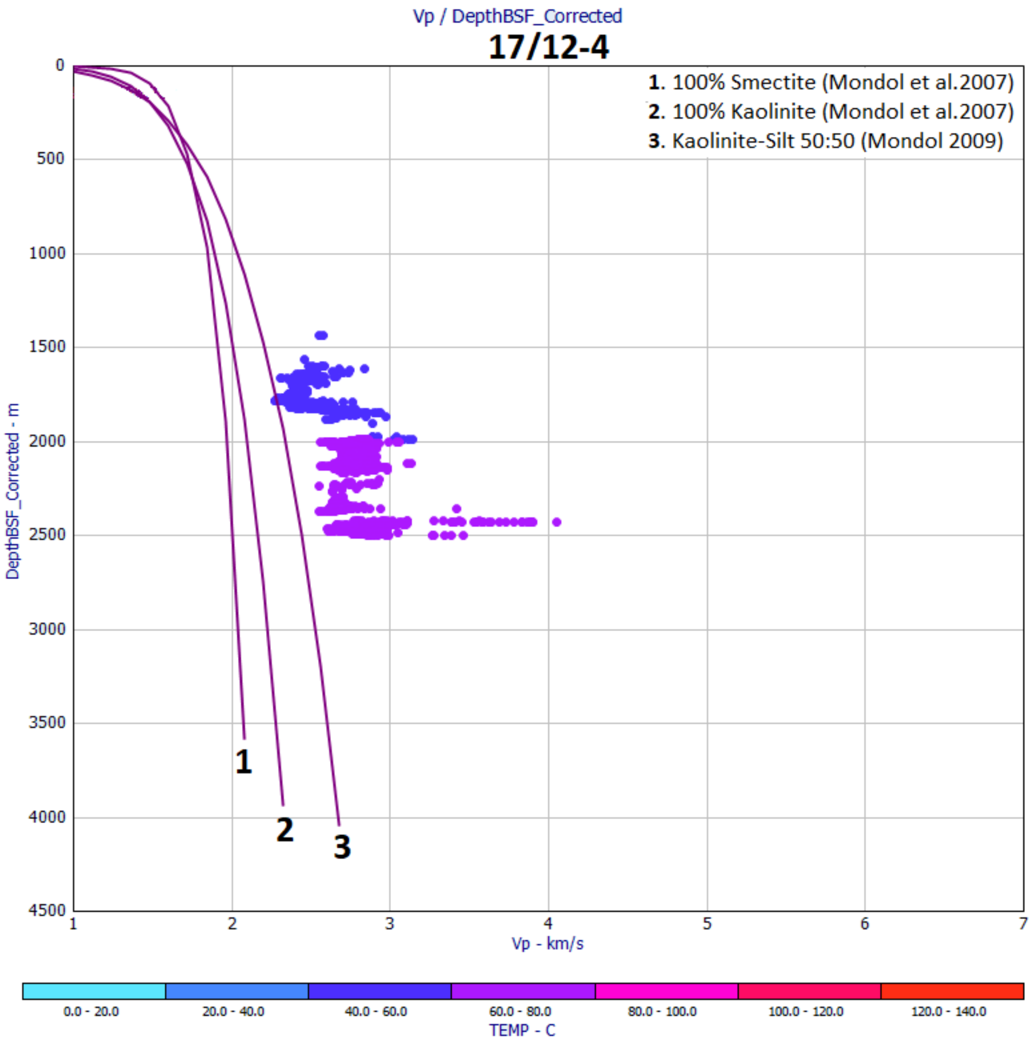

Figure A.16: V_P-depth plot showing shale data from well 17/12-4 corrected for uplift. Depth is adjusted to provide best fit with Kaolinite-Silt 50:50 trend (see legend) above assumed transition zone and hence simulate maximum burial.

Appendix B – Well sections

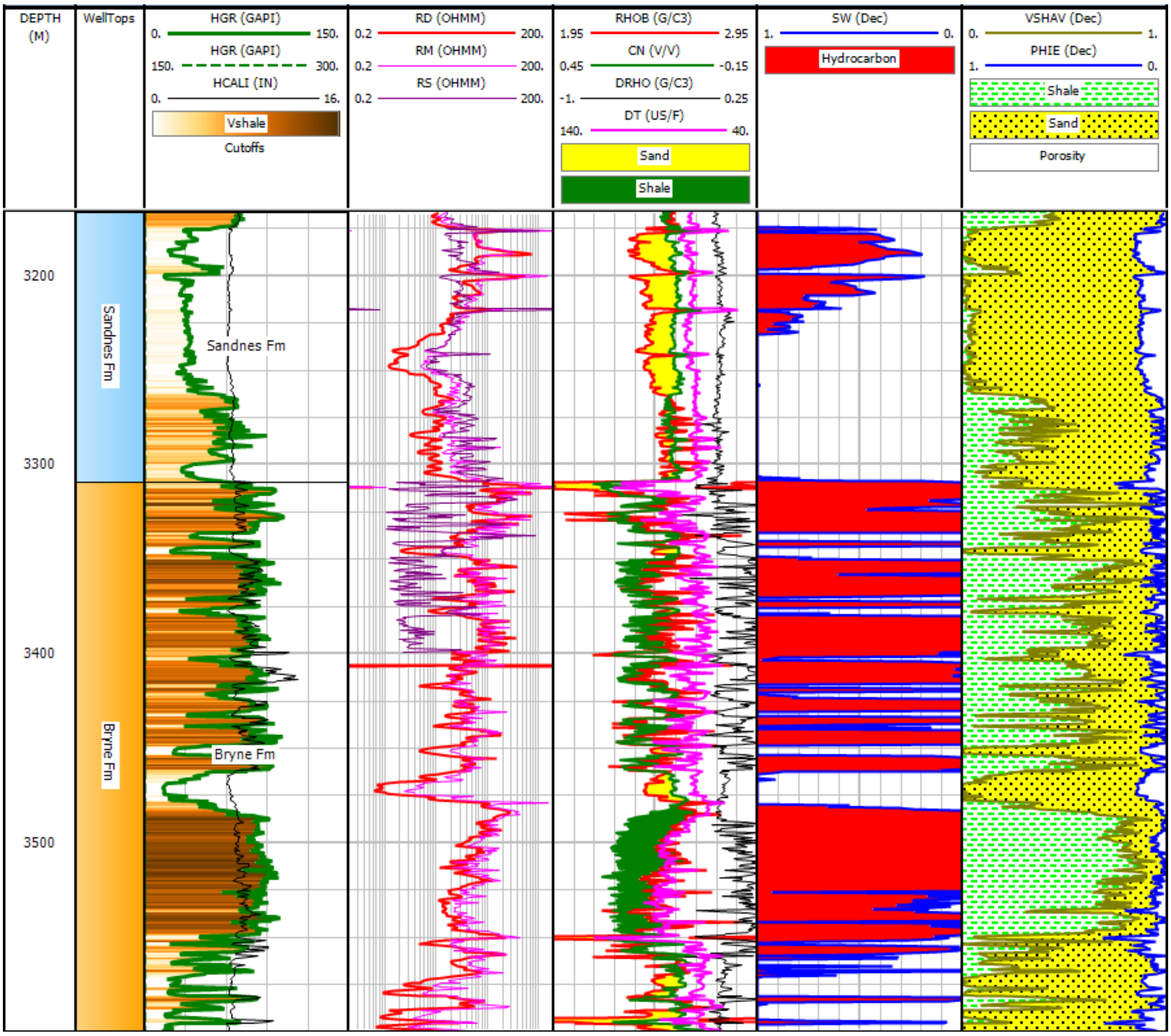

Figure B.1: Complete well 9/2-1 for reservoir target formations.

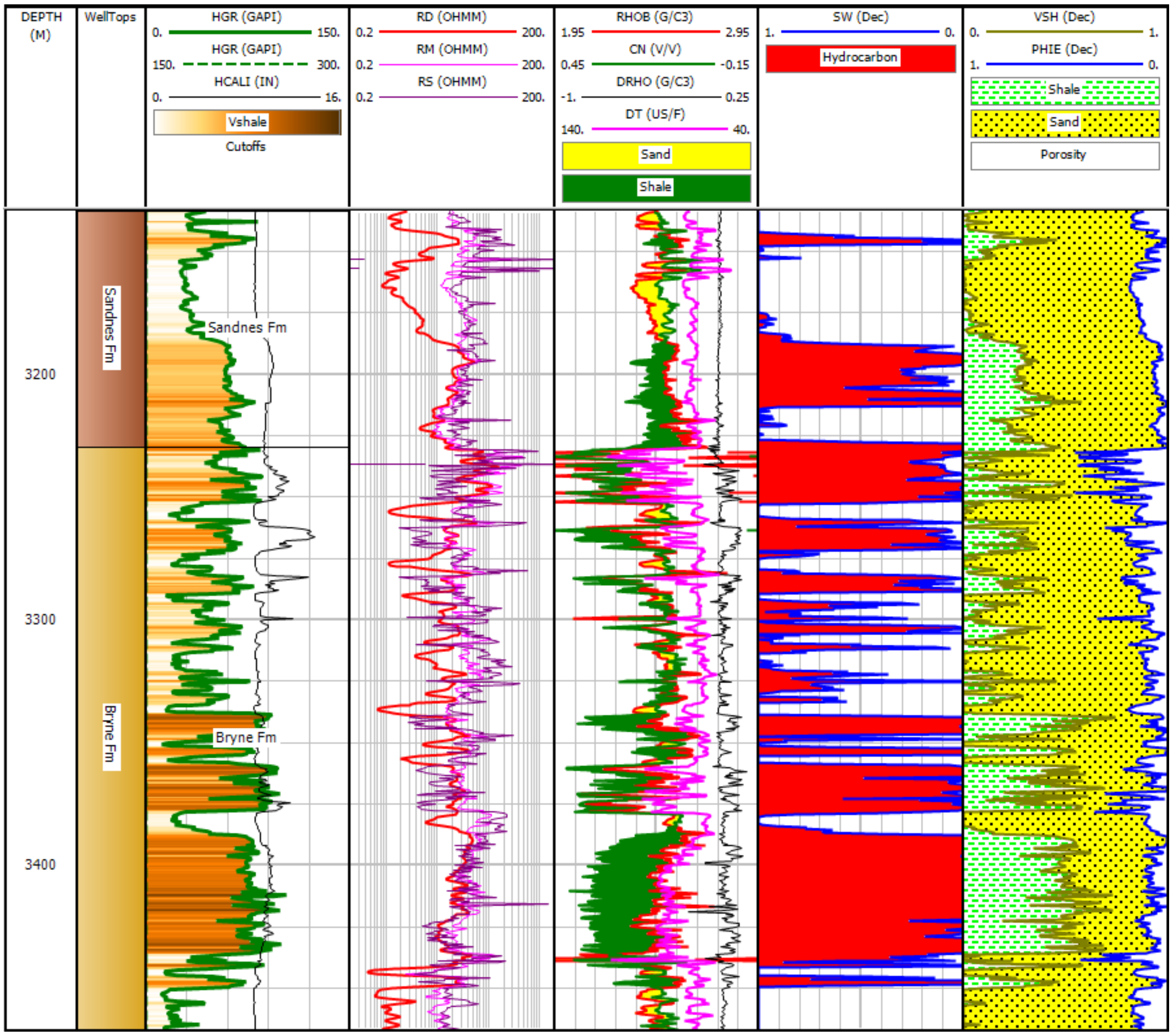

Figure B.2: Complete well 9/2-2 for reservoir target formations.

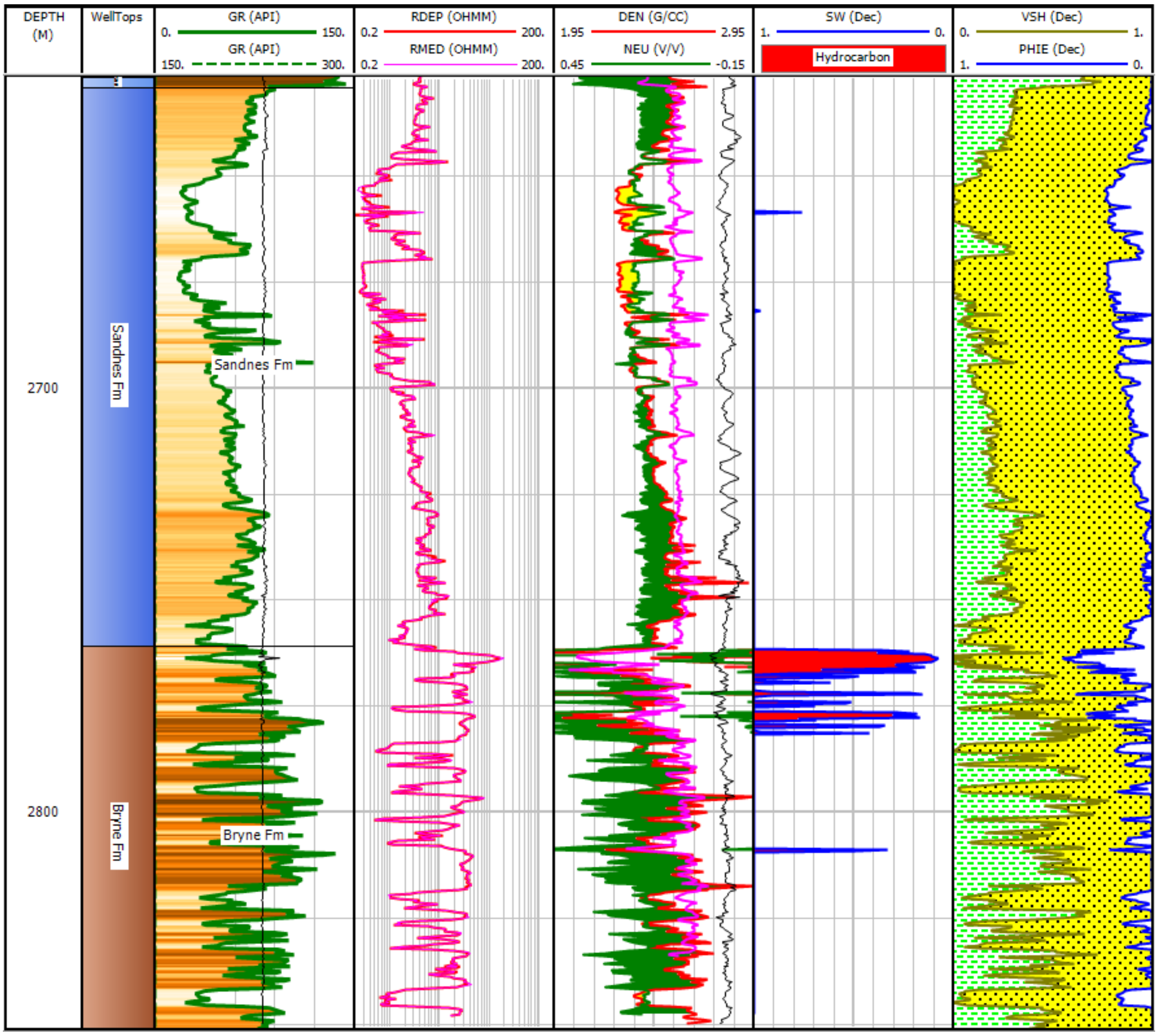

Figure B.3: Complete well 9/2-11 for reservoir target formations.

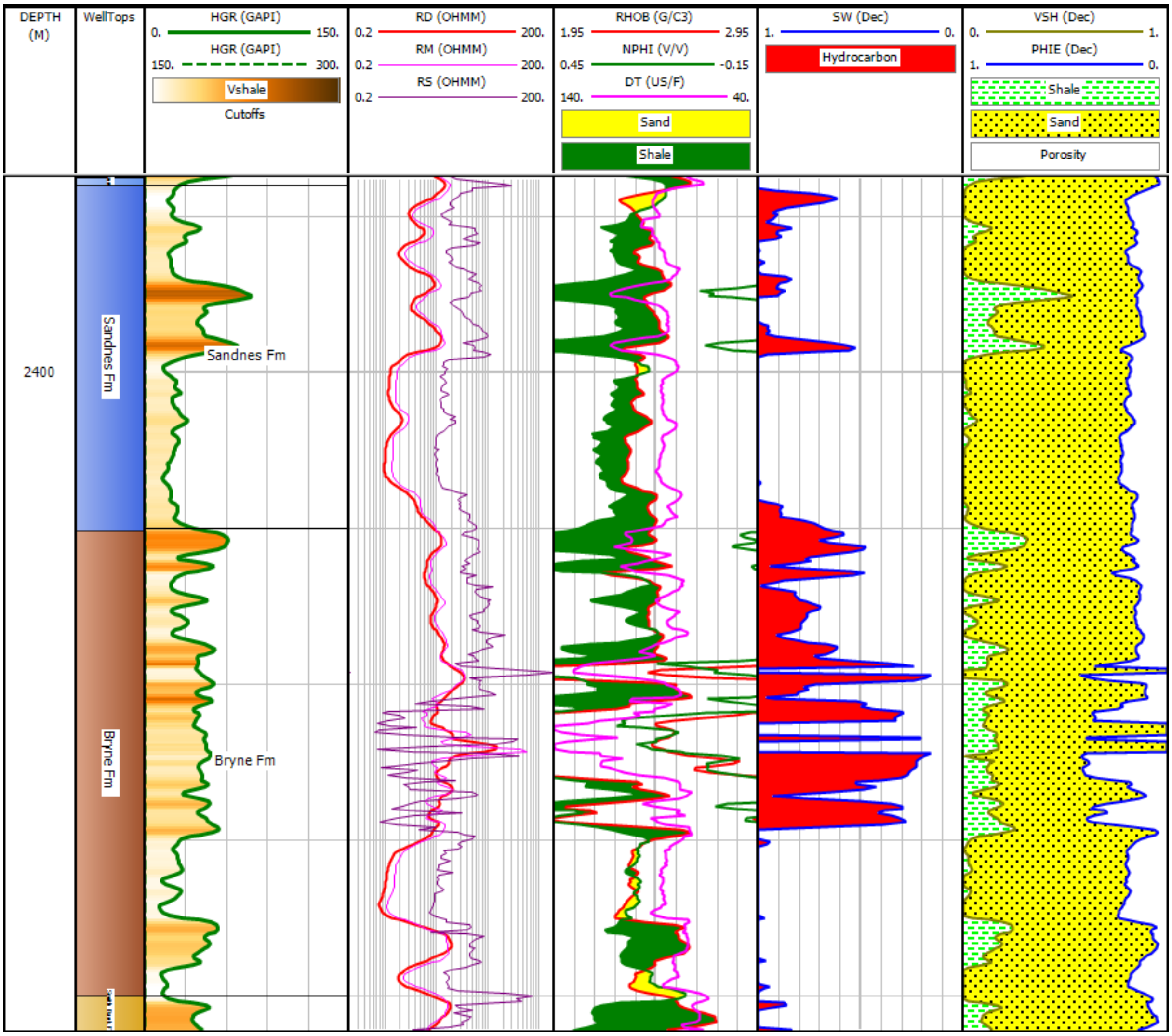

Figure B.4: Complete well 17/3-1 for reservoir target formations.

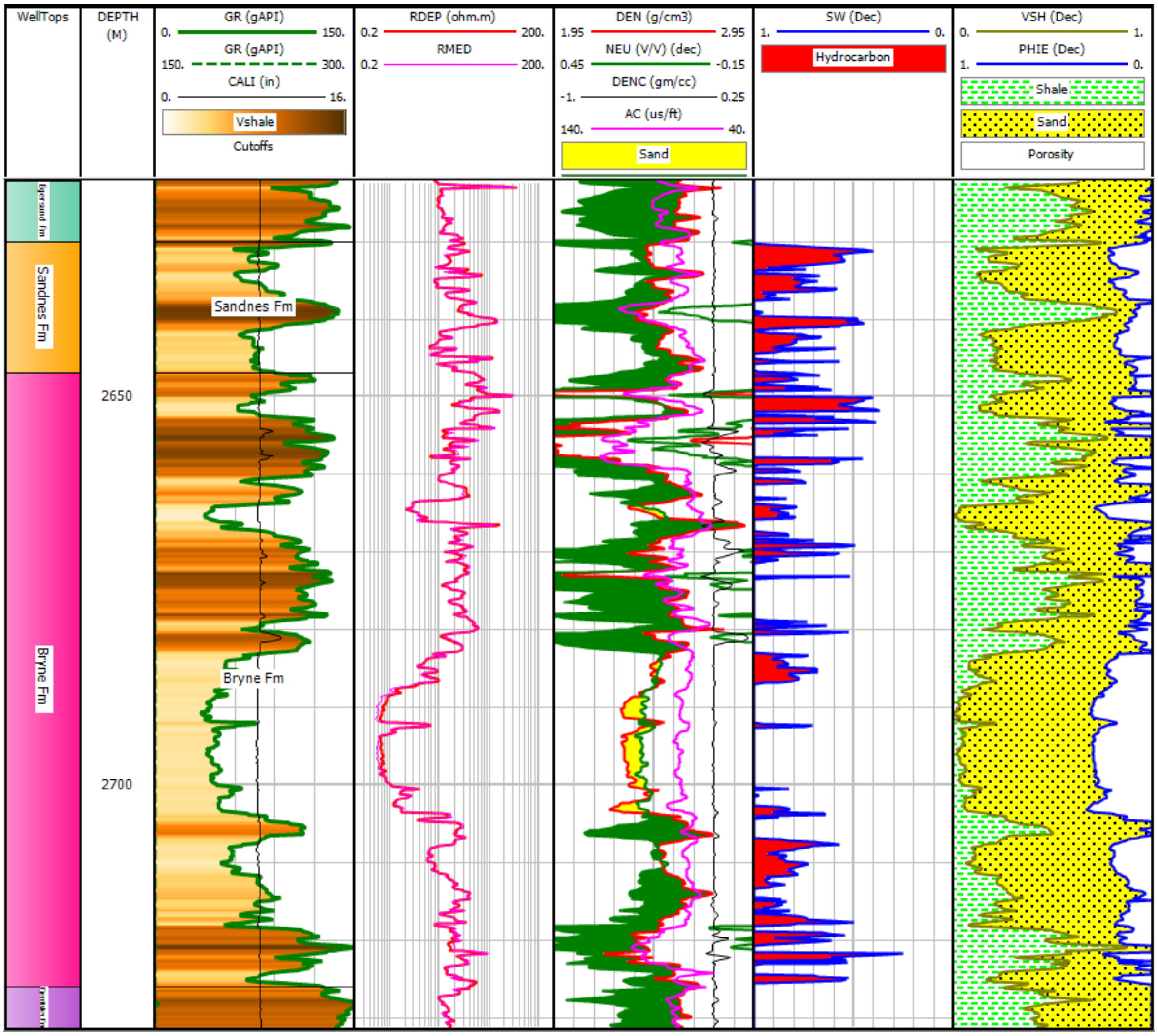

Figure B.5: Complete well 17/6-1 for reservoir target formations.

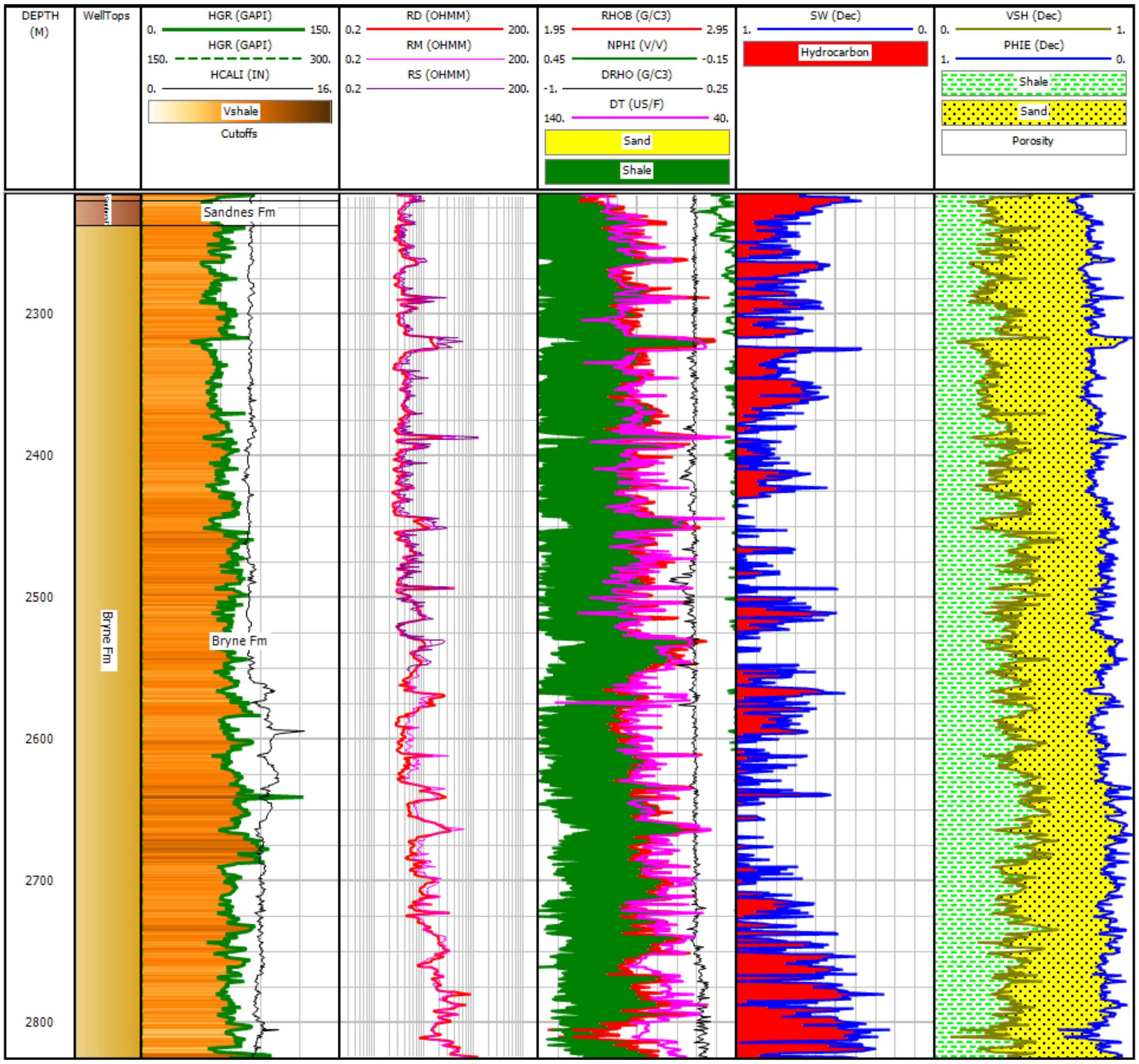

Figure B.6: Complete well 17/9-1 for reservoir target formations.

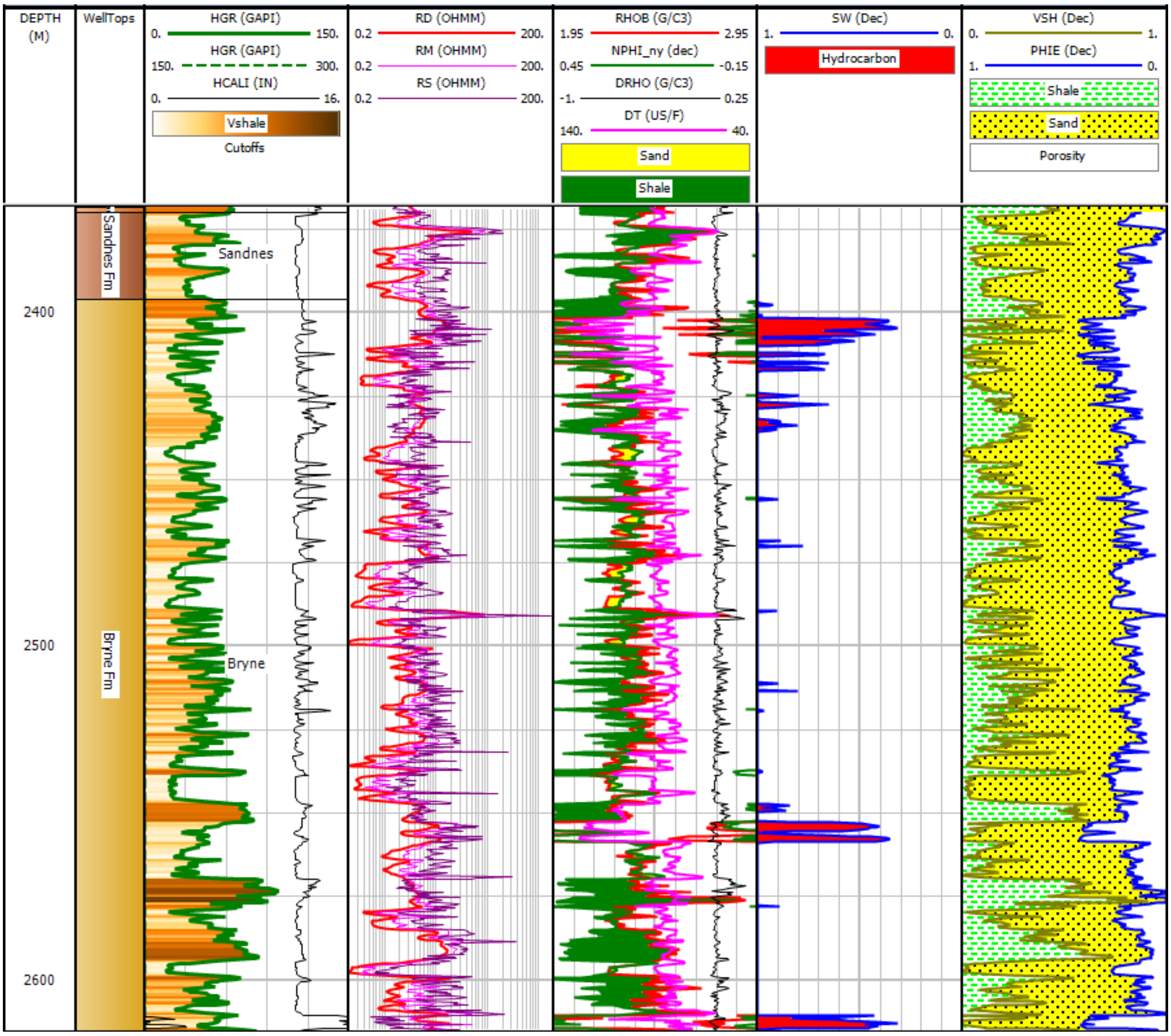

Figure B.7: Complete well 17/12-3 for reservoir target formations.

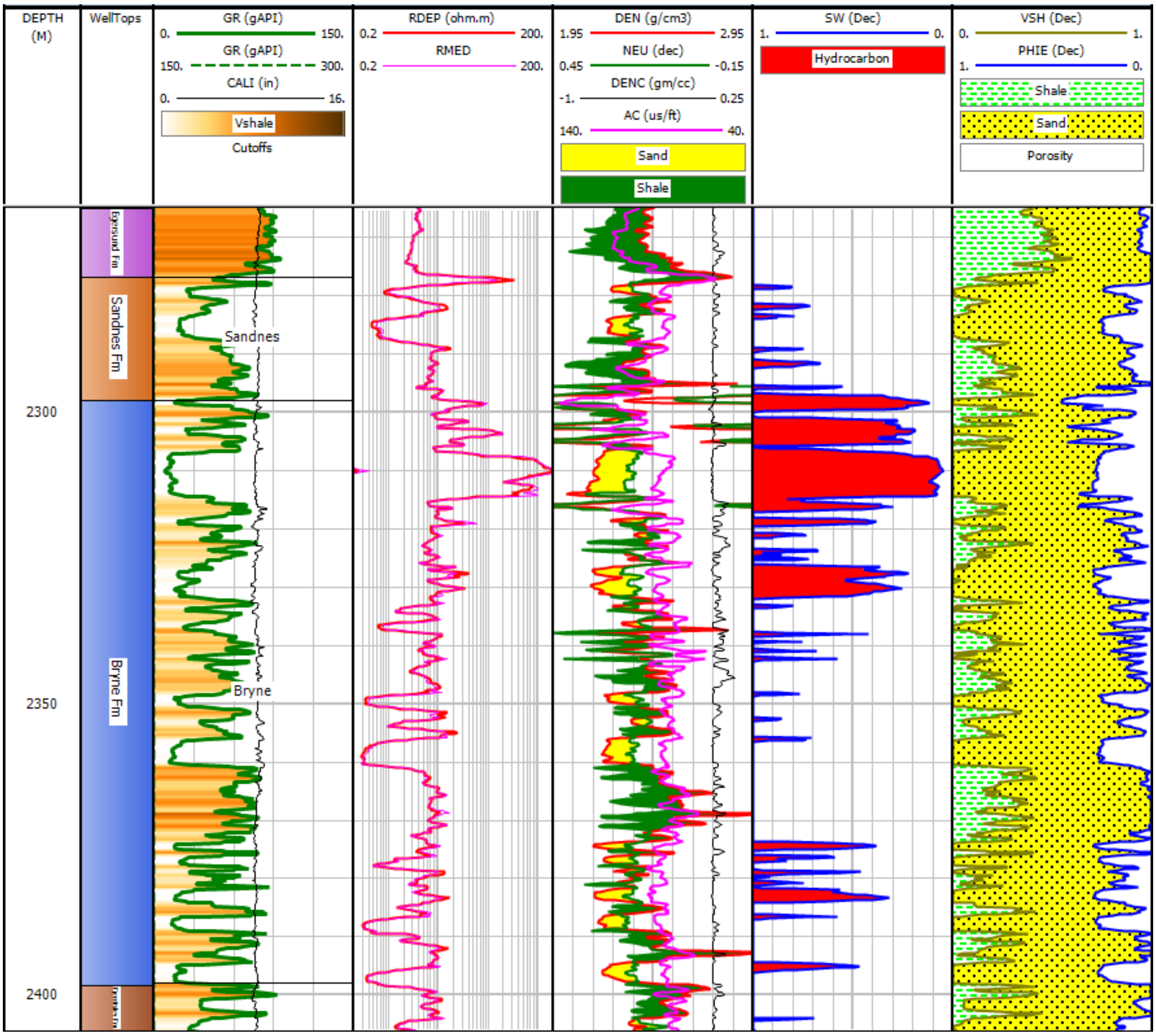

Figure B.8: Complete well 17/12-4 for reservoir target formations.

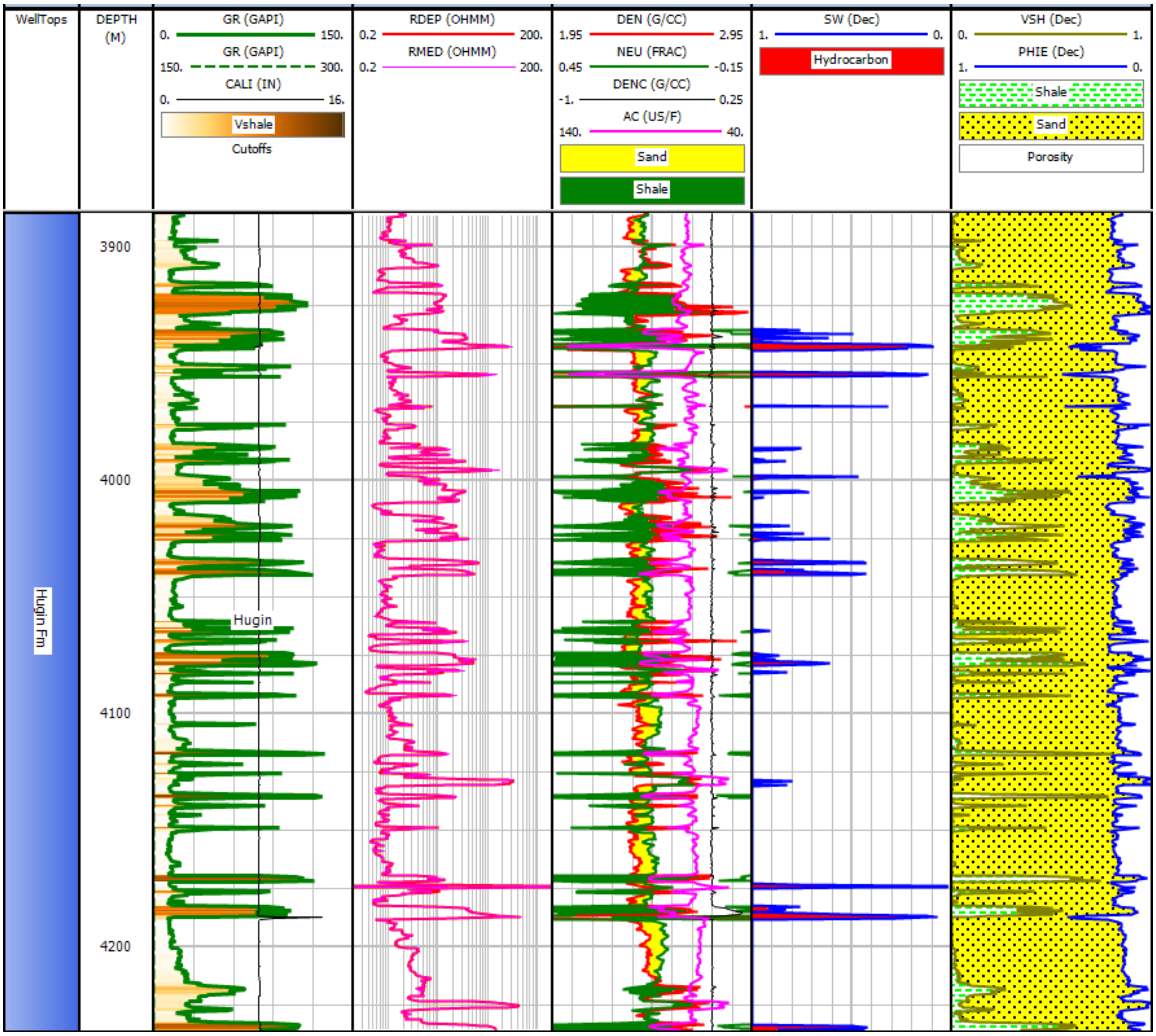

Figure B.9: Complete well 15/8-2 for reservoir target formation.

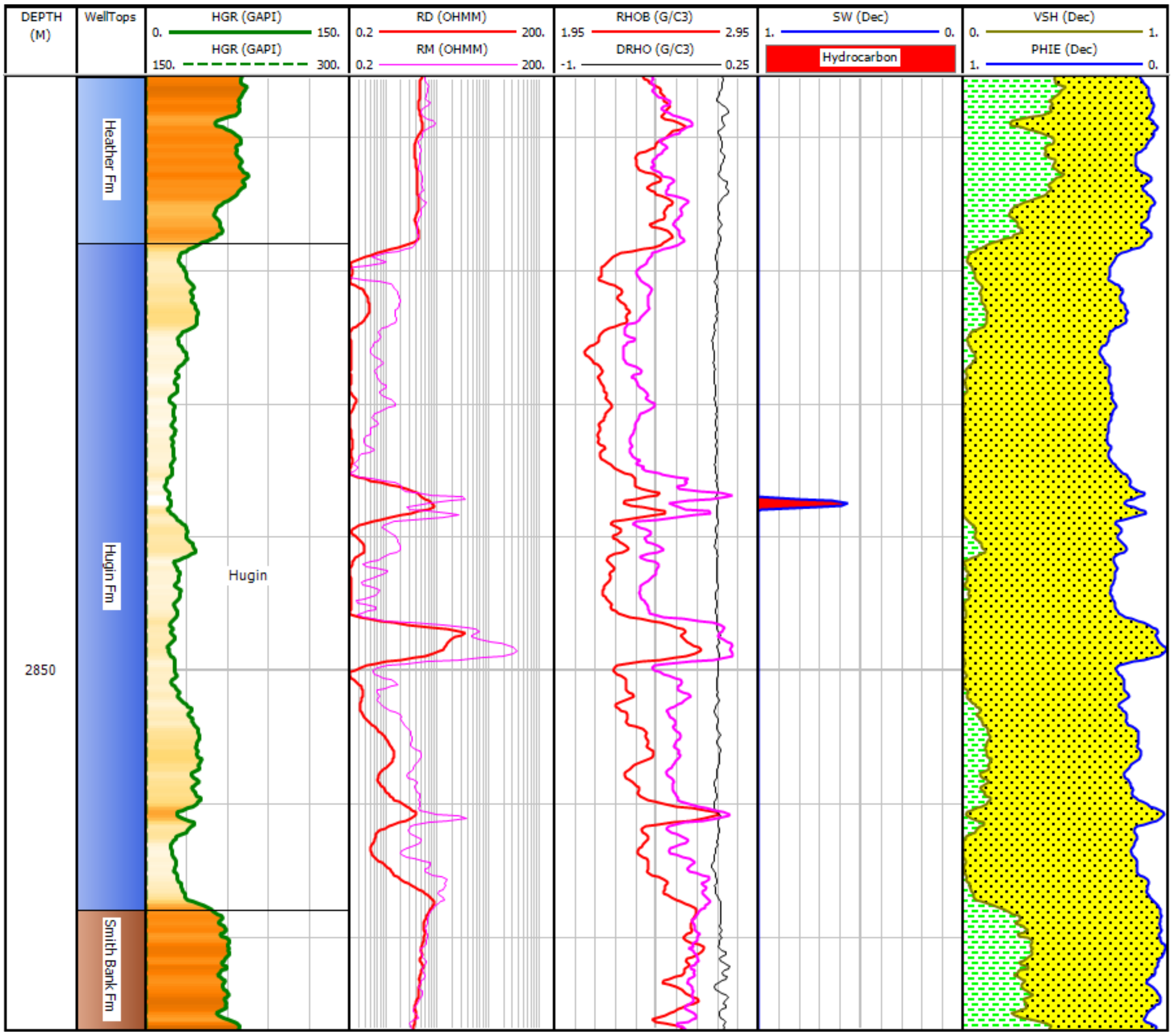

Figure B.10: Complete well 15/12-2 for reservoir target formation.

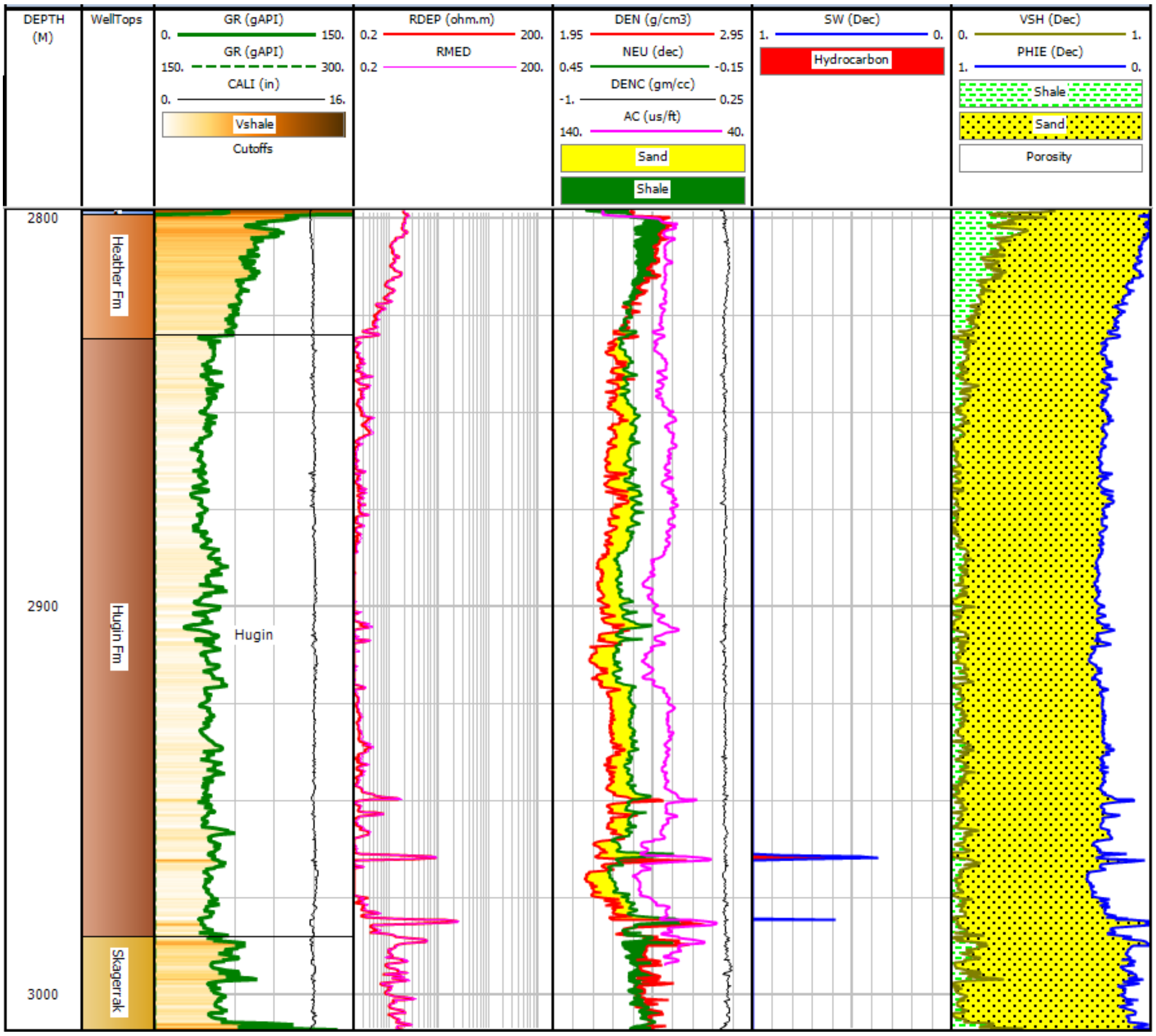

Figure B.11: Complete well 15/12-22 for reservoir target formation.

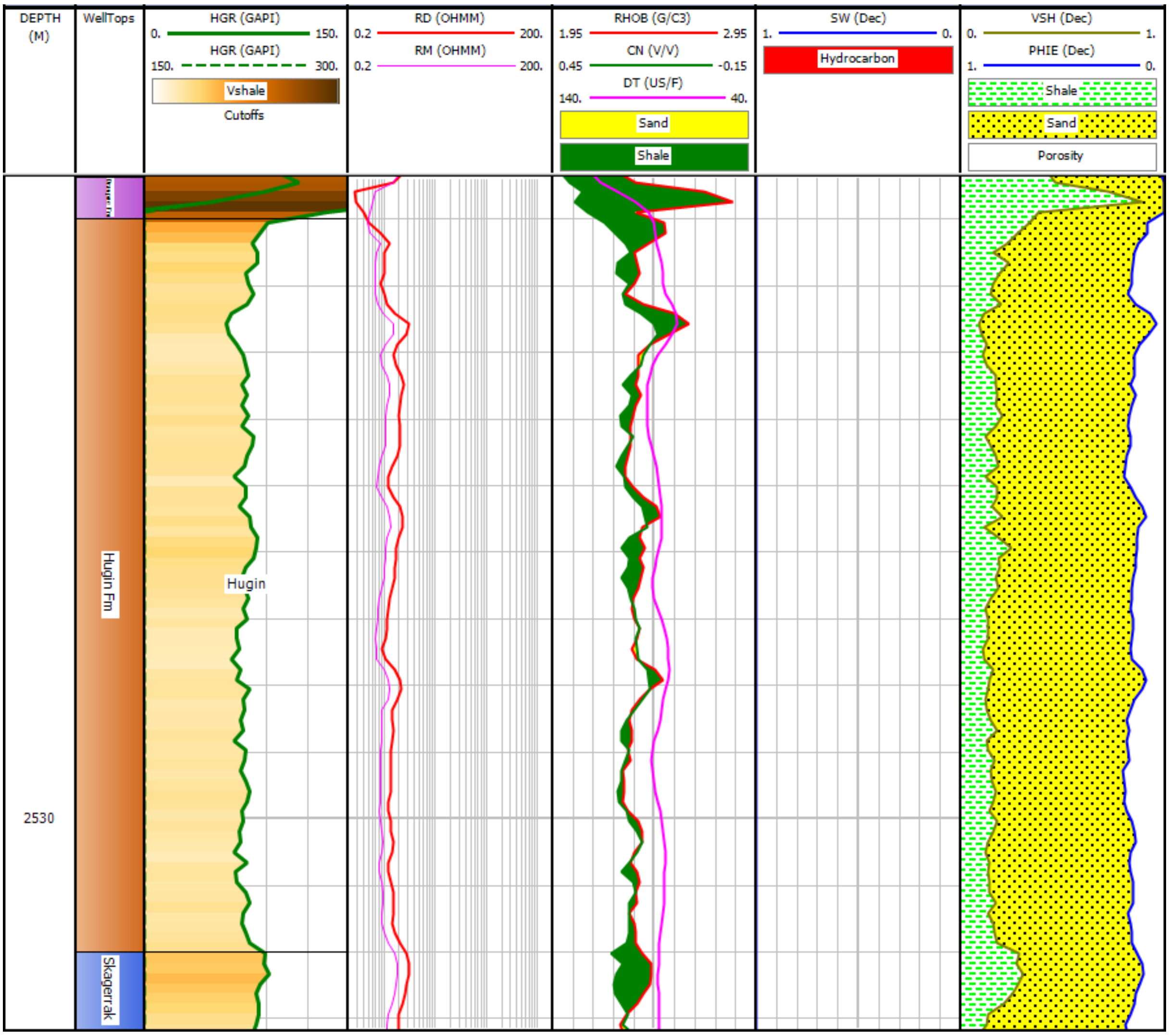

Figure B.12: Complete well 16/10-3 for reservoir target formation.

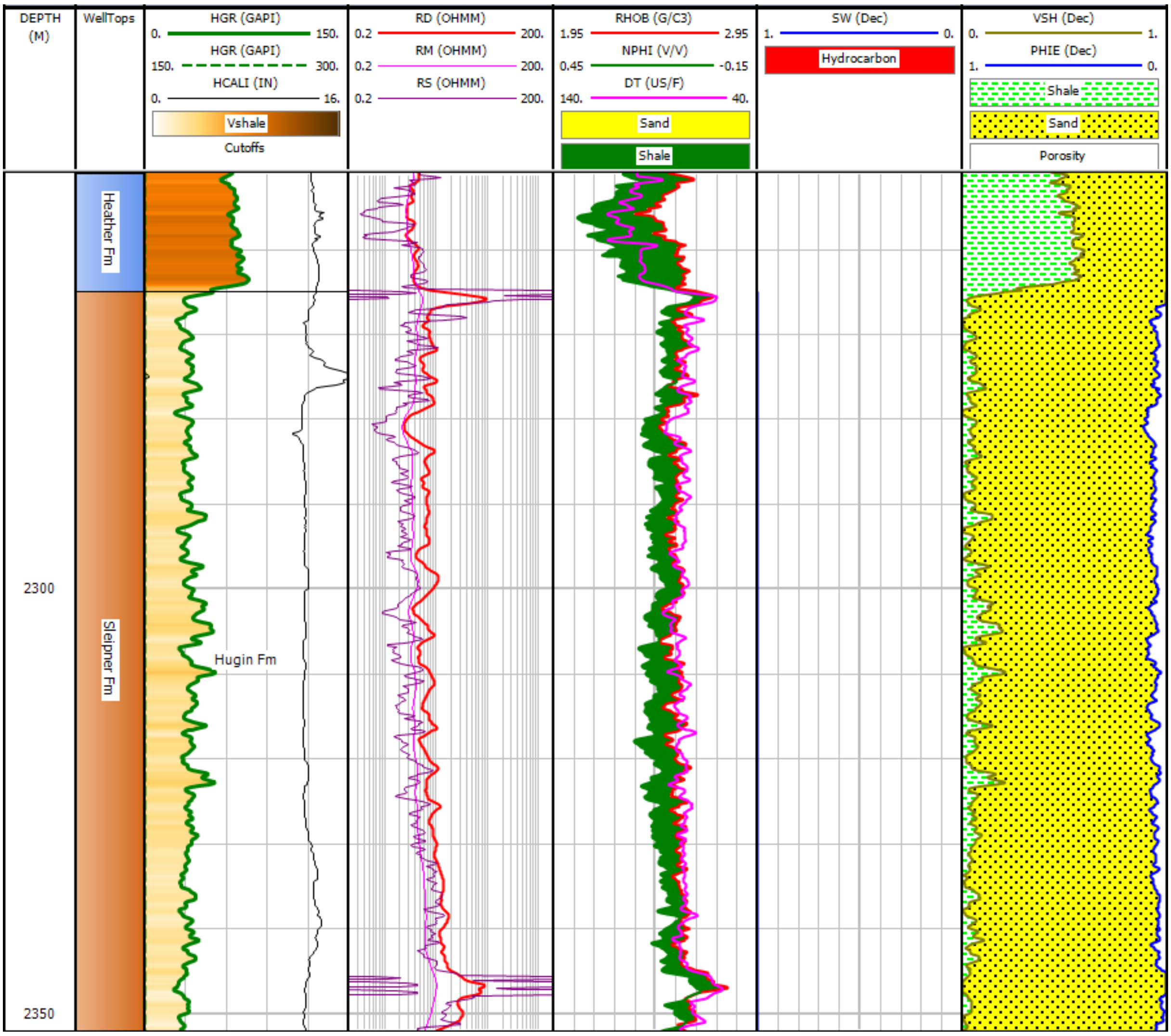

Figure B.13: Complete well 17/4-1 for reservoir target formation.